Optimising the NAOMI adaptive optics real-time control system

Goodsell, S. J.

Optimising the NAOMI Adaptive Optics Real-Time Control System

S. J. Goodsell

A thesis presented for the degree of

Doctor of Philosophy

Centre for Advanced Instrumentation

Department of Physics

University of Durham

October 2008

[INTENTIONALLY BLANK]

Optimising the NAOMI Adaptive Optics Real-Time Control System

S. J. Goodsell

Submitted for the degree of Doctor of Philosophy

October 2008

Abstract

This thesis describes the author's research in the field of Real-Time Control (RTC) for Adaptive Optics (AO) instrumentation. The research encompasses experiences and knowledge gained working in the area of RTC on astronomical instrumentation projects whilst at the Optical Science Laboratories (OSL), University College London (UCL), the Isaac Newton Groups of Telescopes (ING) and the Centre for Advanced Instrumentation (CfAI), Durham University. It begins by providing an extensive introduction to the field of Astronomical Adaptive Optics covering Image Correction Theory, Atmospheric Theory, Control Theory and Adaptive Optics Component Theory. The following chapter contains a review of the current state of world wide AO instruments and facilities. The Nasmyth Adaptive Optics Multi-purpose Instrument (NAOMI), the common user AO facility at the 4.2 William Herschel Telescope (WHT), is subsequently described. Results of NAOMI component characterisation experiments are detailed to provide a system understanding of the improvement optimisation could offer. The final chapter investigates how upgrading the RTCS could increase NAOMI's spatial and temporal performance and examines the RTCS in the context of Extremely Large Telescope (ELT) class telescopes.

Declaration

The work detailed in this thesis is based on research conducted at either the

- Optical Science Laboratories, University College London, United Kingdom
- Isaac Newton Group of Telescopes, La Palma, Spain
- Centre for Advanced Instrumentation, University of Durham, United Kingdom

No part of this thesis has been submitted elsewhere for any other degree or qualification and it is all work I was involved in unless referenced to the contrary in the text.

Acknowledgements

Firstly, I would like to thank former colleagues Mathew Thorn and Peter Gardiner, who encouraged me to apply for the position of Software Engineer at UCL, and Margaret Aderin (HROS Project Manager) for hiring me and supporting my original PhD application. I would like to acknowledge my original UCL supervisor David Walker and colleagues Richard Bingham, Andrew Charalambos, Paolo D'Arrigo, Peter Doel, Francisco Diego, Heshmet Jamshidi, Jim Percival and Trevor Savidge for their support, wisdom and camaraderie through some testing times. Collaborators and 'Reviewers' such as Steven Beard, Alastair Borrowman, Corienne Boyer, Pat Roache, Adrian Russell, Doug Simons, Mel Strachen, Philip Taylor, Chris Tierney and Colin Vincent deserve a mention for providing a wider insight into astronomy and astronomical instrumentation during my time at UCL.

Frank Gribbin deserves a special mention. Thanks to Frank, the ING financially supported my PhD when I accepted work there as a software engineer. He also suggested I approach Richard Myers to see if I could redirect my research from optimising the HROS active optics controller to optimising the NAOMI AO RTCS.

My thanks go to a number of ING staff, for their support, encouragement and friendship - Dennis Armstrong, Richard Bassom, Chris Benn, Craige Bevil, Maarten Blanken, Romano Corradi, Alan Chopping, Shelia Crosby, Colin Davenport, Kevin Dee, Les Edwin, Sebastian Els, Chris Evans, Marian Fisher, Joanne Goodger, Doug Gray, Tom Gregory, Andy Hide, Paul Jolley, Lucy Lawler, Gemma Leeks, Steve Magee, Roy Ostensen, Simon Rees, Robin Rutherford, Rene Rutten, Ilona Soecting, Gordon Talbot, Carrie Trundle, Michael Van Der Hoeven and Shelley Wright.

Whilst at the ING I interacted with many external collaborators, visiting astronomers, instrumentationalists and members of PPARC. In particular I would like to mention Andy Longmore and Sue Worswick for their influence.

Many members of CfAI at Durham University have given their support, in particular Francois Assemat, Alistair Basden, Ali Bharmal, Tim Butterley, Paul Clark, Nigel Dipper, Colin Dunlop, Deli Geng, Gordon Love, Simon Morris, Tim Morris, Chris Saunter, Ray Sharples, David Robertson and Richard Wilson. Support from my John Snow College colleagues has also made this possible especially Fiona Besford, Martyn Evans, Margaret Kuby, Karen Wesson and Laura Wilson.

Since 1999 many personal friends have motivated, supported and encouraged me. Thanks go to Stephanos Gosling, Kathrin Griesser, Katie Marshall, Ian Newman, Andy Rodrigues, Steve Rodrigues, Katya Toropynina, Shirley West and Octavia Woods-Walker.

Most importantly I must acknowledge the love and support of my family, Anne Goodsell, William Goodsell, Clare Worrell, Shane Worrell and Steve Worrell. A special thank you goes to my brother Peter Goodsell and my mother Virginia Goodsell for their unconditional love and support.

Finally, none of this would have been possible if it wasn't for the inspiration, vision and greatness of my supervisor and friend Richard Myers.

Contents

List of Tables

List of Figures

Glossary

AtDC	Atmospheric Dispersion Corrector
ADC	Analogue to Digital Converter
ADONIS	Adaptive Optics Near Infrared System
AdOpt@TNG	Adaptive Optics system for the Telescopio Nazionale Galileo
AdSec	Adaptive Secondary Mirror
AGW	Acquisition, Guiding & Wavefront Sensor
ATST	Advanced Technology Solar Telescope
AIT	Assembly Integration and Test
ALTAIR	ALTitude-conjugated Adaptive optics for InfraRed
AO	Adaptive Optics
AOF	Adaptive Optics Facility
AOS	Adaptive Optics System
AOWG	Adaptive Optics Working Group
APD	Avalanche PhotoDiode
API	Application Programming Interface
AS	Adaptive Secondary
ASTRON	Stichting ASTRonomisch Onderzoek in Nederland
AT	Auxiliary Telescope
ATC	Astronomy Technology Centre
BBST	Big Bear Solar Telescope
BC	Before Christ
BDM	Bimorph Deformable Mirror
BLT	Beam Launch Telescope
BSP	Bulk Synchronisation Parallelism
CAC	Computer Aided Control
CAMCAO	Camera for MCAO
CARA	California Association for Research in Astronomy
CC	Command Control
CCD	Charged Couple Device
CDR	Critical Design Review
CfAI	Centre for Adaptive Optics
CFDM	Continuous Facesheet Deformable Mirror
CFHT	Canadian French Hawaiian Telescope
CHEOPS	Characterizing Extrasolar planets by Opto infrared Polarimetry
CIAO	Coronagraphic Imager with Adaptive Optics
CMOS	Complementary metal–oxide–semiconductor
CNRS	Centre National de la Recherche Scientifique
CO	COME-ON
CoDR	Conceptual Design Review
CONICA	Coudé Near IR Camera
COP	COME-ON-PLUS
COTS	Commercial Off The Shelf
CP	Command Processor
CPU	Central Processing Unit
CRAL	Centre de Recherche Astronomique de Lyon
CRIRES	Cryogenic IR Echelle Spectrograph
CRL	Communications Research Laboratory

CWFS	Curvature Wavefront Sensor
DAC	Digital Analogue Converter
DACR	Digital Analogue Converter Rack
DCS	Double Correlated Sampling
DIMM	Differential Image Motion Monitor
DM	Deformable Mirror
DMA	Direct Memory Access
DNS	Domain Name Server
DSP	Digital Signal Processor
DST	Dunn Solar Telescope
DTM	Data Transfer Mechanism
E-ELT	European Extremely Large Telescope
ELECTRA	Enhanced Light Efficiency Cophasing Telescope Resolution Actuator
ELS	Elektronik Laser System
ELT	Extremely Large Telescope
EPICS	Experimental Physics and Industrial Control System
EPM	Electra Process Monitor
ESI	ESO Shearing Interferometer
ESO	European Southern Observatory
FIERA	Fast Imager Electronic Readout Assembly
FIFO	First In First Out
FLAMINGOS	Florida Multi-object Imaging Near IR Grism Observational Spectrometer
FOV	Field Of View
FPDP	Front Panel Data Port
FPGA	Field Programmable Gate Array
FSM	Fast Steering Mirror
FSMSF	Fast Steering Mirror Signal Filter
FTP	File Transfer Protocol
FWHM	Full Width Half Maximum
GAOS	Gemini Adaptive Optics System
GHRIL	Ground-based High Resolution Imaging Laboratory
GLAO	Ground Layer Adaptive Optics
GLAS	Ground-layer Laser Adaptive optics System
GMOS	Gemini Multi Object Spectrograph
GMT	Giant Magellan Telescope
GP	General Purpose
GPI	Gemini Planet Imager
GRACE	Ground based Adaptive optics Controlled Environment
GSAO	Gemini South Adaptive Optics
GSAOI	Gemini South Adaptive Optics Imager
GTC	Gran Telescopio Canarias
GUI	Graphical User Interface
HAP	Half Arcsecond Programme
HAWK-I	High Acuity Wide field K-band Imager
HET	Hobby Eberly Telescope
HOT	High Order Testbed
HROS	High Resolution Optical Spectrograph
HVA	High Voltage Amplifier
HVA	High Voltage Amplifier Rack
IA-UNAM	Instituto de Astronomia de la Universidad Nacional Autonoma de Mexico

IAC	Instituto de Astrofisica de Canarias
IC	Integrated Circuit
INAOE	Instituto Nacional de Astrofisca, Optica y Electronica
ING	Isaac Newton Group
INGRID	Isaac Newton Group Red Imaging Detector
INT	Isaac Newton Telescope
IR	Infrared
IRACE	InfraRed Array Control Electronics
IRCS	InfraRed Camera and Spectrograph
IRSHWFS	Infrared SHWFS
ISA	Industry Standard Architecture
ISR	Interrupt Service Routine
ISS	Instrument Support Structure
JKT	Jacobus Kapteyn Telescope
JOSE	Joint Observatories Seeing Evaluation
JRA	Joint Research Activity
JTAG	Joint Test Action Group
KPAO	Keck Precision Adaptive Optics
L3	Low Light Level
LAOG	Laboratoire d'Astrophysique l'Observatoire de Grenoble
LBT	Large Binocular Telescope
LC	Liquid Crystal
LCS	Laser Collision System
LCU	Local Control Unit
LGS	Laser Guide Star
LGSAO	Laser Guide Star Adaptive Optics
LGSF	Laser Guide Star Facility
LIA	Link Interface Adaptors
LLNL	Lawrence Livermore National Laboratory
LOWFS	Layer Oriented Wavefront Sensor
LSI	Lateral Shearing Interferometer
LT	Love Train
LTAO	Laser Tomographic Adaptive Optics
LWS	Long Wave Spectrometer
MACAO	Multi Application Curvature Adaptive Optics
MAD	MCAO Demonstrator
MARTINI	Multi-Aperture Real-time Image Normalisation Instrument
MCAO	Multi Conjugate Adative Optics
MEM	Micro Electric deformable Mirror
MFLOPS	Million Floating Point Operations Per Second
MIMO	Multiple input, multiple output
MIPS	Million Instructions Per Second
MIT	Massachusetts Institute of Technology
MMT	Multiple Mirror Telescope
MMTAO	MMT NGS AO
MOAO	Multi Object Adaptive Optics
MPIA	Max Planck Institut für Astronommie
MPIE	Max Planck Institut für Extraterrestrische Physik
MPM	Monolithic Piezoelectric Mirrors
MSR	Multiple Successive Readout

MUSE	Multi Unit Spectrographic Explorer
NACO	NAOS-CONICA
NAOJ	National Astronomical Observatory of Japan
NAOMI	Nasmyth Adaptive Optics Multi-purpose Instrument
NAOS	Nasmyth Adaptive Optics System
NASA	National Aeronautics and Space Administration
NAVIS	Naomi Visualisation
NCSA	National Center for Supercomputing Applications
NCU	Nasmyth Calibration Unit
NFM	Narrow Field Mode
NGS	Natural Guide Star
NGWFC	Next Generation Wavefront Controller
NICI	Near Infrared Coronagraphic Imager
NIFS	Near Infrared Integral Field Spectrograph
NIRC	Near Infrared Camera
NIRI	Near Infrared Imager
NIRSPEC	Near Infrared Spectrometer
NNGRTC	NAOMI Next Generation Real-time Controller
NOT	NAOMI Optical Table
NRC	National Research Council of Canada
NSTT	New Swedish Solar Telescope
NWO	Nederlandse Organisatie voor Wetenschappelijk Onderzoek
OAP	Off Axis Parabola
OASIS	Optically Active System for Imaging Spectroscopy
OHP	Observatoire de Haute Provence
OIWFS	On Instrument Wavefront Sensor
OMC	Opto-Mechanical Chassis
ONERA	Office National d' Etudes et de Recherches Aérospatiales
OPD	Optical Path Difference
OPTICON	Optical Infrared Coordination Network for Astronomy
ORM	Observatory Roque de Los Muchachos
OSCA	Optimised Stellar Coronagraph for Adaptive Optics
OSIRIS	OH Suppressed IR Imaging System
OSL	Optical Science Laboratory
OTF	Optical Transfer Function
OWL	Overwhelmingly Large Telescope
P^4	Projected Pupil Plane Patterns
PBT	Parameter Block Transactions
PCB	Power Control Boards
PCI	Peripheral Component Interconnect
PDR	Preliminary Design Review
PhD	Doctorate of Philosophy
PI	Physik Instrumente
PID	Proportional, Integral, Differential,
PMN	Lead Magnesium Niobate $Pb(Mg_{1/3}, Nb_{2/3})O_3$
PPARC	Particle Physics and Astronomy Research Council
PPC	Power PC
PRA	Piston Removal Algorithm
PSF	Point Spread Function
PUEO	Probing the University with Enhanced Optics

PWFS	Pyramid Wavefront Sensor
PZT	Lead Ziconate Titanate Pb(Zr,Ti)O3
R&D	Research and Development
RGO	Royal Greenwich Observatory
RH	Relative Humidity
ROE	Royal Observatory Edinburgh
RON	Read Out Noise
RP	Reconstruction Parameter
RTAC	Real-Time Atmospheric Compensation
RTC	Real-Time Control
RTCR	Real-Time Control Rack
RTCS	Real-Time Control System
SA	Subaperature
SALT	South African Large Telescope
SBA	Sin Bin Amplifier
SC	Statistical Computing
SCAO	Single Conjugate Adaptive Optics
SCSI	Small Computer System Interface
SDM	Segmented Deformable Mirror
SDSU	San Diego State University
SG	Strain Gauge
SGAR	Strain Gauge Amplifier Rack
SHWFS	Shack Hartmann Wavefront Sensor
SINFONI	Spectrograph for INtergral Field Observations in the Near Infrared
SLODAR	Slope Detection and Ranging
SOWFS	Star Oriented Wavefront Sensor
SPARTA	Standard Platform for Adaptive optics Real-Time Applications
SPIE	Society of Photo-Optical Instrumentation Engineers
SPIFFI	SPectrometer for Infrared Faint Field Imaging
SPLASH	Sky-projected Laser Array Shack Hartmann
SR	Strehl Ratio
STRAP	System for Tip-Tilt Removal with Avalanche Photodiodes
SVD	Singular Value Decomposition
TCP/IP	Transmission Control Protocol / Internet Protocol
TI	Texas Instruments
TIM	TTC Interface Module
TOSC	The Optical Sciences Company
TMT	Thirty Meter Telescope
TNG	Telescopio Nazionale Galileo
TT	Tip-tilt
TTC	Timing, Trigger & Control
TTM	Tip-tilt Mirror
TTMo	Tip-tilt Mount
UCL	University College London
UH	University of Hawaii
UKATC	United Kingdom Astronomy Technology Centre
UKIRT	United Kingdom Infrared Telescope
UoD	University of Durham
USP	Universal Science Port
UT	Unit Telescope

VINCI	VLT Interferometer Commissioning Instrument
VLT	Very Large Telescope
VLTI	Very Large Telescope Interferometer
VME	Versa Module Europa
VSHWFS	Visible SHWFS
VTT	Vacuum Tower Telescope
WCS	Wavefront Control System
WF	Wavefront
WFC	Wavefront Corrector
WFCS	Wavefront Correction System
WFM	Wide Field Mode
WFS	Wavefront Sensor
WHIRCAM	William Herschel Infrared Camera
WHT	William Herschel Telescope
WMKO	William M Keck Observatory
WP	Work Package
XAO	eXtreme Adaptive Optics
YAG	Yttrium Aluminium Garnet
ZIF	Zero Insertion Force

1 Introduction

Adaptive Optics (AO) has become a fundamental requirement for the future generation of ground-based optical/infrared telescopes (30-50m). The purpose of astronomical AO systems is to compensate for aberrations by measuring them and negating their effect. The complex task of designing the 42m European-Extremely Large Telescope (E-ELT) is under way. There are a number of important sub-systems and considerations that will define the capabilities of the telescope. The AO subsystem is amongst them; it is as important as the optical design of the telescope, the global location of the telescope and its instrumentation. Whilst existing telescopes have benefited from AO, the E-ELT will be dependent on AO. The AO systems for the current generation of 8-10 m class telescopes progresses our understanding of the subject. AO instrumentation has successfully demonstrated the ability to overcome the previously limiting effects that the turbulent atmosphere has on the light that propagates through it.

The field of AO research currently includes a range of concepts such as Ground Layer AO (GLAO), Single Conjugate AO (SCAO), Multi-Conjugate AO (MCAO), Laser Tomographic AO (LTAO), eXtreme AO (XAO) and Multi-Object AO (MOAO). Each mode will give the E-ELT a different capability and will allow astronomers to conduct different types of observations. These modes have evolved with the experience of using 4-8m class telescopes. Durham University are currently trying to solve challenges associated with future 8-10 m class AO instrumentation and to mitigate identified risks associated with ELT sized AO systems. They are currently researching a number of novel Laser Guide Star (LGS) concepts that are designed to overcome such problems as anisoplanatism. Durham are involved in many AO activities such as segment co-phasing, simulation, common user launch systems, instrument designs, real-time control systems, ELT MOAO risk mitigation and ELT instrument designs.

Real-time Control Systems (RTCS) is a major area of AO. Each ELT AO mode will require real-time control and some of these modes present significant challenges at ELT scales. This represents an important context for this work. RTCSs are currently spreading into a new technological area. The Central Processor Unit (CPU) has been the main device used in real-time control hardware and embedded systems. The majority of AO RTCS uses CPUs. More specialised applications have used the Digital Signal Processor (DSP) as the main processing device. DSPs have high interconnection bandwidth and have been the host device for many AO RTCS including the Nasmyth AO for Multi-purpose Instrumentation (NAOMI) at the William Herschel Telescope (WHT). More recently, the Field Programmable Gate Array (FPGA) has been considered as the main computation device for AO RTCS. It is predicted that it will eventually replace the CPU and DSP as the standard device of choice. Second-generation VLT instruments will use FPGAs for a significant part of the processing required. ELTs will be dependant on FPGAs; to what extent will depend on how the industry evolves over the next decade. Programming these devices demands a different skill set than that required for traditional software engineering.

AO instruments continue to increase in complexity. Wavefront Sensors (WFS) require more pixels and more subapertures, and Deformable Mirrors (DM) will require more degrees of freedom. Some instruments have multiple DMs and/or multiple WFS. Different AO modes not only require future RTCS to be versatile in their inputs and outputs, but with the increase of order, the RTCS has to deal with increased temporal bandwidth, which requires lower latency (effectively processing delay). Different AO systems require smarter algorithms, more sophisticated reconstructors, DM position feedback (e.g., for MOAO) and self-optimising

algorithms based on the information entering the system. LTAO requires woofer-tweeter control.

Designing next-generation AO facilities for future telescopes is arguably impossible unless one possesses a good theoretical understanding of the subject together with practical experience of operation. There was a significant learning curve associated with the first-generation AO instruments commissioned on the 4m and 8m class telescopes. Those lessons learned have proved to be vital when designing and building subsequent systems. The first-generation of operational systems are still being improved and optimised and they provide a good testbed for new ideas and concepts. An excellent example in this respect is the Keck LGS AO facility, which is currently considered to be world leading. This level of performance was attained through a 3-year post-commissioning programme of comprehensive system-level performance analysis. A similar comprehensive systems approach was taken with respect to the WHT performance analysis presented here, even though the particular emphasis is on the design of a real-time control upgrade.

The work described here was conducted at University College London between January 2000 and February 2001, Isaac Newton Group of Telescopes between February 2001 and July 2004 and Durham University between August 2004 and June 2007.

Thesis Synopsis

This thesis describes a design for an optimised real-time control system for the Nasmyth AO for Multi Purpose Instrumentation (NAOMI) facility on the 4.2 m William Hershel Telescope (WHT).

The thesis introduces the theory required to understand astronomical AO and to optimise a system's real-time controller to maximise performance. A review of the operational systems worldwide is detailed before specifically looking at the inner workings of the NAOMI facility. The experiments to characterise NAOMI's subsystems is described. The component results and system analysis conclude that a new RTCS is required to host an optimised controller. A RTCS design is presented alongside the potential gains of implementing an optimal controller. This work is placed into context of the E-ELT requirements.

This thesis uses as its subject the NAOMI AO system and presents a design for an optimised control system based on NAOMI's measured responses. NAOMI is chosen because extensive characterisation measurements are available from its unique internal DM position monitoring system. The optimisation techniques are also shown to be applicable to other AO systems including those planned for ELTs. The techniques could also, of course, be applied to NAOMI itself, subject to funding for a facility-level implementation of all or part of the design described here.

Chapter 2 Theoretical Considerations for AO System Optimisation

This chapter examines the theoretical material required to understand astronomical AO. The chapter is divided into four subsections: AO image correction theory, atmospheric turbulence theory, control theory and AO system theory. AO image correction theory examines optical telescopes, angular resolution and seeing, wavefront propagation and aberrations, Strehl ratio and the Maréchal Criterion, Zernike Series and phase conjugation. Atmospheric turbulence theory covers Kolmogorov turbulence, propagation effects, Fried's coherence length, temporal

behaviour, angle of arrival statistics and angular anisoplanatism. Control theory introduces Laplace transforms, transfer functions, first and second order systems, frequency domain, controllers and the Smith Predictor. The latter is identified as a promising DM controller. To conclude the chapter, the AO system theory examines the main components, the wavefront sampler, the wavefront sensor, the wavefront corrector and the controller.

Chapter 3 Astronomical AO Systems Review

Chapter 3 examines the major astronomical AO systems worldwide. It starts with a review of the European Southern Observatory and introduces the COME-ON and COME-ON+ prototypes, ADONIS, NAOS, MACAO, MAD and the AOF. The AO history and instruments of Gemini follow, with a description of Hokupa'a, ALTAIR, NICI and MCAO. Descriptions of the AO facilities at Keck Observatory and on Subaru precede a roundup of other telescopes including the MMT, Calar Alto, TNG, Lick Observatory and the CFHT.

Chapter 4 Nasmyth AO for Multi-purpose Instrumentation

This chapter describes the NAOMI facility. The section begins by introducing the WHT telescope. A description of NAOMI's environment and scientific instruments follows, including a description of GLAS, its common user facility laser guide star upgrade. The main components of NAOMI are then discussed; its tip-tilt mirror, its deformable mirror, its wavefront sensors and finally its RTCS and associated hardware.

Chapter 5 Characterisation Experiments

Chapter 5 describes the characterisation experiments executed to understand NAOMI's components performance. Experiments were attempted to measure the temperature stability within GRACE, the latency associated with the FSM, to understand the temporal and spatial response of each SDM actuator, the latency associated with the WFS and the bandwidth and latency of the RTCS. In addition to characterisation, improvements were made, attempted or suggested. They include attempting to balance the load within the RTCS, introducing a PID Controller to the FSM, creating additional WFS modes and suggesting how to stablise the temperature further in GRACE. The results from the characterisation experiments indicate the limitations of the existing controller in terms of latency and bandwidth. These conclusions are discussed. For each the potential increase in performance was estimated.

Chapter 6 NAOMI Next Generation Real-time Controller (NNGRTC)

This chapter looks at the shortcomings of the NAOMI's RTCS and suggests how it could be upgraded and improved to host an optimised controller. The general and specific requirements are discussed for the design of a next-generation controller. Firstly contained is a discussion of the requirements, secondly the control platform is discussed. The control hardware is described. The pipeline design for NAOMI is given. Performance estimations are given before discussing other considerations such as the use of a simulation environment. Finally the RTCS design is placed into context of E-ELTs.

Chapter 7 Conclusion

The thesis concludes by placing the research into context. It reviews the existing limitation of NAOMI and compares its performance with the future possibilities by replacing the RTCS hardware and optimising the new system.

2 Theoretical Considerations for AO System Optimisation

The characterisation and optimisation of an astronomical adaptive optics (AO) instrument requires an appreciation of both Astronomical AO Image Correction and Atmospheric Theory. One must appreciate the relation between the atmosphere and the telescope's adaptive optics system (AOS), enabling one to simulate a complete operational model. Such models are vital to understand the parameters involved in system optimisation. This chapter introduces Astronomical AO Image Correction and Atmospheric Theory before examining the principles behind another essential optimisation topic; Control Theory. The final subsection of this chapter concentrates on AOS Theory, examining the operation of the key components. Again, this is not just important for design but also for optimisation and upgrading the system to improve its performance.

This chapter also prepares the way for the subsequent review chapter that examines the current state of the worldwide astronomical AOS.

2.1 Astronomical Adaptive Optics Image Correction Theory

The definition of AO continues to evolve with the subject. Current popular AO textbooks contain variations of its definition.[1,2,3] AO can be described as a scientific and engineering discipline used to enhance the capabilities of an optical system by real-time closed-loop compensation of aberrations.

There was no 'inventor' of AO. The subject evolved from the understanding of wave propagation. AO combines elements from many disciplines including optics, electro-optics, chemistry and engineering; optical, electrical, mechanical, control and software. Over the last 30 years, hundreds of scientists and engineers have contributed to its development. The desirability of obtaining an undistorted image has made AO a scientific and engineering discipline in its own right.

In astronomy, AO is primarily used to compensate for the aberrations caused by atmospheric turbulence. In addition, AO can also be used to correct for wavefront (WF) errors caused by optical fabrication errors, thermally induced distortions and misalignment errors. Whatever the distortion, it is important to understand and characterise it before trying to compensate and correct it.

AO can be considered as a closely related discipline to **Active Optics**. Active optics most generally is described as the control of an optical component by the way of an intelligent system. The distinction between an AOS and an active optics system is normally based on frequency response, with an AOS capable of much faster corrections (kHz rather than Hz).

The subject of AO can be traced throughout history. In 215 BC AO was used during Archimedes' destruction of an attacking Roman fleet as the fleet approached an army defending Syracuse.[4] Nearly 2000 years later, Isaac Newton commented on the problem of the atmospheric turbulence limitations of astronomy in *Opticks*.[5] Until recently, AO has been severely restricted by the technology available. AO was not pursued until 1953 when Babcock[6] suggested using a deformable optical element, driven by a wavefront sensor, to compensate for atmospheric distortions that affected telescope images.

"*If we had a means of continually measuring the deviation of rays from all parts of the mirror, and amplifying and feeding back this information so as to correct locally the figure of the mirror in response to the schlieren pattern, we could expect to compensate both for the seeing and for any inherent imperfections of optical figure.*"

Babcock's attempt to implement the technique was unsuccessful in astronomical terms. The developmental cost to produce an AOS would have been too expensive. Technology would have limited the performance of all three major sub-systems, the wavefront sensor (WFS), the deformable mirror (DM) and the real-time control system (RTCS). At the time the WFS was dominated by detector noise.

There was little progress made until 1970 when Antoine Labeyrie's speckle interferometry demonstrated that is was indeed possible to overcome the effect of atmospheric turbulence.[7] Following this, astronomers focused their efforts on developing 'post-detection' image processing techniques to improve the resolution of astronomical images. Meanwhile, defence-oriented research started to use segmented mirrors to compensate the effect of the atmosphere in attempts to concentrate laser beams on remote targets.

The first AO system was successfully built by Hardy at Itek[8]. This resulted in a larger version, the "Real-Time Atmospheric Compensation" (RTAC) system being installed at the Air-Force Maui Optical Site on Haleakala. ESO installed the first astronomical AOS on one of their 3.6m telescopes in Chile in the early 90's, see section 3.1.2.

2.1.1 Optical Telescopes

Optical telescopes became the most important instrument in astronomy during the 17th century, when Galileo started using them for astronomical observations. Unlike the refractor telescope used by Galileo, most modern telescopes are **Reflectors**. Reflectors focus light through reflections from mirrors with a conic surface.

Modern telescopes generally contain a number of scientific instruments, each one giving the telescope increased scientific capability. Instruments are placed at various focal points. Telescopes differ from each other in how the focused light reflected by the primary is collected, see Figure 2.1. The focal point of the primary mirror is called **Prime** focus. It is commonly used for imaging of very faint objects and for wide-field spectroscopy.

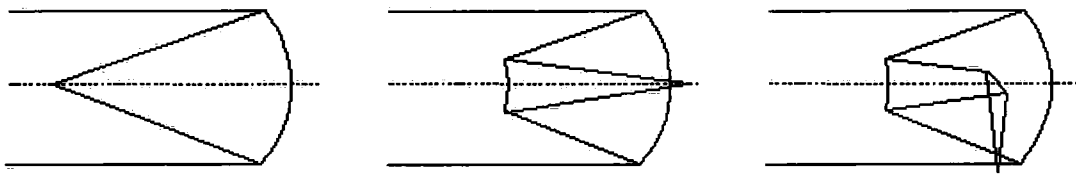

Prime Focus Cassegrain Focus Nasmyth Focus

Figure 2.1 *Different Types of focal points of reflecting telescopes*

For large telescopes the most common focus is the **Cassegrain**. The focal plane is located below the parabolic primary mirror, which provides a convenient place for attaching and changing multiple instruments.

Another popular focus is called **Nasmyth**. The beam, after being reflected by the secondary, is bent at 90 ° with a flat mirror to converge to a point on the side of the primary. Telescopes commonly have two Nasmyth platforms, one either side of the primary mirror.

Another important element in the characterisation of refracting telescopes is their mounting. There are two main types of telescope mounting: equatorial and altazimuthal. The altazimuthal mounting contains two axes of rotation (vertical and horizontal); since the introduction of computerised telescope control and autoguider systems (pioneered at the Russian 6 m telescope), it has been the preferred choice of mounting for large telescopes. Tracking a star requires a combination of the two rotations; thus tracking requires constant changes to the velocity and acceleration of the axis's motors.

As computerised telescope control systems became crucial for the 8-10 m class telescopes, the next generation of 30-50 m telescopes will just be as dependent on multiple optimised AO modes to fulfil their scientific potential.

2.1.2 Angular Resolution and Seeing

A point source emitter of electromagnetic radiation in free space produces a spherical WF. The distance between a star and the Earth's atmosphere is so great that the WF entering the atmosphere can be considered a plane wave.

The plane-parallel WF arriving from a distant star will suffer diffraction effects at the circular aperture of the telescope. As a result, the image at the telescopes focus is not a point, but a circular diffraction pattern with a central bright spot containing approximately 84% of the light, known as the **Airy disc,** see Figure 2.2. The rest of the light will be in the concentric rings surrounding the spot.

The Airy function *Ai(x)* is formally defined as:

$$Ai(x) = \frac{1}{\pi}\int_0^\infty \cos\left(\frac{t^3}{3} + xt\right) dt \tag{2.1}$$

Satisfying:

$$Ai''(x) - xAi(x) = 0 \tag{2.2}$$

The intensity of the Fraunhofer diffraction pattern of a circular aperture is given by:

$$I(\theta) = I_0\left(\frac{2J_1\left(\frac{\pi D}{\lambda}\sin\theta\right)}{\frac{\pi D}{\lambda}\sin\theta}\right)^2 \tag{2.3}$$

Where J_1 is a first-order Bessel function of the first kind.

The angular position of the first minimum of the diffraction pattern corresponds to an angle of incidence α_d and is given by:[10]

$$\alpha_d = \sin\theta = \frac{1.22\lambda}{D} \tag{2.4}$$

Where λ is the wavelength of the incident radiation and D is the diameter of the aperture.

The 1.22 factor arises from the aperture being circular.

The theoretical angular resolution of the telescope is limited by the size of the Airy disc. It is only possible to resolve two point sources if their Airy discs are sufficiently separated to be seen as distinct. The **Rayleigh Criterion** states that for two sources to be distinguishable, the central maximum of the diffraction pattern of one source coincides with the first minimum of the other. When the angular resolution of a telescope, at a given wavelength, is determined by the radius of the Airy disc, it is said to be "**diffraction-limited**".

Before looking in depth at atmospheric turbulence in section 2.2, it is worth mentioning at this stage that for modern large telescopes, angular resolution at optical and near infra-red

wavelengths is almost always limited by the broadening of stellar images by atmospheric turbulence, commonly referred to as the **Seeing**.

Diffraction limits the ability to reproduce an image; it degrades the propagation process. It is impossible to eliminate diffractive effects; they are inherent in Maxwell's laws of electromagnetism.

As the parallel plane WF from a distant object enters our atmosphere and passes through different layers, phase changes due to changing refraction index, differential atmospheric refraction and diffraction can lead to broadening the apparent angular size of the source. It is possible to define a seeing disc as the angular size of this broadened stellar image. For a point source, the time-integrated angular distribution of light intensity is called the **seeing profile**.

To a first approximation, the seeing profile $\sum(\theta)$ is a Gaussian curve of the form:

$$\sum(\theta) = I_0 \exp\left(-\frac{\theta^2}{\sigma^2}\right) \tag{2.5}$$

Where I_0 is the source light intensity and σ^2 is the WF variance.

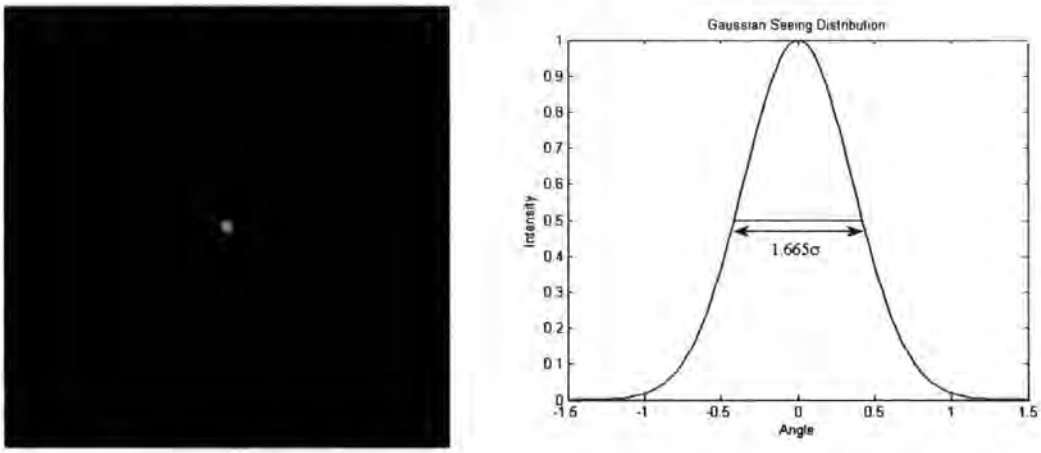

(a) Airy Disc Pattern (b) Gaussian Seeing Distribution (~ PSF)

Figure 2.2 *Airy Disc Pattern and Seeing Distribution*

The diameter of the seeing disc α_s can then be defined as the full width at the half maximum (**FWHM**) of the Gaussian distribution, obtaining:

$$\alpha_s = 2\sqrt{\ln 2}\sigma = 1.665\sigma \tag{2.6}$$

The FWHM is often used in determining the quality of the seeing and it may be used as a measure of correction in an AOS.

2.1.3 Propagation and Wavefront Aberrations

The complex amplitude, *U(z)*, of a plane wave of wavelength λ that has propagated through turbulence is given by:

$$U(z) = |U(z)| \exp^{i\phi(z)} = |U(z)| \exp^{\left(\frac{2\pi i}{\lambda}\Phi(z)\right)} \tag{2.7}$$

Where $|U(z)|$ is the amplitude of the electric field and z is the direction of propagation. The phase fluctuations $\phi(z)$ is the phase of the wavefront $\Phi(z)$:

$$\phi(z) = \frac{2\pi}{\lambda}\Phi(z) \tag{2.8}$$

In AO, the **Wavefront** (WF), Φ, is usually the quantity that will be manipulated to modify the characteristics of the beam. The propagation of light, through mathematical formalism, describes the effects of the phase of an optical field in a pupil plane on the resultant field in an image plane.[10] Figure 2.3 shows the coordinate system for the diffraction calculation with aberration $\Phi(\rho,\theta)$, where ρ,θ are the normalised polar coordinate system of the circular pupil.

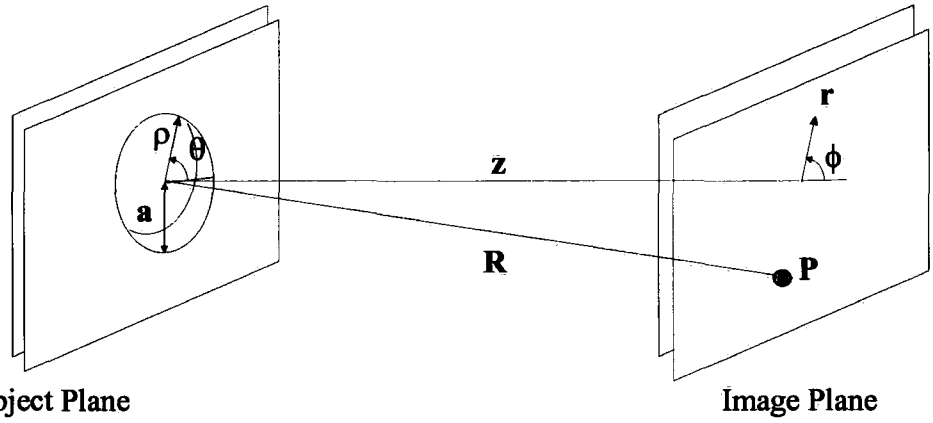

Figure 2.3 *Coordinate system for the diffraction calculation with aberration Φ*

For a beam of coherent light of wavelength λ, the intensity of light, I, at a point P on the image, or focal, plane a distance z away is given by:

$$I(P) = \left(\frac{Aa^2}{\lambda R^2}\right)^2 \left| \int_0^1 \int_0^{2\pi} e^{i\left[k\Phi(\rho,\theta) - v\rho\cos(\theta-\phi) - \frac{1}{2}u\rho^2\right]} \rho d\rho d\theta \right|^2 \tag{2.9}$$

Where a is the radius of the circular pupil,
A is the amplitude of the electric field,
r, ϕ are the polar coordinates system of the image plane,
$k = 2\pi/\lambda$
z is the normal to the pupil plane,
R is the slant range from the center of the pupil to point P,
$k\Phi(\rho,\theta)$ is the deviation in phase from a perfect sphere about the focal plane origin.

The normalised coordinated in the focal plane have been simplified to:

$$u = \frac{2\pi}{\lambda}\left(\frac{a}{R}\right)^2 z \quad \text{and} \quad v = \frac{2\pi}{\lambda}\left(\frac{a}{R}\right)^2 r \tag{2.10}$$

The uniform electric field amplitude in the pupil plane is A/R, and therefore, the intensity in the pupil plane, $I_{z=0}$, *is* A^2/R^2.

For AO, the most important quantity in the above expression is the *wavefront*, Φ, which represents all the aberrations that are present in the optical system prior to its propagation to point P.

If no aberrations are present, the intensity is a maximum on-axis ($r = 0$), which is called the Gaussian image point:

$$I_{\Phi=0}(P_{r=0}) = \pi^2\left(\frac{Aa^2}{\lambda R^2}\right) = \left(\frac{\pi^2 a^4}{\lambda^2 R^2}\right) I_{z=0} \tag{2.11}$$

It can be useful to use **geometric optics** when considering a WF as a two-dimensional map of the phase at an aperture or any other plane of concern that is normal to the line of sight between the origin of the beam and the target. The WF is found by tracing out an equal path (*distance* x *refractive index*) from a source to the region of interest, for example, the entrance pupil of an optical system.

To first order, the WF aberrations introduced by atmospheric turbulence are achromatic; the number of microns of optical path retardance is the same for both the visible and infrared light. It should be noted that the number of wavelengths of optical path is different – there are fewer waves of retardance at (the longer) infrared wavelengths. This suggests that there are fewer distortions at longer wavelengths and that IR wavelength should be easier to compensate for.

Although the main interest is the WF aberration, it is more usual to deal with the phase fluctuation, see Equation (2.8). The phase distortion is specified between $-\infty$ and $+\infty$, whereas optically, at a given wavelength, we cannot distinguish between ϕ and $\phi \pm 2n\pi$, where n is any integer. We shall denote the 2π wrapped phase as $\phi_{\text{Mod}2\pi}$. Clearly the phase distortion of ϕ or $\phi_{Mod2\pi}$ is also a strong function of wavelength.

2.1.4 Strehl Ratio and Marechal Criterion

The **Strehl Ratio** (SR), also known as the normalised intensity, is the ratio between the intensity on-axis of an aberrated point spread function (PSF) and the intensity on-axis of an unaberrated (diffraction limited) PSF. The SR is a measurement used in AO to quantify the quality of the beam:

$$SR = \frac{I(0,0)_{aberrated}}{I(0,0)_{dif.lim.}} = \frac{1}{2\pi^2}\left|\int_0^1\int_0^{2\pi} e^{i\left[k\Phi(\rho,\theta) - v\rho\cos(\theta-\varphi) - \frac{1}{2}u\rho^2\right]}\rho\, d\rho\, d\theta\right|^2 \tag{2.12}$$

Equation (2.12) includes terms for tilt aberrations. If these aberrations are removed and the focal plane displaced to its Gaussian focus then the linear and quadratic terms disappear, leaving:

$$SR = \frac{1}{2\pi^2}\left|\int_0^1\int_0^{2\pi} e^{i\Phi_P}\rho d\rho d\theta\right|^2 \qquad (2.13)$$

The SR will reduce to 1 if the beam at the pupil is unaberrated, i.e. $\Phi_P = 0$, giving a diffraction limited intensity at focus. An important result is that any systems with any aberration $\Phi_P > 0$ will give a SR < 1.

Given small arbitrary WF aberration, the Strehl ratio can be directly related to the variation of the WF aberration. The WF variance $(\Delta\Phi_P)^2$ can be found from:

$$(\Delta\Phi_P)^2 = \frac{\int_0^1\int_0^{2\pi}\left(\Phi_P - \overline{\Phi_P}\right)^2\rho d\rho d\theta}{\int_0^1\int_0^{2\pi}\rho d\rho d\theta} \qquad (2.14)$$

Where $\overline{\Phi_P}$ is the average WF.

The standard deviation of the WF, $\Delta\Phi_P$, is commonly known as the root-mean-square (RMS) phase error. $\Delta\Phi_P$ is directly related to the quality of beam propagation.[22]

A system is said to be "well corrected" or close to the diffraction limit in practical terms when it has reached the SR or **Marechal Criterion**, when $SR \geq 0.8$. This leads to $(\Delta\Phi_P)^2 = 0.2$ rad^2 or a WF aberration of $\approx \lambda/14$.

If $\Delta\Phi_P < \lambda/2\pi$, the SR can be approximated to: [10]

$$S = \exp\left[-\left(\frac{2\pi}{\lambda}\right)^2(\Delta\Phi_P)^2\right] \cong 1-\left(\frac{2\pi}{\lambda}\right)^2(\Delta\Phi_P)^2 \qquad (2.15)$$

This approximation gives a simple method of evaluating the propagation quality of a system by considering only a small WF variance.

2.1.5 Zernike Series

There are a number of mathematical constructs used to describe the WF and WF phase of a beam.

The **Zernike polynomials**, $Z_j(\rho,\theta)$, are an orthogonal expansion over the unit circle, see Figure 2.4.[9] They have a long tradition of use in classical optical aberration analysis and have been adopted by the AO community, who use them for expressing WF distortion. The series is composed of sums of power terms with appropriate normalising factors.[10]

Noll analysed the properties of the Zernike polynomials and applied a description to atmospherically distorted WFs, including their Fourier transforms.

The formulae of the Zernike polynomials, Z, are expressed as:

$$Z_j = \sqrt{(n+1)}R_n^0(\rho) \qquad m = 0 \qquad (2.16)$$

$$Z_{ej} = \sqrt{(n+1)}R_n^m(\rho)\sqrt{2}\cos m\theta \qquad m \neq 0 \qquad (2.17)$$

$$Z_{oj} = \sqrt{(n+1)}R_n^m(\rho)\sqrt{2}\sin m\theta \qquad m \neq 0 \qquad (2.18)$$

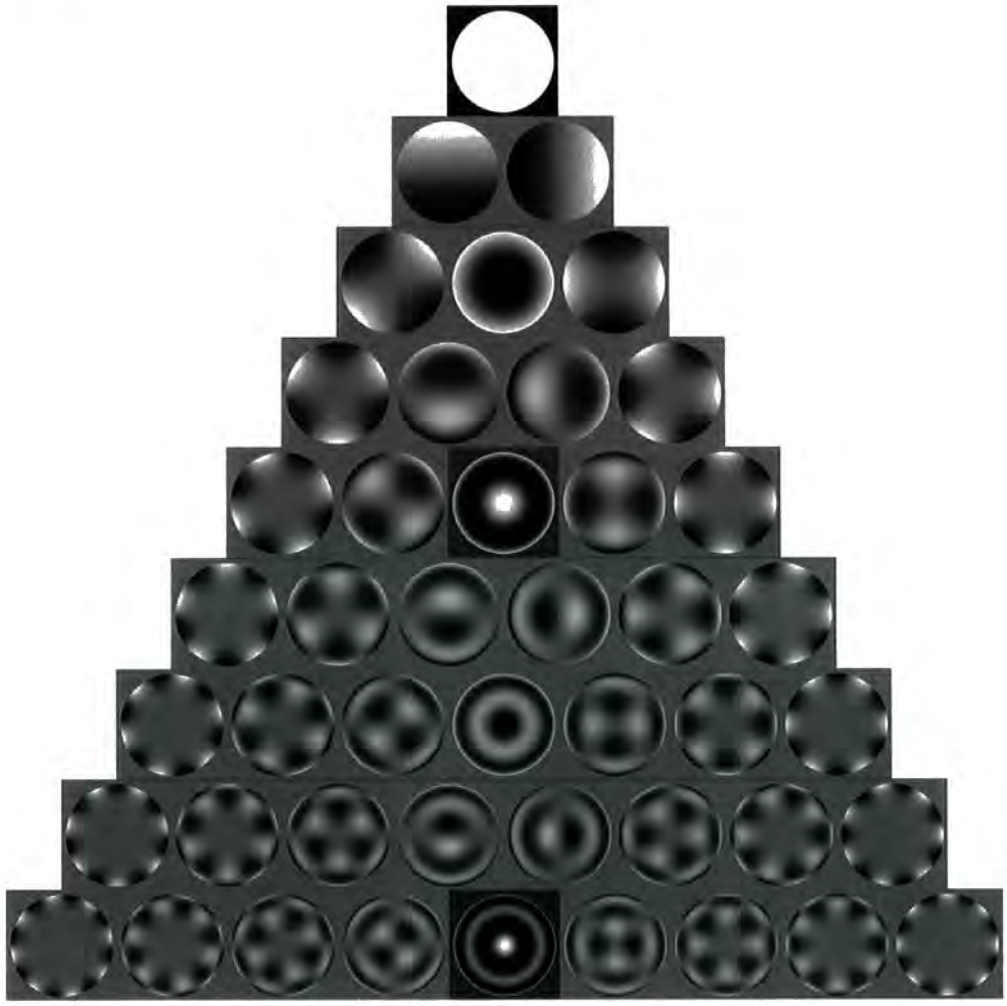

Figure 2.4 *Graphical Representation of the first 45 Zernike Polynomials*

Where R_n^m is defined as:

$$R_n^m(\rho) = \sum_{s=0}^{(n-m)/2} \frac{(-1)^s (n-s)!}{s![n+m/2-s]![n-m/2-s]!}\rho^{(n-2s)} \qquad (2.19)$$

The orthogonality of the Zernike polynomials is expressed by:

$$\int_0^R \int_0^{2\pi} W(\rho) Z_j(\rho,\theta) Z_k(\rho,\theta)\rho d\rho d\theta = \delta_{jk} \qquad (2.20)$$

Where the aperture weighting function is defined by:

$$W(\rho) = 1/\pi \quad r \le 1 \quad \text{and} \quad W(\rho) = 0 \quad r > 1 \tag{2.21}$$

For a circular pupil of radius R, the expansion is:

$$\phi(R\rho,\theta) = \sum_j a_j Z_j(\rho,\theta) \tag{2.22}$$

Where the coefficients, a_j, are given by:

$$a_j = \int_0^R \int_0^{2\pi} W(\rho)\phi(R\rho,\theta) Z_j(\rho,\theta)\, \rho d\rho d\theta \tag{2.23}$$

Equation (2.23) states that the a_j are linear combinations of the pupil phase $\phi(R\rho,\theta)$ and therefore the a_j are Gaussian random variables if the distribution of phase values are Gaussian.

Noll showed that the Zernike coefficients are weakly correlated for atmospheric turbulence; the correlation existing only when both m and n are different.[11] Hence, Zernikes are not statistically independent with respect to Kolmogorov Turbulence.

Noll calculated the RMS phase error that results when the first Zernike terms of atmospheric turbulence are corrected.

2.1.6 Phase Conjugation

The principle of **phase conjugation** is the most common approach used when attempting to correct aberrations.

When a plane WF passes through an aberrator, it must be 'corrected' by an amount proportional to the magnitude of the WF, but with a reverse sign. This is labelled phase conjugation because the electric field $|E|e^{-i\phi}$ is multiplied by its complex conjugate $|E|e^{+i\phi}$ to produce the correction. Perfect correction would be achieved by placing the right amount of phase conjugation at the right place and at the right time.

Obtaining a perfect correction is unrealistic due to limitations such as the inability to make the correction instantaneously after the WF is measured.

To explore phase conjugation, the double pass system in Figure 2.5 shall be considered. Figure 2.5 shows a constant plane wave $|U_1|$ approaching and transmitting through an aberrating object before reaching a mirror. The reflected field propagates through the same aberrator, producing an output field $U_4(x_2, y_2)$.

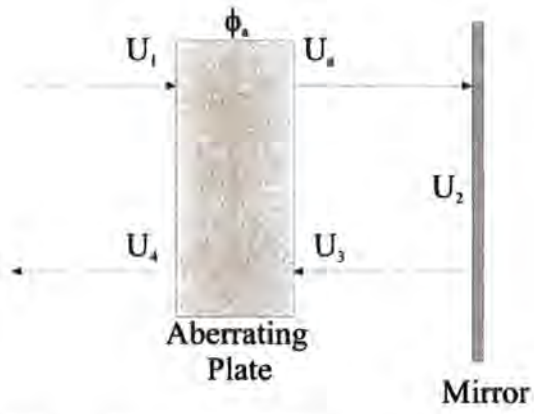

Figure 2.5 *System describing Phase Conjugation*

The field has a phase component $U_a = |U_1| e^{ik\phi_a}$ after transmission through the aberrating plate. Propagation to the mirror results in a field U_2 which is given by:

$$U_2 = \frac{ike^{ikd}}{2\pi d} \int dx_a x_b U_a \exp\left[\frac{ikr_{a2}}{2d}\right] \tag{2.24}$$

Where $r_{a2}^2 = (x_a - x_2)^2 + (y_a - y_2)^2$ (2.25)

d is the distance between the plate and mirror
f is the focal length of the aberrating plate

The integrand in equation (2.24) is integrated over the limiting aperture. The mirror applies a correction to the WF, producing a reflecting field of $U_2 e^{ik\phi_c}$, where ϕ_c is the phase correction applied by the mirror.

After propagation back to the aberrating plate the form of the field is given by U_3:

$$U_3(x_a, y_a) = \frac{ike^{+ikd}}{2\pi d} \int_{mirror} dx_m dy_m U_2 e^{i\phi_c} \exp\left[\frac{ikr_{2a}^2}{2d}\right] \tag{2.26}$$

After a final pass through the aberrating plate, the field has the form:

$$U_4 = e^{ik\phi_a} \frac{-k^2}{(2\pi d)^2} |U_1| \int dx_m dy_m e^{\frac{-ikr_{1a}^2}{2d}} e^{ik\phi_c} \int dx_a dy_a e^{\frac{-ikr_{a3}}{2d}} \tag{2.27}$$

For the general case, equation (2.27) has no analytical solution. The form of aberration and the boundaries of the integration (the apertures) are unspecified. For perfect correction, the field U_4 must exactly equal the field U_1, the aperture effects must be neglected and correction applied $\phi_c = -2\phi_a$, and the correction must be the conjugate of the aberration. It is important to note that the phase conjugation cannot be exactly employed if the diffraction effects dominate or if a WF cannot be precisely determined or replicated.

2.2 Atmospheric Turbulence Theory

As AOS are mainly used to correct for the WF error caused by turbulence in the Earth's atmosphere, a good appreciation of the characteristics of the aberrations and effect of image quality is required. Turbulent motions in the atmosphere, changes in wind velocity (eddies), are caused by naturally occurring small variations in temperature (<1 °C). This leads to small changes to the refractive index, which cumulatively cause significant inhomogeneities in the refractive index profile of the atmosphere.

As light propagates through the atmosphere, turbulent motions cause changes to the beam's WF, leading to the three primary effects of turbulence: scintillation, image motion and beam spreading.

Scintillation is the random intensity variation of starlight caused by interference between waves from the same star passing through slightly different atmospheric paths. Atmospherically propagated light also fluctuates in intensity through small changes in the refractive index of the atmosphere. **Image motion** is caused by the shifting average angle-of-arrival of light from the star due to the change of index of refraction along its path through the atmosphere. **Beam Spreading** is caused by random higher-order aberrations.

The fluctuations in refractive index lead to these aberrations being random. Thus the aberrations are Gaussian to a good approximation and can be described statistically using variances and covariences.

The theories of turbulence are based on statistical analyses, as the instantaneous perturbation of the atmosphere is undeterminable. It shall be shown that many useful theories and scaling laws that describe the average effect on the gross properties may be derived from this approach.[12, 13, 14]

It is common to create Atmospheric simulators using **Monte Carlo methods,** which use pseudo-random numbers to produce statistically generated turbulence simulation. Realistic atmospheric simulations are extremely important for AO system performance modelling. Site evaluations are useful for obtaining parameter values to feed into such Monte Carlo generated Atmospheric Turbulence simulations.

2.2.1 Kolmogorov Turbulence

Fluctuations in the air refractive index are proportional to fluctuations in the air temperature. The statistics of refractive index inhomogeneities follows that of temperature inhomogeneities, which are governed by the **Kolmogorov-Obukhov** law of turbulence. Kolmogorov studied the mean-square velocity difference between two points in space.[15, 16] Corrsin[17] and Tatarskii[18] connected the velocity structure to the index of refraction structure.

The interest lies **not** in the absolute value of the refractive index, ***n(r)***, but the difference over a small three-dimensional separation, ***Δn(Δr)***.

The **refractive index structure function** $D_n(\Delta r)$ is defined as:

$$D_n(\Delta r) = \left\langle \left| n(r+\Delta r) - n(r) \right|^2 \right\rangle \tag{2.28}$$

It was found that if the separation, Δr, is small (within the inertial sub-range of the turbulence), then $D_n(\Delta r)$, takes on a 2/3 law dependence on Δr:

$$D_n(\Delta r) = C_n^2 \Delta r^{2/3} \qquad l_0 << r << L_0 \tag{2.29}$$

Where C_n^2 is the **refractive index structure constant,**
l_0, L_0 are the inner and outer scale respectively.

It should be noted that to first approximation the random process is considered inhomogeneous locally because the refractive index structure function depends on separation and not position. The process is also isotropic, as it depends only on the modulus of r.

The *refractive index structure constant* is a measure of the strength of turbulence. It is by no means constant. It varies with seasons as well as daily and hourly. It varies with geographic location and altitude. It can very easily be perturbed by artificial means such as aircraft. Currently no theoretical model is accurate for many cases and C_n^2 is obtained through experimental observations.

As the separation approaches the turbulence outer scale the fluctuations are expected to become uncorrelated. The value of the outer scale has been highly debated. Experimentally the power law has been found to be quite accurate over distances less than one meter. This suggests that this law is certainly valid for small telescopes.

Equation (2.29) statistically describes the spatial distribution of the inhomogeneities at a given time t.

It is assumed that the atmosphere consists of a mean index of refraction $\langle n(r) \rangle$ and a fluctuating index $n_1(r)$. The covariance of the refractive index field B_n thus becomes:

$$B_n(r) = \langle n_1(r + r_1) n_1(r_1) \rangle \tag{2.30}$$

The power spectrum density, PSD(K), of the phase fluctuations is the Fourier transform of the covariance given by:

$$PSD_n(K) = \frac{1}{(2\pi)^3} \int d^3 r \, B_n(r) e^{-iK \cdot r} \tag{2.31}$$

Where K is the three-dimensional spatial wavenumber.

By using equation (2.31), changing to a spherical coordinate system $K = (K, \theta, \sigma)$, carrying out ensemble averaging[19] and letting the integral limits diverge to $l_0 \to 0$, and $L_0 \to \infty$, the integral reduces to the **Kolmogorov spectrum.**

$$\Phi_n(K) = 0.033 C_n^2 K^{-11/3} \tag{2.32}$$

Finally the modified von Karman spectrum is useful, as it incorporates values for the inner and outer scales.[288]

$$\Phi_n(\boldsymbol{K}) = \frac{0.033C_n^2}{(|\boldsymbol{K}|^2 + K_0^2)^{-11/6}} \exp\left(-\frac{|\boldsymbol{K}|^2}{K_m^2}\right) \tag{2.33}$$

Where K_0 is $2\pi/L_0$ and K_m is $5.92/l_0$.

2.2.2 Propagation Effects

Propagation is affected by the three effects of turbulence:

- High spatial frequency beam spreading
- Low spatial frequency image motion
- Intensity variation scintillation.

Scintillation

Scintillation is usually expressed as the log-amplitude fluctuations. By examining the Kolmogorov spectrum, it is found that for light of wavelength λ travelling a path length L, scintillation is produced by eddies with sizes on the order of $\sqrt{\lambda L}$.

Assuming the Von Karman spectrum and $l_0 << \sqrt{\lambda L}$, for a plane wave, the log amplitude variance σ_χ^2 is given by:[10]

$$\sigma_\chi^2 = 0.307k^{7/6}L^{11/6}C_n^2 \tag{2.34}$$

Where k is the wave number.

Perturbation theory is used to derive this equation, so as expected it isn't applicable to strong turbulence and long paths.

Beam Spreading and Image Motion

Beam spreading is produced by eddies that are smaller than the beam size, while image motion is found to occur when eddies are larger.[14]

The light will experience phase variations as the refractive index is a random function of time and space. The phase difference $\delta\phi$ between two parallel paths through the atmosphere separated by distance ρ is given by:

$$\delta\phi \approx k\rho[\Delta n(\rho)] \tag{2.35}$$

where Δn is the difference in index.

The two-dimensional **phase structure function,** D_ϕ, can be determined by assuming a path length, L and averaging over many statistical realisations:

$$D_\phi = 1.46k^2C_n^2L\rho^{5/3} \qquad l_0 << \rho << L_0 \tag{2.36}$$

The wave can lose coherency when propagation occurs over long paths and many eddies and if the aberrations are too strong. The total beam spread can be derived from the coherence limitation. Lutomirski and Yura[20] used the extended Huygens-Fresnel principle to show that a collimated uniform beam of radius a in uniform turbulence gives an approximate angular spread θ of:

$$\theta^2 \approx \frac{1}{k^2a^2} + \frac{1}{k^2\rho_0^2} \tag{2.37}$$

Where a is the radius of collimated beam and ρ_0 is the coherence distance.

Furthermore, a Gaussian beam that spreads from turbulence can be described as:

$$I = \frac{\omega_0^2}{\omega_b^2}\exp\left(-\frac{2\rho^2}{\omega_b^2}\right) \tag{2.38}$$

Where ω_0^2 is the initial size of the beam and ω_b^2 is the beam waist.

It can be derived that the beam waist ω_b^2 increases for short and long propagation distance respectively:

$$\omega_b^2 = \omega_0^2 + 2.86C_N^2k^{1/3}L^{8/3}\omega_0^{1/3} \qquad \text{for} \qquad z << \pi\omega_0^2/\lambda \tag{2.39}$$

$$\omega_b^2 = \frac{4z^2}{k^2\omega_0^2} + 3.58C_N^2k^{1/3}L^3\omega_0^{-1/3} \qquad \text{for} \qquad z >> \pi\omega_0^2/\lambda \tag{2.40}$$

The turbulences resulting effect implies that when two beams, or two parts of the same beam propagate a distance L, they will reach the same point through a slightly different path. The variance of their angle of arrival difference $\langle\alpha^2\rangle$ is given by:

$$\langle\alpha^2\rangle = \frac{D_\phi}{k^2\rho^2} \tag{2.41}$$

Where D_ϕ is the phase structure function.

For an aperture of diameter D, the angle of arrival variance becomes:

$$\langle\alpha^2\rangle = 1.46C_n^2LD^{-1/3} \tag{2.42}$$

2.2.3 Fried's Coherence Length

The **Fried Coherence Length**, also referred to as **Fried Parameter**, r_0, is one of the most important parameter describing the quality of a wave propagated through turbulence. Fried conducted a study of an optical heterodyne communication receiver. He discovered a relationship to calculate the maximum diameter of a collector allowed before atmospheric distortion limit performance.[21]

If the turbulence isn't too strong then a detailed analysis[22] shows that the covariance function of the complex amplitude for a wave, see Equation (2.8), that has propagated through Kolmogorov turbulence is given by:

$$C(x) = \langle U(x)U^*(x+x')\rangle = \exp^{\left(\frac{1}{2}D_\phi(x)\right)} \tag{2.43}$$

Where $\langle U\rangle = 0$ and $D_\phi(x)$ is the phase structure function as displayed in (2.36).

Considering plane waves experiencing Kolmogorov's turbulence, the phase structure function, $D_\phi(x)$ is given by:

$$D_\phi(x) = 2.91k^2(\cos\gamma)^{-1}|x|^{5/3}\int_0^\infty C_n^2(z)dz = 6.88\left(\frac{|x|}{r_0}\right)^{5/3} \tag{2.44}$$

Where r_0 is the coherence length,
γ is the zenith angle,
$k = 2\pi/\lambda$.

The coherence length, r_0, is given by:

$$r_0 = \left(\frac{2.91}{6.88}k^2(\cos\gamma)^{-1}\int_0^\infty C_n^2(z)dz\right)^{-3/5} \tag{2.45}$$

Coherence length, r_0, is therefore an important quantity, containing the wavelength, turbulence strength and propagation path all in one. It has two functional dependences, it is a simple integral over the $C_n^2(z)$ profile and it is proportional to six-fifths power of the wavelength. The coherence length is used to describe various atmospheric phenomena; if known then both the structure function and the refractive index can be determined.

Fried's parameter has two physical interpretations. Firstly it is the aperture over which there is approximately one radian of RMS phase aberration. Secondly, it is the aperture that has the same resolution as a diffraction-limited aperture in the absence of turbulence.

Due to the properties described, the coherence length is widely used for scaling laws and describing atmospheric turbulence. An example of this is the power spectrum, PSD(κ), of the phase fluctuation corresponding to the structure function is expressed in terms of the coherence length:[11]

$$PSD_{\phi}(\mathbf{K}) = \frac{0.023}{r_0^{5/3}}|\boldsymbol{K}|^{-11/3} \tag{2.46}$$

Where $\boldsymbol{K}$ is the spatial wavenumber.

2.2.4 Temporal Behaviour of Atmospheric Turbulence

The temporal statistics of atmospheric turbulence are equally important. Slow-moving turbulence can be viewed as static, thus corrections would only be required in the spatial domain. Extremely fast-moving turbulence, evolving faster than the exposure time of the WFS, would not be directly detected, but would be measured as time averaged disturbances.

Under most conditions, lifetimes of air temperature inhomogeneities are much longer than the time it takes for a wind-driven inhomogeneity to cross the line of site; thus the winds and the local eddies, which dominate turbulence can be tracked electronically using a WFS. The Taylor hypothesis states that spatial averaging of the turbulence is equivalent to temporal averaging, thus if a layer simply moves rigidly, without changing its refractive index distribution, then that layer contributes a phase in the pupil, which also just moves rigidly across the pupil.

It can be shown that the temporal structure function $D_N(\tau)$ is obtained by substituting $|v\tau|$ for ρ in the spatial structure function:[23]

$$D_N(\tau) = \left\langle |n(r,t) - n(r - v\tau, t|^2 \right\rangle = C_N^2 |v\tau|^{2/3} \tag{2.47}$$

Assuming there to be just one layer moving at velocity $v_{\perp}$, then the temporal power spectrum of the phase in the telescope pupil is given by:[22]

$$\Phi_{\phi}(f) \propto \left(C_N^2 dz\right) \frac{1}{|v_{\perp}|} \left(\frac{f}{|v_{\perp}|}\right)^{-8/3} \tag{2.48}$$

Where f is the frequency of turbulent layer, dz is the change in height of turbulent layer
$v_{\perp}$ is the velocity of turbulent layer perpendicular to Earth's surface

This shows that the temporal power density has a –8/3 power law dependence of the **phase** on the frequency f at any point in the pupil. In wavefront sensing, we are often interested in the time-dependence of the spatial derivative of the phase, such as $\partial\phi/\partial x$. For a single point (no spatial integration effects) the power spectrum of the phase derivative, $\Phi_{\partial\phi/\partial x}(f)$ is:

$$\Phi_{\partial\phi/\partial x}(f) \propto \left(C_N^2 dz\right) \frac{1}{|v_{\perp}|} \left(\frac{f}{|v_{\perp}|}\right)^{-2/3} \tag{2.49}$$

This gives a –2/3 power law dependence of the **phase derivative** at the frequency f at any point in the pupil. In reality, the results are much more complicated and vary depending upon the sub-aperture shape and the wind direction with respect to the direction of the phase derivative. At very low spatial frequencies, the –2/3 dependency holds as the frequencies arise

from low spatial frequencies which are barely affected by spatial integration. At the high frequency limit, Conan et al[23] found a power law between –11/3 and –14/3 for a square aperture depending whether the derivative is parallel or perpendicular to the wind velocity.

An AOS aims to reject phase fluctuations using the closed-loop servo system. Greenwood calculated the bandwidth necessary to provide rejection.[10]

The Greenwood frequency[11], f_G, is defined for an arbitrary $C_N^2(z)$ and $v_\perp(z)$ as:

$$f_G = \left[0.102 \left(\frac{2\pi}{\lambda} \right)^2 (\cos\gamma)^{-1} \int_0^\infty C_n^2(z)(v_\perp(z))^{5/3} dz \right]^{3/5} \tag{2.50}$$

Where γ is the Zenith angle.

For a single layer of turbulence moving at velocity $v_\perp(z)$, it reduces to:

$$f_G = 0.43 \frac{|v_\perp|}{r_0} \tag{2.51}$$

For most cases the characteristic frequency of the atmosphere is in the range of tens to hundreds of Herts.

2.2.5 Angle-of-Arrival Statistics

It is important to determine the arrival angle of light for an AOS. Most systems contain a tip-tilt mirror that primarily corrects for the tip and tilt modes. Determining the (average) slope of a WF is also important as wavefront sensing is often done by sensing the tilt over sub-apertures. Recalling the relationship between the WF $\Phi(x,y)$ and the phase, $\phi(x,y)$ from Equation (2.8), the slopes along the x and y directions can be defined as:

$$\alpha(x,y) \equiv \frac{\partial}{\partial x}\Phi(x,y) = \frac{\lambda}{2\pi}\frac{\partial}{\partial x}\phi(x,y) \tag{2.52}$$

$$\beta(x,y) \equiv \frac{\partial}{\partial y}\Phi(x,y) = \frac{\lambda}{2\pi}\frac{\partial}{\partial y}\phi(x,y) \tag{2.53}$$

It follows that if $\phi(x,y)$ is Gaussian, then both $\alpha(x,y)$ and $\beta(x,y)$ are also Gaussian implying that the image will move around the image plane with a Gaussian probability distribution.

Using the differentiation property of Fourier transforms, the power spectra of the WF slopes, $\Phi_\alpha(\boldsymbol{K})$ and $\Phi_\beta(\boldsymbol{K})$ can be written as:

$$\Phi_\alpha(\boldsymbol{K}) = \lambda^2 K_x^2 \Phi_\phi(\boldsymbol{K}) \quad \text{and} \quad \Phi_\beta(\boldsymbol{K}) = \lambda^2 K_y^2 \Phi_\phi(\boldsymbol{K}) \tag{2.54}$$

Where K_x and K_y are components of $\boldsymbol{K}$,

$\Phi_\phi(\boldsymbol{K})$ is the power spectrum of the phase as given in Equation (2.46).

This leads to a total variance of:

$$\sigma_{\alpha\beta}^2 = \lambda^2 \int_{bandpass} |K|^2 \Phi_\phi(K) dK \tag{2.55}$$

Fried pursued a rigorous analysis of this problem which led to:[24]

$$\sigma_{\alpha\beta}^2 = 0.36\lambda^2 D^{-1/3} r_0^{-5/3} = 0.36\left(\frac{\lambda}{D}\right)^2 \left(\frac{D}{r_0}\right)^{5/3} \tag{2.56}$$

The results show that the apparent wavelength dependence does not exist, remembering that r_0 is proportional to $\lambda^{6/5}$. It is also worth highlighting that the (λ/D) is approximately the angular width of the diffraction-limited image, so that the standard deviation of the image motion is approximately $0.6(D/r_0)^{5/3}$ in units of the width of the diffraction-limited PSF. This result can be used to calculate the sensed tilt over sub apertures.

2.2.6 Angular Anisoplanatism

For the majority of most scientific observations, the guide star is not the object under study. Thus the guide star will be angularly displaced from the science object. This means that the WF sampled by the guide star will be different from the science object because of this angular displacement. When the WFs are the same as those from the science object, then the system is **isoplanatic**, when they aren't, they are **anisoplanatic**.

The **Isoplanatic Angle**, Θ_0, quantifies the region over which there is approximate isoplanatism, and is given by:

$$\Theta_0 = \left[2.91\left(\frac{2\pi}{\lambda}\right)^2 (\cos\lambda)^{-1} \int_0^\infty C_n^2(z) z^{5/3} dz\right]^{-3/5} \text{ rad} \tag{2.57}$$

The integral over $C_n^2(z)$ has a $z^{5/3}$ weighting unlike the integral for r_0, therefore in this case the 3D spatial structure is important.

The mean squared WF error, σ_Θ^2, for a science object observed, Θ, away from the guide star is given by:

$$\sigma_\Theta^2 = \left(\frac{\Theta}{\Theta_0}\right)^{5/3} \text{ rad}^2 \tag{2.58}$$

The isoplanatic angle is proportional to $\lambda^{6/5}$, thus it is approximately 5.3 times larger (28 times in solid angle) at 2.2 μm than at 0.55 μm.

For a single layer of turbulence at height z, then:

$$\Theta_0 \approx 0.31\frac{r_0}{z} \text{ rad} \tag{2.59}$$

Hence the isoplanatic angle for a layer of a few kilometres is in the order of a few arcsecs at visible wavelengths. This unfortunately small result has a profound influence on AO. An AOS will only correct for a small field of view. This limitation can be overcome by using a Multi Conjugate AOS.

2.3 Control Theory

AO makes full use of the well-developed field of linear control theory. This section contains the essential aspects of Control Theory required for astronomical AO optimisation. [25,26,27,28,29,30,31,32]

2.3.1 Laplace Transforms

The **Laplace Transform** is used extensively throughout linear control analysis to relate physical phenomena to control phenomena, dealing with complicated time responses of a system. Differential and integration operations are transformed into much simpler algebraic operations in Laplace space, s.

The Laplace transform as a function of time is defined as:

$$X(s) = \mathcal{L}[x(t)] = \int_0^\infty x(t)e^{-st}dt \qquad (2.60)$$

Where $s = \sigma + j\omega$ is a complex variable, σ - real, $j\omega$ - imaginary (ω is the frequency)

The Laplace transform takes the time signal, $x(t)$, and integrates out the time variable to produce a function $X(s)$ of the complex variable s. Unfortunately, the inverse transform is usually difficult to evaluate.

$x(t), t \geq 0$	$X(s)$
$\delta(t)$ (unit impulse)	1
1 (unit step)	$\frac{1}{s}$
T (ramp step)	$\frac{1}{s^2}$
$\frac{1}{(n-1)!}t^{n-1}$	$\frac{1}{s^n}$
e^{-at}	$\frac{1}{(s+a)}$

$X(t), t \geq 0$	$X(s)$
$\frac{1}{(n-1)!}t^{n-1}e^{-at}$	$\frac{1}{(s+a)^n}$
$\frac{1}{a}(1-e^{-at})$	$\frac{1}{s(s+a)}$
$\frac{\omega_n}{s^2+\omega_n^2}$	$\sin \omega_n t$
$\frac{s}{s^2+\omega_n^2}$	$\cos \omega_n t$
$\frac{1}{s(s^2+\omega_n^2)}$	$\frac{1}{\omega_n^2}(1-\cos \omega_n t)$

Table 2.1 *Formal Laplace transform properties*

Table 2.1 displays some common Laplace Transform pairs and Table 2.2 contains a list of useful Laplace Transform properties. The use of both known transforms and partial fractions are usually required. Both the step function and the ramp step function are commonly used in optical control system testing. The transient response of many optical systems is the decaying exponential.

Operation on signals	Formal transform operation
Laplace transform of simple signal	$L\{x(t)\} = X(s)$
The multiplication of a signal by an Exponential	$L\{e^{at}x(t)\} = X(s+a), \qquad a>0$
Delayed signals	$L\{x(t-T)\} = e^{-Ts}X(s)$
Scaling a signal	$L\left\{x\left(\frac{t}{a}\right)\right\} = aX(as)$
Multiplying a signal by a constant	$L\{kf(t)\} = kL\{f(t)\} = LF(s)$
Combinations of signals	$L\{k_1f_1(t) \pm k_2f_2(t)\} = k_1L\{f_1(t)\} \pm k_2L\{f_2(t)\}$ $= k_1F_1(s) \pm k_2F_2(s)$

Table 2.2 *Formal Laplace transform properties*

2.3.2 Transfer Functions

A **transfer function** is the ratio of the Laplace Transforms of the output and input for an element of the system. If the system only has one element, as shown in Figure 2.6, then it is referred to as the **system transfer function,** *G(s)*.

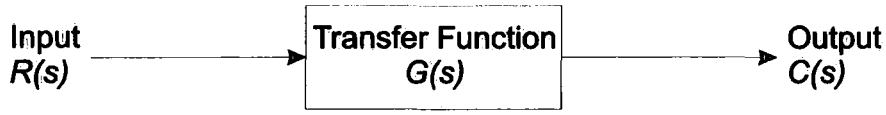

Figure 2.6 *Single element Control System*

If the input function of a linear system is given by the function *r(t)* and its output by *c(t)*, then for zero initial conditions (*c(0)* = 0, *r(0)* = 0), the dynamic behaviour of a linear system is given by the differential equation:

$$\frac{d^n c(t)}{dt^n} + a_{n-1}\frac{d^{n-1}c(t)}{dt^{n-1}} + \ldots + a_0 c(t) = b_m \frac{d^m r(t)}{dt} + \ldots + b_0 r(t) \qquad (2.61)$$

Taking the Laplace transform and using the differentiation operation property of Laplace transforms:

$$\left(s^n + a_{n-1}s^{n-1} + \ldots + a_0\right)C(s) = \left(b_m s^m + \ldots + b_0\right)R(s) \qquad (2.62)$$

Where *C(s)* and *R(s)* are the Laplace transforms of *c(t)* and *r(t)* respectively.

The **transfer function,** *G(s)*, of the system is the ratio of the output and input transforms:

$$G(s) = \frac{C(s)}{R(s)} \qquad (2.63)$$

If there are *n* elements of the control system with individual transfer functions, then linear theory shows that *G(s)* is the product of the transfer functions individual elements:

$$G(s) = G_1(s)G_2(s)...G_n(s) \qquad (2.64)$$

Open-loop systems can be used if the relationship between the input and output signals is known exactly and there are no major disturbances, this is usually **not** the case in astronomical AOS.

The use of feedback is generally applied to AOS to reduce the effects of parameter variations and disturbances and to improve transient response and reduce steady state errors. The closed-loop system involves the use of a **comparator** to calculate the error between the reference and the measured output value.

Figure 2.7, shows an example of a closed-loop control system with *n* elements and a **feedback transfer function**, *H(s)*. The system transfer function is given by:

$$G(s) = \frac{C(s)}{R(s)} = \frac{G_1(s)G_2(s)...G_n(s)}{1 + G_1(s)G_2(s)...G_n(s)H(s)} \qquad (2.65)$$

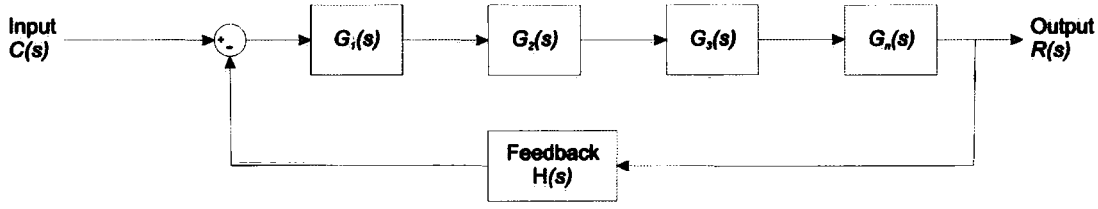

Figure 2.7 *Multi-element control system with feedback*

System performance information can be derived from the system transfer function. The denominator and numerator polynomials produce the poles and zeros of the system. The **stability** of the control system can be inferred by examining the system poles. Stability depends on whether a bounded input signal produces a bounded or unbounded output signal. The zeros of a system are also important, since they will affect the system performance.

2.3.3 First- & Second-Order Systems

Although the dynamics of AOS are complex, it is common practice to often approximate their behaviour to either a first- or second-order system.

2.3.3.1 First-Order System

Figure 2.8 shows the first-order response of a system. The exponential rise of the system resembles the typical response for all first-order linear systems.

It is usual to analyse the response of an *n*-order system to a step change in the input level, response to an impulse. In most cases the response produces two distinct regions, a **transient region** and a **steady-state region.**

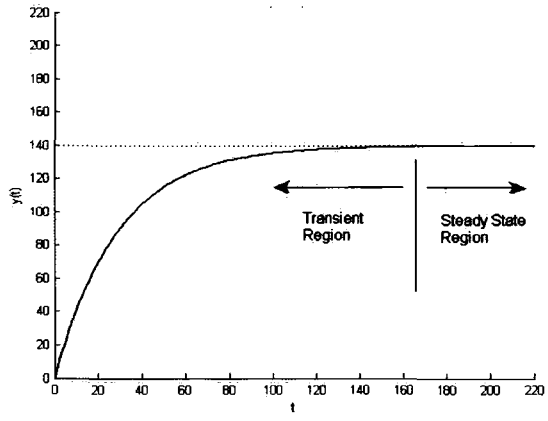

Figure 2.8 *Transient and Steady-State Region*

If a steady-state value of a system exists, it can be calculated using the **Final Value Theorem.** The steady-state, x_{ss}, value is given by:

$$x_{ss} = \lim_{t\to\infty} x(t) = \lim_{s\to 0} sX(s) \tag{2.66}$$

x_{ss} will exist if it is a bounded signal and if the system's poles lie in the left hand plane of the s-plane diagram (with the exception of only a single pole at the origin). The transient period should be sufficiently short, but not so sudden that the response of the system is oscillatory or result in unacceptable overshoot.

The transfer function for a **first-order system** is given by:

$$G(s) = \frac{K}{\tau s + 1} \tag{2.67}$$

Where K is referred to as the **system gain** and τ is called the **time constant.**

The system gain can be varied to alter the steady-state value of the system. The steady-state value, y_{ss}, is the product of the system gain, K, and the input step size, r_0:

$$y_{ss} = Kr_0 \tag{2.68}$$

The gain has an effect on the steady state of the final value of the output. The time constant, τ, represents the time taken for the output to rise to 63% of the change in output. The system output when the time reaches the value of the time constant is given by, y_τ:

$$y_\tau = 0.63Kr_0 \tag{2.69}$$

The time constant influences the shape or speed of the output response. The smaller the time constant the quicker the system will reach steady state.

2.3.3.2 Second-Order System

It is common to approximate a system to second-order, especially when a system is dominated by second-order dynamics. Control design methods will allow for the modelling inaccuracy.

The **second-order system** transfer function unity constant coefficient form is given by:

$$G(s) = \frac{K}{\frac{1}{\omega_n^2}s^2 + \frac{2\zeta}{\omega_n}s + 1} \tag{2.70}$$

Where K is the **system gain,** ζ is the **damping ratio** and ω_n is the **natural frequency.**

The **damping ratio** is an indicator of the type of transient behaviour expected in the systems response. A second-order system can be classified by its value. Figure 2.9 shows the four different classifications, oscillatory, overdamped, critically damped and underdamped.

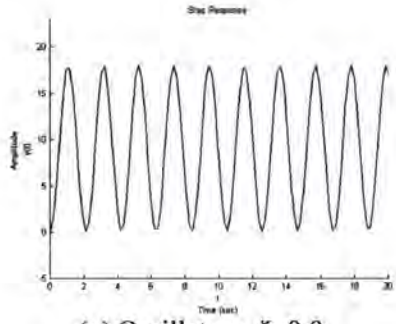

(a) Oscillatory, ζ=0.0

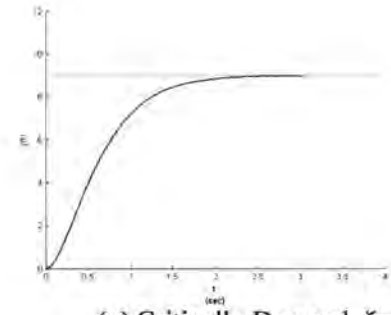

(c) Critically Damped, ζ=1.0

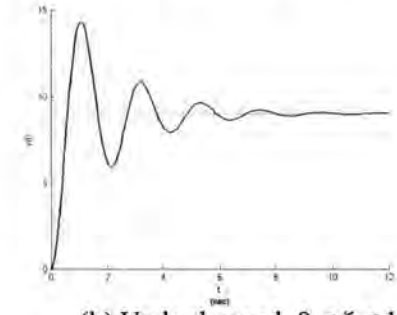

(b) Underdamped, $0 < \zeta < 1.0$

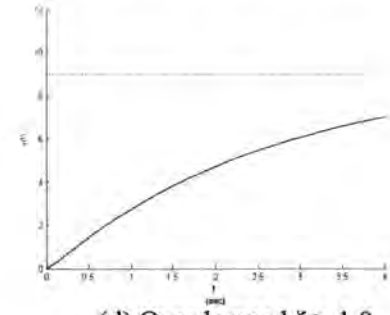

(d) Overdamped $\zeta > 1.0$

Figure 2.9 *Different classification of a second-order system*

The **natural frequency** of a second-order system is the frequency of oscillation of the system if the system were oscillatory, i.e. $\zeta = 0.0$. As all real systems display damping, a more useful parameter is defined as the **damped natural frequency,** ω_d, the frequency of oscillation:

$$\omega_d = \omega_n\sqrt{1-\zeta^2} \tag{2.71}$$

There are a few useful parameters that can be defined for the transient region of the response, these being system overshoot, settling time, the rise time and deadtime.

The **system overshoot** is an indication of the largest error between the reference input and the output. It is usually given as a percentage, given by:

$$\text{OS (\%)} = \text{(peak value – final value)/ final value x 100\%} \tag{2.72}$$

The **settling time** is the time taken for the system time to rise and settle within a given percentage of its final value. The usual bonds referred to are 5% or 2%. Hence, the settling time is denoted by $t_s(5\%)$ and $t_s(2\%)$, respectively.

The approximate settling time is given by:

$$t_s(2\%) \sim \frac{4}{\zeta\omega_n} \qquad \text{and} \qquad t_s(5\%) \sim \frac{3}{\zeta\omega_n} \tag{2.73}$$

The **rise time** of a system is the time necessary to change from either 0% to 100% or 10% to 90% of its final value. These definitions are denoted as $t_r(0\%, 100\%)$ and $t_r(10\%, 90\%)$ respectively. A short rise time indicates a fast response, but this can also cause a large peak value.

The **deadtime** or **transport delay** is the latency before the system begins to respond to a demand.

2.3.4 Frequency Domain

The frequency analysis of control systems builds on the Fourier analysis of signals, where any time-varying signal may be resolved into a sum of sinusoidal functions of different frequencies with varying magnitudes and phases.

Frequency domain information can be obtained by applying input sinusoidal signals of different frequencies and monitoring the change in amplitude and phase at the system output. By repeating this over a range of frequencies, one can measure the system's frequency response. For a linear system the input and output frequency will be the same.

The standard form of a sinusoidal signal is:

$$u(t) = A\sin(\omega t + \phi) \tag{2.74}$$

Where ω is the frequency, A is the amplitude and ϕ is the phase shift of the signal.

2.3.4.1 System Gain

The **system gain** can be calculated by looking at the ratio of the amplitude of the input and output sinusoids. The system gain is usually expressed in decibels (dB) where:

$$Gain = 20\log_{10}\left(\frac{V_o}{V_i}\right) \tag{2.75}$$

Where V_o is the output voltage and V_i is the input voltage.

The factor of 20 comes from gain being defined as a power ratio and not an amplitude ratio. Therefore the above definition assumes that the same resistance is used. It is important to note that the system gain is not necessarily the same as a gain parameter within a given control system.

2.3.4.2 Phase Shift

The **system phase shift**, ϕ_s, is calculated by simply subtracting the input phase, ϕ_i, from the output phase ϕ_o:

$$\phi_s = \phi_o - \phi_i \tag{2.76}$$

2.3.4.3 Frequency Response

Frequency responses are usually divided into three ranges: low, mid and high. The **low-frequency** range covers the near-zero frequencies, most systems display constant or constantly decreasing gain. The **mid-frequency** range usually determines the closed-loop stability of the system and displays significant gain and phase change, and will contain the transfer function component's corner frequencies. The **high-frequency** range determines how the closed-loop system reacts to disturbances such as noise and displays the system's cut-off rate.

An input signal component at frequency ω is **amplified** if the gain on the frequency plot is greater than 0 dB. Conversely the input signal at frequency ω is **attenuated** if the frequency response is less than 0 dB. Amplification and attenuation usually occur in the low and high frequency ranges respectively, see Figure 2.10.

There are three ways to visually display frequency response data: the Bode plot, Nichols chart and the Nyquist diagram.

2.3.4.4 Bode Plot

The Bode Plot, comprising of a magnitude and phase plot, graphically represents frequency response as shown in Figure 2.10.

Marked on the magnitude plot are both the d.c. gain and the cut-off rate (roll-off rate). The d.c. gain is effectively a signal with 'zero' frequency. The cut-off rate is the gradient of the magnitude/frequency slope in the high-frequency range. This parameter is important as high-frequency attenuation is required for reducing electrical noise. The cut-off rate is measured in dB/decade.

The phase plot indicates regions of both rapid and gradual phase change. The rapid phase change occurs at the mid-frequency range, where the phase alters from -20 ° to -160 °. The shape of the phase plot indicates the level of phase lag within the system. There is almost no phase lag at low-frequencies.

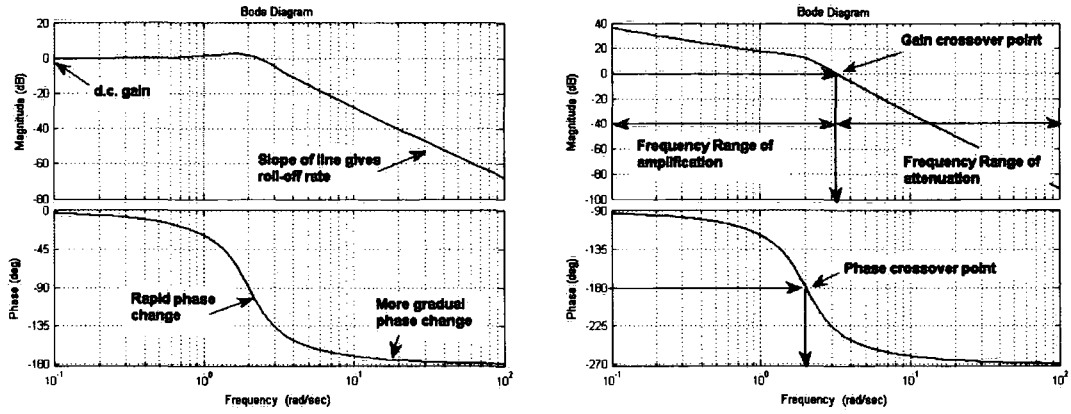

Figure 2.10 *Example of a system Bode Plots*

The combination of phase lag and amplification can cause closed-loop system instability. There are two characteristic frequency points that are used to access the stability of a closed-loop system.

The Gain Crossover Frequency, ω_{gco}, is the frequency at which the magnitude of the response is unity (0 dB) and the Phase Crossover Frequency, ω_{pco}, is the frequency at which the phase angle is $-\pi$ (180 °), see Figure 2.10.

The relative stability indicators **gain margin** and **phase margin** are defined in terms of the system open-loop frequency response and can be determined easily from a Bode plot at the crossover frequencies. The **gain margin** is the number of decibels that the magnitude is below 0 db at the phase crossover frequency. The **phase margin** is π plus the phase angle ϕ at the gain crossover frequency.

Control systems design should allow for an implementation error margin. It is common to have a phase margin of between 45 ° and 60 ° and to have a gain margin of between 6-8 dB.

The aim of the temporal control design is to firstly achieve a stable system, and then to maximise performance, which is usually expressed in terms of system closed-loop bandwidth.

2.3.4.5 Nichols Charts

A Nichols Chart represents the open loop gain and phase. The frequency is an implicit parameter on the frequency response line as shown in Figure 2.11. The graph shows the d.c. gain and the values for amplification and attenuation. The Nichols Chart gives an example of an unstable system, displaying the phase and gain crossovers.

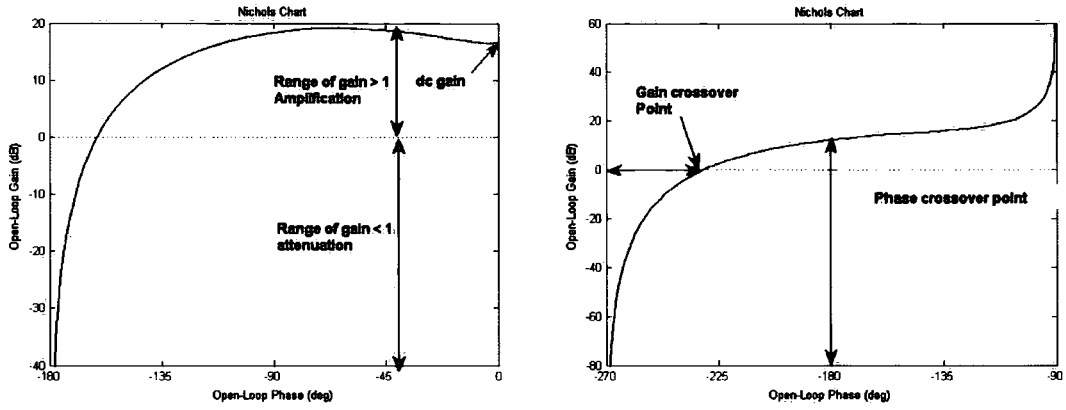

Figure 2.11 *Nichols Charts displaying left - dc gain, amplification and attenuations ranges and right - gain and phase crossover*

The Nichols Chart graphically relates the open-loop and closed-loop transfer functions on one plot, as shown in Figure 2.12. The superimposed coordinates consist of M contours (closed-loop gain) and N contours (closed-loop phase), thus relating the open loop to the closed-loop system. Nichols Charts can be used to look at the closed-loop response during open-loop modification processes.

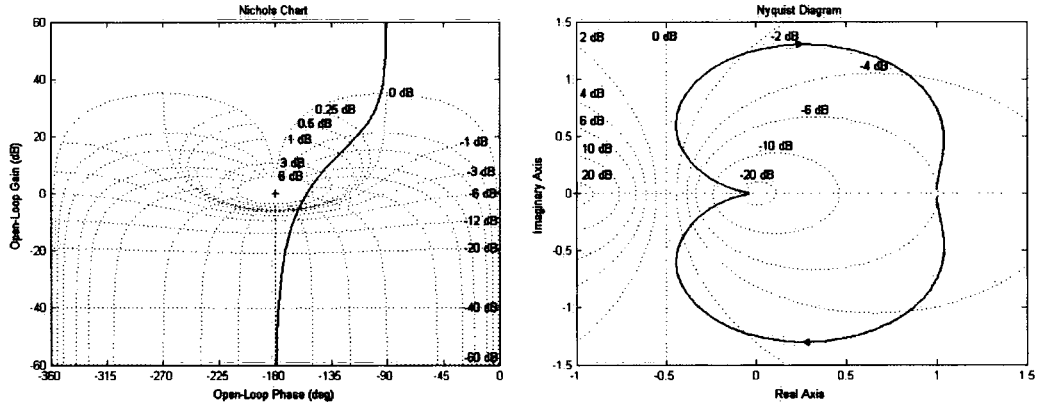

Figure 2.12 **Left** - *Nichols Chart containing closed-loop M and N contours*
Right – *Example of a Nyquist Diagram*

2.3.4.6 Nyquist Diagram

For completeness a plot of a Nyquist Diagram is shown in Figure 2.12b. The gain and phase are plotted using polar coordinates.

2.3.4.7 Control Bandwidth

In Control Theory, **Control Bandwidth** indicates the range of frequencies over which the system will have a significant magnitude of output power. This parameter applies to both signals and systems. There are slightly different, but important, interpretations of this parameter when it is related to signals, open-loop systems or closed-loop systems.

The **signal bandwidth** is defined for those signals which have a midband range and for those signals with a constant d.c. gain. It is defined as the range of frequencies over which the gain

is greater than -3 dB. For a midband range the lower and upper half power points are referred to ω_L and ω_H respectively. The constant d.c. gain will only have an upper-half power point, ω_{bw}.

The **open-loop system bandwidth** is defined as the frequency that corresponds to a gain that is 3 dB lower than the d.c. level. Control systems usually refer to the bandwidth occurring at the -3 dB point. The open-loop bandwidth is defined only for those systems with a constant d.c. gain.

The **closed-loop system bandwidth** is defined as the frequency range over which the gain is -3 dB down on the zero-frequency gain. Unity gain (0 dB) at low frequencies is desirable since it implies that slowly changing control demands will be passed through the system and not attenuated. The bandwidth is at -3 dB and indicates the speed of response of the control system and the frequency above which the system may reduce the effects of noise.

The closed-loop system bandwidth is strongly related to the open-loop system gain crossover. This is important for control system design, which is frequently performed by manipulating the open-loop frequency response plot. The system bandwidth design specification is often translated to an equivalent gain crossover specification that can be applied to design the open-loop frequency response.

2.3.5 Controllers

Controllers are used to stabilise and change the performance of an AO system. The set point is the desired output of a closed-loop system. The controller feeds back a manipulated error or modification of the difference between the set point and the measured output signal.

2.3.5.1 PID Family of Controllers

The three-term Proportional-Integral-Differential (**PID**) family of controller is the most widely used controller and most commonly found in AO systems. The PID family of controllers are displayed in Table 2.3.

Each component is briefly discussed, examining the effect of the transient and steady state portions of both a reference response and load disturbance.

Proportional Control, K_p, introduces an action proportional to the size of the error signal, ensuring system stability. Increasing the proportional gain speeds up the transient portion of the reference-tracking response and the transient portion of the load-disturbance response. It decreases the offset in the output from the reference value and to a constant load disturbance, decreasing the steady-state error. Negatively it may cause the controller signal to be too large which may lead to saturation, limiting problems with system actuation or for overshoot to increase.

Integral Control, K_i, is used to correct for any steady and continuous offset from the desired reference signal. It overcomes the shortcomings of proportional control by eliminating offsets (constant load disturbance signals) without the use of an excessively large proportional gain.

In a closed-loop AOS it is important to have the ability to keep process outputs at reference levels despite the appearance and disappearance of load disturbance signals such as noise.

Selecting a value for integral gain shapes the dynamics of both reference-tracking and disturbance-rejection responses. The presence of integral action in a controller usually leads to a wider range of closed-loop system response, but unfortunately some can be unstable.

Label	Time domain form	Laplace domain form
P	$u_c(t) = K_p e(t)$	$U_c(s) = K_p E(s)$
I	$u_c(t) = K_i \int e(\tau) d\tau$	$U_c(s) = \left[\frac{K_i}{s}\right] E(s)$
D	$u_c(t) = K_d \frac{de}{dt}$	$U_c(s) = [K_d s] E(s)$
PI	$u_c(t) = K_p e(t) + K_i \int e(\tau) d\tau$	$U_c(s) = \left[K_p + \frac{K_i}{s}\right] E(s)$
PD	$u_c(t) = K_p e(t) + K_d \frac{de}{dt}$	$U_c(s) = [K_p + K_d s] E(s)$
PID	$u_c(t) = K_p e(t) + K_i \int e(\tau) d\tau + K_d \frac{de}{dt}$	$U_c(s) = \left[K_p + \frac{K_i}{s} + K_d s\right] E(s)$
PI-D	$u_c(t) = +K_i \int e(\tau) d\tau + K_p y(t) - K_d \frac{dy}{dt}$	$U_c(s) = \left[K_p + \frac{K_i}{s}\right] E(s) - [K_d s] Y(s)$
I-P	$u_c(t) = K_i \int e(\tau) d\tau - K_p y(t)$	$U_c(s) = \left[\frac{K_i}{s}\right] E(s) - [K_p] Y(s)$
I-PD	$u_c(t) = K_i \int e(\tau) d\tau - K_d \frac{dy}{dt} - K_p y(t)$	$U_c(s) = \left[\frac{K_i}{s}\right] E(s) - [K_p + K_d s] Y(s)$

Table 2.3 *Parallel textbook form of the PID family of controllers*

Derivative Control, K_d, uses the rate of change of the error signal, introducing a derivative term. Derivative action is usually associated with the controller anticipating the future direction of error signals. The damping ratio of the closed-loop system response can be tuned by changing the amount of derivative gain in the controller. Derivative control will affect the shape of both the reference tracking (demand value) and load disturbance rejection (noise) but has no effect on constant offsets because, unlike integral control, the derivative of a constant error is zero and so the controller does not respond to the presence of the constant error.

Control Term	Effects of Reference Tracking (Step Response) and Disturbance rejection (Constant Load Disturbance)	
	Transient	**Steady State**
P	Increasing $K_p > 0$ speeds up the response	Increasing $K_p > 0$ reduces but does not remove steady state offset
I	Introducing integral action, $K_i > 0$, gives a wide range of response types	Introducing $K_i > 0$ eliminates offset in reference response
D	Derivative action $K_d > 0$ gives a wide range of responses and can be used to tune response damping	Derivative action has no effect on steady state offset

Table 2.4 *Summary of PID Controller Effects*

Most AOSs currently use some combination of the three terms. A PI controller will eliminate steady offsets in reference tracking and remove similar offsets caused by constant load disturbances. Applying a D-term to the process output avoids **derivative kick**. A summary of effects of individual controller terms: P, I, D is display in Table 2.4.

2.3.5.2 Phase Lag and Phase Lead Controllers

The phase lag and phase lead controllers are defined as:

$$G_{lag}(s) = \frac{\tau s + 1}{\alpha \tau s + 1} \quad \alpha > 1 \quad \text{and} \quad G_{lead}(s) = \frac{\tau s + 1}{\beta \tau s + 1} \quad \beta < 1 \qquad (2.77)$$

Both controllers have a lag and lead term; their Bode Plots are shown in Figure 2.13. The lag controller decreases the phase in the mid-frequency range whereas the lead controller increases the phase. Both give zero phase change at low and high frequencies. The maximum change in phase is determined by how close the two corner frequencies are placed. The peak change in phase is given by ω_m where:

$$\omega_m = \frac{1}{\tau \sqrt{x}} \qquad (2.78)$$

Where, $x = \alpha$ for the lag controller
$x = \beta$ for the lead controller

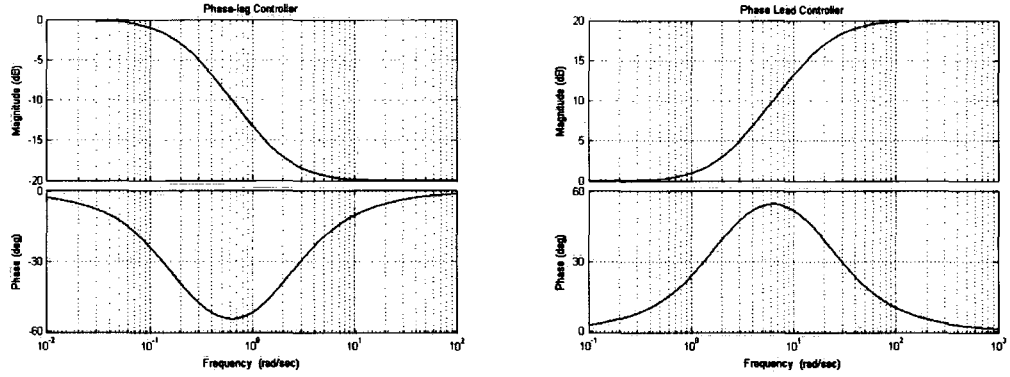

Figure 2.13 *Bode plots of a Phase Lag and Phase Lead Controller*

The phase lag controller is used to move the gain crossover to a lower frequency, improving the gain margin for the open-loop system, thus reducing the bandwidth and slowing down the system transient response. This results in an increase in gain at higher frequencies, making it more sensitive to noise. It is used when a system exhibits a satisfactory transient response but a poor steady-state performance. At large α the phase lag's dynamic gain characteristics are similar to an integral controller.

The aim of the phase lead controller is to use the additional phase from the controller to improve the phase margin of the system by adding phase at the gain crossover frequency. This increases the systems bandwidth, making the system faster. At small β the phase lead's dynamic gain characteristics are similar to a derivative controller in the mid- and high-frequency ranges.

Another controller variation is the lag-lead controller, which is occasionally used when the lead controller is insufficient due to noise amplification. The lag-lead controller, $G_{lag\text{-}lead}$, is defined as:

$$G_{lag-lead}(s) = \left(\frac{\tau_{lag}s+1}{\alpha\tau_{lag}s+1}\right)\left(\frac{\tau_{lead}s+1}{\beta\tau_{lead}s+1}\right) \tag{2.79}$$

The controller characteristics will depend on the values of its parameters and will display a mixture of the characters for the separate characteristics as described.

2.3.5.3 Selecting and Tuning a Controller

Designing and tuning an optimised controller for an AOS demands a full understanding of the closed-loop performance requirements and mechanical response of the system; only then should a capable controller be selected and coefficients tuned.

Manual controller tuning is time-consuming, inefficient and requires the actual hardware. Models and simulations can achieve the same results. Tuning requires a trade-off between reference tracking and load disturbance rejection. Steady-state accuracy is essential for complicated AOS, yet there are many other factors involved, such as the required frequency response.

There are various methods of selected the correct controller. PID controller gains may be tuned by setting system requirements for parameters such as the time constant, damping ratio and natural frequency from a derived closed-loop transfer function of a first- or second-order system.

Pole placement is another method that requires system modelling or identification methods and exploits any knowledge of the process. Tools such as root locus diagrams are used to check the closed-loop system is stable and to tune the system.

Bode plots can be used to give system stability by introducing phase lag or phase lead control. As Nichols Charts display both closed-loop and open-loop information they can be used to analyse the closed-loop system response when altering the open-loop performance.

2.3.5.4 Common Implementation Problems

AOSs contain nonlinear effects such as actuator and WFS saturation, which is known to deteriorate PID control. This leads to the phenomenon of integral wind-up. Anti-wind-up techniques are used to mitigate the wind-up effect, and usually the integral term is switched off as soon as the control signal enters the saturation regime.

AOSs aren't noiseless; thus it is wise to introduce a filter on the derivative term of a PID controller to reduce noise amplification. The introduction of a low-pass filter will attenuate high-frequency signals.

Real actuators may not respond well to rapidly changing input signals. Certain controllers can create unwanted spikes on the actuator input if the reference signal changes in a stepwise manner. These are known as kicks. For example, a PI and PID controller can give

proportional and derivative kicks respectively. These kicks are often removed by moving different control terms to the feedback path of the control loop. Thus the architecture or structure of the PID controller is changed, expanding the family of PID controllers to include the PI-D, I-P and I-PD controllers, see Table 2.3.

2.3.5.5 Digital Implementation

AO systems are digitally sampled. The sampling frequency should be greater than 15 times the closed-loop natural frequency of the system; otherwise the performance of the digitally controlled system will not achieve the required specification. Numerical approximations do not hold if the sample time T is large in comparison with the time constants within the process.

2.3.6 Smith Predictor

The **Smith Predictor** is an example of a feedforward controller. It attempts to remove the effects of the time delay, τ, from the closed-loop control system.[33] Figure 2.14 displays the transfer function system model for the Smith Predictor.

The feedback branch of the system is given by B(s) where:

$$B(s) = e^{+\tau s} Y(s) \tag{2.80}$$

The predictor block predicts the effect of the manipulated variable *U(s)* on the plant output *Y(s)* and adjusts the feedback signal accordingly.

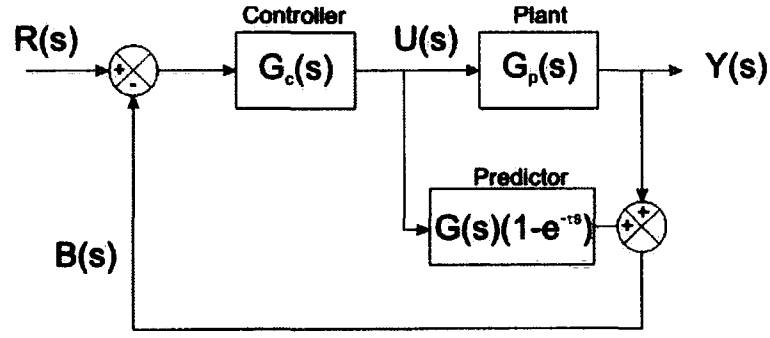

Figure 2.14 *Smith Predictor Transfer Function System Model*

A time delay in a system adds to the phase lag at a given frequency without altering the magnitude, yet it can reduce the system's stability margin and make the system difficult to control. Indeed, for disturbance inputs, unless the digital controller samples very rapidly, it can be worse than a continuous controller; the reason being that the sampled system takes longer to detect the disturbance. Under these circumstances one often very successful solution is to use a Smith Predictor or a similar feedforward controller.

2.4 Adaptive Optics System Theory

Conventionally, most astronomical **adaptive optics systems** (AOS) contain the required three key components, the wavefront sensors (WFS), the wavefront corrector (WFC) and the real-time control system (RTCS). Astronomical AOS are expensive to produce and their conception and design requires an enormous amount of thought and detail. This subsection examines each of these components.

A simple AOS is displayed in Figure 2.15. The WF, after being aberrated by atmospheric turbulence, passes through a train of transmissive and/or reflective telescope and instrumentation optics. Each optical surface will contribute to the total WF aberration.

The WF is either transmitted or, more commonly, reflected through the WFC, section 2.4.3, before being divided at the WF Sampler, section 2.4.1.

Part of the light enters the scientific instrument, commonly either an imager or spectrograph, whereas the other portion enters the WFS, section 2.4.2. The WF is measured and data electronically processed by the RTCS, section 2.4.4, which calculates and generates signals used to apply the phase conjugate to the corrector. As the star or target is generally a point source, the WFS and RTCS will try and optimise its PSF. Thus a closed loop is created where the light is sampled, WF calculated and WFC controlled by the RTCS.

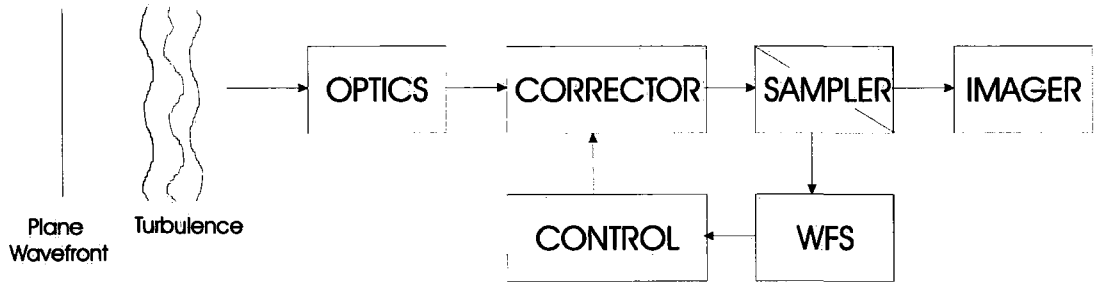

Figure 2.15 *Simple Astronomical Adaptive Optics System*

The sampler is placed after the WFC to correct any aberrations caused by the WFC. The system cannot correct for unpredictable dynamic aberrations. The RTCS collects and processes data as fast as possible but is limited by the capability of the hardware to sense and correct the beam at a sufficient rate. The fainter the starlight, the lower the SNR will be on the detector. This leads to longer integration times on the WFS which ultimately constrains the AOS's operating bandwidth.

2.4.1 Wavefront Sampler

In astronomy all AOSs will have a separate WFS and science instrument requiring the beam to be divided. Part of the beam will travel to the instrument and part to the WFS.

The **Wavefront sampler** can be divided into transmissive and reflective devices; often the device is just a single component of the beam train. The most common device is a coated-glass component named the **beamsplitter**. The operational requirements of the AOS often dictate the type of component needed.

Beamsplitters come in three basic types; they are flat-plate, cube or pellicle, see Figure 2.16. Each has its advantages and disadvantages. The cube beamsplitter flexures less when stressed through its mounting than a flat-plate, but will impart aberrations onto the transmitted beam due to its finite thickness. The fragile pellicle beamsplitter is only 5 μm thick, making the transmitted aberrations negligible. A disadvantage is that its small thickness allows it to be easily distorted by mounting stress and vibrations. They transmit a narrow wavelength due to their thickness and lack of coating.

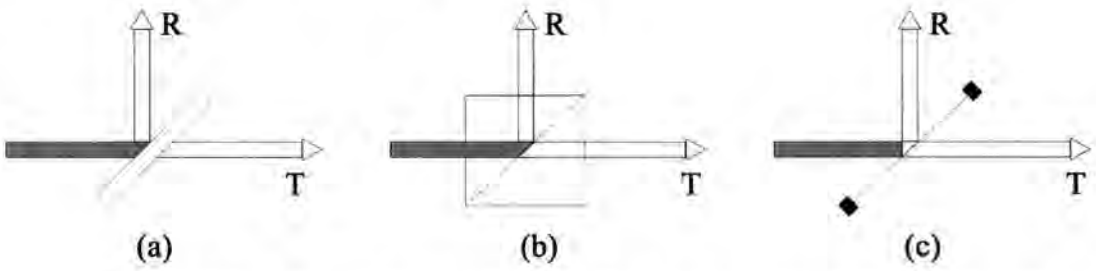

Figure 2.16 *Beamsplitter (a) flat plate, (b) cube, and (c) pellicle. R is the reflected beam and T is the transmitted beam*

Light can either be split by intensity, wavelength, polarisation or spatially. The **dichroic beamsplitter** divides the light by wavelength; it is coated to allow transmission of one wavelength and reflection of another.

Other WF samplers include hole gratings and reflective wedges, but in general they haven't been ideal and have lead to hybrid systems involving more optical surfaces. Temporal duplexing is another possibility but is not popular. For astronomical AOS the dichroic beamsplitter has been the reliable choice. The WF sampler must crucially provide a high-fidelity sample of the WF to the WFS.

2.4.2 Wavefront Sensor

Part of the light, hopefully containing a high-fidelity replication of the WF to be corrected, is redirected from the WF sampler to the **Wavefront sensor** (WFS). The WFS needs to sense the WF with sufficient spatial resolution and speed for the WFC to apply a real-time correction to compensate for WF aberrations.

If the WF can be measured then it can be reconstructed by the RTCS and WFC commands can be calculated. Reconstructing the WF requires knowledge of its phase and intensity.

In astronomy AOS the WFS must be as sensitive and accurate as possible. The WFS is required to work with limited magnitude sources and faint objects, thus requiring the capability to detect with low noise and high quantum efficiency.

The astronomical WFS is also required to operate successfully with extended and white light sources, which are required when the absolute **optical path difference** (OPD) cannot be determined at a single wavelength. The AOS will sense a difference of intensity non-uniformities leading to the WFS requiring the ability to determine the OPD independent of intensity.

With today's technological limitations, no detector is capable of directly measuring the WF phase at optical wavelengths due to the temporal frequencies required. The optical detectors that are available are used to measure the intensity of light and indirect methods are use to determine the phase.

There are ways of deriving the phase of a WF from its intensity distribution both at the focal and pupil planes. Focal plane techniques eliminate the need for phase reconstruction, as it allows direct access to the WF phase from the intensity distribution. Unfortunately they have not matured enough to be used in an operational AOS.

Pupil plane techniques are either based on interferometry or optical testing. Interferometry techniques use light beam superposition to form interference fringes that contain phase differences between the two beams of light.

The most common techniques of WFSing in AO have been derived from methods used in optical testing. AO WFSing differs by requiring real-time measuring and reconstruction. AO WFSing requires dealing with random WFs caused by atmospheric turbulence, requiring greater degrees of freedom. AO WFSing requires a dynamic range of many wavelengths to account for vast OPD over the pupil of interest. The WFS described in this section and Appendix A detects the WF in the **image plane of the pupil**. The Shack Hartmann WFS (SHWFS), Pyramid WFS (PWFS) and Shearing Interferometer are used to measure the first spatial derivative of the phase, the WF slope, whereas the Curvature WFS (CWFS) is capable of measuring the second spatial derivative, the Laplacian. The Shack Hartmann WFS and the Pyramid WFS evolved from the Hartmann and Knife Edge optical tests respectively.

2.4.2.1 Shack-Hartmann Wavefront Sensor

The **Shack-Hartmann WFS** (SHWFS) uses a variation on the traditional Hartmann test for real-time WF measurements.[34,35] The original test passes light through an opaque mask with an array of holes placed behind a lens or mirror under test to produce an array of spots. The position of each spot directly provides information of the local WF tilt at each hole, providing the instrument is carefully calibrated.

The SHWFS uses this concept. The holes are replaced with lenses, causing diffraction effects to be reduced and the light-gathering efficiency of the mask to be increased. This lenslet array is placed in a conjugate pupil plane in order to sample the incoming WF.

Figure 2.17 shows both a plane wave and a wave passing through turbulence reaching a lenslet array. Each of the beams in the subapertures (SA) is focused onto detector arrays, giving the resultant spot patterns.

The SHWFS provides **zonal** WF information, as the WF is expressed in terms of the OPD over a small spatial area. When the WF is expressed in terms of coefficients of the modes of a polynomial expansion over the entire pupil, it is said to be **modal**. As the WF is divided spatially, the individual SA tilts (WF slopes) can be determined and used to calculate the entire complete modal WF across an aperture.

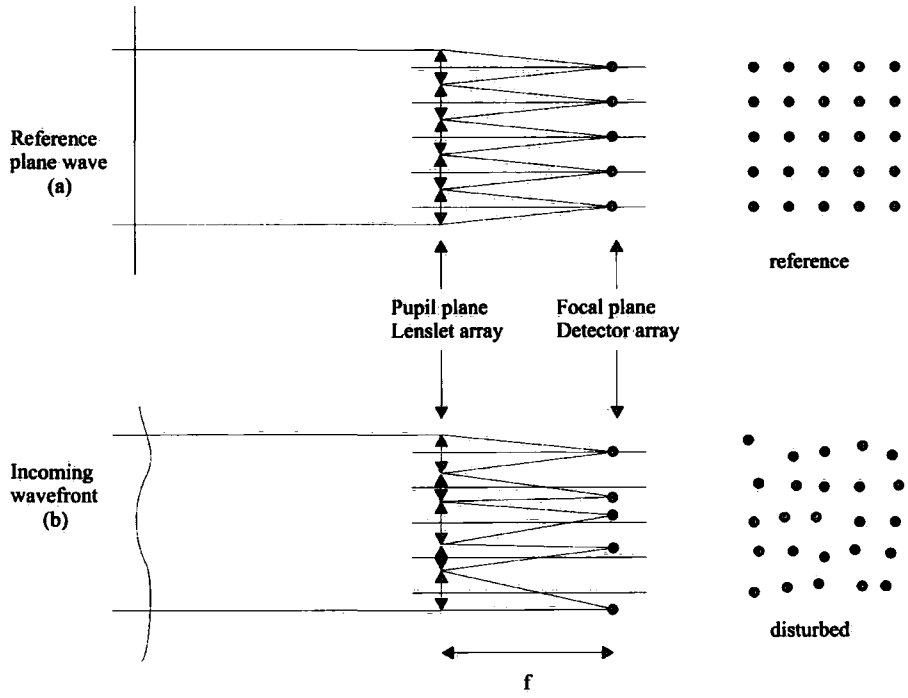

Figure 2.17 *Principle of the Shack-Hartmann wave-front sensor (a) plane wave, (b) disturbed wave*

The SHWFS exploits the fact that the WF tilt displaces a focused image in the direction of the tilt and at a distance proportional to the amount of tilt.[36]

Figure 2.18 shows the simple geometry of the beam of light passing through a single lenslet forming a spot image on the detector.

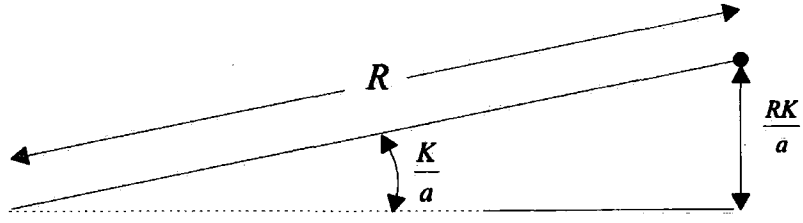

Figure 2.18 *Displacement of the centre of a beam due to wavefront tilt of magnitude K*

Consider the light entering a lenslet of radius a, and tilt K. The small angle formed between the beam and the plane of the aperture is K/a. After a distance R, the displacement from the normal is given by RK/a.

One can derive that the centroid of the intensity distribution is equal to the shifted origin of the image plane, which is proportional to the tilt. Hence the tilt shifts the position of the intensity centroid in the focal plane.[3]

The measurement of the image position gives a direct estimate of the angle of arrival of the wave over each lenslet. A map of WF slopes is obtained on an array of SAs, here defined by the lenslets. The positions of the SH images formed by the lenslet array can be measured by a number of point estimators.[37, 38]

Each SA uses either a quad-cell detector or a CCD for detection. To attain very high speed, centroid measurement with a single detector and high-speed processing is the desired direction. It is possible to use an array of CCDs as a quad-cell.

To compensate for the effects of atmospheric turbulence, it is vital that the local WF tilt is accurately measured for each lenslet SA. This is only possible if the lenslet is large enough to resolve the isoplanatic patch.[39] For an extended object, the detector would display a convolved image, that of the object's shape and the SA diffraction pattern.

The system must contain optical components of high optical quality. Its lenslet array must to aligned to a high level of accuracy. The introduction of a plane-wave reference beam provides a reliable way of removing alignment errors. The beam and unknown WF can differ in wavelength; there is no need for interference.

There are a number of documented methods of enhancing specific aspects of Hartmann sensors. [40,41] One way of improving the response of the basic Hartmann sensor is the introduction of a reference with beam nutation.[42]

2.4.2.2 Wavefront Sensor Detectors

Each WFS contains different optical elements to manipulate the WF so that it is possible to detect and measure the intensity to deduce phase information. Collecting the light efficiently is equally important to being able to interpret the results. WFS performance strongly depends on the characteristics of the detector. The WFS detector requires high quantum efficiency (sensitivity) at WFSing wavelength and a high frame rate. It requires low dark-current, read-out, and amplifier noise. Other considerations include its spectral bandwidth, the time lag due to the read-out of the detector, the array size and its spatial resolution.

The main choice of detectors for astronomical WFSs is the **Avalanche Photodiodes** (APD) and **Charged Couple Devices** (CCD), both of which are solid-state devices. [43,44]

In the APD, the classical photodiode high quantum efficiency is combined with an internal gain by operating the photodiode in a Geiger mode. Incident light promotes electrons to the conduction band. The APD emits light which causes a self-sustaining avalanche effect. Single-element photon counting devices are available using various semiconductors operating in the visible or in the near infrared spectrum.[45] Devices need to be electronically "quenched" so they do not saturate. A limitation of APDs is that it is currently impossible to make them into arrays. However, they have been made into single element assemblies.[3] The implementation of large assemblies is complex and APD arrays are under development.

The main type of CCD that is currently used is the back-illuminated thinned CCD. It contains a thin layer of Silicon and a backside coating. It is illuminated from behind so that light is not incident through control electronics. This dramatically improves the CCD quantum efficiency and the spectral bandwidth. The CCD technology is well suited to large array integration and low noise. The devices are multi-output, producing a reduced read-out time lag, pixel rate per output and read-out noise.

Even though the back-illuminated CCD has low read-out noise, it has a greater spectral bandwidth and quantum efficiency than an APD. The APD still makes a better detector when considering limiting magnitude and closing the real-time loop on faint objects. The main

limitation of the back-illuminated CCD is the time lag associated with read-out. The APD has no time-lag problem.

For high-order AO systems the back-illuminated CCD is preferential but is limited to a certain magnitude and servo-loop bandwidth. For low order AO systems, APD are best. In general, all detectors must be cooled to reduce the contribution of the dark current to the detector's noise.

2.4.3 Wavefront Correctors

A correction device must be added to the optical path to conjugate the beam to correct for phase fluctuations indirectly measured by the WFS. This device is commonly known in AO as the **Wavefront Corrector** (WFC). The WFC introduces into the system an optical phase shift ϕ by producing an OPD δ. The phase shift is given by:

$$\phi = \frac{2\pi}{\lambda}\Delta(ne) \tag{2.81}$$

Where n is the refractive index,
e is the geometrical path spatial distribution of the corrector.

Two types of correction are possible. Either the adaptive control of the reflective surface of a mirror is used to introduce geometrical path differences Δe, or a birefringent electro-optical material can produce difference in refractive index, Δn.

Currently, mirrors remain the only option for astronomical AO application because of properties absent from birefringent materials. Mirrors can have a large wavelength-independent optical path difference; they can provide extremely short response times and contain a uniform reflectivity that is relatively insensitive to wavelength and polarisation.

This section, accompanied with Appendix B, examines various Deformable Mirrors (DM) and Liquid Crystal (LC) devices.

The defence industry has researched, fabricated and tested a wide variety of DMs since the early 70s. Most of the performance requirements for the defence applications are more demanding than for astronomy although astronomical AO requires operation with light of different wavelengths.

The astronomical AOS uses multi-channel devices to correct the aberrations caused by the atmosphere. Requirements such as the required temporal bandwidth, the number of zones, the maximum phase correction stroke[46], the spatial response for each channel (the influence function)[47,48] and the fitting error for many types of DM has been investigated.[49]

Many astronomical AOSs have a dedicated tip-tilt mirror to correct for tilt aberrations. The segmented DM grows in potential due to the future ELT requirement to have large DMs. The continuous facesheet mirror remains the popular choice within second generation VLT instruments. The bimorph and MEMS DMs are briefly mentioned. Finally, LC devices are briefly touched, completing a brief overview of the currently WFC technology.

2.4.3.1 Tip-tilt Mirror

The most dominant and simplest form of WF error to correct for is WF tilt, the variation in the beam's direction; this is why most AOS will have dedicated **Tip-tilt Mirrors** (TTM).

TTMs were available before AOSs; they require a dynamic range of a few tens of microns peak-to-peak, to steer the beam into the correct place. This is much more than DMs, which require high voltages to operate.

Flat TTMs often use ferroelectric, electromagnetic and linear voice coil type actuators to move the TTM into position.[50,51,52,53,54] Most have dedicated driver systems with feedback position sensors to accurately drive the TTM. Ideally the TTM should produce no vibrational aberrations. Their main limitation for AO is their inability to accurately correct at high temporal frequencies. TTMs usually operate at kilohertz speeds providing between 10-100 Hz bandwidth correction allowing the residual higher-order frequencies to be corrected by the DM. The TTM will only control one optical mode. Approximately the maximum atmospheric tilt that a TTM should be able to remove is:

$$M_{tilt} = \pm 2.5\sigma_{tilt} \tag{2.82}$$

The standard deviation of atmospheric tilt motion, σ_{tilt}, is given by:

$$\sigma_{tilt} = \sqrt{0.184\left(\frac{D}{r_0}\right)^{\frac{5}{3}}\left(\frac{\lambda}{D}\right)^2} \tag{2.83}$$

Where D is the diameter of the telescope's primary mirror and r_0 is Fried's coherence length

The motion of the tilt stroke is twice the angular tilt motion of the beam; therefore the total stroke of the tilt mirror should be at least:

$$Stroke = \frac{1}{2} M_{tilt}\left(\frac{D_{telescope}}{D_{tilt\ mirror}}\right) \tag{2.84}$$

Some AO systems have mounted their high-order DM onto a tip-tilt mount, making the need for a separate TTM redundant. This has the advantage of reducing an optical surface in the system, increasing the throughput.

2.4.3.2 Segmented Deformable Mirror

The **Segmented Deformable Mirrors (SDM)** are becoming more potentially interesting as the next generation of telescopes plan to contain segmented primary mirrors. SDM consist of an arrangement of individually controlled elementary mirrors, either of square or hexagonal shape. Each mirror segment will have a number of actuators per segment. NAOMI has three actuators per segment, allowing control of piston, tip and tilt modes, as seen in Figure 2.19. Mirror manufactures are currently researching into developing SDM with higher spatial frequency zonal control.

Figure 2.19 *SDM displaying 3 actuators per segment*

SDM are scalable structures. They are well suited to provide a large number of mirror segments and actuators. Mirrors containing more than 10,000 segments have been produced using modules as large as 14 x 14 segments[55,56,57] An appealing strength is the ability to assemble and replace single elements.[58]

SDM do have discontinuities between segments, which have an impact on overall performance as they introduce edge-diffraction effects. Although these gaps can be a fraction of a millimetre, they still represent a loss of light by absorption and scattering and can create misleading diffraction patterns on the science camera. They also have emissivity contributions at longer wavelengths. Each segment operates independently, which allows fast movement of the segments, and SDM can operate with closed-loop bandwidths as high as 5 kHz.[57]

A relative drawback is their high fitting error compared to continuous facesheet DMs, if a segment has a single actuator then it has been calculated that between four to eight times more piston actuators per unit area of pupil are required to obtain the same fitting error.[49] The more actuators per segment there are, the less of an issue this becomes.

The number of segments in a SDM can be matched to the number of SAs in a SHWFS. Adding piston value to a segment would be undetected by the SHWFS. Providing the number of actuators is three or less, the measurement of tip-tilt is purely atmospheric slope difference with respect to current segment tilt.

Co-phasing techniques are employed to provide accurate piston reconstruction. This combined with tilt detection gives a bandwidth gain (in theory a factor of two or even more) due to the elimination of hysterisis.

The physical separation of the segments eliminates the 'cross-talk' between actuators on other segments. A three actuator per segment mirror will prove a completely diagonalised adaptive mirror/WFS response matrix for a SHWFS with one segment per subaperature. The mirror can have direct matching with the WFS and won't contain badly observed modes. This major benefit leads to a simplification in the control system design allowing modal control to exclusively be optimised for atmospheric correction.

2.4.4 Real-time Control

The purpose of the **real-time control system** (RTCS) is to interpret the WFS data to produce a set of meaningful control signals to position elements of the WFC, usually by reconstructing the WF.

AOS are multiple input, multiple output systems (MIMO) having multiple input WFS signals and multiple output WFC actuator channels, containing a highly complex spatio-temporal

behaviour. Few systems have a simple one-to-one relationship between input and output channels. Designing and optimising such a system is a complex problem. In many AOS, the RTCS simultaneously controls lower-order aberrations using a two-channel TTM and controls high-order aberrations using a multi-channel DM.

Each system component, including the RTCS, has a finite temporal response. The typical AO closed-loop system consists of a large number of highly coupled feedback loops working in parallel.

The continually varying disturbances in the WF presented to the AOS changes rapidly. It is necessary to have a system of WFS, RTCS and DM with sufficient response to compensate for the disturbance.

Most of the AO RTCS are based on single-channel linear processing algorithms.[59] This can be examined in both the temporal and frequency domains using tools and methods described in Section 2.3. Although the optical system may not be linear throughout its entire range, the optical and electronic signals are often linear near the point of control, and the temporal response of the system components does not vary much from channel to channel. All actuators in a WFC have to good approximation the same temporal response. This makes it possible to separate out the RTCS into a purely spatial task of wavelength reconstruction and a purely temporal single-channel controller. As most adaptive operations are linear, straightforward methods of linear algebra are usually sufficient.

This section contains generalised theories, examining the fundamental principles of AO real-time control (RTC). It places no restriction on which WFS or WFC is used. The system can be analysed modally and zonally. Zonal control can be seen as a particular case of modal control. The following analysis reveals the advantages of modal analysis.

2.4.4.1 Wavefront Reconstruction

The spatial control task is referred to as **Wavefront Reconstruction**. Conceptually there are two aspects to this task. Firstly to reconstruct the WF aberration by either interpreting the modal or zonal set of WFS data. Secondly to calculate a set of control signals in a form that can be supplied to the WFC, to correct for the aberration. The RTCS must be able to reconstruct the phase in a form that the WFC can use, regardless whether the WFS calculates or measures the phase directly.

Often the intermediate stage of explicit reconstruction of the WF aberration is not computed; rather, the two aspects are combined into a single operation. The intermediate stage may be calculated for diagnostic purposes.

Linear matrix algebra is used to translate a large number of signals to a large number of commands. Most DMs and WFSs are linear over a large range. If not, the system has to be linear over only a small range for results to be valid.

AOS can be categorised into three types: underdetermined, determined and overdetermined. The WFS spatial resolution is given by the number of useful SAs.

An **underdetermined** system has more actuators to move than WFS measurements. This situation gives an infinite number of solutions; determining the actuator commands cannot be

solved. It is possible to use methods to overcome this, such as surface matching, providing the measurements are in modes that can be reconstructed into a WF surface and the actuator influence functions can also be decompressed into a WF surface.

A **determined** system exists if the number of WFS signals equals the number of actuator commands. A SDM with a SHWFS is a good example. Each SA sends two slope signals for a segment that can slope in two directions. Pistoning can be resolved by a simple circuit or algorithm that zeros the average of all piston motions without regard to their tilt motion.

An **overdetermined** system is the most commonly used, giving more WFS signals than actuators to control. Careful optical and mathematical alignment of the WFS SAs and actuators is required.

2.4.4.2 Influence, Interaction, Control and Response Matrices

Figure 2.20 contains a block diagram for a closed-loop AOS. The aberrated WF, ϕ_0, enters the system and falls on the DM. The operation of the mirror will be represented by the Influence Matrix, $\boldsymbol{M}$. The WF altered by the DM then falls on the WFS, whose operation can be expressed using the Interaction Matrix, $\boldsymbol{S}$. The reconstruction operation is denoted by the Control Matrix $\boldsymbol{C}$. Finally, the Response Matrix, $\boldsymbol{B}$ is defined.

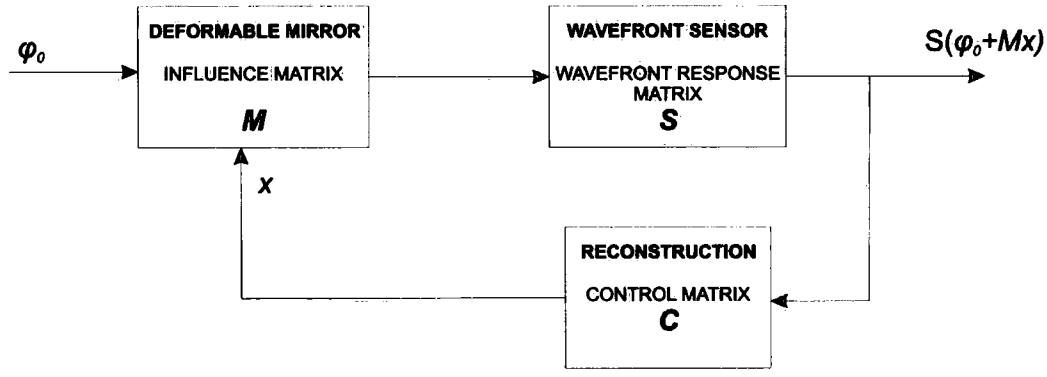

Figure 2.20 *Block Diagram of AOS for Spatial Control*

The influence matrix

Using a DM as an example WFC, a static linear model describes a set of DM deformations using **influence functions**, $r_j(x,y)$, one function for each of its N_A actuators.

Applying a set of RTC signals, x_j, to the N_A actuators produces a resulting phase, given to the surface of the DM, $\Phi_M(x,y)$. This can be written as a linear superposition of the influence functions:

$$\Phi_M(x,y) = \sum_{j=1}^{N_A} r_j(x_i,y)\,x_j \tag{2.85}$$

Where $\Phi_M(x,y)$ can be expanded in terms of an orthonormal basis.

Assuming the mirror aperture is circular and using the Zernike basis gives:

$$\Phi_M(x,y) = \sum_{i=1}^{\infty} \phi_i Z_i(x,y) \tag{2.86}$$

Where the Zernike coefficients of the expansion ϕ_i are given by the inner product integrals:

$$\phi_i = \int\int W(x,y)\Phi_M(x,y)Z_i(x,y)dxdy = \sum_{j=1}^{N_s}\left[\int\int W(x,y)Z_i(x,y)r_j(x,y)dxdy\right]x_j \tag{2.87}$$

Where $W(x,y)$ is the circular aperture function.

This can be represented in **influence matrix**, $\boldsymbol{M}$:

$$\boldsymbol{\phi} = \boldsymbol{Mx} \tag{2.88}$$

Where $\boldsymbol{x}$ is the vector of RTC signals x_j and $\boldsymbol{\phi}$ is the vector of Zernike coefficients ϕ_i,

$\boldsymbol{\phi}$ describes the resulting DM deformation. The matrix $\boldsymbol{M}$ represents the operation of the DM, its elements are given by:

$$M_{ij} = \iint W(x,y)r_j(x,y)Z_i(x,y)dxdy \tag{2.89}$$

Equation (2.89) shows that each column of $\boldsymbol{M}$ is the set of Zernike expansion coefficients for a single influence function of the mirror.

The influence matrix can be used to determine the correcting potential of a mirror by looking at its fitting error. The DM is limited in the aberrations it can correct given the number of influence functions.

Given a WF aberration, ϕ_0, the vector of actuator RTC signals which gives the least squares best fit correction is given by:

$$\boldsymbol{x} = \boldsymbol{M}^{-1}\boldsymbol{\phi}_0 \tag{2.90}$$

Where $\boldsymbol{M}^{-1}$ is the least squares inverse of $\boldsymbol{M}$.

The residual WF error, ϕ_e, after correction is given by

$$\boldsymbol{\phi}_e = \boldsymbol{M}\boldsymbol{M}^{-1}\boldsymbol{\phi}_0 - \boldsymbol{\phi}_0 \tag{2.91}$$

This can be used to evaluate the fitting errors associated with different mirrors for different aberrations.

The Interaction Matrix

The **interaction matrix**, $\boldsymbol{S}$, is calculated as the interaction of the WFS with the input aberration basis. It is also referred to as the WFS **response matrix**. The operation of the WFS in terms of a matrix operation:

$$s = S\phi_0 \tag{2.92}$$

Where $\boldsymbol{S}$ is the interaction matrix, s is the WFS signals vector and ϕ_0 is the WF aberration.

The interaction matrix is determined experimentally in astronomical AOS.

For the SHWFS, the WFS signal vector has a length equal to twice the number of SAs N_A because the slopes in two directions are measured. For the CWFS the length of the vector is equal to N_A.

For a SHWFS using centroiding to calculate the position of each image, the elements of $\boldsymbol{S}$ are given by:

$$S_{ij} = \iint W(x,y) W_i(x,y) \frac{\partial Z_j(x,y)}{\partial e} dxdy \tag{2.93}$$

Where $W_i(x,y)$ is the lenslet array aperture corresponding to the i^{th} signal,
e is either x or y depending on the components of the gradient to which the signal corresponds.

By examining Equation (2.93), it is seen that each column of $\boldsymbol{S}$ is the vector of WFS signals produced with the corresponding Zernike mode as the input aberration.

The Control Matrix

The **Control Matrix**, $\boldsymbol{C}$, is used in the reconstruction operation, which takes a vector of WFS signals, s, and produces a vector of actuator RTC signals, x. This can be written as the matrix operation:

$$x = Cs \tag{2.94}$$

The Response Matrix

The **response matrix**, $\boldsymbol{B}$, represents the interactions between the actuator commands, the WF that's modified, and the WFS signals in a closed-loop system. The WFS receives a WF that is the sum of the mirror's deformation $\phi = Mx$ and the aberrated input wave ϕ_0. In a noiseless system, the resulting WFS signal, s, is given by:

$$s = S[\phi_0 + Mx] = s_0 + Bx \tag{2.95}$$

Where s_0 is the WF aberration WFS signal

To find the values of response matrix, it is necessary to determine how the WF surface changes with the each actuator command.

The ease of this depends on the mirror-sensor combination. For a SDM, the influence function of each segment covers only those SAs overlapping this segment, leaving **B** nearly diagonal and sparse. If there is a one-to-one relationship, the inversion of **B** would be relatively easy, providing the square matrix isn't singular, which isn't normally the case.

For CFDM, each actuator can affect a large part of the surface and the signals in many SAs. The response matrix, **B**, can be completely filled with meaningful signal-command interactions. The most common DM is a CFDM with a relatively small amount of coupling (15% or so) between actuators.

If there were the same number of signals as actuators, the inversion of **B** would be relatively easy, providing the square matrix isn't singular, which isn't normally the case. This leads to the most common method of reconstructing used in AO, the **least squares reconstructor**.

2.4.4.3 Least Squares Reconstructor

The **least squares reconstructor** is very simple to implement. The least squares control method describes the minimisation of the WF signal error.

Considering the AOS displayed in Figure 2.20 and the response system matrix, see equation (2.95), the WFS signals can be used as a measure of correction error, as the WFS measures the net WF aberration after correction. The squared sensor signal error, ε^2 , is given by:

$$\varepsilon^2 = |s|^2 = s \bullet s = s^T s = \left[x^T \boldsymbol{B}^T + s_0^T \right] \left[s_0 + \boldsymbol{B} x \right] \tag{2.96}$$

By differentiating ε^2 with respect to x, the minimum can be found:

$$\frac{\partial \varepsilon^2}{\partial x_i} = \frac{\partial}{\partial x_i} \left\{ \left[x^T \boldsymbol{B}^T + s_0^T \right] \left[s_0 + \boldsymbol{B} x \right] \right\} = 0 \tag{2.97}$$

Rearranging the solution to this is the normal equation that gives the required x as a linear operation on the WFS signal s:

$$x = -\left[\boldsymbol{B}^T \boldsymbol{B} \right]^{-1} \boldsymbol{B}^T s_0 \tag{2.98}$$

Thus the method of least squares has produced a new matrix called the pseudoinverse of $\boldsymbol{B}$, this makes the control matrix $\boldsymbol{C}$:

$$\boldsymbol{C} = -\left[\boldsymbol{B}^T \boldsymbol{B} \right]^{-1} \boldsymbol{B}^T \tag{2.99}$$

The first thing to note is that the Control Matrix, $\boldsymbol{C}$, only depends on the system matrix, **B**.

Calculating the control matrix involves finding the inverse of the symmetric matrix $\left[\boldsymbol{B}^T\boldsymbol{B}\right]$. This N_A x N_A matrix will have an inverse only if the mirror actuators produce linearly independent signal vectors. The matrix is singular if the number of mirror actuators is greater, leading to no unique least squares solution.

Even when $\boldsymbol{B}^T\boldsymbol{B}$ is invertible, the resulting control matrix $\boldsymbol{C}$ can give very poor performance.

The powerful technique of **singular value decomposition** (SVD) is used to give an alternative, modal view of a system, giving a one-to-one correspondence between the WFS signal modes and the DM actuator modes.

The SVD of the response matrix **B**, is given by:

$$\boldsymbol{B} = \boldsymbol{U}\boldsymbol{\Lambda}\boldsymbol{V}^T \tag{2.100}$$

Where $\boldsymbol{U}$ is an N_S x N_S orthogonal matrix, $\boldsymbol{V}$ is an N_A x N_A orthogonal matrix and $\boldsymbol{\Lambda}$ is an N_S x N_A diagonal matrix.

Considering the mirror-sensor system:

$$s = \boldsymbol{U}\boldsymbol{\Lambda}\boldsymbol{V}^T x \tag{2.101}$$

$$s = \begin{pmatrix} u_1 & u_2 & \ldots \end{pmatrix} \begin{pmatrix} \lambda_1 & & & \\ & \lambda_2 & & \\ & & \ldots & \\ & & & \lambda_N \end{pmatrix} \begin{pmatrix} v_1^T \\ v_2^T \\ \ldots \end{pmatrix} x$$

Since $\boldsymbol{V}$ and $\boldsymbol{U}$ are orthogonal, their columns $\boldsymbol{v_i}$ and $\boldsymbol{u_i}$, form a complete orthonormal basis for the vector space $\boldsymbol{x}$ and $\boldsymbol{s}$ respectively, forming a complete set of DM control and WFS signal system modes.

The diagonal values of $\boldsymbol{\Lambda}$, λ_i are the singular values of the matrix $\boldsymbol{B}$. Each non-zero singular λ_i relates the orthogonal basis component $\boldsymbol{v_i}$ in $\boldsymbol{x}$ to the orthogonal basis component $\boldsymbol{u_i}$ in $\boldsymbol{s}$, linking a single DM control mode to a single WFS signal mode. The dimensionality of the transformation $\boldsymbol{B}$ is given by the number of non-zero singular values.

The SVD has created separate system modes. This view gives a one-to-one correspondence between the WFS signal modes and the DM actuator control modes. There are three types of system modes.

Correctable modes are modes where $\lambda_i \neq 0$. In this case actuator RTC signal $\boldsymbol{x} = \boldsymbol{v_i}$ results in the corresponding WFS signal $\boldsymbol{s} = \lambda_i \boldsymbol{u_i}$, allowing the component of the WFS signal $\boldsymbol{s} = \boldsymbol{u_i}$ to be corrected completely by applying the corresponding actuator mode $\boldsymbol{x} = -\lambda_i^{-1}\boldsymbol{v_i}$.

The sensitivity of the mode, λ_i, determines how much of a given sensor mode is obtained when applying the corresponding RTC signal mode to the DM. Unfortunately there is at least one null λ_i which corresponds to the WFS undetected piston mode. This mode is, however, interferometrically interesting.

Unsensed mirror modes do not affect the WFS signal. These actuator control modes have no non-zero λ_i resulting in a zero-sensor signal.

Uncorrectable sensor modes are impossible to correct for with the mirror. These mirror actuator modes have no non-zero λ_i resulting in a zero-sensor signal.

Due to the orthogonal nature of the WFS signal modes, each independently contributes to the squares error ε^2. Therefore the value of ε^2 is reduced for each mode that can successfully be corrected.

The outcome is that the least-squares controller gives complete correction for all the correctable modes of the system. The control matrix is then given by the least-squares or pseudoinverse of $\boldsymbol{B}$:

$$\boldsymbol{C} = -\boldsymbol{B}^{-1} = -\boldsymbol{V}\boldsymbol{\Lambda}^{-1}\boldsymbol{U}^T \tag{2.102}$$

Where $\boldsymbol{\Lambda}^{-1}$ is the pseudoinverse of $\boldsymbol{\Lambda}$

$\boldsymbol{\Lambda}^{-1}$ is formed by transposing $\boldsymbol{\Lambda}$ and replacing all non-zero diagonal elements λ_i by their reciprocals λ_i^{-1}, which become the **gains** of the modes in the control matrix. Modes with small sensitivity λ_i result in modes with large system gains λ_i^{-1} in the control matrix $\boldsymbol{C}$, which can cause problems with stability. Modes with large gains are sensitive to WFS aliasing, subject to the possible effects of actuator clipping and very sensitive to WFS noise, which can result in means very large actuator control signal.

The ratio of the largest to the smallest λ_i is called the **condition factor** of the matrix. A large condition factor gives an ill-conditioned matrix. Modes with small λ_i are sometimes discarded to restrict the condition factor, by setting the corresponding singular values to zero in the pseudoinverse. This can give better correction for fewer correction modes. Correcting all spatial modes won't provide a better performance than correcting for one.[60] In this case discarding modes makes an enormous difference. A balance between discarding too few and too many must be found, and is usually done so experimentally by measuring the performance of the system for different modes.

For all but the simplest configurations the matrix $\boldsymbol{B}$ can be measured experimentally by poking each mirror actuator in turn and measuring the corresponding response on the WFS. The system must be calibrated very carefully, although the effects of calibration errors so far have been found to be small. Most AOSs have hundreds of actuators. Thus, the inversion of matrix $\boldsymbol{B}$ should be performed once, preferably before any RTC takes place.

The least squares reconstructor is the most common use mainly because it is very simple to implement. Better reconstructors, that minimise the actually WF error and that use statistical knowledge of the aberrations exist, see Appendix C.

2.4.4.4 Temporal Control

For astronomical AOS, the Greenwood frequency, (typically in the range 10-1000 Hz) characterises the temporal behaviour of the aberrations requiring correction. To make the temporal control analysis easier it is important to find a set of independent inputs and

outputs.[61,62,63] The system modes already described define a set of independent inputs and outputs, which makes it possible to split the AOS control loop into n independent single-input/single-output servos working in parallel, allowing the temporal behaviour of each channel to be analysed independently.

The timescales in most closed loop AOSs are dominated by system latency or time delays, which result from the time required to collect WFS data and evaluate the spatial control or reconstruction. The AOS is a servo using both continuous and sampled data.

Temporally, the AOS can be divided into 6 subsections as shown in Figure 2.21.[64,65,66] It shows a WF, $\phi_{tur}(x,y,t)$, entering the AOS and the DM corrected WF as $\phi_{corr}(x,y,t)$. The resulting residual phase after correction, $\phi_{res}(x,y,t)$, is given by:

$$\phi_{res}(x,y,t) = \phi_{tur}(x,y,t) - \phi_{corr}(x,y,t) \tag{2.103}$$

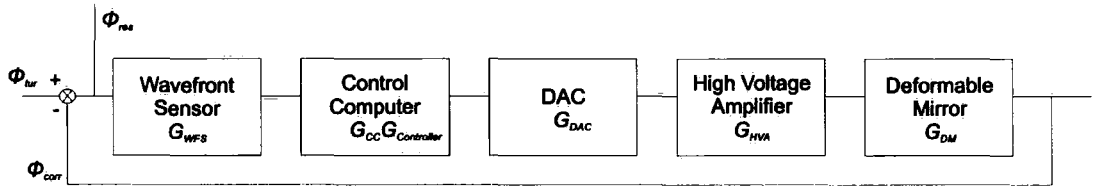

Figure 2.21 *Adaptive Optics System Block Diagram*

The **WFS transfer function,** G_{WFS}, depends on the integration time T of the detector and the effects of getting the data from the detector. The WFS temporal resolution is determined by the sampling frequency of the detector. Many WFSs contain one or more CCDs, which integrate the signal for a finite time T to give a signal at time t:

$$g(t) = \frac{1}{T}\int_{-T}\phi(t)dt = \frac{1}{T}\int_{-T}^{\infty}\phi(t)dt - \frac{1}{T}\int^{\infty}\phi(t)dt \tag{2.104}$$

Equation (2.104) gives the difference between integration and an integration delay. Thus G_{WFS} is given by:

$$G_{WFS}(s) = \left(\frac{1}{Ts}\right) - e^{-Ts}\left(\frac{1}{T}\right) = \frac{1-e^{-Ts}}{Ts} \tag{2.105}$$

At the end of each CCD integration cycle there are often readout delays. Interface to the RTCS can also introduce additional system delays. In many this delay can be considerable, accounting for most of the total delay. For this reason, astronomical AOSs make use of multi-port CCD devices, up to 32 to significantly speed up the data transfer, reducing the time delay. Additional time delay can be introduced if the CCD performs pre-processing on the data within the camera controller, although time can be saved by discarding unwanted pixels rather than transferring them.

The **RTCS delay transfer function,** G_{CC}, results in a time delay. The RTCS firstly digitises the WFS signals, then it applies specific algorithms to derive the WF measurements.

The magnitude of the time delay compared to the WFS depends on the spatial order of the system and the speed of the RTCS. Moderately spatially ordered systems contain relatively small control computer delays. With a single time delay of τ, the transfer function, $G_{CC}(s)$, is given by:

$$G_{CC}(s) = e^{-\tau s} \tag{2.106}$$

Highly spatial ordered astronomical AOS try and overcome delay by employing multiple parallel processors to cope with the large data flow.

The RTCS also applies the temporal controller to optimise the AOS closed loop response, ensuring stability by compensating for the transfer function of the various system components. As previously mentioned, a common **Controller transfer function**, $G_{Controller}(s)$, is the integrator:

$$G_{Controller}(s) = \frac{K}{s} \tag{2.107}$$

where K is the controller gain.

The WFS detector integration time is synchronised with the Digital-to-Analogue Convertor (DAC). The control voltages of the DM are held constant during time T, until the next voltages are available from the control computer. The **DAC transfer function**, G_{DAC}, of this device is called a zero-order hold:

$$G_{DAC}(s) = \frac{1 - e^{-Ts}}{Ts} \tag{2.108}$$

For the DACs the input signals are sampled, but the output signals are continuous. The low voltage outputs of the DACs are amplified to drive the DM actuators by the High Voltage Amplifiers (HVA). The HVAs are considered to be either first or second order analogue filters and are characterised by the temporal bandwidth. Generally, the bandwidth of the HVAs is adjusted so that it is greater than the frequency domain of interest of the AOS. There, within this domain, the **HVA transfer function**, G_{HVA}, is close to unity:

$$G_{HVA}(s) \approx 1 \tag{2.109}$$

The technology used determines the **DM transfer function**, G_{DM}, of the DM. Its temporal behaviour is characterised by damping factors and resonance frequencies, given by its mechanical response. The DM is considered to be a second order filter. The Transfer Function will include the DAC, the analogue voltage amplification and the mechanical behaviour of the mirror. The DAC and the analogue voltage amplification are often chosen such that their sufficiently rapid responses give a unity transfer function over the frequencies of interest. Typically the first resonance frequency is greater than a few kHz and is damped by the high voltage amplifiers. This assumption keeps the generality of the results and simplifies the analysis.

$$G_{DM} = 1 \tag{2.110}$$

2.4.4.5 System Transfer Functions

The system's open-loop transfer function can be written as the overall product of its component's transfer functions.[66] One problem is the combination of continuous and sampled elements. From a physical viewpoint, the input and the output of the AOS servo are the turbulence WF fluctuations and the residual phase errors after correction by the DM respectively. These signals are continuous so are given in terms of the Laplace variable *s*.

In the expression of the AOS open-loop transfer function, the Laplace transform and Z-transform are both required. However, it can be assumed that, since the Z-transform is the expression of the transfer function of a process taking place in the sampled time domain, it can be studied in the continuous time domain using the following classical transformation:

$$z = e^{Ts} \tag{2.111}$$

This assumption is valid within the low frequency domain, which is restricted to one quarter of the sampling frequency.[288] The overall open-loop transfer function of an AOS, denoted by *G(s)*, is given as:

$$G(s) = \frac{e^{-\tau s}\left(1 - e^{-Ts}\right)^2}{T^2 s^2} G_{Controller}(e^{Ts}) \tag{2.112}$$

This has been found to be a good approximation for many systems; where $G_{controller}(e^{TS})$ defines the controller. It should be optimised to reach the best correction efficiency within the limit of the overall system stability.

With the exception of the controller, all components of an AOS demonstrate an overall behaviour which can be represented as a pure time delay $T+\tau$. The one frame time delay T cannot be reduced. It is due to the exposure time of the detector and to the DAC. τ is referred to as the AOS time delay. The correction efficiency of an AOS is highly dependent on τ.

Closed-loop transfer function

The **closed-loop transfer function,** *H(s)*, is given by:

$$H(s) = \frac{\phi_{corr}(s)}{\phi_{tur}(s)} = \frac{G(s)}{1 + G(s)} \tag{2.113}$$

and the **closed-loop error transfer function,** $\varepsilon(s)$, is related to the open-loop transfer function *G(s)* by:

$$\varepsilon(s) = \frac{1}{1 + G(s)} \tag{2.114}$$

The closed-loop error transfer function is defined as the transfer function between the turbulence WF fluctuations and the residual phase. It corresponds to the ability of the AOS to compensate for phase perturbations as a function of frequency, characterising the system's correction efficiency.

A fundamental limitation of an AOS is the WFS measurement noise, whether it is photon noise, sky background or read-out detector noise. From a servo viewpoint, it may be represented by an additive white spectrum signal introduced after the WFS.

To characterise its effect on the residual phase after correction, the noise transfer function, *N(s)*:

$$N(s) \approx H(s)e^{-Ts/2} \tag{2.115}$$

N(s) is defined as the ratio between the residual phase due to noise propagation and the measurement noise. Consequencly, the gain of *N(s)* is equal to the gain of the closed-loop transfer function at low frequencies.

3 Astronomical Adaptive Optics Systems Review

In the world of constructing astronomical adaptive optics instrumentation the most useful conference tends to be the bi-annual Astronomical Telescope and Instrumentation conference hosted by the Society of Photo-Optical Instrumentation Engineers (SPIE).

Year	Volume No.	SPIE Conference	AO Papers
1990	1271	Adaptive Optics and Optical Structures	36
1991	1542	Active and Adaptive Optical System	48
1991	1543	Active and Adaptive Optical Components	45
1993	1920	Active and Adaptive Optical Components and Systems II	37
1994	2201	Adaptive Optics in Astronomy	107
1995	2534	Adaptive Optical Systems and Applications	41
1997	3126	Adaptive Optics and Applications	71
1998	3353	Adaptive Optical System Technologies	130
1999	3762	Adaptive Optics Systems and Technology	41
2000	4007	Adaptive Optical System Technology	129
2001	4494	Adaptive Optics Systems and Technology II	37
2002	4839	Adaptive Optical System Technologies II	121
2003	5169	Astronomical Adaptive Optics Systems and Applications	40
2004	5490	Advancements in Adaptive Optics	163
2005	5903	Astronomical Adaptive Optics Systems and Applications II	29
2006	6272	Advances in Adaptive Optics II	174
2007	6691	Astronomical Adaptive Optics Systems and Applications III	22

Table 3.1 *Overview of SPIE Adaptive Optics Papers*

The proceedings provide an excellent world-wide snapshot of the subject. Most of the material provided within this chapter originates from SPIE proceedings. Table 3.1 summarises the SPIE AO conferences dating back to 1990.

With the noticeable exception of the Isaac Newton Group of Telescopes (ING) observatory, which is covered in Chapter 4, the world's major observatories and telescopes are listed in Table 3.2. Each telescope's AO systems are reviewed in this chapter.

Observatory	Telescope	Diameter (m)	Location
ESO	UT1, 2, 3 & 4	8.2	Cerro Paranal, Chile
	3.6 m	3.6	La Silla, Chile
Gemini	North	8.1	Mauna Kea, Hawaii
	South	8.1	Cerro Pachon, Chile
Keck	Keck I & II	10	Mauna Kea, Hawaii
Suburu	Suburu	8.2	Mauna Kea, Hawaii
MMT	MMT	6.5	Mt Hopkins, Arizona
Calar Alto	3.5 m	3.5	Sierra de Los Filabres, Spain
TNG	3.6 m	3.6	Roque de Los Muchachos, La Palma
Lick	3 m	3.0	Mt Hamilton, California
CFHT	CFHT	3.6	Mauna Kea, Hawaii
SOAR	4.1	4.1	Cerro Pachon, Chile
GTC	GTC	10.2	Roque de Los Muchachos, La Palma
LBT	LBT	8.4 (x 2)	Mt Graham, Arizona
SALT	SALT*	11.0	Sutherland, South Africa
McDonald	HET*	9.2	Davis Mountains, Texas

*Telescopes without AO Systems

Table 3.2 *List of worlds major ground-based telescopes*

The aim of the review was to investigate the similarities and differences between AO systems at the world's leading observatories. The investigation revealed the progression of astronomical AO systems within the community and the various different combinations of WFSs, WFCs and RTCS.

Technology has evolved to allow progressively higher order systems. The community has recognised the requirement to collaborate internationally to fund the construction of common high cost components such as DMs, yet there are many different implementations of AO RTCSs. The investigation reveals the requirement to produce a RTCS from common COTS components reusing and standardising code already created for different AO projects.

3.1 European Southern Observatory

The European Southern Observatory (ESO)[67] operates the four 8.2 m unit telescopes of the Very Large Telescopes (VLT) and the VLT interferometer (VLTI) on Cerro Paranal; see Figure 3.1.

Figure 3.1 *ESO's VLT UT1-4*

ESO has a long history of Adaptive Optics (AO) and after a decade of development ESO have set the standard for turn-key AO systems. AO is now considered a mature technique for the 8-10 m class telescopes.[68] This section reviews each 3.6 m system and 8.2 m system contained in Table 3.3 and Table 3.4 respectively.

AO System	Key Dates
COME-ON	First Light: April 1990*
COME-ON PLUS	First Light: July 1993
ADONIS	Common Use: January 1995

*Tested on the 1.52 m telescope at the OHP, France in October 1989

Table 3.3 *List of ESOs 3.6 m f/8 Cassegrain AO systems*

AO System	Key Dates
NAOS	Initial Study: Dec 1993,[69] Kick Off: 1995, First Light: November 2001 Common Use: October 2002, LGSF Close loop: February 2006[70,71]
MACAO (x7) (4 for VLTI) (1 for SINIFONI) (1 for CRIRES)	Initial Study: 1998, Kick Off: 2000, Commissioning between April 2004 and August 2006 SINFONI LGSF Close loop: February 2006
MAD	Kick Off: 2002, SO mode First Light: March 2007
AOF – GRAAL	Initial Study: 2001, FDR 2008, Commission 2012
AOF – GALACSI	Initial Study: 2001, FDR 2008, Commission 2012
SPHERE	Initial Study: 2001, FDR 2008, Commission 2012

Table 3.4 *List of ESOs 8.2 m AO systems*

3.1.1 COME-ON and COME-ON+ Prototype Systems

The first AO system to obtain astronomical results was the VLT AO prototype system 'COME-ON' (CO), which was developed by the Paris Observatory, Office National d' Etudes et de Recherches Aérospatiales (ONERA), ESO and Cilas (formally Laserdot). CO first light achieved 0.12 arcsec images at 1.7 μm.[72]

The main components of the COME-ON and COME-ON+ are contained in Table 3.5. Two visible WFS and one IR WFS detectors were evaluated on COME-ON. The first images were collected on a 32x32 InSb IR (1 to 5 μm) camera with a 3.2 x 3.2 " FOV.[72] The main COME-ON-PLUS improvements were due to a high-detectivity WFS and a new modal control algorithm. The new SHWFS contained both an Intensified Reticon detector for high flux and an Electron-Bombarded CCD for low flux. The system was operated testing four different science cameras: a 32 x 32 InSb array IR imaging camera, an ESO 512 x 512 CCD camera, a MPIE 256 x 256 NICMOS3 HgCdTe array SHARP II camera and an intensified visible CCD camera. Like CO the RTCS consisted of a WFS computer and a Control computer containing a DSP 56000 Motorola coprocessor VME board. The control loop ran at a maximum frequency of 200 Hz. The system achieved an image FWHM of 0.1 " in the H band.[73, 74]

Component	COME-ON	COME-ON+
DM Type / No Piezoelectric Actuators	CFDM / 19	CFDM / 64 (52 useful)
TTM	4 push-pull actuator	4 push-pull actuator
WFS Type	SHWFS	SHWFS
No Supaperatures	20 (5 x 5 grid)	32 (7 x 7 grid)
Correction	9 Hz (April 1990) 25 Hz (April 1991)	30 Hz
Optical Throughput	3%	30%

Table 3.5 *COME-ON and COME-ON+ main components*

3.1.2 ADaptive Optics Near Infrared System (ADONIS)

Various upgrades to COME-ON resulted in the first common-user facility 'ADaptive Optics Near Infrared System' ADONIS. The ADONIS upgrade retained most of the COME-ON components. Its main addition was a commercial Shakti TMS3202C40 DSP-based real-time control system, increasing the WFS sample rate to a maximum of 400 Hz, allowing a maximum bandwidth of 60 Hz.

Two science cameras were created for ADONIS. The first camera, SHARP II, contained a 256 x 256 NICMOS-3 HgCdTe detector array covering the 1 to 2.5 μm spectral range providing a 12.8 x 12.8 " FOV. The second, COMIC, covered the 1 to 5 μm spectral range, contained a HgCdTe 256 x 256 detector providing a 4.5 x 4.5 " FOV for J, H and K bands with a 12.8 x 12.8 " FOV for L and M bands.[75, 76]

3.1.3 Nasmyth Adaptive Optics System (NAOS)

A French-led consortium produced NAOS, which currently resides on the Nasmyth B platform of the UT4 VLT.[77] First light was achieved with the dedicated 'Coudé Near IR CAmera' (CONICA). 'NAOS-CONICA' (NACO) was later upgraded to accommodate the ESO 'Laser Guide Star Facility' (LGSF).

Its main components are given in Table 3.6.

The VSHWFS is connected to a 'Fast Imager Electronic Readout Assembly' (FIERA) controller, which provides 48 different readout modes. The 'readout noise' (RON) is between 2.9 and 5.4 e^- depending on the configuration. On a bright NGS the VSHWFS has a maximum frame rate of 444 Hz (achieving a system bandwidth of 27 Hz at 0 dB).[78]

The entirely cryogenic IRSHWFS detector has both a fast 'multiple successive read-out' (MSR) mode and a slower 'double correlated sampling' (DCS) readout mode. The IRSHWFS uses three different configurations, leading to 36 different readout modes. The noise measured on the detector ranges from 8.7 to 20.1 e^- RMS depending on quadrant, frame rate and configuration. On a bright NGS the IRSHWFS has a useful maximum frame rate of 178 Hz (achieving a 22 Hz system bandwidth at 0 dB).

Each WFS contains two exchangeable micro-lens arrays. (operating at -110 °C) The magnitude of the NGS dictates which micro lens array is selected. A 14 x 14 lenslet subaperture configuration is used with a bright NGS ($m_v < 13$) and a 7 x 7 with a faint NGS ($14 < m_v < 17$).[79]

Component	**NAOS**	
DM Type / No PZT Actuators	CFDM / 185	
TTM	4 push-pull voice coil actuator *H(s) = -3db @ 350 Hz*	
WFS field selector	±1 ' FOV (feeds either WFS)	
WFS Type	VSHWFS[80] (0.8 to 2.55 μm)	IRSHWFS[81] (0.8 to 2.55 μm)
WFS Detector	128 x 128 pixel EEV CCD-50 focal plane array	1024 x 1024 HgCdTe HAWAII array (100 x 100 pixels from each quadrant used)
Readout Ports	16 (14 used)	4
RTCS	VME based	

Table 3.6 *NAOS main components*

The RTCS contains VME based Shakti boards and modules. The instrument's computer architecture 'Computer Aided Control' (CAC) is built around a workstation and four VME based local control units (LCU) connected by LAN.[82] The RTCS LCU consists of a PPC running VxWorks and four specialised modular Shakti power control boards (PCB) based on C40 modules each containing three Texas Instrument TMS320C40 DSPs clocked at 50 MHz. The system contains a Wavefront board (WF PCB), two Command Control boards (CC PCB) and a Statistical Computing Board (SC PCB). The WF PCB contains one equalization/acquisition module, two C40 modules and a graphics module. The board extracts WFS data from the VSHWFS and IRSHWFS LCUs. The two CC PCB both contain two C40 modules and two DAC modules which are used to calculate the mirror commands and send voltages to the DM and TTM. Finally the SC PCB contains two C40 modules dedicated to embedded statistics. The RTCS runs an automatic monitor and displays both atmospheric conditions and system performance data. The RTCS provides a control loop time lag smaller than 200 μs.[83]

NAOS feeds the 1024 x 1024 ALADDIN2 InSb imager CONICA. NAOS-CONICA (NACO) provides imaging, imaging polarimetry and coronography in the 1 to 5 μm range and long-slit low-resolution spectroscopy in the 1 to 4 μm range. The 7 sets of camera optics of CONICA provide a FOV range from 13 x 13 " to 73 " circular.

Figure 3.2 *Photograph of NACO*

3.1.4 Multi-Application Curvature Adaptive Optics (MACAO)

The 'Multi-Application Curvature Adaptive Optics (MACAO)' program provided 7 MACAO modules: four to fulfil the high angular resolution requirements of the VLTI, one for the 'Spectrograph for INtergral Field Observations in the Near Infrared' (SINFONI) instrument, one for the 'CRyogenic IR Echelle Spectrograph' (CRIRES) instrument and one spare.[84]

The key AO components of each of these 7 systems are similar, although the opto-mechanical implementations are different for VLTI, SINFONI and CRIRES. Each of the 7 modules contains a 60-element bimorph DM (development by CILAS), a CWFS containing a 60 APD WFS detector and a PPC-based RTCS.[85]

The bimorph contains a single piezo layer 1 mm thick sandwiched between two 0.2mm glass plates and is mounted in a 2-axis (2 pairs of voice coil motors) Tip-Tilt mount (TTMo). The DM is held by a spring-loaded radial 3-point support in the dural-ring TTMo. The bandwidth of the tip-tilt mount is tuned at 100 Hz for both axes.

The CWFS unit contains a 2.1 kHz membrane mirror, relay optics and a two-step lenslet array which feeds 60 100 µm optical fibres, which in turn feeds the reference light to 60 PerkinElmer Avalanche Photo Diodes (APD). The lenslet array is distributed in a 5-ring keystone geometry and splits the light into 60 distinct optical channels. The first lenslet (*Figure 3.3- left lenslet)* reproduces the DM and focuses the light on to each subaperture of the second lenslet *(Figure 3.3 – right lenslet*), which acts as a Fabry lens and images the subaperture on the fibre entrance. The oscillating membrane produces a signal whose figure modulation is proportional to the local wavefront curvature.

The three main VME boards in the RTCS are a PPC2604 (400 MHz) standard LCU controller, a PPC2604 (400 MHz) real-time computer and a Shaktiware APC Counter Board which provides the number of detected photons to the PPC. The RTCS processes the APD signals with the pseudo-inverse of the interaction matrix. It accumulates 6, 5, 4 or 3 frames resulting in a DM speed of 350 Hz, 420 Hz, 525 Hz and 700 Hz respectively. The control matrix is used to reconstruct the wavefront and a PID controller is used when applying the signals to the DM, although normally only the integral part is used.[86]

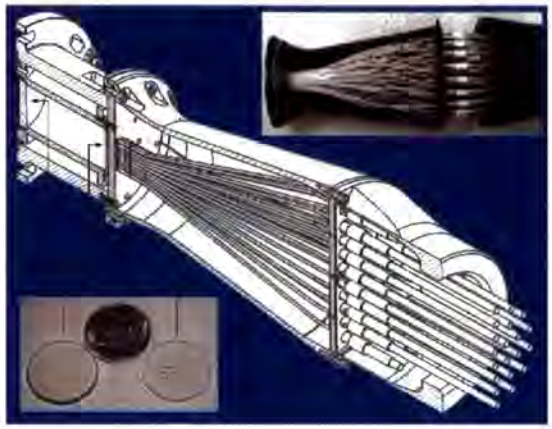

Figure 3.3 *MACAO Lenslet Geometry*

3.1.4.1 MACAO-VLTI

The VLTI will combine the AO corrected wavefronts from the four 8.2 m UTs with the tip-tilt only (planned to be upgraded to full AO) and corrected wavefronts from the three future 1.8 m Auxiliary Telescopes (AT). The telescopes will relay the corrected wavefronts to the VLTI recombination laboratory for VLTI instrumentation.[87, 88]

Each of the four MACAO-VLTI systems equips the f/46.7 Coudé foci of each VLT to provide beam recombination for the VLTI instruments. The original 8th mirror (M8) of the Coudé optics train was replaced by the MACAO-VLTI DM, with a flat 45° dichroic, transmitting the light to the CWFS. The 150 mm DM (pupil diameter of 100 mm) is mounted on the rotating telescope structure whereas the WFS is placed on the Coudé floor, so the WFS contains a derotator prism. An IR test camera consisting of an engineering grade Hawaii chip with a 13.6 x 6.8 '' FOV was used during commissioning. System tests provided the transfer function of the MACAO-VLTI system, indicating a system bandwidth of 28 Hz. After switching from a zonal to a modal interaction matrix, increasing the loop control frequency from 350 Hz to 420 Hz and introducing a Piston Removal Algorithm (PRA) led to the piston RMS reduced from 164 nm to 40±20 nm. However, increasing the control loop further to 700 Hz caused the system to become unstable.[85, 89]

3.1.4.2 MACAO-SINFONI

SINIFONI, the Cassegrain instrument placed on UT4, confusingly consists of two parts, the MACAO-SINFONI AO module and the focal plane "SPectrometer for Infrared Faint Field Imaging" (SPIFFI). The MACAO module differs from the VLTI versions by containing a 60mm pupil DM. This is due to the tight-volume Cassegrain constraint. SPIFFI provides 2048 spectra simultaneously with a spectral resolution of ~3500.[90, 91]

3.1.4.3 MACAO-CRIRES

CRIRES is a cryogenic, pre-dispersed, infrared echelle spectrograph resides at the Nasmyth A focus of UT1. Its MACAO module contains the same specification DM as SINFONI but contains different relay optics. In normal operation the CRIRES spectrograph uses a 0.2 " slit to provide high-resolution spectra (R = 10,000) in the NIR (1 to 5 μm) to a mosaic of 4 Raytheon 1024 x 1024 pixel InSb Aladdin III arrays.[92, 93, 94]

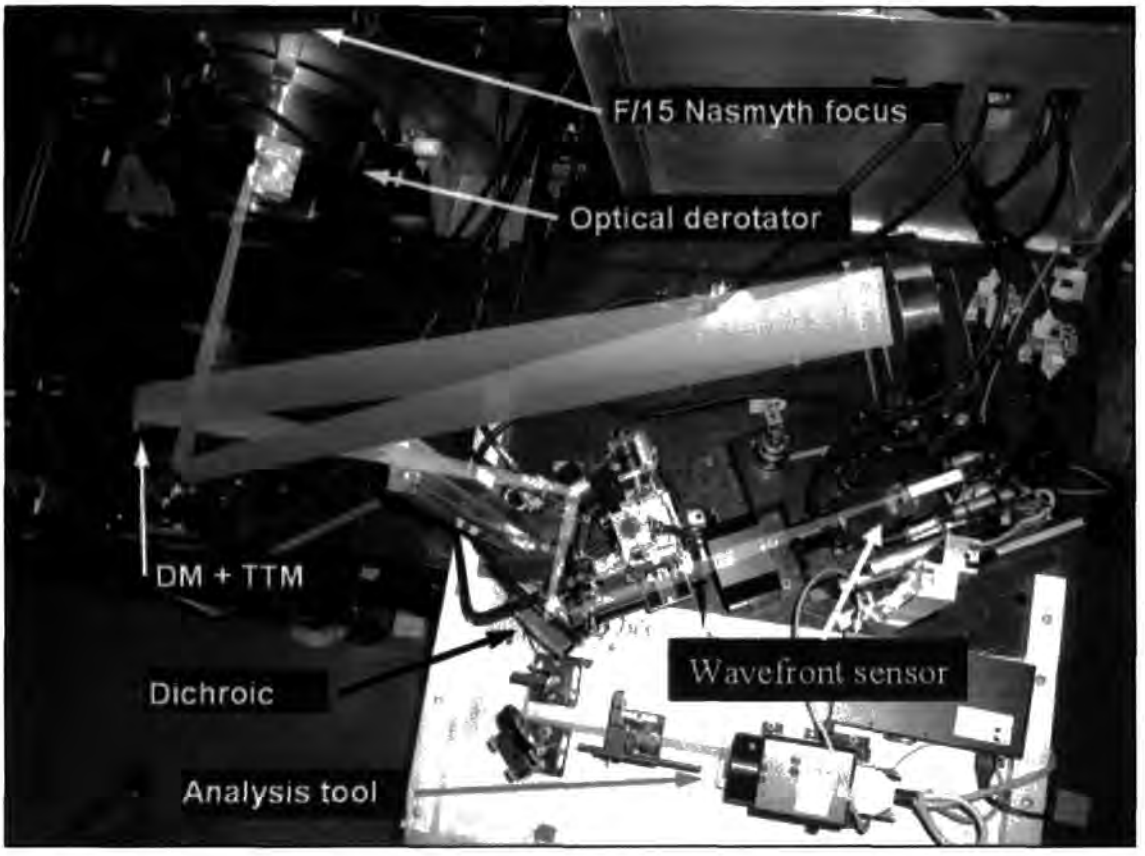

Figure 3.4 *MACAO CRIRES*

3.1.5 Multi-Conjugate Adaptive Optics Demonstrator (MAD)

The VLT Multi-Conjugate Adaptive Optics Demonstrator (MSD) prototype was constructed to demonstrate the on-sky feasibility of the MCAO technique. The system aimed to achieve diffracted limited performance over a wide field of view (2 ' in the K-band) on the sky using bright NGS and both modal and zonal reconstruction approaches.[95] MAD currently operates in Star Oriented mode. The Layer Orientated mode of operation is yet to be commissioned.

The correction system of MAD contains two deformable mirrors, two multi-reference wavefront sensors and a PPC-based RTCS to provide a K-band wide field AO corrected wavefront to the 'CAmera for MCAO' (CAMACO).[96]

The demonstrator contains both a 60 mm and a 100 mm bimorph DM conjugated to the telescope pupil and to a layer at an altitude of 8.5 km above the telescope aperture respectively. The 60 mm DM is supported by a tip-tilt mount.

MAD investigates two different approaches to MCAO correction using two independent WFS techniques. The first wavefront sensing technique, Star Oriented Wavefront Sensing (SOWFS), uses 3 SHWFS detecting 3 NGS (one per SHWFS) to create a multiple star wavefront sensor. Each SHWFS contains an 8 x 8 lenslet array, which focus the light onto separate 80 x 80 E2V CCD39 Peltier cooled chips.

The second wavefront sensor technique, Layer Oriented Wavefront Sensor (LOWFS) simultaneously senses 8 NGS in a circular 2 ' FoV using 8 PWFS (2 per quadrant), to project

light onto two 80 x 80 E2V CCD39 Peltier cooled chips. One detector corresponds to the ground layer conjugation has a fixed 2 x 2 binning while the other detector corresponding to the 8.5 m conjugation has a fixed 4 x 4 binning, thus simultaneously imaging the turbulence at different layers. The maximum WFS frame rate required is 400 Hz. The two techniques do not work together, hence a single WFS is connected to the FIERA WFS controller at any one time.

The MAD real-time computer is a Dy4 CHAMP-AV board containing a Quad-G4 board hosting 4 PPC 7410 running at 500 MHz.[97] The RTC makes high-order corrections between 400-500 Hz, low-order tip/tilt corrections at 5 Hz and slow drift corrections at 0.2 Hz. The RTCS supports wavefront sensing techniques to implement both Global and Local Reconstructions. SOWFS Global Reconstruction is required as it takes all the data coming from all the WFS at once and reconstructs the wavefront at an altitude of interest whereas LOWFS Local Reconstruction takes the data from a single altitude and directly drives the mirror conjugated to that altitude.

MAD will use the 1'x1' FOV CAMCAO IR camera for evaluating the performance of MAD in the K-band.[98]

3.1.6 The ESO Adaptive Optics Facility (AOF)

A VLT second-generation instrument workshop eventually resulted in ESO funding two instrument-requiring AO modules 'Multi Unit Spectrographic Explorer' (MUSE) and the 'Spectro-Polarimetric High-contrast Exoplanet Research' (SPHERE) and an accompanying new Adaptive Optics Facility (AOF).[99] SPHERE will have its own AO module, whereas MUSE will make use of the AO facility. The AO Facility is to include a deformable secondary mirror, four Sodium Laser Guide Stars, a GLAO AO module for MUSE and a GLAO AO module for the 'High Acuity Wide field K-band Imager' (HAWK-I).[100] HAWK-I is currently in operation without adaptive optics correction.

The Adaptive Optics Facility is a project to convert one VLT-UT into a specialised Adaptive Telescope. A new M2-Unit hosting an 1170 actuator DM will replace an existing secondary mirror (M2). The three focal stations will be equipped with specialised instruments containing new AO modules. HAWK-I will connect to the GRAAL AO module for GLAO correction and MUSE will connect to the GALACSI AO modules for GLAO and LTAO correction. These two instruments will use the Nasmyth foci. The Cassegrain instrument remains undefined. In addition, a four Laser Guide Star Facility is being development to complete the AOF.[100]

3.1.6.1 Deformable M2-Unit

The current DM design has a diameter of 1120 mm, a thickness of 2 mm and contains 1170 voice coil actuators. Each actuator has its own position feedback and the DM's internal control loop runs at 80 kHz. The design shall provide a full stroke and inter-actuator stroke of 50 μm and 1.3 μm respectively with a rise time of < 1 msec. It is planned to operate the DM in closed loop with SHWFSs and with a RTC operating at a 1kHz sampling rate.[101]

3.1.6.2 Ground layer Adaptive optics system Assisted by Laser (GRAAL) for HAWK-I

The Hawk-I NIR cryogenic imager (0.9 to 2.5 μm) will have a wide field of view of 7.5 x 7.5 ' and will contain a mosaic of four 2k x 2k HgCdTe Hawaii 2RG arrays.[102] It currently operates without AO corrected light.[103] GRAAL is a module designed to provide GLAO correction for HAWK-I with a high emphasis on the PSF uniformity over the FOV sampled at 0.1 " pixels. GRAAL is designed to host four 30 x 30 SHWFSs for LGS and one tip-tilt sensor for a NGS. The SHWFS must co-rotate with the pupil. The NGS could either be visible (outside the FOV) and sensed by the tip-tilt sensor or alternatively an IR NGS (inside the FOV) could be read out at high speed on a small window (16 x 16 pixels) on the Hawaii2RG detector. GRAAL will also host an on-axis high-order WFS with 40x40 subaperatures and an objective to change the plate scale within a subsection of HAWK-I FOV to sample the diffraction limit of the VLT for DM commissioning. The four LGS system is being studied to provide HAWK-I with 99% sky coverage.

3.1.6.3 GALACSI for MUSE

MUSE will be a gigantic integral-field spectrograph seated at a Nasmyth platform consisting of 24 field splitters, image slicers and spectrographs. Potentially MUSE will be able to obtain 90,000 spectra with a resolution of 3000 in a single exposure.

MUSE will operate in two modes simultaneously covering the 0.465 to 0.93 μm spectral range. A wide field mode (WFM) will cover a large 1 x 1 ' FoV with a 0.2 " resolution while the narrow field mode (NFM) will cover a 7.5 x 7.5 " FoV sampled at 0.025 ". This instrument will provide ultra deep fields with a predicted limiting magnitude for spectroscopy of R = 28 from an 80-hour integration.[104,105, 106]

MUSE requires a GLAO correction for the WFM and LTAO correction for the NFM. In both modes 4 LGS WFS and one tip-tilt NGS WFS is used but in different configurations. The visible tip-tilt NGS WFS for the WFM will be acquired within a 4' technical FOV with a field selector but outside the scientific FOV to prevent occultation of the scientific FOV. An IR on-axis tip-tilt NGS WFS will be used for the NFM. Light separation will be done with a dichroic located after the AO focal plane.

Four 32 x 32 subaperture (256 x 256 pixels) SHWFS would be used to sense the light from each laser. The WFS unit would rotate with the telescope pupil to follow the laser images.

3.1.7 Spectro-Polarimetric High-contrast Exoplanet Research (SPHERE)

The Spectro-Polarimetric High-contrast Exoplanet Research (SPHERE) planet finder instrument includes an extreme AO system (SAXO), coronographic devices, the differential camera (IRDIS) an Integral Field Spectrograph (IFS) and the ZIMPOL dual imaging polarimeter. SPHERE is a Planet Finding instrument designed to detect flux ratios of $\sim 10^5$ at very small angular separations. [107]

SAXO requires a 41 x 41 actuator DM consisting of a 180 mm diameter with an inter-actuator stroke > ±1 μm and a maximum stroke of ±3.5 μm. It also requires a 2-axis TTM with a ±0.5 mas resolution. The 40 x 40 SHWFS requires a focal-plane filtering device with variable size for aliasing control. Its spectral range will be between 0.45 and 0.95 μm. A temporal sampling frequency of 1.2 kHz is achieved using a 240 x 240 pixel electron multiplying CCD

with a read-out noise < $1e^-$ and a 1.4 excess photon noise factor. The global AO loop delay is maintained below 1 ms. The main AO loop will work at 1.2kHz. [108]

3.2 Gemini Observatory

The Gemini Consortium[109] operate two 8.1 m telescopes, one on Mauna Kea, Hawaii (Gemini North) and the other on Cerro Pachon in Chile (Gemini South); see Figure 3.5.

Figure 3.5 *Gemini North (Hawaii) and Gemini South (Chile)*

Gemini began research into feasible adaptive optics systems at the same time as the telescopes were being designed.[110, 111, 112, 113] Table 3.7 lists Gemini's AO System and associated key dates.

AO System	Key Dates
Hokupa'a	First Light on Gemini North: June 2000*
ALTAIR[114, 115]	Initial Study: 1993, PDR October 1997, CDR February 1999 Commissioned July 2003
NICI[116]	CDR 2002, First Light: February 2007
MCAO[117, 118, 119]	Initial Study: 1999, First Light due 2008[120]
GPI[121]	Initial Study 2003, First light due 2010
GLAO[122]	Feasibility Study 2005, awaiting decision as to proceed

* First light on CFHT in November 1997

Table 3.7 *List of Gemini AO systems*

3.2.1 Hokupa'a

Gemini used visiting instrument to obtain early science. One of the instruments was the University of Hawaii's (UH) Hokupa'a (coupled with the infrared spectrograph QUIRC).[123] Hokupa'a was modified to accommodate Gemini North's f/16 Cassegrain focus.[124] Hokupa'a was removed from Gemini North in 2002 to make way for the facility instrument ALTAIR.

Hokupa'a was originally developed for the 3.35m 'Canadian-French-Hawaiian Telescope' (CFHT). UH pioneered the CWFS, using it in Hokupa'a, the instrument's light path is shown in Figure 3.6.

Originally, the experimental instrument contained a 13-actuator piezoelectric bimorph DM (developed by Laserdot) and a CWFS connected to a 13-element avalanche photodiode sensor array sampling typically at 1 kHz. The matching geometry led to an optimum, near-diagonal control matrix.[125] The original control system was a mixture of analogue and digital stages, but was soon upgraded to a VME-based system containing a Force Sparc2ce CPU running

VxWorks. The system's closed loop bandwidth at 0 dB easily exceeded 100 Hz. Observations were conducted both on the CFHT (coudé focus) and the 'United Kingdom Infrared Telescope' (UKIRT) (Cassegrain focus).[126]

The experimental instrument was upgraded to a 36-element system (DM & CWFS), moved to the Cassegrain focus (f/35) of the CFHT and renamed Hokupa'a. The upgrade increased its performance to obtain diffraction-limited performance in the I-band.[127]

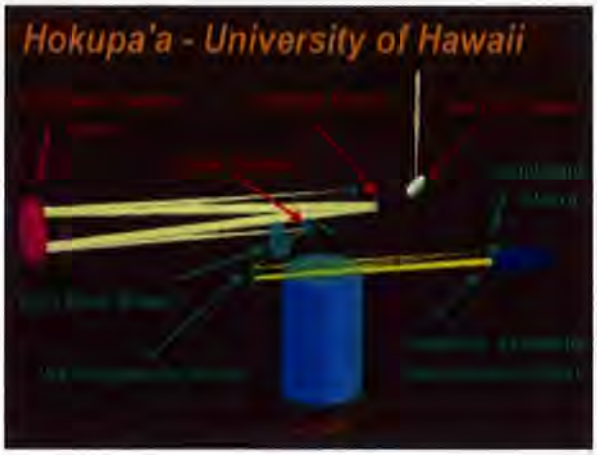

Figure 3.6 *Hokupa*

3.2.2 ALTitude-conjugated Adaptive optics for the InfraRed (ALTAIR)

The Cassegrain-mounted ALTAIR was offered to the community with the 'Near Infra-red Imager' (NIRI) for the 2004A semester.

ALTAIR was optimised for the 0.85 to 2.5μm spectral waveband. Its main components consist of a 177-element continuous facesheet deformable mirror, a tip-tilt mirror, a 12 x 12 Shack-Hartmann wavefront sensor containing a frame transfer EEV CCD-39 controlled by an SDSU-II controller and a VxWorks PPC processor-based RTCS VME system interfaced to a standard Gemini EPICS/VxWorks MVME167 controller.

ALTAIR, suspended from the Gemini 'Instrument Support Structure' (ISS) accepts and corrects the Cassegrain-bound f/16 beam. Uniquely ALTAIR's DM was optically conjugated to the turbulent layer height of 6.5 km above Mauna Kea with a hope to increase the isoplanatic patch and to double the diameter of the corrected field (as revealed by early tests)[115]. Before this, the LGS-commissioned NGS system allowed for a worst-case 1 ' radius offset between science target and guide star. However, after examining commission data, it was found that ALTAIR's conjugation is not optimal and that the dominant turbulent layer is probably considerably lower.[128]

The WFS and DM are optically registered to each other in a classic Fried geometry. Each four-pixel quad cell is surrounded by a guard ring. The WFS image scale is 0.4 '' per pixel. Different guide star positions illuminate a subset of lenslets, therefore only the corresponding quad cells are read out to minimise readout time.

NIFS, NIRI and GNIRS all have a 2 x 2 SHWFS labelled the 'On Instrument Wavefront Sensor' (OIWFS), which is mounted as close as possible to the focal plane to sense tip/tilt and

focus. The signals from the OIWFS and ALTAIR's SHWFS are combined to control ALTAIR's TTM and DM. The ISS also contains a 20 x 20 SHWFS mainly used for offline calibrations of the non-common path errors between the ALTAIR WFS and the image plane.

The Wavefront Correction System (WFCS) consists of two dual SVGM5 350 MHz PowerPC750 VME processor cards, connected by a PCI interconnect across a VME64 backplane.[129] The four CPUs labelled WFCS1x, WFCS1y, WFS2x and WFCS2y are dedicated to 'WFS Control, EPICS interface and Reconstruction Parameter (RP) Generation', 'Reconstruction', 'Statistics and Display', 'RP Optimisation' and 'Modal Gain and Centroid Gain Optimisation' tasks respectively. WFCS1y, also known as the real-time controller (RTC), manages all the highest speed hard real-time duties. The Optimiser manipulates various RP to deliver a new reconstruction matrix to the RTC every 0.1 Hz.[130] The SDSU II controller produces a readout latency of 600 μs and the real-time processing introduces an additional latency of 215 μs. Under typical conditions the reconstructor controls the deformable mirror at a rate of 1 kHz.

ALTAIR, Figure 3.7, truly is a facility instrument as it provides wavefront corrected light to every Cassegrain instrument on Gemini North. These instruments include the 'Near Infra-red Imager' (NIRI)[131, 132] the 'Near Infrared Integral Field Spectrograph' (NIFS)[133] and 'Gemini Multi Object Spectrograph' (GMOS)[134, 135]. These instruments don't have to be reconfigured when ALTAIR is in use as ALTAIR recreates the exit pupil, focal ratio and focus location of the original telescope beam.

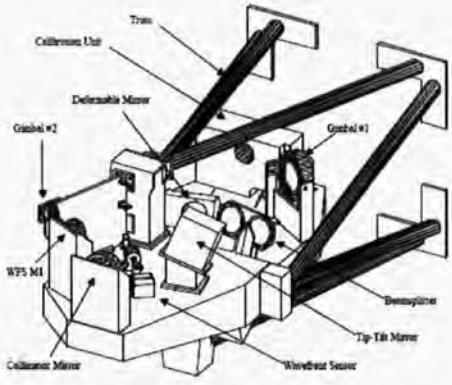

Figure 3.7 *Altair Alignment and Instrument Design*

3.2.3 Near Infrared Coronagraphic Imager (NICI)

NICI, Figure 3.8, is a dual-beam coronagraphic camera operating over the 1.0 to 5.5 μm wavelength range with a dedicated adaptive optics system placed on an optical bench. NICI contains an 85-element DM and the world's first 85-element curvature system including a 2 kHz membrane mirror and 80 APDs, built at the University of Hawaii (also used in the Hokupa'a upgrade). NICI hopes to achieve 50% Strehl ratio in the K band when fully commissioned.[116, 136]

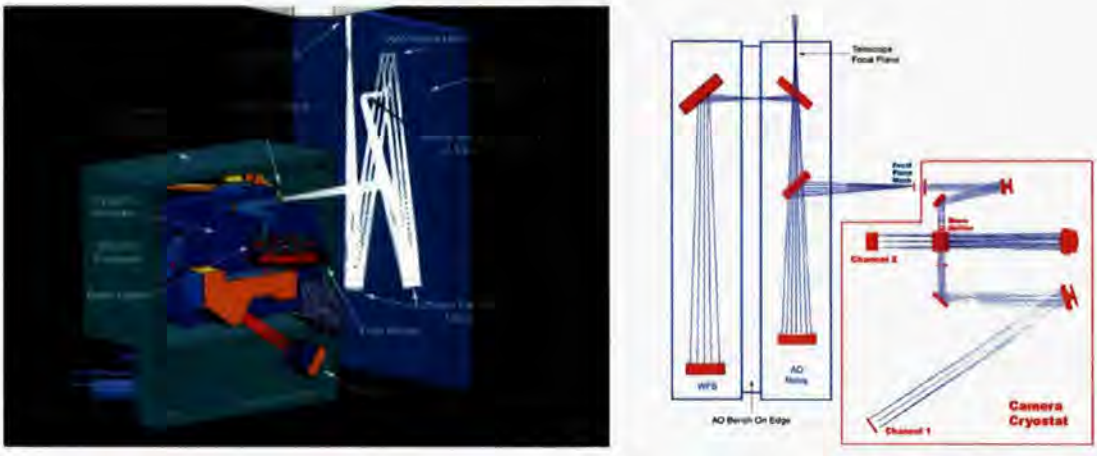

Figure 3.8 *NICI*

3.2.4 Multi Conjugate Adaptive Optics (MCAO)

The Gemini South MCAO design requirement was to deliver near-infrared near-diffraction limited images over a 2 ' FOV.

The instrument contains three continuous Xinetics CFDMs, conjugated to altitudes of 0, 4.5 and 9 km containing 349, 468 and 208 actuators respectively. The optical design includes a flat tip/tilt mirror at a conjugate range of -2 km providing a dynamic range of ±2 " on-sky. Five sodium laser guide stars (produced by a single 50 W laser) and 3 NGS are used to compensate for turbulence providing correction and uniform Strehl ratio over a 1 ' to 2 ' FOV. Five 16 x 16 Sub aperture LGS SHWFS and three tip/tilt NGS WFS will be used to measure the wavefront error, sampled at 800 Hz. In addition to the 10-fold gain in angular resolution, MCAO also pushes the detection limit by 1.7 magnitudes on unresolved objects with respect to seeing limited images. [117, 137]

Each SHWFS sub-aperture will compose of a pixel quad-cell surrounded by a guard ring as in ALTAIR. Each 80 x 80 four-port EEV CCD39 will have a total of 204 illuminated sub-apertures. The WFS shall be read out by an SDSU III controller, providing a maximum pixel read rate of 12.5 Mpixels/s. The readout time will be 1 ms with the RTCS requiring an additional 250 μs.

'The Optical Sciences Company' (TOSC) were contracted to build the RTCS. The RTCS, a subsystem of the MCAO control system, contains four dual 7400 processor PPC boards mounted on a PCI backplane controlled by a separate 1.8 GHz Pentium computer. The first board computes the LGS slopes as pixels, which are digitised from the WFS and the second processor calculates the tip/tilt signals from the NGS and drives the Tip/Tilt mirror. The other 6 processors reconstruct the wavefront and compute the DM commands (one board per DM). The architecture achieves the required 3 Gflops performance with a processing latency of less than 100 μs, achieving a required closed-loop bandwidth of 300 Hz. The host Pentium runs Windows 2000 to provide the engineering GUI.[138]

The MCAO module will be mounted to the ISS and will accept the f/16 science beam to provide a (60nm RMS uncorrectable and non-common path error) f/33 beam (0.85 to 2.5 μm) to science instruments. MCAO will feed the planned 'Florida Multi-object Imaging Near IR

Grism Observational Spectrometer' (FLAMINGOS-2)[139, 140] and 'Gemini South Adaptive Optics Imager' (GSAOI)[141], covering an 80 x 80 " FOV with 0.02 " sampling.

3.2.5 Gemini Planet Imager

The Gemini Planet Imager (GPI), Figure 3.9, aims to achieve contrast levels of 10^{-7} to 10^{-8} to perform direct imaging detection. The instrument consists of an adaptive optics system, a coronagraph, calibration system and a science field spectrograph.[142] The AO system comprises of a visible-light spatially-filtered SHWFS, a low-order "woofer" DM, a 4k actuator Boston Micromachine MEMS "tweeter" DM and a quad Intel Xeon server-based RTCS capable of 3 billion operations per seconds for a 2.5 kHz system. The wavefront controller will use an Optimal Fourier Control adaptive algorithm. The system will use a computationally efficient Fourier Transform Reconstructor. GPI will be able to achieve Strehl ratios > 0.9 at 1.65 μm.

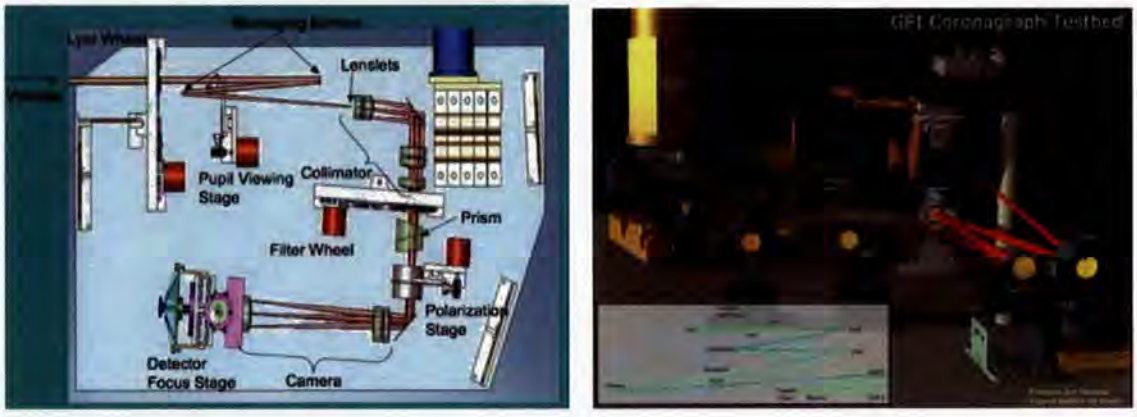

Figure 3.9 *GPI Camera and Coronagraph*

3.2.6 Gemini 'Ground Layer Adaptive Optics' (GLAO)

In 2004 Gemini decided to conduct a 'Ground Layer Adaptive Optics' (GLAO) feasibility study to support wide-field high-resolution near-infrared imaging and spectroscopy on Gemini North. The University of Durham in collaboration with the National Research Council of Canada (NRC) and the University of Arizona submitted a feasibility report and a conceptual design study, which included an adaptive secondary mirror, a laser guide star system and an acquisition and wavefront sensing system.[143] Data provided by the Mauna Kea Site Monitoring (MKSM) project will be fed into GLAO models[144] to determine whether to conduct a further conceptual design in 2008.[120]

3.3 Keck Observatory

The twin 10m telescopes, Figure 3.10, of the William M. Keck Observatory (WMKO)[145] are currently the world's largest operational optical and infrared telescopes; see Figure 3.10. Both Keck I and Keck II 10 m primary mirrors consist of 36 hexagonal segments.

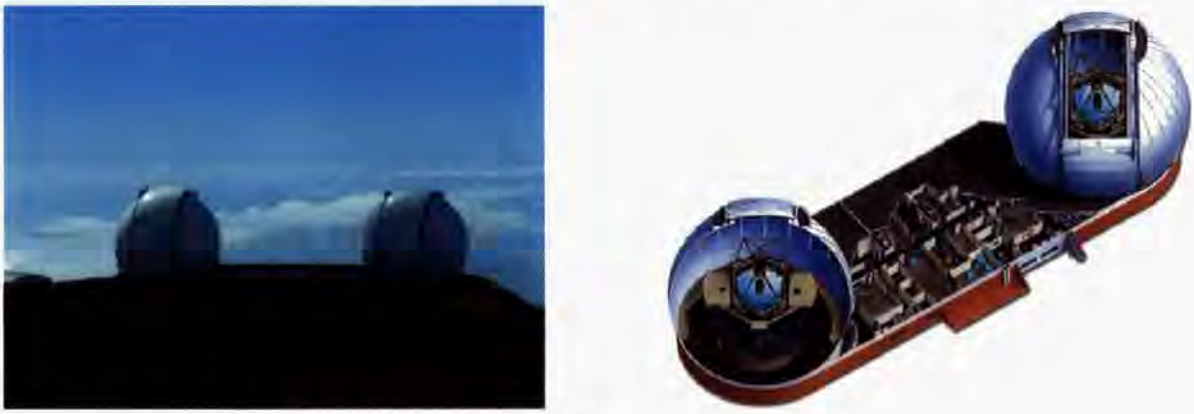

Figure 3.10 *Keck Telescopes (Photo and Schematic)*

Key dates associated with the Keck AO systems are summarised in Table 3.8.

AO System	Key Dates
Keck I	First Light: December 2000
Keck II	Initial Study: 1993[146, 147], PDR November 1995, CDR August 1996[148] First Light: Febraury 1999, Common Use: August 1999[149]
Keck Interferometer	First Light: March 2001, Science Operation 2004
Keck I LGS	Expected end 2008[150]
Keck II LGS	Laser Delivered: 1998, First projection December 2001 First light: September 2003[151], Common Use: 2005[152]
Keck I NGWFC	Initial Study: January 2004, Commissioned October 2006
Keck II NGWFC	Initial Study: January 2004, Commissioned February 2007[153]

Table 3.8 *List of Keck AO systems*

The Next Generation Wavefront Controller (NGWFC) project upgraded the real-time processors and wavefront sensors.

The long-term goal is to build a next-generation 'Keck Next Generation Adaptive Optics (NGAO) facility. NGAO should deliver high Strehl ratios and extend to visible wavelengths. It should also have a MOAO mode. WMKO are currently defining its science case. A conceptual design phase was due to start in 2005 but has been delayed due to other AO activities taking priority. [154]

3.3.1 The Keck Adaptive Optics Facility

The AO facility is located on the left Nasmyth platform of the Keck telescope at the f/15 focus. The output beam from the AO system has the same focus ratio and exit pupil location, with respect to the focal plane, as the telescope's output.

The system contains a Xinetics 349 PMN actuator continuous DM, a custom 3 PZT-actuated silicon carbide tilt-tilt mirror, a 20 x 20 SHWFS and a Mercury Computer VME based RTCS.

The 7 mm spaced 349 actuator DM is mapped to a 0.56 m separation on the primary mirror. It can be flattened to a RMS value of 19 nm, with individual actuators driven up to 1.5 kHz.[155] The TTM shows signs of amplitude resonance at 700 Hz with a first clear peak at 1 kHz. These characteristics support the ability to obtain closed-loop bandwidth up to 100 Hz. The TTM patrols a 2 ' FOV.

After the TTM and DM, a dichroic beamsplitter reflects light to the visible SHWFS. The SHWFS contains 20 x 20 lenslet array focussing light onto an Adaptive Optics Associates 4-port 64 x 64 MIT-LL CCD camera which provides 7e^- RON, operating at frame rates in the range 55 - 672 Hz. Each subaperture is projected onto a quadcell contained within a guard band. There are 3 selectable subaperture arrays of different focal lengths that are selected depending on the seeing. The WFS subapertures are aligned to directly correspond to the DM actuators in the Fried geometry. The WFS must access the entire 40 x 40 " science FOV.

In LGS mode, the tip-tilt error signal is detected by a 'System for Tip-Tilt Removal with Avalanche Photodiodes' (STRAP) sensor to compensate for global tip-tilt errors.[156] In addition to this tip-tilt sensor is a further 512x512 CCD Low Bandwidth WFS (LBWFS) to compensate for laser-projection elongation.[157] The LBWFS is used to obtain focus and wavefront information from the NGS. Since the LBWFS is monitoring a much dimmer star it must typically integrate for a few minutes to get the required signal level. Hence, it receives time average information.

The Keck's AO 'Wavefront Control System' (WCS), constructed by LLNL, is divided into 3 subsystems: the command processor (CP) subsystem, the real-time DM control subsystem and the real-time TT subsystem.[158]

The CP is implemented on a Force Sparc-5 computer running UNIX and is used for communications, diagnostics, data storage and calibration. It translates EPICS commands into real-time commands, returning real-time diagnostic data to the user or storing it to disk. Telemetry data is streamed from the system at a rate of between 10 – 20 Hz.

The DM control subsystem does the real-time processing on a Mercury Computer parallel computer system containing 16 Intel i860 processors. The wavefront error is reconstructed by a matrix-vector multiply parallelised across all the processors. As the telescope tracks a star the hexagonal pupil image rotates on the WFS; therefore the illuminated subapertures change with time and a new reconstruction matrix is used every time the image rotates by a degree. No more than 240 of the useful 304 subapertures are illuminated at any one time. A Bayesian reconstructor is currently used instead of the commonly used SVD technique. The Bayesian reconstructor uses the relative noise in each subaperture as prior information. The error signals are thus used to calculate the next DM values. The DM's original PI controller compensated for loop delay. It had a disturbance rejection bandwidth of 23 Hz for a 0.5 loop gain factor. More recently an optimised variable gain controller containing a leaky factor is used. It is frequently updated using centroid telemetric data.[159]

The TT control subsystem is based on a Motorola MVME162 68040 embedded computer. The subsystem is used to correct for wavefront tip-tilt. The separate control system interfaces to the tip/tilt mirror. In LGS mode it receives inputs from the separate tip/tilt sensor. The

controller accommodates a range of integration times, automatic light level control and an adaptive control algorithm that optimises the control system performance. [156] In NGS mode the controller receives an estimation of the average wavefront tilt from the DM controller, applies a loop gain, integrates and finally applies a new tip-tilt mirror position vector. Originally the controller had a fixed gain of 0.4 and produced a disturbance rejection bandwidth of 33 Hz.[160] Now the PI controller has a variable loop gain and a fixed scaling gain of 0.8.

The computed delay times from the time the CCD is read until the time the TT and DM voltages are updated are 1.65 ms and 2.13 ms respectively.

The dichroic beamsplitter transmitted light encounters two fold mirrors feeding two separate science ports. NIRC2, the high-resolution near-infrared (1 to 5 μm) camera, is placed at one. The other is for NIRSPEC, a near-infrared (1 to 5 μm) cross-dispersed echelle grating spectrometer. This second-generation instrumentation was constructed for the AO facility.

The WMKO are currently constructing their third-generation of instrumentation with an aim to decommission some of their first-generation instruments. One third-generation instrument 'OH Suppressed IR Imaging System' (OSIRIS) for Adaptive Optics has already been commissioned.[161] OSIRIS will employ a 64 x 64 focal plane lenslet array to create an integral field spectrometer capable of simultaneous diffraction-limited imaging and R = 3,900 spectroscopy.

Since the commissioning of the NGS AO system the team have spent a great deal of time and effort on system optimisation. The characterisation and optimisation of the NGS have been very successful and have been responsible for a Strehl ratio increase of 10%. The AO system is shown to deliver images with an average Strehl ratio of up to 0.37 at 1.59 μm with a bright guide star; this corresponds to a wavefront error of 260nm. [162, 163]

3.4 Subaru

The Subaru telescope, see Figure 3.11, is an 8.2 m optical-infrared telescope at the summit of Mauna Kea, Hawaii operated by the National Astronomical Observatory of Japan (NAOJ).[164, 165]

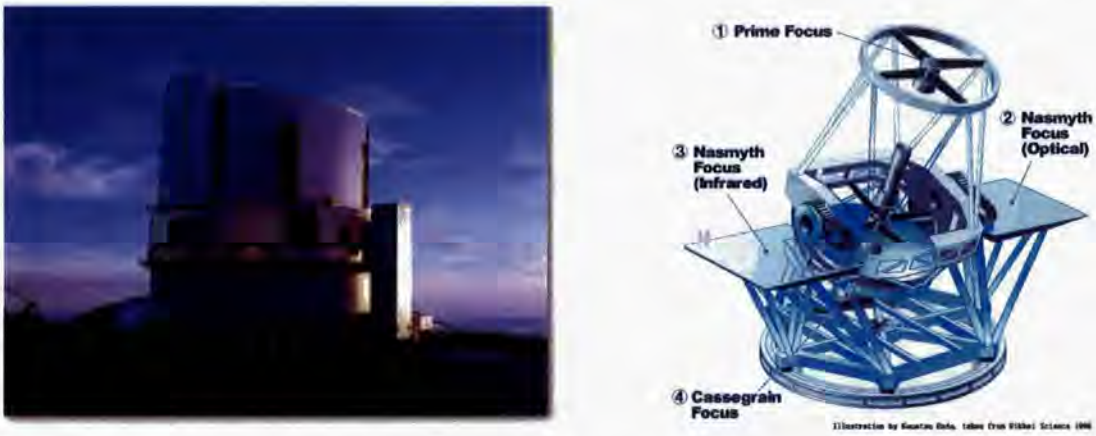

Figure 3.11 *Subaru Telescope (Photo and Schematic)*

Suburu's AO systems and key dates are listed in Table 3.9.

AO System	Key Dates
AO36	Initial Study: Early 1990s[166], First light: December 2000, Common Use: April 2002
LGSAO[167]	Prototype: 1999[168], Commonissing: due 2009[169]
AO188[170]	CoDR: May 2002[171], First Light 2006, Common Use: due 2008

Table 3.9 *List of Subaru AO systems*

3.4.1 The Subaru Cassegrain AO System (AO36)

The full Cassegrain AO system (AO36) achieved first light at Subaru with the 'InfraRed Camera and Spectrograph' (IRCS) instrument.

The AO system contains a tip-tilt mirror, a CILAS 36-electrode PZT bimorph DM to compensate wavefront aberrations measured by a 36-APD CWFS system and a VME rack-mounted RTCS, see Figure 3.12. The system provides an unvignetteed 2 ' diameter FOV. The AO module containing the DM and TTM is embedded in the hard-to-access Cassegrain skirt unit attached under the primary mirror cell. For observations with AO, the f/12.4 beam is reflected by a retractable mirror, taken through the AO layer optics and returned to the Cassegrain light path.[172, 173]

The 6-point supported DM has an effective aperture size of 62 mm, with a first resonance frequency of 550 Hz. The tip-tilt mirror can cover a 3 " x 3 " field and is often used for dithering instead of the telescope, reducing the time by 90%. In the near future Subaru are planning to implement tip/tilt correction using their secondary mirror in the AO loop.[174]

The visible WFS, containing an air-driven vibrating membrane mirror resonating at 2 kHz, is attached to the scientific instrument to minimise the relative mechanical flexure between the

WFS and the instrument. Inside each instrument there is a cooled beamsplitter to reflect the visible wavelengths to the WFS and transmit the infrared to the science instrument. The wavefront sensing beam is divided and directed to the 36 avalanche photodiodes through a custom-designed lenslet array via 200 μm core diameter optical fibres to cover a 5 " FOV. The distribution of the electrodes on the bimorph mirror matches the distribution of the CWFS.

The Subaru AO RTCS contains a dual 200 MHz processor MIPS R4600 computer running MaxOS 4.2, a real-time UNIX system. The real-time software contains 3 main processes, a diagnostic data-handling task, a command server task and a closed-loop control task. The closed-loop performance of the system is affected by the calculated control matrix, mirror gain values, APD count rate (SNR), optical gain and latency time. A new control matrix is calculated before operation using calibration data. It was found that a correction frequency of the system is 2.1 kHz with a servo gain of 0.18; this gives a control bandwidth greater than 100 Hz.[175]

The Cassegrain AO system is optimised for the K band and is fed to either the 'InfraRed Camera or Spectrograph' (IRCS)[176] or the 'Coronagraphic Imager with Adaptive Optics' (CIAO)[177] Cassegrain instruments. Both instruments cover a 1 to 5μm spectral range. The IRCS is used for near-infrared imaging (FOV 1 x 1') and spectroscopy (R = 10 to 20000) at diffraction-limited special resolutions. The CIAO 1k x 1k detector supplies a FOV of 22 x 22" with a spectral resolution range of 10 to 600 and is dedicated for diffraction-limited imaging of faint object around a bright point source. AO images obtained give a 0.065 " FWHM in the K-band, with a Strehl ratio of 0.35.

3.4.2 The 'Laser Guide Star Adaptive Optics' (LGSAO) and AO188 systems

The f/13.9 IR Nasmyth system (0.45 to 5 μm) contains the world's largest control-element CWFS system, fibre feeding 188 photon counting APD modules. The WFS updates at 2 kHz. The tip, tilt and defocus will be measured with either a 2 x 2 visible SHWFS using 16 photon-counting APDs or an infrared SHWFS with a HgCdTe arrray.[178,179]

A 188-element electrode bimorph mirror[180], manufactured by CILAS, shall be placed within a fast tip/tilt mount. The mount uses voice coil type actuators in a closed-loop system and should produce a tip/tilt stroke of ±3.7 '.

The RTCS hardware, manufactured by the Concurrent Computer Corp. will contain the real-time RedHawk Linux operating system running on a iHawk Series 864 platform containing four Xeon CPU processors clocked at 2 GHz. One CPU will perform matrix calculations at 2 kHz, two will be used for fast-loop calculations including DM voltage update and the APD counter readout. One CPU will be allocated for data transfer to the data-handling computer (used for diagnostics and auto parameter tuning). Data will be transferred from the APDs and to the DM and TTM using a serial 'Front Panel Data Port' (FPDP) interface.

A 4 to 5 W solid-state sum frequency 589 nm laser fibre will be fed to the laser-launch telescope situated behind the secondary mirror with an optical relay fibre. A mode-locking 1064 nm YAG laser will be used to generate the laser guide star. A prototype is currently in development.[181]

This system hopes to achieve diffracted limited images in the J band and expects a 0.46 Strehl ratio at H-band under average seeing conditions (0.6 "), with a 0.85 Strehl ratio in the K-band under very good seeing conditions.

The existing IRCS and CIAO instruments shall be modified and moved to the IR Nasmyth platform.

Figure 3.12 *Subaru AO and CIAO Modules*

3.5 Other Ground Based Telescopes

This section contains a selection of other operational telescopes' AO systems. A brief description of each is given.

3.5.1 Multiple Mirror Telescope (MMT)

The Multiple Mirror Telescope (MMT), see Figure 3.13, currently contains a monolithic 6.5 m primary mirror.[182]

The MMT NGS AO (MMTAO) system is the first in the world to use an Adaptive Secondary (AS) DM. The 2.0 mm thin shell AS has a 70 cm diameter and is controlled by 336 voice coil actuators and capacitive sensors. The AS electronics crates house 168 DSPs which runs a 40 kHz internal positioning loop. With the 12 x 12 SHWFS camera running at 550 Hz and a readout delay of 3.2 ms, the correction bandwidth of the system is about 18 Hz.

MMTAO achieved first light in Nov 2002 and MMT have since been operating and improving the system. In 2005 MMT planned to upgrade the WFS camera, the RTCS and to experiment with different reconstructors.[183]

Figure 3.13 *MMT and its Deformable Secondary Mirror*

3.5.2 Calar Alto Observatory

The Astronomical Center at Calar Alto is located at Sierra de Los Filabres, Andalucia, Spain operates a 3.5 m telescope; see Figure 3.14.[184]

The 3.5 m telescope contains the Cassegrain 'Adaptive optics with a Laser For Astronomy' (ALFA) facility which is currently is the process of being upgraded. The current operational ALFA facility contains a Xinetics 97 PMN ceramic piezo actuator DM, a tip-tilt mirror with accompanying CCD based sensor, a visible SHWFS containing a 1.2 kHz 256 x 256 6e^- RON CCD camera and a 68k and Ariel DSP processor based VME mounted RTCS. ALFA delivers an f/25 corrected beam to the Cassegrain OMEGA-CASS instrument. ALFA operates only in NGS mode; the laser has been decommissioned.

The Max Planck Institut für Astronommie (MPIA) are constructing a new near-infrared PWFS (PYRAMIR) using a HAWAII-1 1024 x 1024 pixel array from Rockwell. PYRAMIR will be delivered with a new Primergy R450 4-way rack server real-time computer.[185]

Figure 3.14 *Calar Alto Observatory*

3.5.3 Telescopio Nazionale Galileo (TNG)

The 3.58 m TNG sited on the Roque de Los Muchachos Observatory (ORM), La Palma is shown in Figure 3.15.[186]

The Nasmyth 'Adaptive Optics system for the Telescopio Nazionale Galileo' (AdOpt@TNG) is the only operational AO system with a PWFS. The main components of the AdOpt@TNG system are a Xinetics 97 magnetostrictive actuator DM, a four voice-coil actuator tip-tilt OAP mirror, a PWFS connected to a four port 80 x 80 EEV39 CCD and a RTCS.

In 2005 TNG replaced their ThermoTrek VME mounted RTCS with a dual Pentium processor real-time Linux PC and upgraded their WFS CCD controller to a SciMeasure.[187]

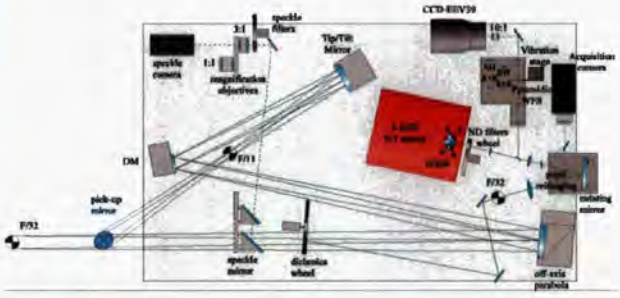

Figure 3.15 *TNG Telescope and AdOpt schematic*

3.5.4 Lick Observatory

The largest telescope at the Lick Observatory is a 3m Shane Reflector telescope, which from 2001 has offered an Adaptive Optics facility to users.[188]

The LLNL AO system can be operated in both LGS and NGS mode, routinely achieving the diffraction limit at 2.1 μm. The AO system contains a LLNL built 127 electro-restrictive PMN actuator DM (61 controllable), a two axis 3 " mirror mounted on a Physik Instrumente tip-tilt platform, a 40 subaperture SHWFS with an Adaptive Optics Associates camera with a Lincoln Lab 64 x 64 CCD running at 500 Hz. The LGS system contains a tip-tilt sensor which

is a quadcell photon-counting avalanche photodiode with a FOV of ±2 ". The RTCS is currently based on a 160 Mflop Mercury VME with 4 Intel i860 processors. Lick Observatory plan to upgrade the RTCS to a Pentium PC platform in the near future.

The AO system supplies a corrected wavefront to an AO-optimised Rockwell PICNIC HgCdTe 256 x 256 CCD, RON 30 e^- array IRCAL camera, sensitive to 0.8 to 2.5μm.[189]

3.5.5 Canadian-French-Hawaiian Telescope (CFHT)

The CFHT is a 3.6 m optical/infrared telescope located atop the summit of Mauna Kea.[190]

The Cassegrain AO bonette for the CFHT is named 'Probing the University with Enhanced Optics' (PUEO), which is also the name of a Hawaiian owl, and was offered to the scientific community in 1996. PUEO evolved from the same experimental system at the UH as Hokupa'a. The existing system consists of a tip-tilt signal corrector, a 19-element bimorph DM, a 19-APD CWFS and a VME based RTCS. Sampling of 1 kHz produces a maximum bandwidth 0 dB rejection of 105 Hz.

Currently CFHT are considering upgrading PUEO to a higher-order system containing a 104-electrode bimorph DM, a new CCID-35 CWFS detector and a new RTCS (capable of 104 x 104 matrix multiplication at 2 kHz). The CWFS lenslet array would also be upgraded to 104 elements. The CCID-35 has a RON of 2 e^- and a 250 μs read-out delay.[191]

3.5.6 Southern Observatory for Astrophysical Research (SOAR)

SOAR is a high-performance 4.1m aperture astronomical telescope atop Cerro Pachon, Chile.

A SOAR Adaptive Module (SAM) will provide SOAR with a LGS GLAO system in 2008. The correction of the wave-front will be achieved using a low-altitude (10km) Rayleigh laser guide star. The nominal average optical power of the Nd:YAG solid-state laser beam will be 8W, wavelength 355nm, pulse frequency 10kHz.

3.5.7 Gran Telescopio Canarias (GTC)

GTC is a high-performance segmented 10.4m telescope currently being installed on the Roque de los Muchachos Observatory, La Palma; see Figure 3.16.[192]

Currently, a preliminary design for the NGS GTC-AO system is available based on the top-level requirements. A dual-conjugate sodium LGS upgrade path has also been defined. The design includes a piezo-stack DM containing approximately 350 actuators (300 controllable) combined with a 128 x 128 pixel E2V CCD visible SHWFS. The system's tip/tilt correction will be provided by the telescope's secondary mirror. The AO system optimistically aims to provide a high-order corrected wavefront in the IR, with an on-axis Strehl ratio of 0.75 at 2.2 μm during good seeing.[193]

Figure 3.16 *GTC (left) and LBT (right)*

3.5.8 Large Binocular Telescope (LBT)

The Large Binocular Telescope is a large optical telescope that utilises two 8.4 m mirrors separated by 14.4 m centre to centre and provides an interferometric baseline of 22.8m edge to edge.[194]

The full binocular telescope received first light in March 2008. [195]

The single conjugate AO system called WLBT is part of the Acquisition, Guiding & WFS unit (AGW), which is attached to the front bent Gregorian focus derotator. The LBT contains a 672 actuator adaptive secondary mirror (ASM), with WLBT containing a variable (5 x 5 to 30 x 30 subaperture) sampling PWFS and a 84 DSP based RTCS obtaining closed loop rates of 800 Hz. The AO system should be available for the telescope's commissioning.[196]

LINC-NIRVANA is a future strategic instrument for the LBT. LINC is a 1.0-2.4 μm beam combiner and Fizeau interferometer for the LBT. Initially it will use the on-axis adaptive optics system previously described to produce interferometric images. NIRVANA is a future MOAO upgrade. Two folding flats in the optical path will be replaced by a system containing a 349 actuator Xinetics DM, which can be conjugated to an atmospheric altitude of between 4 and 15 km. The Ground Layer Wavefront Sensor (GWS) will contain 12 pyramids to collect lights from individual references to create four images of the pupil on the 128 x 128 pixel CCD. The information will be used to drive the AS. A Mid-High Layer Wavefront Sensor (MHWS) containing 8 pyramids will be used to drive the Xinetics DMs. The MHWS contains an 80 x 80 pixel CCD. The system aims to compensate for turbulence over a field of 2 arcminutes.[197] LINC-NIRVANA passed its FDR in 2005 and is currently scheduled in be installed in late 2008.

A conceptual design to construct a Rayleigh LGS GLAO system was completed in 2008. The system will make use of the ASM.

3.6 Solar Observatories

Over the last few years adaptive optics has become an indispensable tool and several major ground-based solar telescopes have deployed systems. Solar AO faces different challenges from nighttime AO. The ground layer is far more turbulent due to the heat of the sun, which implies that Solar AO requires a very high closed loop bandwidth (between 100 and 200 Hz).

Another challenge is the WFS. Although Solar AO systems never have to worry about faint sources, they do have to contend with the sun being an extended object. An AO system has to lock and track on particular features. LGS are not a practical solution as they would have to be either extremely bright or contain very special narrow band filters.[198]

The solar telescopes that include operational AO systems are the 97 cm New Swedish Solar Telescope (NSST) located in La Palma, Spain, the 70 cm Vacuum Tower Telescope (VTT) located in Tenerife, Spain, the 76 cm Dunn Solar Telescope (DST), and the 65 cm Big Bear Solar Telescope (BBST). The next generation solar telescopes such as the 4 m Advanced Technology Solar Telescope (ATST) will require powerful adaptive optics systems, and possibly MCAO systems. AO is just as critical to daytime Solar Telescopes as for Optical and Infrared nighttime telescopes.

3.7 Extremely Large Telescopes (30 – 50 m)

The astronomy community are placing a lot of time and effort into the design and planning of the next generation of ground-based optical/infra-red telescopes. Three are currently planned. Each telescope is expected to become operational between 2015 and 2020. Although each design is rapidly evolving, a present description of the AO systems under consideration and RTCS research and plans is given.

3.7.1 Giant Magellan Telescope (GMT)

The Giant Magellan Telescope (GMT) plans to use seven 8.4 m mirrors to construct a telescope with a total collecting area equivalent to a 21.4 m filled aperture telescope.[199]

The GMT Conceptual Design report mentioned that the planned first-generation AO modes include all-sky LTAO, GLAO, and high-contrast, high Strehl ratio XAO. The telescope plans to have a segmented deformable secondary mirror that allows AO operation with just two mirrors for high throughput giving a low IR background.[200, 201]

The GMT Organisation has begun to consider the RTCS requirements for LTAO. They want to process the 1500 SHWFS subaperatures and update the DM's 4620 actuators every millisecond. Their reconstructor matrix would then naively have 18000 x 4620 elements.

In this case, for every iteration, the wavefront reconstruction with a fully populated matrix would require 8×10^7 floating point operations. Hence, the RTC would have to be capable of sustaining a minimum of 100 GFlop. However, as there is no coupling of actuator influences across the segment boundaries, the wavefront reconstruction can be broken into two. The first reconstructs the 8.4 m sections of wavefront across each of the segments independently. The second predicts those low-order modes across the full pupil, which contribute significantly to the atmospheric piston errors.

It has been computated that the demand can be reduced by a factor of seven, since actuators on a given secondary segment are driven almost entirely by Shack-Hartmann slopes measured within the same segment. Thus the RTCS is required to operate with a ~15 GFlop sustained throughput.

The MMT tomographic RTCS will be designed and constructed by Microgate. It is designed to accept up to 1500 WFS slope inputs and drive the MMT's 336-actuator ASM at 1 kHz frame rate. Current hardware is capable of sustained calculation at ~1 GFlop. The future RTCS will be designed around custom boards, with computation handled by floating point DSPs, and high-speed communication handled by large FPGAs. The GMT will adopt Microgate's readily expandable architecture. It is anticipated that it will be implemented with upgraded hardware to be accepted on the timescale of the telescope's construction. No information regarding the RTCS requirements of the other AO modes is available at this stage.[202]

3.7.2 Thirty Meter Telescope (TMT)

The TMT Foundation are designing and planning to construct a 30.0 m telescope either in Mauna Kea or Cerro Armazones, Chile.[203]

The TMT Construction proposal was completed on the 12th September 2007. They plan to commission an 'Early Light' AO system with the telescope to feed the first-light instrumentation. To provide a near-diffraction-limited wavefront and high sky coverage in the near infrared, the TMT will have an LGS MCAO architecture consisting of facility Narrow Field IR AO System (NFIRAOS), a LGS facility and an AO Sequencer.

A feasibility study for NFIRAOS was conducted in 2007. Two competing conceptual designs are currently being conducted. NFIRAOS requires a 4k actuator and a 5.6k actuator DM and seven SHWFS (six LGS, one NGS), each containing 3.6k subaperatures.

The RTCS will be required to process 25.2k subaperatures and drive ~7.5k actuators in total. Currently novel reconstructors are being explored to reduce the processing requirement. A complex custom design RTCS was presented in the feasibility study, containing 13 custom embedded processor boards. Twelve contained 8 DSPs and 1 FPGA and one contained 8 FPGAs and 1 DSPs. Xilinx Virtex-4 FPGAs and TigerSHARC DSPs were used in the design.[204]

3.7.3 European-Extremely Large Telescope (E-ELT)

ESO are continuing the design of an ELT class telescope. Currently a 42 m telescope design is being considered for the European-ELT (E-ELT).[205]

ESO are currently considering nearly all forms of AO including SCAO, LTAO, XAO, MCAO, GLAO and MOAO. Some AO modes will be provided by telescope facility while others will be associated with an instrument. For example, the EAGLE instrument design study will include a MOAO module. All instruments and facilities are currently at a feasibility stage. A number of risk-mitigating experiments are being designed to overcome ELT-sized problems. For example, challenges associated with ELT multi-LGS are to overcome spot elongation, depth of field, laser defocus and the fratricide effect. The EAGLE instrument study is conducting a risk-mitigation project CANARY where LGS MOAO will be demonstrated on a 4.2 m telescope.

ESO's ELT AO Working Group researched the area of RTCS for ELT for the 'Re-baselinging the ESO ELT project' report in 2006.

The XAO and MCAO will require up to a few 10k actuators and around 2 kHz frequency for an ELT. Following on from their VLT 2nd Generation AO RTCS Research (See Chapter 6) they believe that the best solution is a common standard platform that can achieve all the goals of the AO systems. Hence the SPARTA platform would be used to provide AO systems that met the requirements of each mode. [264]

The 'Re-baselinging the ESO ELT project' report continues to mention that the critical factor is latency, rather than the processing requirement. It is relatively simple to process gigabytes of data per second, given a pipeline of CPUs which is sufficient. Ensuring the computation completes in the total available time is difficult. It is required to do so in hundreds of microseconds. FPGAs must be used to reduce the latency to the minimum. ESO predict that such architecture, properly scaled to the timeframe of an ELT, will be able to deal with several of the AO systems for an ELT. The challenge is the XAO system, which is currently an exception.[206]

4 Nasmyth Adaptive Optics for Multi-purpose Instrumentation

The **Nasmyth Adaptive Optics for Multi-purpose Instrumentation** (NAOMI) is the common-user AO facility on the 4.2 m William Hershel Telescope (WHT). NAOMI contains a 76-element SDM, an 8 x 8 SHWFS and a DSP-based RTCS for its key components. In addition to NAOMI, the WHT AO instrument suite also includes two science instruments, the 'Isaac Newton Group Red Imaging Detector' (INGRID) and the 'Optically Active System for Imaging Spectroscopy' (OASIS), a coronagraph, 'Optimised Stellar Coronagraph for Adaptive Optics' (OSCA) and the common user Rayleigh LGS system, 'Ground-layer Laser Adaptive optics System' (GLAS). The AO suite is housed in the 'Ground-based Adaptive optics Controlled Environment' (GRACE).

This chapter begins by introducing NAOMI's host telescope, the WHT, followed by a brief review of previously hosted AO instruments. The present components of the AO instrumentation suite are introduced in the third subsection, followed by a description of NAOMI, which includes details of the instrument's three main components, the SDM, the SHWFS and the RTCS; covering both hardware and software. Finally, the chapter concludes with a subsection presenting the instrument's performance.

4.1 William Herschel Telescope

The Isaac Newton Group of Telescopes (ING) operates the 4.2 m WHT on behalf of the Particle Physics and Astronomy Research Council (PPARC) of the United Kingdom, the Nederlandse Organisatie voor Wetenschappelijk Onderzoek (NWO) of the Netherlands, and the Instituto de Astrofisica de Canarias (IAC) of Spain. The telescope is located 2,350 m above sea level on the Roque de Los Muchachos Observatory (ORM), La Palma, Spain.[207]

Figure 4.1 *WHT Telescope (Solid Model and photograph)*

The WHT was the third largest single-mirror telescope when completed in July 1987; see Figure 4.1. The reflecting Alt-Az telescope contains Cassegrain, Prime and 2 Nasmyth Foci. The WHT remains competitive mainly due to the quality of its optics, range of common-user instrumentation and support for visitor instrumentation, allowing for a wide range of astronomical observations.

The telescope's 4.2 m paraboloidal primary mirror (M1) reflects light to the 1m convex hyperboloidal secondary mirror (M2) and hence to the Cassegrain focus through a hole in the primary. The effective focal length for the Nasmyth focus is 46.2 m (f/11). An "optical" (transmissive) or "infrared" (reflective) image derotator can be installed to provide a 2.5 ' and 2.9 ' diameter unvignetted field of view respectively.[208] Further WHT parameters are tabulated in Table 4.1.

M1 Diameter	4.2 m
M2 Diameter	1.0 m
f-ratio at Prime focus	2.8
f-ratio at Nasmyth focus	10.94
Distance of exit pupil from focus	12850 mm
Diameter of exit pupil	1175 mm
Nasmyth FOV	2.9 arcmin
Plate scale at Nasmyth focus	4.49 "/mm or 223 μm/arcsec

Table 4.1 *WHT Parameters*

There are two Nasmyth Platform environments, the 'Ground-based High Resolution Imaging Laboratory' (GHRIL), which was the original focus of NAOMI, and the newer GRACE, which became dedicated to the common user AO facility in 2003.

4.2 Evolution of Adaptive Optics at the WHT

The 'Multi-Aperture Real-time Image Normalisation Instrument' (MARTINI) was the first adaptive optics prototype system designed and engineered in the mid eighties for the WHT by the University of Durham (UoD). Achieving first light in September 1988, MARTINI's original design purpose was to provide image-sharpening performance of a factor of approximately two at visible wavelengths. MARTINI provided un-phased tip-tilt-only correction of the incoming wavefront using a six-segment deformable mirror, see Figure 4.2, containing three actuators per segment. It also contained an imaging photon counter detecting SHWFS, matching one SA per segment and a 16 MHz M68020 real-time control computer providing a closed-loop bandwidth of between 10 - 20 Hz. Its DM was conjugated to 3.6 km above the telescope, the predicted mean height of turbulence. MARTINI evolved with two major upgrade programmes, MARTINI-II provided automation of observation and fully remote control and MARTINI-III provided an IR feed for the 256 x 256 InSb-based near infrared (1 - 5 μm) science camera, labelled the 'William Herschel Infra-red Camera' (WHIRCAM), a CCD-based WFS and a segmented piston reconstructor. MARTINI-III was commissioning in co-phased mode in August 1996. It became a heavily supported common-user instrument and was available until NAOMI's commissioning. [209,210,211,212,213]

In 1993, while MARTINI was being developed, the UK initiated a national AO programme.[214] One main aim of the programme was to equip the WHT with common-user AO instrumentation starting with the aforementioned MARTINI-III upgrade. The programme included the design of a common-user NGS AO system for the WHT, which was to become NAOMI.[215,216] The programme also supported the developments of site evaluation, IR instrumentation and laser beacons.

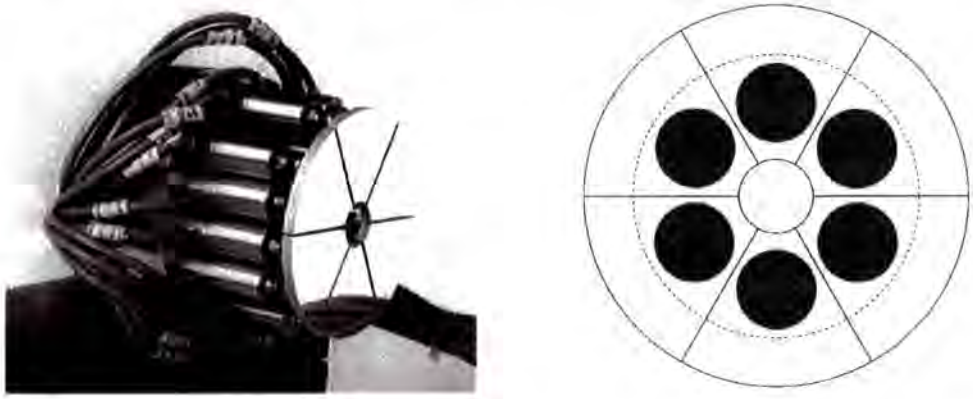

Figure 4.2 *MARTINI SDM (photograph and schematic matching position of SA and telescope pupil)*

Independently UoD had designed their second-generation WHT prototype system. The 'Enhanced Light Efficiency Cophasing Telescope Resolution Actuator' (ELECTRA) was designed to provide a full-aperture equivalent of MARTINI, supporting a mode for minimising the residual variance of the full WHT aperture. ELECTRA was constructed with the aim of prototyping higher-order correction on the WHT, supporting LGS research, prototyping AO-optimised instrumentation and launching adaptively corrected light into coherent fibres.[217,218,219]

In April 1995 the conceptual design review for the instrument to become NAOMI was held. Shortly after, in September 1995 a scientific case was presented and the design of the

instrument progressed. An agreement was made in July 1996 between UoD, the Royal Greenwich Observatory (RGO) and the Royal Observatory Edinburgh (ROE) / United Kingdom Astronomy Technology Centre (UKATC) to produce NAOMI. UoD agreed to supply hardware and software components brought and developed for the ELECTRA project.[220] ELECTRA's WHT on-sky testing helped mitigate some of the technical risks associated with NAOMI's design. ELECTRA's first commissioning run was in June 1997 during which time it closed loop in tip-tilt only mode. Its last run was in June 1999.

With the closure of the RGO in October 1998, NAOMI became a development between the UoD and ROE. UoD were responsible for the DM and the RTCS, while ROE were responsible for building the opto-mechanical chassis. NAOMI passed Critical Design Review in 1997. After construction, NAOMI achieved first light in GHRIL in September 2000 with the science detector INGRID.

4.3 NAOMI Environment and Instrumentation

The AO instrumentation suite is housed in GRACE. NAOMI currently contains two science instruments, INGRID and OASIS, and the coronagraph, OSCA. The common-user LGS system GLAS was commissioned in 2007.

4.3.1 Ground based Adaptive optics Controlled Environment (GRACE)

GRACE is a dedicated structure at a Nasmyth focus designed to facilitate routine AO use by providing a controlled environment for the instrumentation suite.[221] NAOMI used GHRIL as a temporary base during commissioning. Between observation runs NAOMI was craned from GHRIL and housed in the WHT Test Focal Station for characterisation. These experiences led to the requirement for a suitable dedicated fixed environment, which led to the design and construction of GRACE.

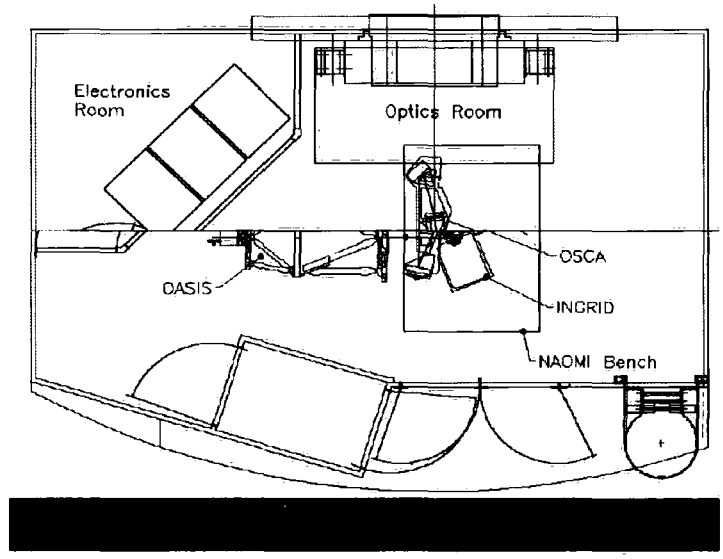

Figure 4.3 *Plan of GRACE*

GRACE is divided into two independent environmentally controlled and monitored light-tight rooms; an optics room containing the AO bench hosting NAOMI and an electronics room hosting various racks and control units. A user can control the air quality, temperature and air flow of each room as well as monitor the air flow and humidity. GRACE is environmentally conditioned using two roof-mounted air handling units.

Room	Parameter	Value
Optics	Temperature Range	10-18 °C
	Temperature Stability	±1.5 °C
	Settling Time	1 hour
Electronics	Temperature Range	12-18 °C
	Temperature Stability	±2°C
	Settling Time	1 hour
Both	Relative Humidity	50% ±10%

Table 4.2 *GRACE Design Parameters*

A plan of the building is shown in Figure 4.3. GRACE measures 6.8 m by 4.4 m (maximum), with a height of 3.3 m. The design was constrained around placing the optical bench on the Nasmyth optical axis, feeding the light from the optical bench to OASIS. Personnel access is provided by an airlock two-door system; equipment access is provided by wide double doors and removable access in the ceiling.

A key requirement for GRACE was temperature stability in the optics room, due to the sensitivity of the DM. The design specifications are tabulated in Table 4.2. GRACE characterisation experiments, results and conclusions are detailed in section 5.1.

4.3.2 Isaac Newton Group Red Imaging Detector (INGRID)

The near-IR camera INGRID was first commissioned at Cassegrain focus on the WHT in March 2000. It alternated between foci until 2004 when INGRID become permanently attached to NAOMI in GRACE.

INGRID contains a 1024 x 1024 HgCdTe Hawaii detector array and has a pixel scale of 0.04 "/pixel with a resulting field of view of approximately 40 x 40 " over a wavelength range from 0.8 to 2.5 μm. A 3D model of INGRID can in viewed in Figure 4.4. [222]

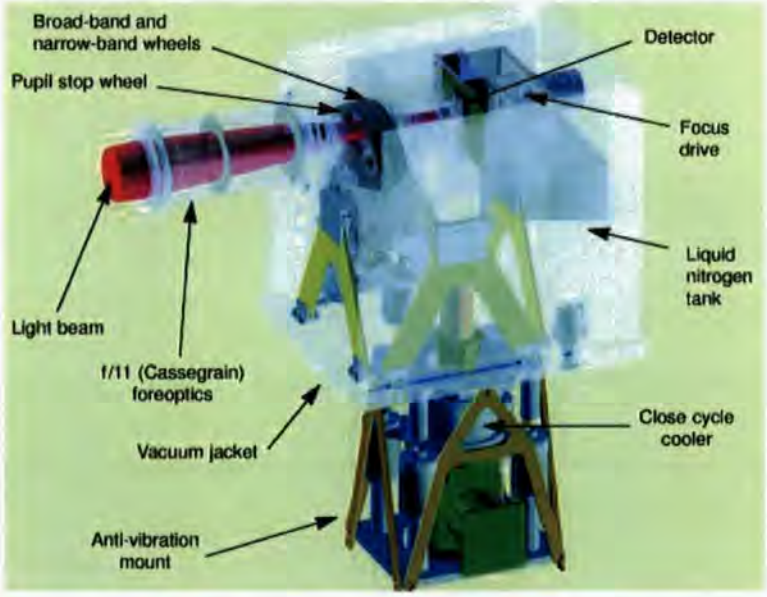

Figure 4.4 *3D Model of INGRID*

The dual cooling system shown in Figure 4.4 was used at Cassegrain focus; only the liquid N_2 tank was operational when configured with NAOMI. Figure 4.5 displays the instrument's optical layout showing the division between room temperature and cryogenic components.[223]

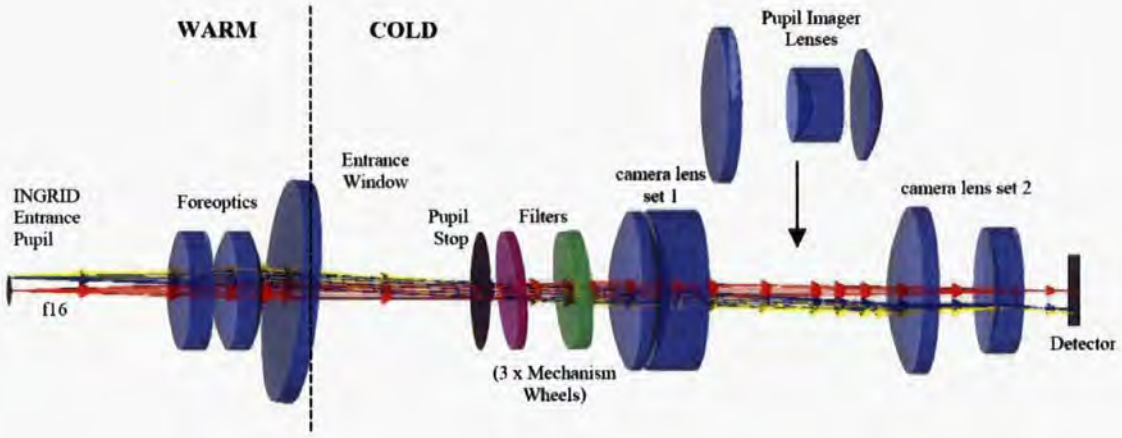

Figure 4.5 *INGRID's Optical path*

4.3.3 Optimised Stellar Coronagraph for Adaptive Optics (OSCA)

The Lyot coronagraph OSCA was added to NAOMI's optical bench and commissioned in May 2002 with INGRID. Constructed at the University College London (UCL), OSCA provides 10 different occulting mask sizes from 0.25 to 2.0 ", some containing a novel Gaussian profile; and a choice of two different Lyot stops.

Pneumatically deployable, OSCA contains seven optical surfaces mounted onto two horizontal plates fixed onto NAOMI's optical bench, as shown in Figure 4.6.[224,225]

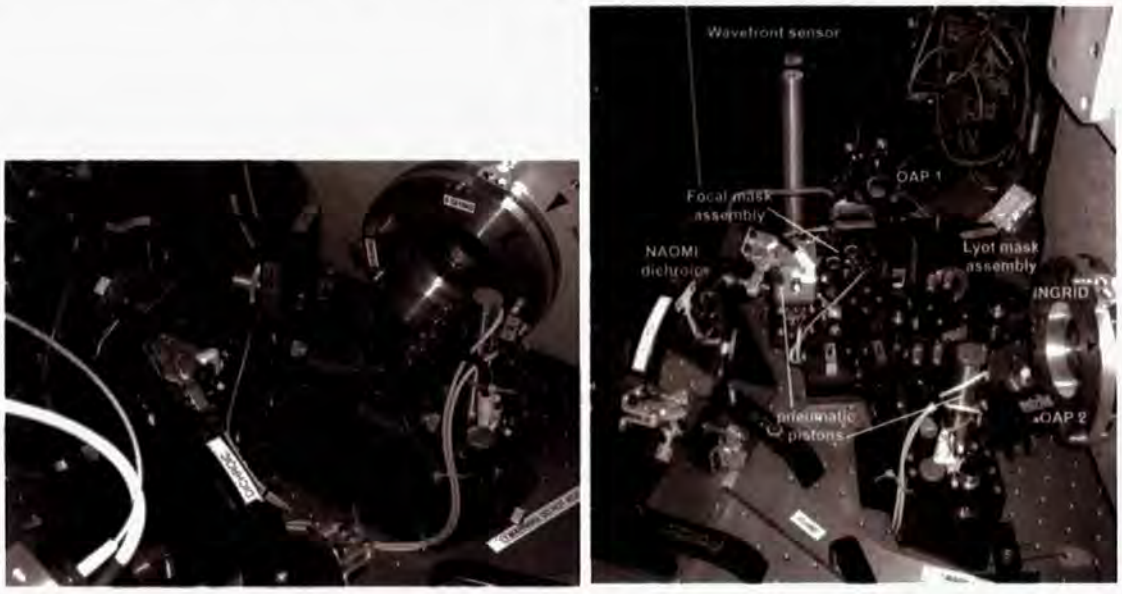

Figure 4.6 *OSCA integrated with NAOMI*

The optical design ensured that the focal position of NAOMI was unaltered when deploying OSCA into the optical path. OSCA operates in the 0.4 to 2.4 μm wavelength; it has a 90% transmission across the entire specified wavelength range.

Although OSCA was designed to operate with OASIS, this configuration has not yet been commissioned.

4.3.4 Optically Active System for Imaging Spectroscopy (OASIS)

The lenslet-based integral-field spectrograph OASIS was built and developed by Centre de Recherche Astronomique de Lyon (CRAL). It was designed to perform high-resolution observations on AO-corrected sources at visible wavelengths, see Figure 4.7. OASIS offers a range of spatial and spectral resolutions; an area of between 3 " and 16 " in diameter which can be imaged onto an array of 1100 lenslets in the focal plane. The 1100 resulting spectra are imaged onto a deep-depletion CCD provided by Lincoln Labs, with a dispersion of 1 to 4 Å/pixel. Six grisms and a composite grism provide spectral resolutions in the range of $1000 < R < 4000$. The CCD has a low readout noise of 2.3 electrons RMS in slow readout mode and a high QE of 0.9 at 0.75 μm. The instrument's resulting fringing level is low, giving ~3% at 0.8 μm, and 10% peak-to-peak at 1 μm. OASIS can also be used in imaging mode, primarily for target acquisition, with a field diameter of 28 ". [226]

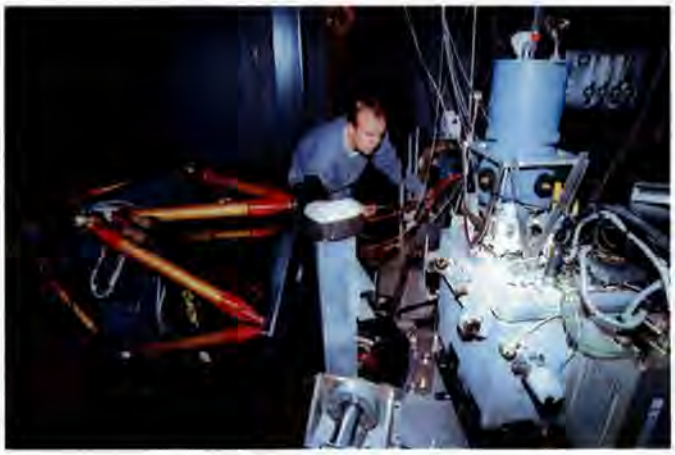

Figure 4.7 *OASIS configured with NAOMI inside GRACE*

Originally OASIS was designed for and commissioned on the CFHT. Early in 2003 the ING signed an agreement with CRAL to integrate OASIS with NAOMI. OASIS obtained first light in the summer of 2003 after the ING made a number of modifications to the NAOMI bench; see section 4.5.1.2.[227]

4.3.5 Ground-layer Laser Adaptive optics System (GLAS)

At the beginning of 2004 the ING were awarded funds by NWO to design, construct and commission a common-user Rayleigh LGS upgrade for NAOMI. This project/upgrade became GLAS, which was successfully commissioned in 2007. [228,229,230,231]

GLAS was a collaboration between the ING, IAC, UoD, Leiden Observatory and the Netherlands Foundation for Research in Astronomy (ASTRON). The aim of GLAS was to increase sky coverage available to NAOMI from ~1% to nearly 100%. An overview of the GLAS system can be seen in Figure 4.8. An Elektronik Laser System (ELS) 20 W 515 nm solid state, diode-pumped Ytterbium-YAG disk laser providing 400 ns pulses at a 5 kHz repetition rate produces the light for the LGS. The laser is mounted in a gravity-stabilised cradle on the top ring of the WHT. Its light is relayed using enclosed reflective optics to a 350 mm refractive Beam Launch Telescope (BLT) located behind the WHT secondary completing the laser launch system. The LGS is projected at a height of 15 km.

The return light passes through NAOMI and reflects to the LGS WFS from a Rugate dichroic beamsplitter. An optical train, including a two-arm Pockels Cell shutter, a series of stops and an 8 x 8 SHWFS focuses the 15 km LGS spots on to a LGS WFS E2V CCD39; see section 4.5.1.3.

A E2V Low Light Level (L3) CCD60 is used as the NGS WFS detector. Other GLAS upgrades include a new deployable calibration source for laser wavelengths, additional software for the RTCS system, a dedicated tip/tilt PC, new mechanism control hardware and software, a new laser safety system and a laser collision system (LCS). The LCS purpose is to ensure that the LGS light doesn't cross the line of sight of other telescopes on the ORM during observations.

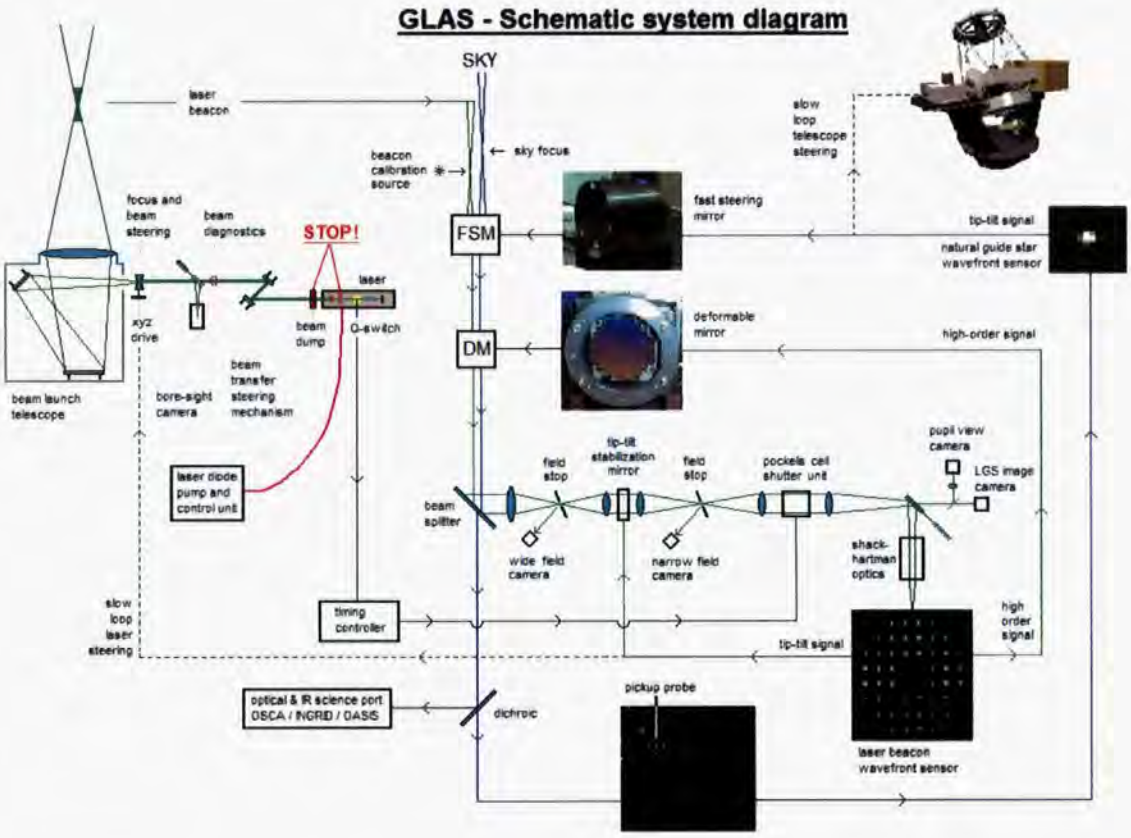

Figure 4.8 *Overview of GLAS LGS system upgrade*

4.4 NAOMI Site Evaluation, Modelling and Simulation

Site information should be obtained before producing an AOS design in order to accurately model and simulate a system's performance.

The Half Arcsecond Programme (HAP) was initiated by the ING in 1993 with the objective of reducing the seeing at the WHT to the intrinsic sight seeing.[232] The ING installed a Differential Image Motion Monitor (DIMM) approximately 50 m away from the WHT to record the intrinsic seeing. The measurements gained by DIMM were independent of errors such as wind shake, tracking, defocus and dome seeing. The seeing quality at the WHT was monitored between 1995 and 1998 by the Joint Observatories Seeing Evaluation (JOSE) monitor.[233,234,235] The results gave good correlation with the DIMM. The key results for atmospheric parameters are tabulated in Table 4.3.[233]

Monitor	Parameter	Value
DIMM	Median r_0	14.9 cm
	Annual Median seeing	0.69 "
	May to Sept Median seeing	0.64 "
	Oct to April Median seeing	0.82 "
JOSE	Median r_0	14.8 cm
	Mean L_0	15 m

Table 4.3 *Key results from the Half Arcsecond Programme*

These atmospheric parameters resulting from HAP were used in atmospheric modelling and simulations to verify NAOMI's design.

Initial simulations for NAOMI were conducted at Durham University and were used to give indicative performance estimates. Detailed design was based on semi-analytical model and verified by a Monte Carlo simulation used to derive the detailed Strehl-based error budgets, which in turn provided the specifications for the OMC and WFS subsystems.[236, 237]

Durham subsequently produced performance simulation for commissioning the as-built instrument and for observatory planning with input from the ING.

In 2003 the ING used a unique combination of empirical data collected simultaneously by INGRID, the NAOMI WFS and the site evaluation "Slope Detection and Ranging" (SLODAR)[238] instrument to discuss the accuracy of the analytic approach to modelling AO performance.[239]

Simulation of NAOMI continued as part of the GLAS upgrade project with Durham creating a predicted performance model of GLAS building on Durham's experience with GLAO experiments.[240, 241]

Although many attempts were made to simulate performance, none took into account the actual measured characteristics of NAOMI's FSM, DM, control hardware and software. By doing so it would be possible to both derive a more accurate performance model and to construct a controller to attempt system optimisation. The ING now use a MASS/DIMM to measure atmospheric turbulence.

4.5 NAOMI: The Instrument

The footprint for the commissioned instrument is shown in Figure 4.9. Originally NAOMI was divided into 3 main opto-mechanical subassemblies, the 'Nasmyth Calibration Unit' (NCU), the 'Opto-Mechanical Chassis' (OMC) and the 'Wavefront Sensor' (WFS). These subassemblies were placed on the 2500 mm by 1350 mm NAOMI Optical Table (NOT) where focus was positioned at x = 300 mm, y = 150 mm z = 16mm from the corner nearest the derotator.

NAOMI was designed to have the ability to observe the same FOV at IR and visible wavelengths simultaneously using different science instruments at the infrared and optical science port respectively.

This subsection begins with the evolution of the opto-mechanical aspects of the OMC and the NCU. The WFS is then described by examining its optomechanics, detector, readout electronics and overall functionality. This is followed by an examination of the OMC FSM and DM in more detail, describing their control electronics. This leads on to the section on NAOMI's RTCS before finally describing subsidiary systems and calibration.

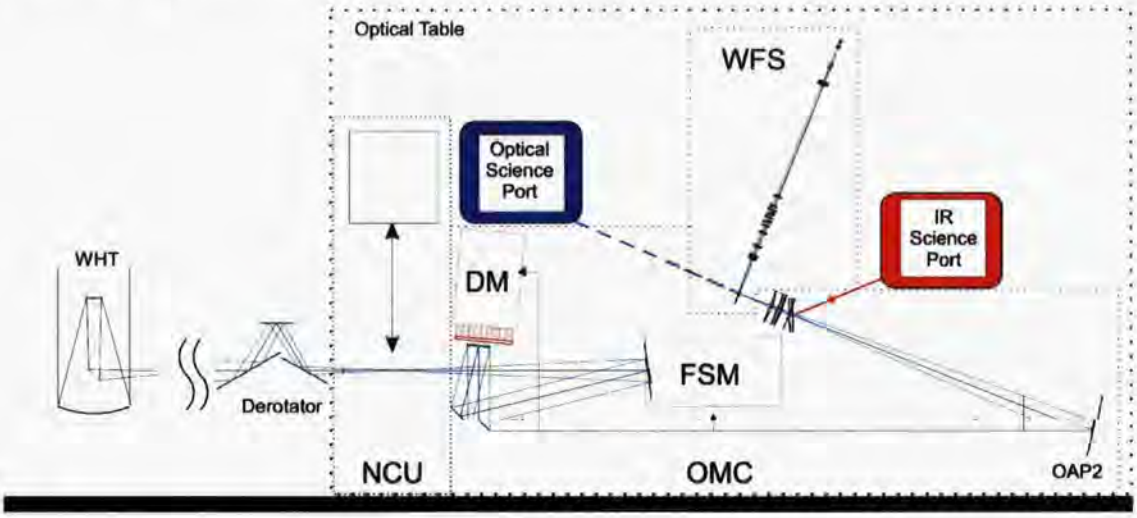

Figure 4.9 *Footprint of original subassemblies on the NOT (not to scale)*

4.5.1 Opto-Mechanical Chassis

The original OMC subassembly consists of five optical components: an off-axis parabola fast steering mirror (OAP1) or (FSM), a double pass fold mirror, a DM, a second off-axis parabola (OAP2) and a dichroic wavefront sampler, see Figure 4.10. The OMC relays the whole of the unvignetted 2.9 ' field of view (FOV) available at the f/11 Nasmyth focus to two spectrally divided f/16 foci, at a magnification of 1.5.

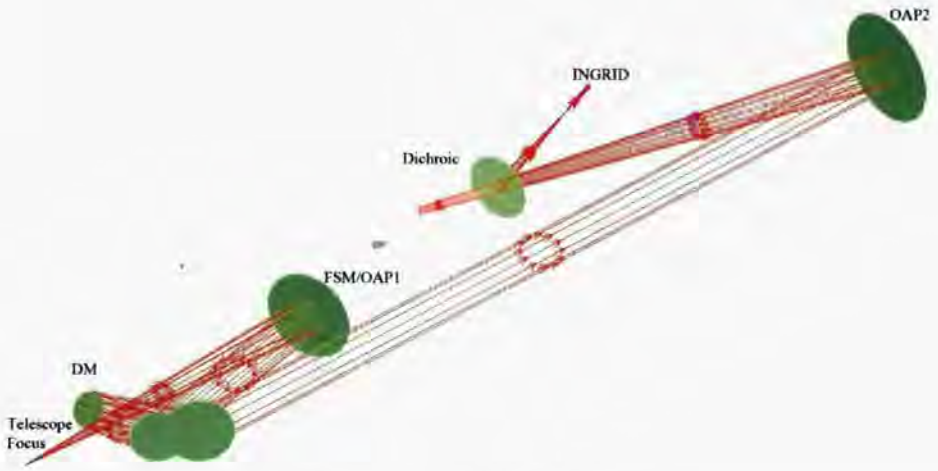

Figure 4.10 *The Optical Components of NAOMI*

Light arriving from the WHT's Nasmyth derotator is collimated by the FSM/OAP1. The 56 mm collimated beam reflects from a double pass fold mirror towards the DM, which is placed at a conjugate of the WHT exit pupil. The DM is mounted on a X-Y stage to aid alignment and segment cophasing. After the second reflection of the double pass fold mirror the light is reimaged by OAP2 at a 1.5x magnification. NAOMI was commissioned with a dichroic which reflects infrared and transmits the visible. The specifications of OAP1 and OAP2 are displayed in Table 4.4 and additional geometric information is given in Table 4.5.

Component	**OAP1/FSM**	**OAP2**
Radius (mm)	1210	1754.8
Off-axis distance (mm)	149	338.5
Off-axis angle (°)	14.04	21.84
Off-axis focal length (mm)	614.17	910.2
Sag (mm)	9.17	32.65
Form error over central area	75 mm diameter area	94 mm diameter area
	8.2 nm RMS	6.3 nm RMS
Form error over clear aperture	110 mm diameter area	175 mm diameter area
	10.7 nm RMS	10.7 nm RMS

Table 4.4 *Specifications of OAP1 and OAP2*

Distance	**Value (mm)**
OAP1 to fold mirror	466
Fold mirror to DM	217
DM to fold mirror	179
Fold mirror to OAP2	1483
OAP2 to dichroic	785

Reflection	**Angle of incidence (°)**
Fold Flat #1	30
DM	7
Fold Flat #2	45

Table 4.5 *Further geometry specifications*

The OMC has iteratively evolved with the addition of OSCA, OASIS and GLAS. The number of opto-mechanical components populating the optical bench has increased. The OMC also contains an interferometer for calibration; this is discussed further in section 4.5.8.

4.5.1.1 OSCA upgrades

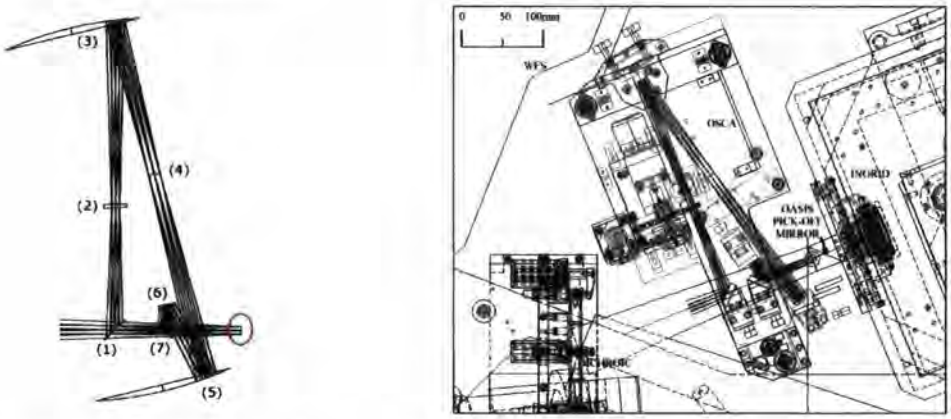

Figure 4.11 *The optical and mechanical design of OSCA on the NOT.*

The complete OSCA opto-mechanical chassis was added to the bench when commissioned and is now permanently mounted between the dichroic and INGRID. The instrument's pickoff mirror can be pneumatically deployed when required. It receives, and later returns, the modified f/16 beam. The optical and mechanical design is shown in Figure 4.11.

In order of photon arrival, OSCA's seven opto-mechanical components consist of a flat pickoff mirror, a focal plane occulting mask, an off-axis parabola (OAP1), a Lyot stop, a second off-axis parabola (OAP2) and two flats to return the beam to the original NAOMI focal position. OSCA fits inside a 200 mm by 400 mm space envelope on the NOT.[224,225]

4.5.1.2 OASIS upgrades

In addition to the second-generation NCU, covered in section 4.5.2.2, there were other additions to the NOT to produce a third instrumentation port, labelled the Universal Science Port (USP). The pickoff mirror to provide an f/20 focus was placed after OSCA and before the IR Science port hosting OASIS as seen in Figure 4.11. Additional relay optics was added to the bench after the pickoff mirror to reshape the beam and provide focus adjustments.

An operational atmospheric dispersion corrector (AtDC) was required for OASIS and was placed into the collimated path between the folding flat and OAP2. OASIS generated the requirement to deploy various dichroics. An automated dichroic changer was placed on the bench above OSCA, restricting its access. Finally a dedicated "Simplexing" Camera was added; see section 4.5.8.3.

4.5.1.3 GLAS upgrades

As pictorially displayed in Figure 4.8, the LGS WFS is located on the NOT. Figure 4.12 displays the GLAS LGS WFS design.

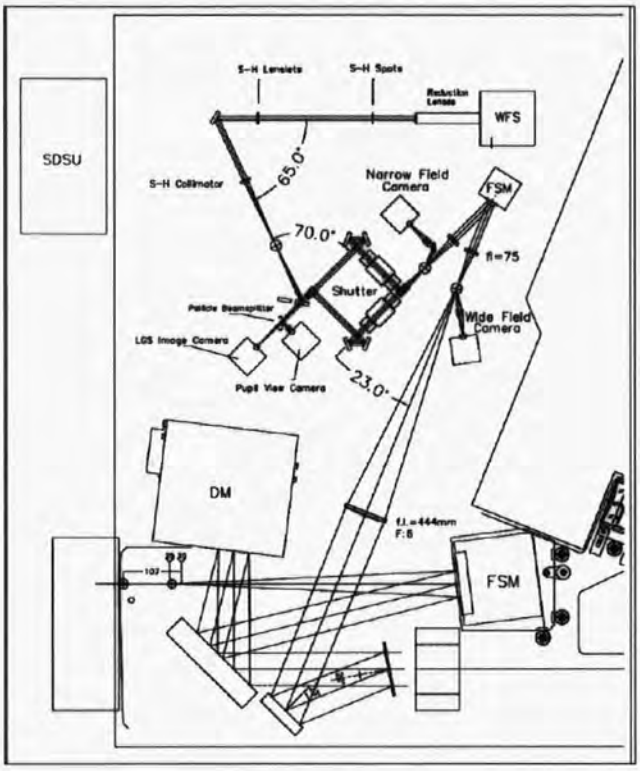

Figure 4.12 *The LGS WFS bench upgrades expected for GLAS*

The GLAS notch-filter dichoric is positioned after the double pass folding flat and before the OASIS AtDC. The reflected LGS passes through a correction lens before reaching the LGS FSM. The light passes through Pockel Cell return arms before being collimated and sent to the LGS SHWFS. Figure 4.13 pictorially displays the complete NOT, including GLAS components.

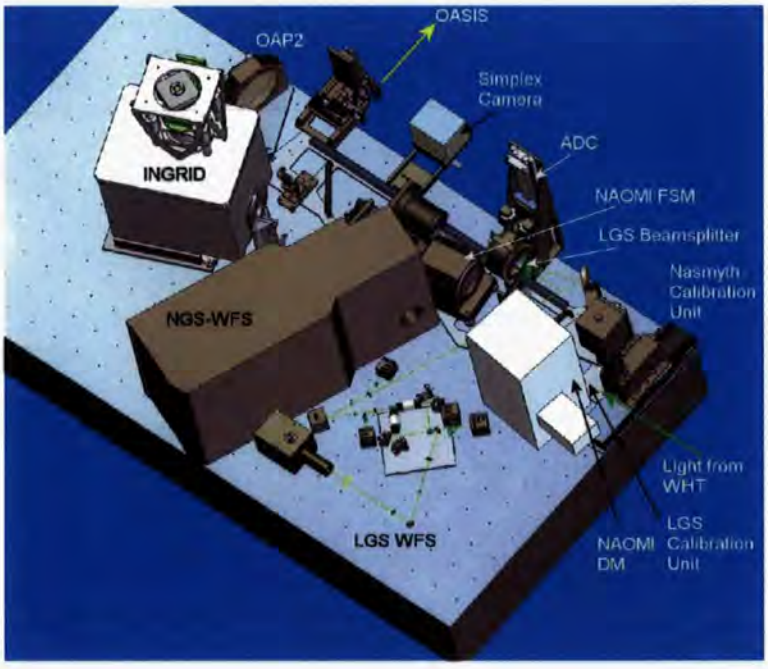

Figure 4.13 *NOT footprint including GLAS*

4.5.2 Nasmyth Calibration Unit

The original commissioned NCU (NCU#1) was replaced in 2003 with NCU#2 to aid the alignment and calibration of OASIS.

4.5.2.1 NCU#1

The original NCU provided an on-axis point source for calibration; its components are displayed in Figure 4.14.

NCU#1 was never fully commissioned. It provided illumination of pinholes in the Nasmyth focal plane mask, a flat-field source for INGRID and an on-axis f/11 point source. This source could have potentially moved by about 1 " at the Nasmyth focus using a small tip-tilt mirror in the NCU, but was never used at Nasmyth.

A white light source illuminates an integrating sphere which in turn illuminates a set of holes in a mask. The set of holes correspond to the holes in the Nasmyth focal plane mask, with a larger on axis aperture, which could illuminate the whole of the IR science port for flat fielding. The image of the mask was transferred to the Nasmyth focal plane by an Offner relay. An on-axis pinhole could be introduced at the integrating sphere output; the image of this pinhole could be moved using the secondary mirror of the Offner relay, which was mounted on a tip-tilt piezo stage. The light was inserted into the NAOMI optical path by a removable beamsplitter. The beamsplitter also allowed light from the telescope to be seen by the NCU acquisition camera.

Component	Controllable
Beamsplitter	Yes
Motorised Mask	Yes
Calibration Source	Yes
Tip/Tilt Injector Mirror	Yes*
Pinhole Mirror	No
White Light Source	No
Integrating Sphere	Yes
Acquisition Camera	Yes

* never commissioned

Figure 4.14 *Photograph of NCU#1 and component list*

4.5.2.2 NCU#2

OASIS required spectral calibration sources so a second NCU was built. NCU#2 comprises two units connected to the light sources by fibre optics. A sealed water-cooled light box base unit is located under the NOT which contains two white light sources, a neon spectral lamp and a helium spectral lamp. The NOT unit, containing apertures, deployment stages and acquisition camera, fits inside the space envelope of NCU#1. Figure 4.15 displays both units of the NCU#2.[227]

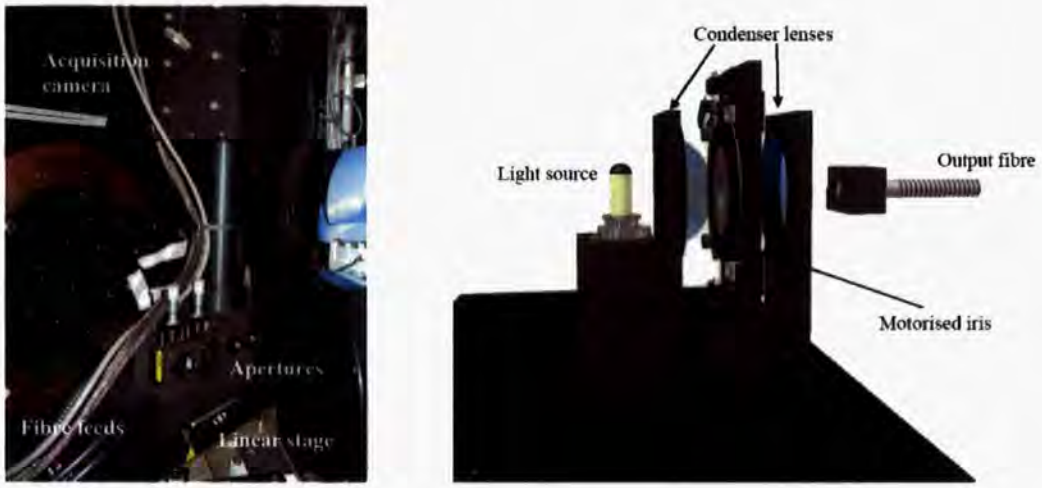

Figure 4.15 *NCU#2 a) Photograph of NOT unit b) Solid Model of base unit*

The base unit contains two high-powered condensing lenses either side of a motorised iris used to alter the intensity of light passed to the output fibre. A good diffuse illumination across the aperture is achieved by mounting the diffuser directly in front of the non-coherent fibre bundle. The pickoff and acquisition camera is mounted such that calibration and acquisition can occur simultaneously. A field stop is placed at focus allowing a 3' field to pass unvignetted.

4.5.3 NAOMI Wavefront Sensor

The NAOMI SHWFS was designed to sense the WF from any point source within the 2.9 ' FOV. The associated opto-mechanical subassembly, detectors and readout electronics are described.

4.5.3.1 WFS Opto-Mechanic Subassembly

Light reaches a field lens, which provides a telecentric beam for the WFS. Opto-mechanically the WFS can be divided into three sub-assemblies, the components of which are each mounted on a separate carriage; see Figure 4.16 for a solid model and Figure 4.17 for a schematic.

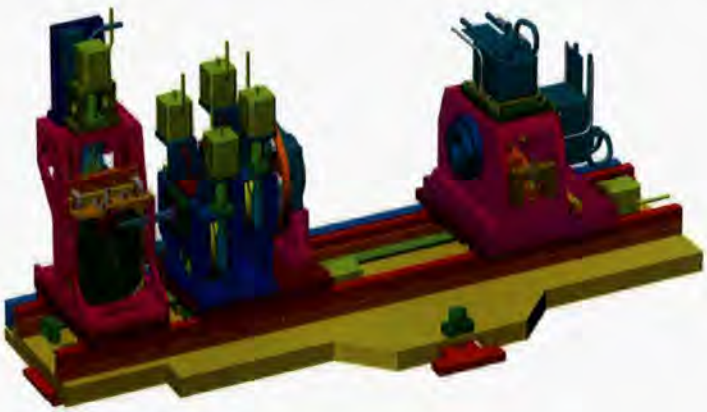

Figure 4.16 *Shack Hartmann WFS Solid Model*

Carriage 1
The first optical component is a pickoff mirror. It is mounted on a 3 mm thick glass plate, which is in turn fixed on an x-y translation stage. The light enters the WFS telecentrically; i.e. the same angle in any point in the field. The pickoff mirror can be placed at a mean focus position, which gives a 0.14 " defocus at the centre and edge of this field. The focus within the WFS is maintained by translating its 2nd and 3rd carriages. The glass plate transmits the rest of the optical field around the reference star to the optical science port.

A manually removable baffle, acting as a field stop, can be placed around the pickoff mirror to reduce the FOV, eliminating optical cross-talk within each subaperture. The baffle is removable to accommodate extended objects.

The pickoff mirror reflects the light upwards through 90 ° towards a fold mirror. The fold mirror reflects the light through 90 ° towards carriage 2 so the beam is parallel to the optical table. The fold mirror is attached to the pick off x-carriage, but not to the y-slide, so that the output remains at a constant height above the optical table.

Carriage 2
The first optical component is a collimating doublet giving a beam of 8.1 mm in diameter which ensures correct one-to-one imaging of the DM segments onto the lenslets. A filter wheel was installed for two reasons; to reduce certain spectral background contributions and to limit the wavelength range to improve background rejection. Filters are selected remotely. An AtDC consisting of two pairs of cemented prisms was included in an axially rotating mount. The WFS AtDC was included to deal with dispersion in the sense of differential atmospheric refraction but was never commissioned.

A lenslet array is placed at the pupil image produced by the WFS collimator. The magnification between DM and lenslets gives a one-to-one correspondence. There are three lenslet arrays and a full aperture lens, which were mounted in a wheel; since commissioning additional lenslets have been installed.

Carriage 3
On commissioning, the final carriage contained two sets of CCD relay optics, a deployable 50/50 beamsplitter and two E2V CCD39s. The WFS contained the functionality of splitting the light and detecting on two CCDs to double the frame rate by synchronising the WFSs readouts. However, the beamsplitter was replaced by a single block of glass and permanently used in single CCD readout mode until the arrival of GLAS. The telecentric design gives low distortion and insensitivity to spot displacements caused by focus shifts. The final optical component is a fused silica window 2.5 mm in front of the CCD.

Table 4.6 contains some specifications of the SHWFS main optical components.

WFS Opto-mechanic Subassembly	
Carriage 1	
Pickoff Mirror	
Angle of incident	45 °
x-y movement	30 mm
Aperture	3 x 4.2 mm
Position(in front of focus)	3 mm
Unvignetted FOV	8 "
Folding Flat	
Angle of incident	45 °

Carriage 2	
Collimator	
Type	Doublet
Surface 1 radius	164.9 mm convex
Lens 1 Thickness	3.1 mm
Lens 1 material	SF15
Common surface radius	53.4 mm concave to input
Lens 2 Thickness	7.05 mm
Lens 2 material	BALKN3
Surface 3 radius	79.6 mm convex
Filter Wheel	
No of Slots	6
Filter Thickness	3 mm
Lenslet Wheel	
No of Slots	6
Aperture 1	1.1 x 1.1 mm
Focal Length 1	209 mm
Aperture 2	1.1 x 1.1 mm
Focal Length 2	105 mm
Aperture 3	2.2 x 2.2 mm
Focal Length 3	209 mm
Aperture 4	Full aperture double lenslet

Carriage 3	
CCD Relay Lens 1	
Surface 1 radius	48.3 mm convex
Lens 1 Thickness	7.4 mm
Lens 1 material	BALKN3
Common surface radius	38.99 mm concave to input
Lens 2 Thickness	2.5 mm
Lens 2 material	SF15
Surface 3 radius	105.92 mm convex
Beamsplitter	
Material	BK7
Thickness	10 mm
CCD Relay Lens 2	
Surface 1 radius	33.1 mm convex
Lens 1 Thickness	1.6 mm
Lens 1 material	SF8
Common surface radius	5.17 mm concave to input
Lens 2 Thickness	4.41 mm
Lens 2 material	SSK4
Surface 3 radius	9.19 mm convex
CCD Window	
Material	Fused Silica
Thickness	2.5 mm

Table 4.6 *WFS Opto-mechanical Subassembly Components*

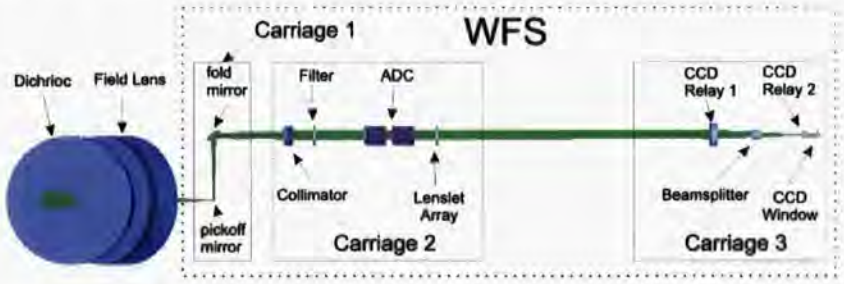

Figure 4.17 *The opto mechanical components of the NAOMI WFS*

4.5.3.2 CCD39

The CCDs commissioned in the NAOMI WFS were the E2V CCD39-01 Back Illuminated High-Performance CCD Sensor, shown in figure 4.17.

CCD39 Features

- 80 by 80 1:1 Image Format
- Image Area 1.92 x 1.92 mm
- Split-frame Transfer Operation
- 24μm Square Pixels
- Symmetrical Anti-static Gate Protection
- Four very low noise output amplifiers
- High Frame Rate Operation (up to 1000 fps)
- High Spectral Response
- 100% active area

Figure 4.18 *CCD39 Key Features*

The CCD39 typical manufacturing performance is shown in Table 4.7.

CCD39 Features			
Typical Performance		**Format**	
Max. Readout frequency	>3MHz	Image Area	1.92 x 1.92 mm
Output amplifier sensitivity	4.5μV/e^-	Active pixels (H) & (V)	80 & 80±4
Peak Signal	300 ke^-/pixel	Pixel size	24 x 24 μm
Spectra Range	200-1100 nm	Storage Areas (x2)	1.92 x 0.96 mm each
Readout noise @ 20kHz	3 e^- rms	No output amplifiers	4
QE at 500nm	90%		
Peak Charge Storage	300 ke^-/pixel	**Package**	
Peak output voltage	1350 mV	Package size	32.89 x 20.07 mm
Dark signal at 293 K	75ke^-/pixel/s	Number of pins	24
Charge transfer efficiency	99.9999%	Inter-pin spacing	2.54 mm
Dark signal non uniformity	7.5 ke^-/pixel/s	Type	Ceramic DIL array

Table 4.7 *CCD39 Typical Performance*

The CCD39 devices are water-cooled to run at 8 °C to reduce thermal noise. The devices are controlled using second-generation 'San Diego State University' (SDSUII) CCD Controllers.[242]

4.5.3.3 SDSUII Controller Software

Both CCD39s were connected to SDSUII controllers located on the NOT. The controllers were placed on damping material (high frequency and low frequency) to minimise vibrational energy transfer to the optical components. The SDSUII controllers contain an analogue clock board, a video board and a timing board. The video board receives data from the CCD and transfers the data to the timing board. The timing board, on request, sends the data to a SDSU interface card housed in the NAOMI SDSU VME Rack, see section 4.5.6.1.

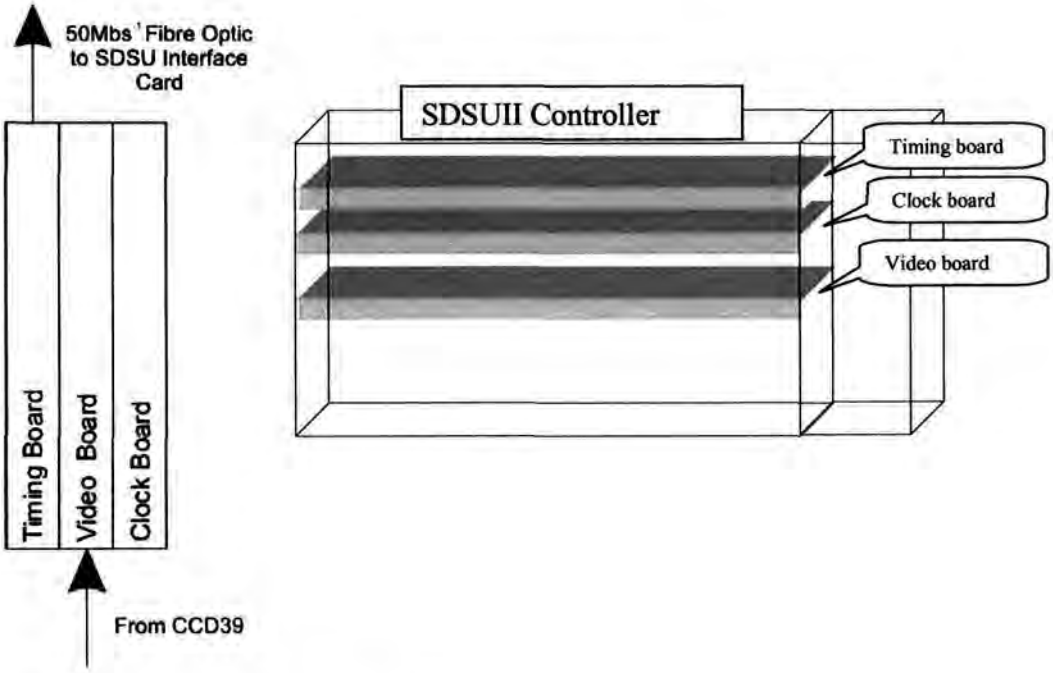

Figure 4.19 *SDSUII Controller*

The Motorola DSP inside the SDSUII controller runs code to configure the readout mode of the CCD.[243] The original modes were coded at the ATC.[244, 245] Although software was provided for NAOMI to operate in synchronisation mode, this will not be discussed. The original unsynchronised modes are provided and given in Table 4.8. Test scripts were created to test these modes during commissioning runs.[246, 247]

Mode	Lenslet	Sub-Aps	Visible Pixels	Binning	Name
1	8 x 8	8 x 8	8 x 8	1 x 1	8x8_8x8_1x1
2	8 x 8	8 x 8	2 x 2	2 x 2	8x8_2x2_2x2
3	8 x 8	8 x 8	4 x 4	1 x 1	8x8_4x4_1x1
8	4 x 4	4 x 4	4 x 4	1 x 1	4x4_4x4_1x1
9	4 x 4	4 x 4	2 x 2	2 x 2	4x4_2x2_2x2
10	Doublet		2 x 2	2 x 2	1x1_2x2_2x2

Table 4.8 *WFS Modes*

4.5.4 Fast Steering Mirror

The FSM was manufactured by Zeiss-Jena. Table 4.9 shows a list of tests on delivery of the mirror.[248] These tests were performed on the original mirror at the ATC. When the mirror was delivered to the ING it malfunctioned and was sent back to Zeiss to be repaired.

Figure 4.20 shows the FSM in its operational mount. The original tests gave an unacceptable response time because the FSM was commissioned with a signal protection filter to protect the mirror from damage. This was used during commissioning to test the FSM before software protection was placed into the system, see section 4.5.6.1 for further details.

Parameter	Requirement	Achieved	Compliance
Full stoke	± 500 μrad (± 102.6 arcsec) beam deflection 0 @ 20 Hz	> ± 600 μrad	Yes
Tilt stroke at 250 Hz	49.8 μrad (10.2 arcsec) beam deflection	> 50 μrad	Yes
Tilt range	$R_i = -0.41 \log(f_i) + 1.033$ f_i - frequency [Hz]		Yes
Resolution	1.5 μrad (0.3 arcsec)	< 0.5 μrad	Yes
Repeatability	4 μrad (0.8 arcsec)	± 3.5 μrad	Yes
Static jitter	1 μrad RMS (0.2 arcsec)	0.34 μrad	Yes
Resonance	> 250 Hz	582 Hz	Yes
Reactionless	< 2% @ 250 Hz	13%	
Linearity error	< 1%	< 2.5%	No
Pivot stability	± 0.05 mm	< ± 0.005 mm	Yes
Response time	1 ms	< 1.89 ms	No

Table 4.9 *Original ATC Test Compliance Matrix for FSM*

Figure 4.20 *NAOMI's FSM*

4.5.5 Deformable Mirror

NAOMI contains a ThermoTrex Corporation 76-element SDM. With internal Strain Gauge (SG) feedback capabilities, the SDM provides 228 degrees of freedom, as each segment contains three piezoelectric actuators, separated by 120 degrees. The SDM is pictured in Figure 4.21.

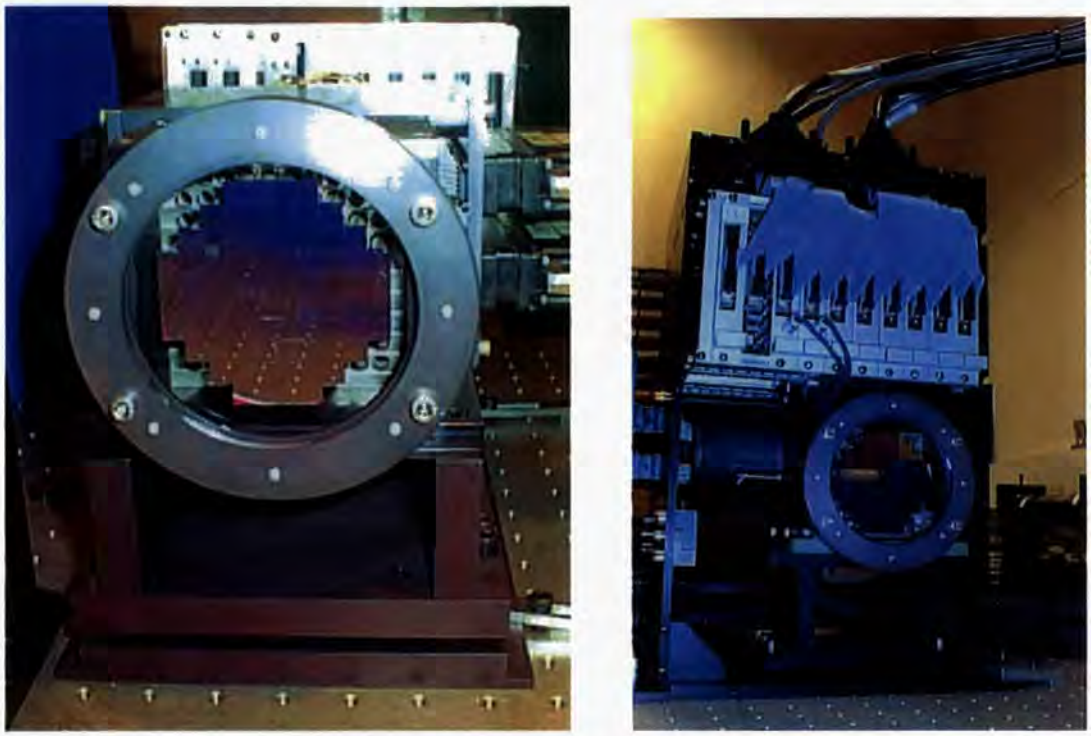

Figure 4.21 *NAOMI's ThermoTrex SDM and Strain Gauge Rack*

Each segment can move in tip, tilt and piston. Each actuator has three drive-signal connections and one common return. In addition they have pairs of miniature strain gauges fitted to measure the actual actuator position in order to overcome the effects of hysterisis. One strain gauge is used for position sensing and the other for temperature compensation. The position strain gauges are adhered to the inside of the actuator, whereas the temperature compensating gauges are adhered to a small ceramic circuit board, which also provides connection points to a five-core screened signal cable. Figure 4.22 displays the cross-section profile of actuator. Hysterisis correction was originally characterised during the ELECTRA project.[218] The signals from the strain gauges are amplified before being relayed to the analogue to digital converter (ADC) boards within the real-time rack.

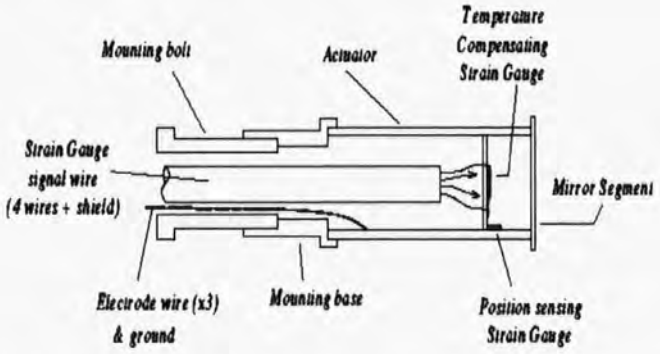

Figure 4.22 *Cross section profile of a Piezoelectric Actuator* [218]

The main specifications of the SDM are given in Table 4.10.

ThermoTrek SDM	manufactured 1995
Parameter	**Requirement**
Number of segments	76
Mirror spacing	7.62mm
Total Stroke	6 μm
Segment mirror flatness	< λ/10
Settling Time	< 5ms
Degrees of Freedom	228
Intra segment spacing	80 μm
Stroke available after flattening	4 μm
Stroke Linearity	< 3%

Table 4.10 *Deformable Mirror Design Specifications*

4.5.6 NAOMI Real-Time Control System

This section describes both the control hardware and software architecture of the RTCS as commissioned. [249, 250, 251, 252, 253, 254]

4.5.6.1 RTCS Control Hardware

NAOMI's control system hardware is illustrated in Figure 4.23. The heart of the control hardware is the Real-time Control Rack (RTCR), which performs all of the control system real-time calculations. The DM requires the use of a Digital Analogue Converter Rack (DACR) and a High Voltage Amplifier Rack (HVAR) to drive its actuators to calculated demand positions. The DM's SG feedback system includes the use of a Strain Gauge Amplifier Rack (SGAR) and a "Sin Bin Amplifier" (SBA) to send signals, containing positional information, back to the RTCR. The SBA is only used for channels with failing isolation between SG signals and drive ground. The FSM is driven by sending values to the DACR, which passes voltages to a dedicated amplifier and then a FSM Signal Filter (FSMSF) before reaching the mirror.

Real-time Control Rack (RTCR)

The 19 " RTCR is populated with 11 VME cards, as listed in Figure 4.23 and photographed in Figure 4.24.

The Force SPARC CPU-5 processor card is commonly referred to as AOControl1 and the VME Controller. It is responsible for booting and configuring the RTCS and communicating (commands and diagnostic data) with the higher-level engineer/observer level software running on the NAomi VISualisation (NAVIS) workstation using a 10-BaseT Ethernet interface. It runs Solaris 2.5 and has a 9 Gb hard drive attached, which contains sources, executables and configuration files for the SDSU CCD Controller MVME167 processor card and the Texas Instruments (TI) Digital Signal Processors (DSP). It also contains real-time 'flight recorder' data.

The UoD master and slave WFS interface cards buffer the pixel data supplied by the two interface boards contained within the SDSU WFS VME Rack via RS-422 in a FIFO manner. The cards pass on pixel data to the Blue Wave Systems WFS DBV44 card on demand via a communication port interface.

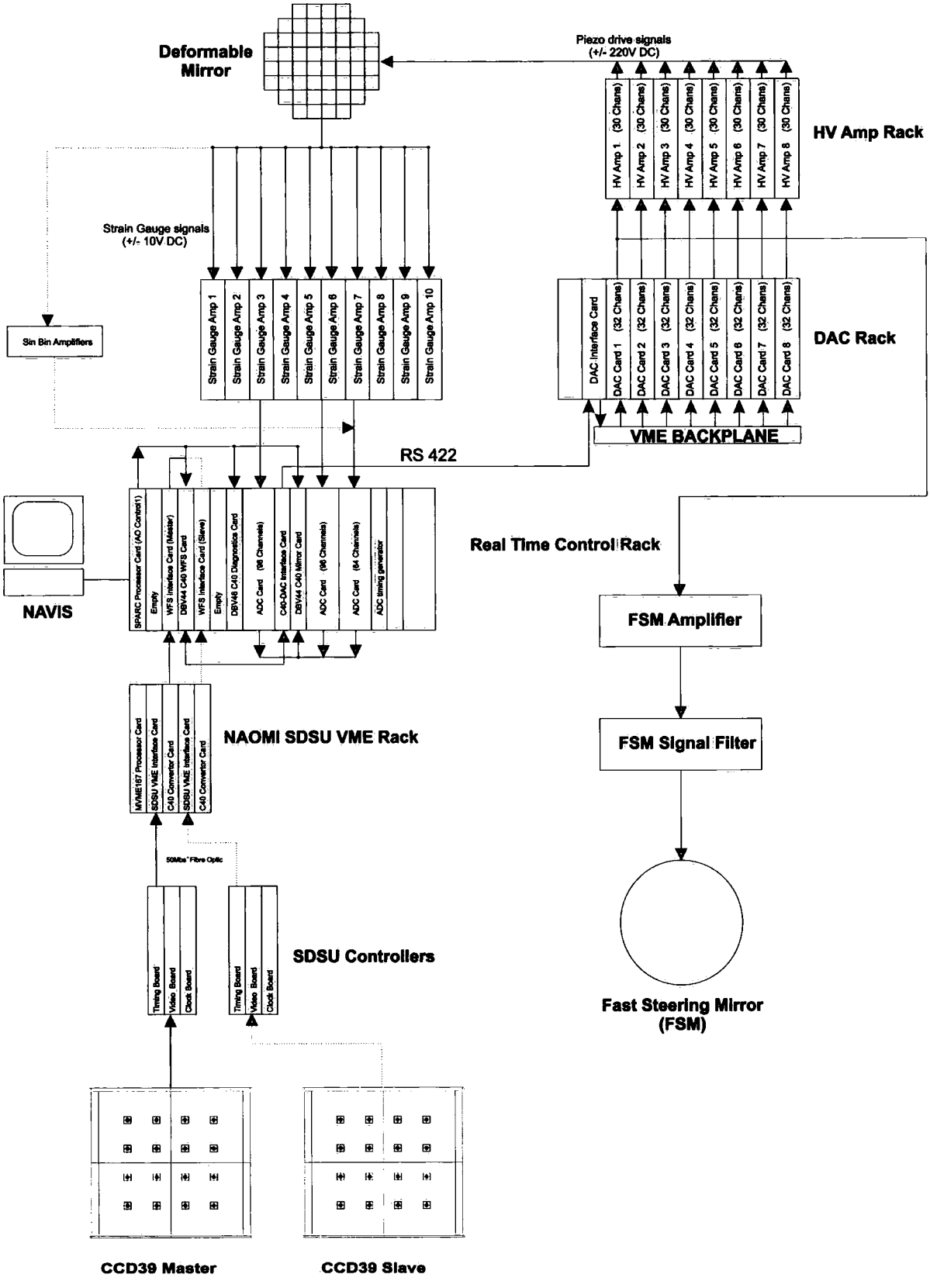

Figure 4.23 *Overview of the NAOMI Real-time Control System Hardware*

The DBV44 hosts four dual C40 TIM daughter cards. Each TIM card contains two TI TMS320C44 DSPs. This card is responsible for reception of the WFS pixel data, calculating centroid positions and performing wavefront reconstruction, calculating demand positions for the DM and FSM. These demands are then passed onto the identical Mirror DBV44 card, which sends the demanded values to the UoD C40-DAC interface card. It accepts the mirror demand values via a communication port and passes this data to the DAC interface card hosted in the DACR.

The Mirror DBV44 monitors the actual position of the actuator strain gauges via two 96-channel and a 64-channel 16-bit Pentland ADC cards. Each channel is capable of sampling at 85 kHz. Due to hysterisis the demands to the mirror are modified and re-applied to ensure the piezoelectric actuators are sent to the hysterisis compensated position. The ADC cards are synchronised by timing pulses produced by the ADC timing card triggered by one of the C40s, which is programmed to interrupt itself.

The Diagnostics DBV46 VME card houses two TMS320C40 processors and a large amount of local memory. The C40 differs from the C44 by having 6, instead of 4, communications ports. The DBV46 is used to provide real-time diagnostic information to the user. It receives and interprets data packets from both the WFS and Mirror DBV44 cards. The data is processed and passed to AOControl1 via the VME backplane, which in turn records and passes data to NAVIS via Ethernet.

Figure 4.24 *NAOMI Real-time Control Rack*

Mirror Control Electronics

The calculated demand position for each DM actuator and FSM axis passes from the RTCR via RS-422 to the 19 " DACR, Figure 4.25a, which in-turn passes analogue signals to the HVAR, Figure 4.25b, before a piezoelectric actuator drive signal reaches the DM.

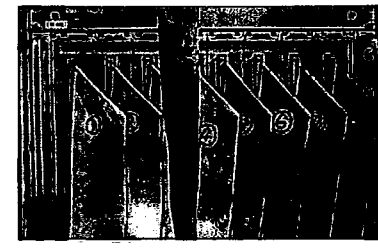

Figure 4.25 *DAC Rack (left) and HV Amp Rack(right)*

The UoD DAC interface card accepts successive RS-422 16-bit data writes from the RTCR C40-DAC interface card and outputs these values together with an incrementing 16-bit address onto a VME backplane. Each of the eight UoD 32-Channel DAC card provides channels of 13-bit, ±10V outputs from four Maxim MAX547 DAC ICs. The last two channels on the first DAC card are used to send drive signals for the tip and tilt axis of the FSM. Each board contains a 60-way and a 10-way IDC connector, providing 30 and 2 DAC output and ground pairs, respectively.

The HVAR houses the eight UoD 30-channel high voltage amplifier cards. The circuits are based around an inverting, differential input, amplifier circuit with a forward gain of 20. The circuit accepts ±10 V input signals and amplifier them to ±200V using Apex PA15 amplifiers. The HV signals are passed from the HVAR to the DM via two custom cables with ITT Canon 144-way ZIF connectors.

DM and SG Feedback

The strain gauges within the piezoelectric actuators are driven from a 2 V precision source; the nominal output of each strain gauge pair is 1 V ±7.7 mV. The signals from the strain gauges are passed to the amplifier cards via ThermoTrex reverse DIN41612 style daughter boards. A small backplane is included to allow the ±12 V, +3 V power to be passed to all ten amplifier cards. A rack of Burr-Brown INA118 precision amplifiers is used to boost the signal to a level which will survive the 5 m cable run to the ADCs and to be at a useable level for digitisation.

Each amplifier card carries 32 amplifiers which buffers the outputs from one entire column of segments. The amplifier rack is mounted above the mirror itself; see Figure 4.21. The output signals from these ten cards are combined onto eight SCSI-type cables for connection to the Pentland ADCs.

Unfortunately some of the strain gauges are not fully electrically isolated. These strain gauges signals skip the SG Amplifier and pass through the SBA which restores the faulty actuators to normal use but does leave them prone to greater electrical noise than the isolated ones.

FSM

The FSM drive signals leaving DAC Card 1 passes through a dedicated FSM Amplifier then the FSMF before driving the FSM.

WFS Control Electronics

Each CCD39 detector has a SDSUII controller. The WFS frame data is streamed from the SDSUII controller to the SDSU interface card housed in the SDSU VME Rack.

The SDSU VME rack contains a MVME167 processor card, two SDSU interface cards and two C40 Converter cards. Data passes from the SDSU Interface card to the Converter Card via a "Steward" port, allowing direct access to parallel digital data output without the data being transmitted along the VME bus.

4.5.6.2 RTCS DSP

The main processor used in the RTCS is the TI TMS320C44 DSP. They were chosen because:

- They are optimised for digital filtering.
- Each processor has four processor-to-processor bi-directional links and contains an 8 x 32bit FIFO buffer on input and output.
- Each communications port is connected to a separate on-chip Direct Memory Access (DMA) engine which may be programmed to move data between the communications port and memory without further programme intervention. With suitable hardware the communications ports can be used to transfer data to or from external systems as well as between c40s.
- They have separate instruction and data buses.
- JTAG scan chain hardware for external debugging access to processor registers and hardware breakpoints. It is possible to set up synchronised hardware breakpoints on several processors.

4.5.6.3 RTCS DSP Architecture

Figure 4.26 shows the connections of the c44 ring structures and communications. The DSPs contained within the WFS Loop are labelled 1-8 whereas the DSPs contained within the SG Loop are labelled 11-18. Together with the software architecture the ring structure enables the real-time processing requirements to be fulfilled with fewer DSPs than with an equivalent farm architecture. The development overheads were also reduced.

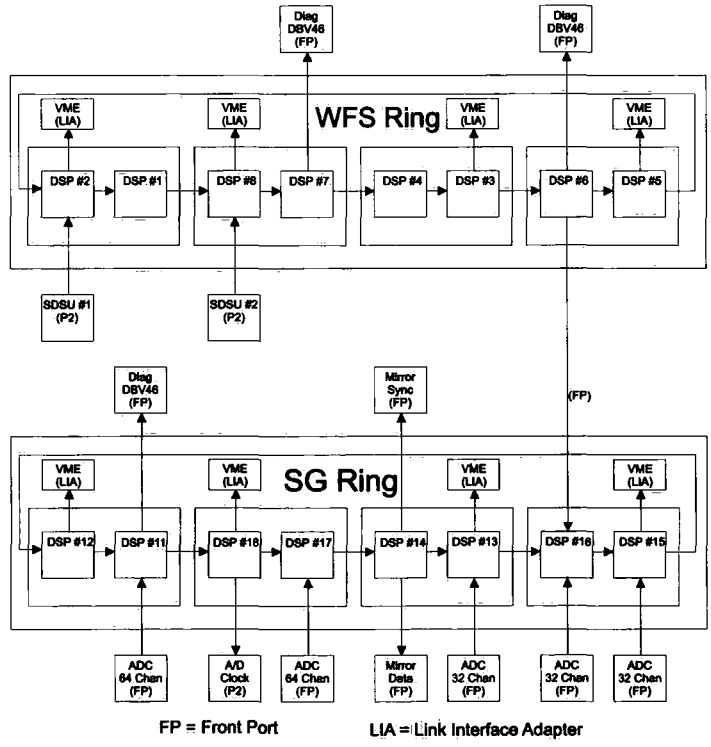

Figure 4.26 *NAOMI RTCS Processor Architecture*

4.5.6.4 RTCS Real-time Pipeline

Figure 4.27 displays the NAOMI RT pipeline. The SDSUII controller interleaves pixels from the quadrants of the CCD. The data from each quadrant therefore becomes available concurrently, starting at each corner and progressing by rows towards the centre. The RTCS determines the current readout mode of the CCD from the header data preceding each frame. It adjusts the size of the expected data transfer and the parameters of the signal-processing algorithm accordingly. Different modes support different numbers of subapertures and have different on-chip binning and skipping.

The RTCS processes the WFS pixel data to produce centroid estimates of the WFS spot positions, and therefore, estimates of the local WF slopes. This involves background subtraction and optional sky subtraction. The pixels are then divided into SAs.

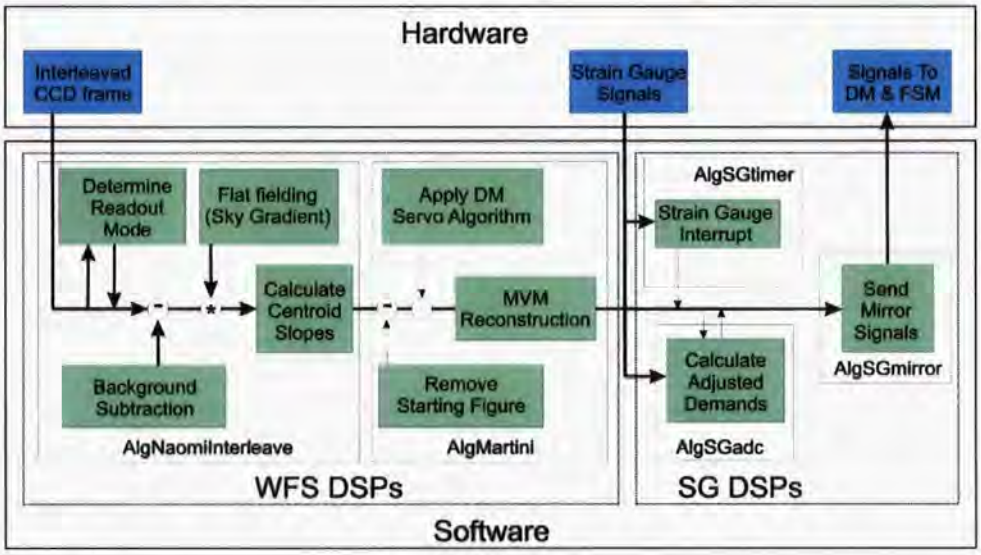

Figure 4.27 *Flowchart of the RT processing*

Generally there is one SA per DM segment but in some modes a SA covers several segments. If this is the case then the RTCS copies the centroid estimates as required. It proceeds by removing an optional calibrated DM offset from the WFS centroid estimates.

A servo algorithm is applied to the current estimator to update the current DM segment x-y slope demands. This is followed by a MVM of x-y slope demands. There is one x-y measurement per SA. The result of the MVM is a vector of piston values: one per SA.

DSP No.	Ring	Algorithm
1	WFS	AlgNaomiInterleave
2	WFS	AlgNaomiInterleave
3	WFS	AlgNaomiInterleave
4	WFS	AlgMartini
5	WFS	AlgNaomiInterleave
6	WFS	AlgNaomiInterleave
7	WFS	AlgNaomiInterleave
8	WFS	AlgNaomiInterleave

DSP No.	Ring	Algorithm
11	SG	AlgSGadc
12	SG	AlgSGadc
13	SG	AlgSGadc
14	SG	AlgSGmirror
15	SG	AlgSGadc
16	SG	AlgSGadc
17	SG	AlgSGadc
18	SG	AlgSGtimer

Table 4.11 *Algorithm running on DSPs*

The RTCS converts the x-y piston command for each mirror segments into the A,B,C equilaterally sectored actuator commands that are actually required to drive the mirror. The resulting command vector is the mirror input demand.

When SG feedback is operating, the RTCS compares the actuator input demand to a calibrated digitised sample of the SG voltages and adjusts the final demand to the DM using a servo algorithm. This algorithm samples and updates substantially faster than the WFS servo algorithm.

In total there are 5 different algorithms across the 16 DSP running the real-time control pipeline. Table 4.11 displays those algorithms.

4.5.6.5 RTCS Software Architecture

The software architecture fulfils the overall real-time requirements of NAOMI within the constraints imposed by the selected hardware. It is essential that both the WFS and SG processing must be performed with deterministic latencies, with timing uncertainties of no more than a few microseconds. Based on the readout time of the WFS, it was estimated that the performance will degrade if the latency exceeds 1ms. The faster the WFS readout the faster the WFS must execute. It is good practice for the WFS readout and WFS data processing to happen concurrently.

One requirement is that diagnostic, visualisation and logging activity should have no effect on the timing or dataflow within the latency critical processing.

Interrupt Service Routines (ISR) and Bulk Synchronisation Parallelism (BSP)

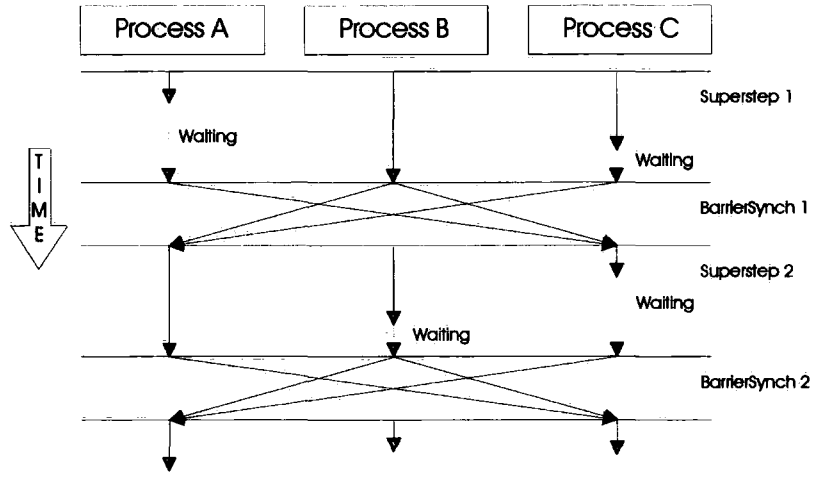

Figure 4.28 *Concept of Bulk Synchronisation Parallelism*

ISRs are used to perform latency critical data processing. They are normally invoked by an external interrupt signal such as the arrival of a new frame of WFS data or newly digitised strain gauge data.

NAOMI adopted selected aspects of the BSP methodology[255] to be used within their ISRs. Developed by Oxford University, this methodology gave ease of development and stability. Consequently there is no proprietary code within the real-time software.

The BSP methodology requires that all processes wait to communicate until a global synchronisation step. All processes wait for this step to complete regardless of whether they have anything to transmit or receive. The step is not complete until all interprocess communications have finished. The global progress of the parallel processing system is therefore divided into supersteps by these synchronisation barriers. Figure 4.28 illustrates the BSP concept. The BSP methodology is applied separately to the two rings of C44 processors.

LoveTrain (LT) and Cowcatcher System

The LoveTrain is a synchronous, interprocessor communications protocol created by Durham. It embodies Barrier Synchronisation and is required for use by the ISRs.

LTs use the ring of interconnections of the C44s to broadcast information between them. Each processor in the ring sends its own output information for broadcast (if any) to its downstream neighbour and then copies information from its upstream neighbour to downstream. The processor's output information is therefore copied right around the ring to the processor immediately upstream, which does not copy it further (i.e., information does not return, redundantly, to its origin). The LT implements the BarrierSynch because communication is global and cannot finish until all processes have started communicating. The expected quantity of data to be sourced, copied and removed by each processor is coordinated near the beginning of each ISR. This is done by an initial, special BarrierSynch which uses the first LT, after some initial interrupting words, to broadcast the anticipated number and size of LT contributions from each processor. The final BarrierSynch of each ISR is also special. It contains the *StopMessage*, which is used to decide if real-time processing should cease at the current interrupt. The *StopMessage* also implements the transaction system, whereby real-time parameter changes, which have been scheduled on several processors, all become effective at the next ISR.

The deleterious effects of most of the interrupt latency are overcome by arranging for a high degree of concurrency. Each interrupted CPU, whatever the cause of the interrupt, immediately sends to its downstream neighbour a single word on their connecting communications port. This has the effect of interrupting the neighbour promptly so that it will almost certainly have completed its interrupt latency before useful data could be sent to it. Because these interrupting words precede the first LT carrying operational data they are dubbed "Cowcatchers". The interrupt latency of the WFS ring is concurrent with the arrival and decoding of the WFS header and the processing of the first row of centroid data. The interrupt latency of the SG ring is concurrent with the conversion time of the SG ADCs. The ADC conversion is initiated by the SG timer CPU immediately on its timed interrupt.

The effects of processor interrupt latency are effectively eliminated by the use of DMA transfers for the interrupting WFS and SG data, combined with the Cowcatcher system.

General Purpose (GP) Messing System

UoD created an asynchronous GP message-passing protocol used for transmission of command and status information to/from the C40/C44 processors.

The diagnostics/visualisation activity effectively forms a background activity and clearly needs to use an interruptible, and therefore asynchronous, communications system to exchange data with external workstation processes. The physical medium for this background communication is the network of interconnecting communications ports. GP is well suited to retrieving status data and can also be used for sending commands to the C44s provided there is some means of synchronising the actual changes in real-time parameter states on different processes. This requirement is fulfilled by the transaction system.

GP message packets originating from a C40/C44 processor are forwarded from processor to processor according to a destination address embedded within the packet. Other internal data fields further identify their contents. Diagnostic data packets arriving at the diagnostic C40 (GP number 9) are placed in a shared memory buffer, ready for transmission via the VME bus to the VME host. Other packets typically travel via Link Interface Adaptors (LIA) to the VME host. Either way, the server process, running on the VME host, embeds the GP packets within appropriately addressed TCP/IP packets for onward transmission via the internet. The server process also performs a reverse procedure, extracting GP packets from TCP/IP wrapping and forwarding them via LIAs into the C40/C44 network.

The ISR code cannot use the GP system directly for interprocessor communications. Firstly, this is because GP is not synchronous and would not meet the processing latency requirement. Secondly, in the context of an ISR the GP system will have been interrupted by the ISR code and such a protocol could hardly be made re-entrant without a significant loss of efficiency.

The communication port links used by the ISRs to transmit LTs can also be used by the GP system outside of the ISRs. This is achieved by insisting that the two protocols travel in different directions on the bi-directional links. This is possible because each link direction has its own FIFO buffer system.

Parameter Block Transactions (PBT)

PBTs implement the synchronised changing of real-time parameters and even algorithms ring-wide. Essentially a set of changes can be queued up in advance on each CPU in a ring and then made active simultaneously on a particular interrupt. The queuing of changes is accomplished by the GP commands of the *RT_CLASS* and can be activated by either C or Python workstation programs, but is most elegantly implemented in python, where a single Python function call can carry out a very complex ring-wide transaction.

Data Transfer Mechanism (DTM)

The DTM, developed by the NCSA, is the system that is used for message passing. It is layered on the TCP socket libraries and provides a relatively simple message passing API for use between (potentially remote) processes. The DTM API allows the destination port to be named either via an IP address/port (which can be in symbolic or numeric form) or using a *name,* which is known to the TCP/IP Domain Name Server (DNS) system. Such names are translated using a *Nameserver* process, which also allows names to be registered (by association with IP address/ports). One *Nameserver* process can serve several machines. All the machines that share the *Nameserver* must "know" the IP/port address on which it can be contacted.

The GP commands from workstation clients are wrapped in DTM packets addressed to `c40Comms`, which then extracts the GP command and forwards it via an LIA to the C40 network. The reverse process happens to a reply GP message from the C40s to a workstation client.

DTM communication always begins with a freeform text *header* message followed by a number of binary *data* messages. The header generally serves to describe the format and contents of the data packets. Although the header is freeform in a sense, its contents must normally be parseable in order to achieve automatic data description. GP messages are very straightforwardly copied into DTM data. DTM is also used for communication between workstation applications and display tools and these re-use some of the DTM header conventions. New-style commands are sent over DTM as python embedded into the data packet with "meta data" in the header describing the reply and acknowledge addresses.

4.5.7 Additional NAOMI Software

An overview of the software structure is given in Figure 4.29.

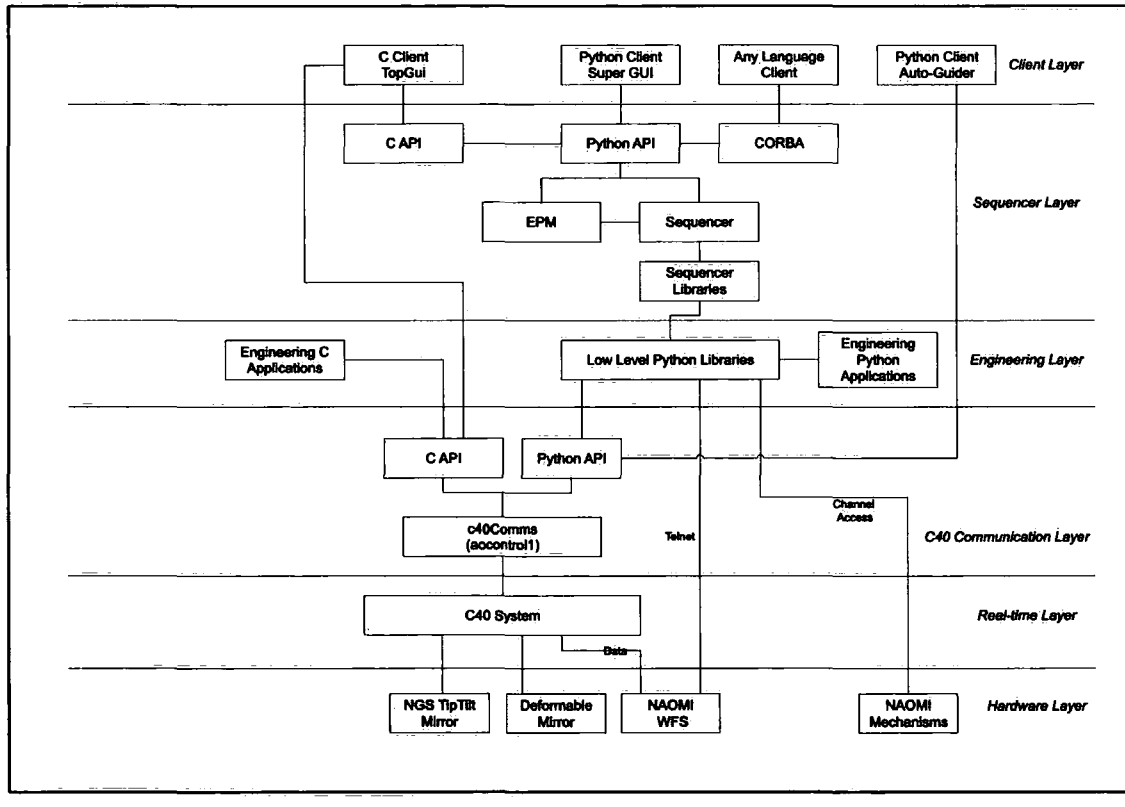

Figure 4.29 *NAOMI Software System Overview*

In addition to the C40 and WFS Controller software, then are additional layers of real-time and non real-time software.

4.5.7.1 Real-time Mechanism Control Software

The real-time software which controls the instrument electro-mechanical NOT components, was written using open source 'Experimental Physics and Industrial Control System' (EPICS)

software tools. Embedded 68k and PowerPC (PPC) processors hosting VxWorks run EPICS code to send and receive control and status signals from a number of input/output cards connected to a VME backplane.

4.5.7.2 NAVIS Software

NAVIS, located in the WHT Control Room, is the Sun Workstation used to host engineering and user applications include EPICS Display Managers, the UoD Sequencer, the UoD TopGUI display and command GUI and other user applications for Astronomers. The NAOMI software source tree was delivered with NAVIS, thus NAVIS acted as a development platform. NAVIS's graphics card was capable of displaying legacy 8-bit displays simultaneously with 32-bit displays.

Top GUI

TopGUI is an engineering application used to send control commands and review diagnostic data. It is used both for calibration and observing. TopGui consists of two panes. The fixed right pane displays WFS display; Figure 4.30. The left pane is selectable from about 10 GUIs. The mirror control and diagnostic pages are displayed in Figure 4.30b and c respectively.

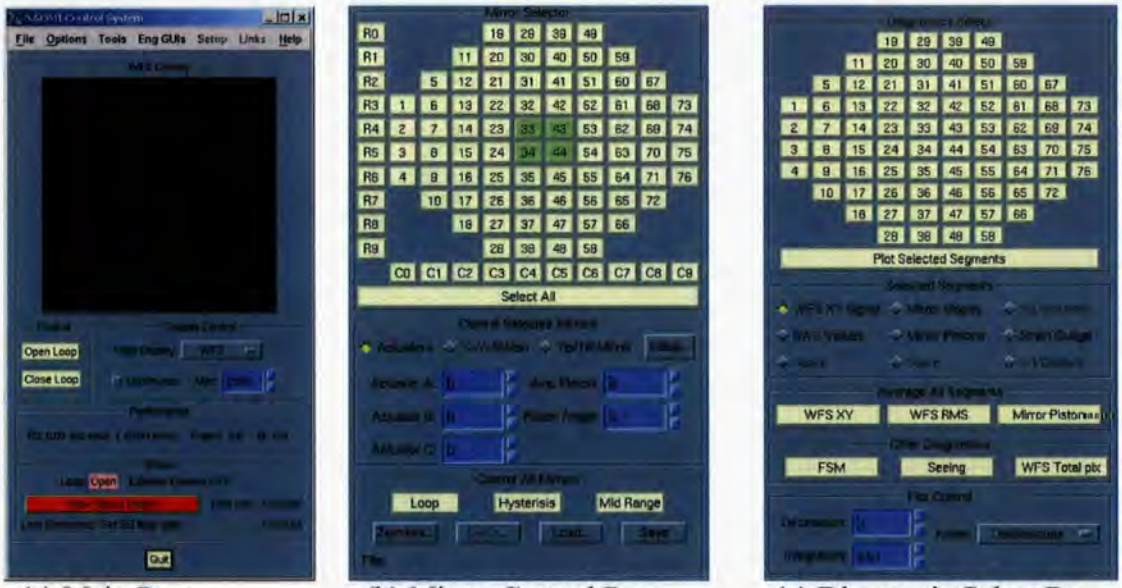

(a) Main Page (b) Mirror Control Page (c) Diagnostic Select Page

Figure 4.30 *TopGui Pages*

NAOMI Sequencer and Electra Process Monitor

The NAOMI Sequencer is a process used to order and track various commands sent to the NAOMI subsystems, preventing two commands being issued to a subsystem at the same time, which could produce an error condition. Every command sent to the sequencer has an Electra Process Monitor (EPM) tag, holding the full status of the relevant command. TopGui, which uses the EPM, creates and frees tags as it sends commands to the NAOMI sequencer. The EPM process is a state monitor that stores the status of various parameters.

Python Scripts

There are two types of Python Scripts residing on NAVIS, scripts which directly communicate with the RTCS and higher level 'Super scripts', which execute a sequence of commands using the sequencer.

4.5.8 Instrument Calibration

Instrument Calibration is a three-staged process which involves DM flattening, Segment Cophasing and Simplexing.

4.5.8.1 DM Flattening with the FISBA Interferometer

Additional optics was placed on the NOT to allow the use of a FISBA Interferometer to obtain a flat DM. The system comprises of a μPhase Fisba Interferometer fed from a stabilised HeNe laser with mono-mode fibre output, expanding optics, a double-pass folding mirror and a PC containing a FISBA ISA interface card and running dedicated software.

Monochromatic light passes through a fibre optic from a HeNe laser positioned on the gantry above the optical bench to a small unit containing a mirror and a camera. The light is expanded and collimated to a footprint, which covers the DM. The light reflects as follows: NAOMI folding flat, Fisba flat, NAOMI folding flat, FISBA flat, DM, NAOMI folding flat, Fisba flat, NAOMI folding flat and finally enters the interferometer device.

The Fisba PC grabs interferometric images of the DM and automatically sends the data to NAVIS using File Transfer Protocol (FTP) during the flattening process on request. The user can either attempt to flatten the mirror manually using individual commands or by running an automated script. Often the user has to use individual commands to place the segments at an approximate position for the automated script to be successful.

The double pass system is susceptible to vibration, therefore the NOT has to be floated, using pneumatic legs, during the flattening procedure. An analogue Video display of the DM is also available in the control room.

4.5.8.2 Segment CoPhasing

The interferometer cannot detect the segmented piston outside a relative range of $\pm\frac{\lambda}{4}$, therefore adjacent segments could be displaced by a factor of $\frac{n\lambda}{2}$. Cophasing is achieved by using sheered lenslets with respect to the DM segments. The lenslet wheel contains both a X-displaced and Y-displaced lenslet (overlapping two segments). This process is now automated with the use of scripts. During commissioning, only one of these lenslets was available and the SDM was physically displaced to achieve the same effect. Unfortunately moving the SDM caused alignment issues.

4.5.8.3 Simplexing – Removal of Non-Common Path Errors

After a successful Cophasing procedure, the final calibration procedure is to check the ability to remove non-common path errors from the science instrument images of the calibration source with the control loop open and closed. This determines the attainable image quality.

The removal of the non-common path errors is accomplished using a variant of the simplex "hill-climbing" techniques employing metrics computed from either the science camera, in the case of INGRID or a dedicated simplex camera, in the case of OASIS. The procedure optimises the base figure of the DM, whose associated off sets are stored in a file and uploaded and used in the RTCS.

4.6 AO Performance on the WHT

The measured on-sky corrected FWHM for a range of observed wavelength using various magnitude guide stars for seeing of 0.7 " and 0.5 " are tabulated in Table 4.12 and Table 4.13 respectively. Z, J, H and Ks bands were obtained using INGRID while B/V, R and I were measured with OASIS.

Guide star	B/V (0.5 μm)	R (0.65 μm)	I (0.82 μm)	Z (1.05 μm)	J (1.25 μm)	H (1.65 μm)	Ks (2.15 μm)
<= 8	0.3	0.3	0.3	0.3	0.25	0.15	0.15
9							
10	0.5	0.4	0.3				
11	0.4	0.4	0.35		0.25	0.2	0.2
12	0.5	0.5	0.5		0.3	0.3	0.3
13					0.4	0.4	0.4
14	0.5	0.6	0.5		0.4	0.4	0.4
15	0.5		0.5		0.4	0.4	0.4
16			0.5				

Table 4.12 *Natural Seeing 0.7"(median for La Palma)*

Guide star	B/V (0.5 μm)	R (0.65 μm)	I (0.82 μm)	Z (1.05 μm)	J (1.25 μm)	H (1.65 μm)	Ks (2.15 μm)
<= 8	0.2	0.2	0.15		0.2	0.15	0.15
9	0.25	0.2	0.2				
10							
11	0.40		0.30			0.2	0.2
12						0.2	0.2
13						0.3	0.25
14						0.4	
15						0.4	

Table 4.13 *Natural Seeing 0.5"*

The performance and results given here were 'best performance' measurements which have been slowly improved over the last 5 years.

4.6.1 INGRID Performance

Figure 4.31 shows an image of the N6543 planetary nebula in Paschen beta taken in May 2002. The 600 s exposure shows an AO correction from 0.7 " to 0.2 " at a wavelength of 1.2 μm. A V=11 central star was used as a wavefront reference. The finest structures visible in the nebula are ~ 0.3 " across; with the image being 19 " in height.

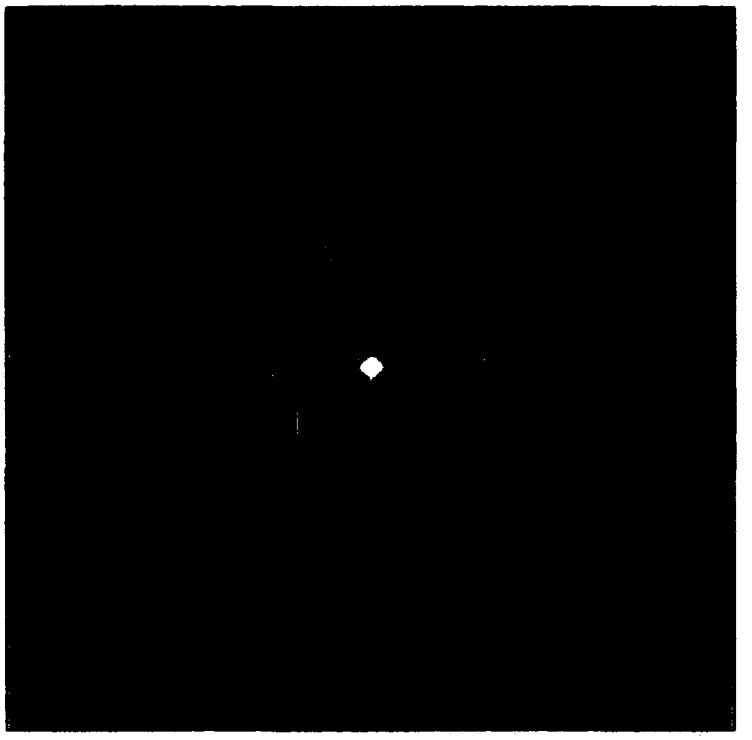

Figure 4.31 *N6543 planetary nebula in Paschen beta*

4.6.2 OSCA Performance

Figure 4.32 shows the reduced data for one of the commissioning targets, HD150451AB obtained by INGRID during the May 2002 run. The image reveals the later-identified cool white dwarf companion HD150451C.[256]

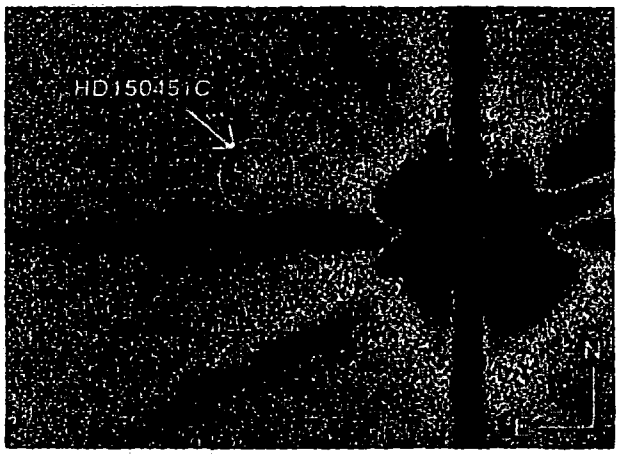

Figure 4.32 *NAOMI+OSCA image of HD150451C*

4.6.3 OASIS Performance

Figure 4.33 shows an I-band image of a 0.36 " binary star taken with NAOMI/OASIS in July 2004. The FWHM of the open loop image is 0.7 " is compared with 0.3 " when the loop is closed.

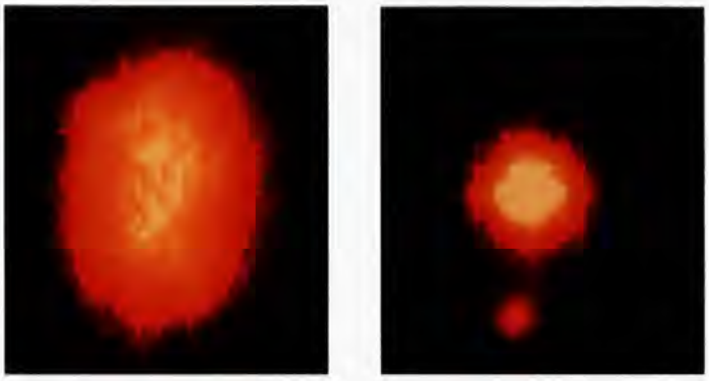

Figure 4.33 *NAOMI and OASIS Image of a binary star in the I-band*

4.6.4 GLAS Performance

Figure 4.34 shows comparison of H-band images of Uranus with GLAS and adaptive optics correction off (left) and on (right). The faint point at the bottom is the moon Miranda, which has moved aproximately 0.7 arcseconds between the times both images were taken.

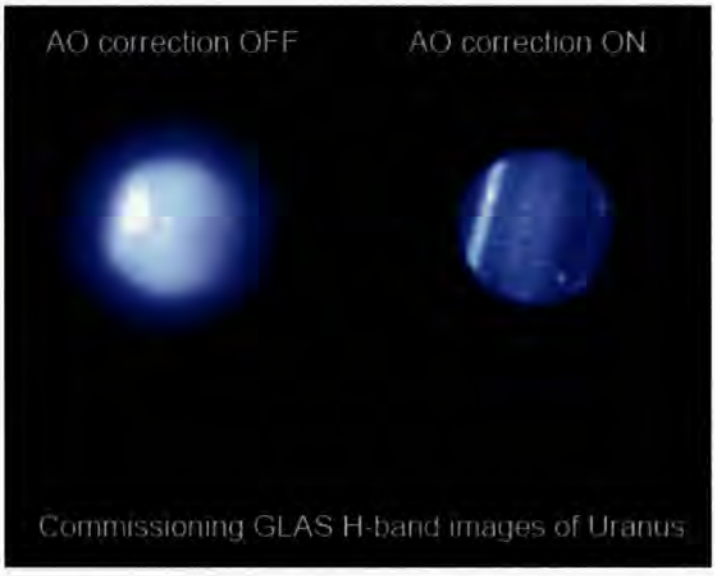

Figure 4.34 *GLAS Commissioning Images*

5 Characterisation Experiments

This chapter describes the NAOMI characterisation work conducted between July 2002 and December 2004. The effort includes separate investigations to characterise the temperature stability of GRACE, the performance of the FSM, the SDM, the WFS and the bandwidth and latency of the RTCS. Acknowledgements are contained within Table 5.1.

Characterisation was required to estimate the potential gains in optimising the RTCS. The following important realisations were apparent from the offset:

- The RTCS control hardware required upgrading before any significant optimisation controller algorithms could be implemented.
- A number of other system improvements (such as GLAS) would give greater benefits to NAOMI than optimising the RTCS.
- Hence, producing an optimised controller was low priority for the ING.
- There would be greater benefits of the optimisation the RTCS with the introduction of GLAS.

The aim of the characterisation experiments was to gain sufficient information from each subsystem to estimate the level of potential improvement an optimised controller could give. A further aim was to produce system-level information on wavefront error degradation and latency.

Characterisation	Start Date	End Date	Acknowledgements
GRACE	December 2003	December 2003	Doug Gray (ING) Sebastian Els (ING)
FSM	January 2004	May 2004	Andy Hide (ING) Olivier Martin (ING) Tom Gregory (ING) Roy Ostensen (ING) Chris Benn (ING)
SDM	July 2004	December 2004	Richard Myers (Durham)
WFS	November 2003	February 2004	Ilona Sochting (ING) Xiaofeng Gao (ATC) Simon Tulloch (ING)
RTCS	July 2002	November 2003	Richard Myers (Durham)

Table 5.1 *Characterisation Experiments Acknowledgements*

5.1 GRACE Characterisation

Between 1st and 5th December 2003 the author performed a number of temperature stability tests.

5.1.1 Temperature Monitoring Equipment

There were four separate systems used to measure temperature during this period, the TREND system, the Monacor temperature probes, the NAOMI DM temperature probes and a Technoterm 7200 mobile probe. Figure 5.1 shows the TREND IQ 204 controller unit and the Monacur DTM 506.

Figure 5.1 *TREND IQ 204 controller unit and the Monacur DTM 506*

5.1.1.1 TREND Monitoring System

Installed in GRACE is the TREND Air-conditioning system, which continuously monitors both temperature and Relative Humidity (RH). The monitor system contains three temperature and two humidity sensors. One temperature sensor was placed on the roof, one placed in the air duct taking air from the Electronics Room to the roof and the other placed in the air duct taking air from the Optics Room to the roof. These are referred to as GRACE Roof Temp (TREND), Electronics Room Temp (TREND) and Optics Room Temp (TREND) respectively. The two TREND RH sensors were placed in the electronics room and optics room.

The Electronics Room (TREND) and Optics Room (TREND) temperatures were logged every minute whereas the GRACE Roof (TREND) temperature was logged every 15 minutes. The system recorded the RH of both rooms at a minute interval.

A trial version of TREND analysis software was installed on a laptop to continuously log the temperature and humidity data. The data were recorded into a binary file (.mdb) and reformatted into ASCII format and examined.

5.1.1.2 Monacor Temperature

Two temperature probes were connected to a laptop via a Monacor DTM 506RS recording system. The temperature sensors were moved around the optical bench, recording temperatures of various components as shown in Table 5.2. The system records temperature every ten seconds and stores the data into an .xls file.

Date	Temp Sensor 1 (Monacor)	Temp Sensor 2 (Monacor)
1st December 03	Above Optical Rail (AT)	DM (Casing)
2nd December 03	Near Folding Flat (AT)	Near OAP 2 (AT)
3rd December 03	Inside WFS Entrance (AT)	Near WFS Detector (AT)
4th December 03	Inside WFS Entrance (AT)	Near WFS Detector (AT)
5th December 03	OAP1 (Casing)	Folding Flat (Casing)

(AT) = Air Temperature

Table 5.2 *Position of Monacor Temperature Sensors*

5.1.1.3 NAOMI DM Temperature Sensors

There are two temperature sensors within the DM; referred to as DM Temp 1 (NAOMI) and DM Temp 2 (NAOMI). Measurements were taken by running the *SG GetTemperature* python script.

A script was written to log the temperature to an ASCII file at ten-second intervals for the first two days and then at two minute intervals.

5.1.1.4 Technoterm Mobile Probe

This mobile probe was mainly used for calibration. It was used to record the temperature in various locations within the DOME and GRACE on the 4th December, see section 5.1.2.4.

5.1.2 Results

Initial experiments were conducted for calibration to test the reliability and reproducibility of the temperature probes. The key results are:

- At 10 °C the Technoterm mobile probe and the Monacor probe varied by about ±0.1 °C.
- The Technoterm mobile probe was reliable to ±0.2 °C when conducting temperature tests inside the dome.
- The GRACE Roof Temp (TREND) sensor was found to have a reading of 1 °C higher than its surrounding temperature. Either it produces its own heat or has heat transferred from its cable.
- The accuracy of the other (TREND) sensors and the DM (NAOMI) sensors could not be directly determined. Data analysis infers that:

  The Optics Room (TREND) sensor must be accurate to at least ±0.3 °C.

  The DM sensors are estimated to be accurate to ±0.2 °C by comparing data between the Monacor probes and the DM (NAOMI) sensors.

Each system records data at different intervals and times. Data was timestamped and appropriate shifts were made to align the data. The start point for each graph is Midday. Each graph contains 24 hours worth of data and has been labelled the day the data recording started.

5.1.2.1 1st December 2003 Actions, Results and Observations

The data gathered for 1st December 2003 is graphically displayed in Figure 5.2.

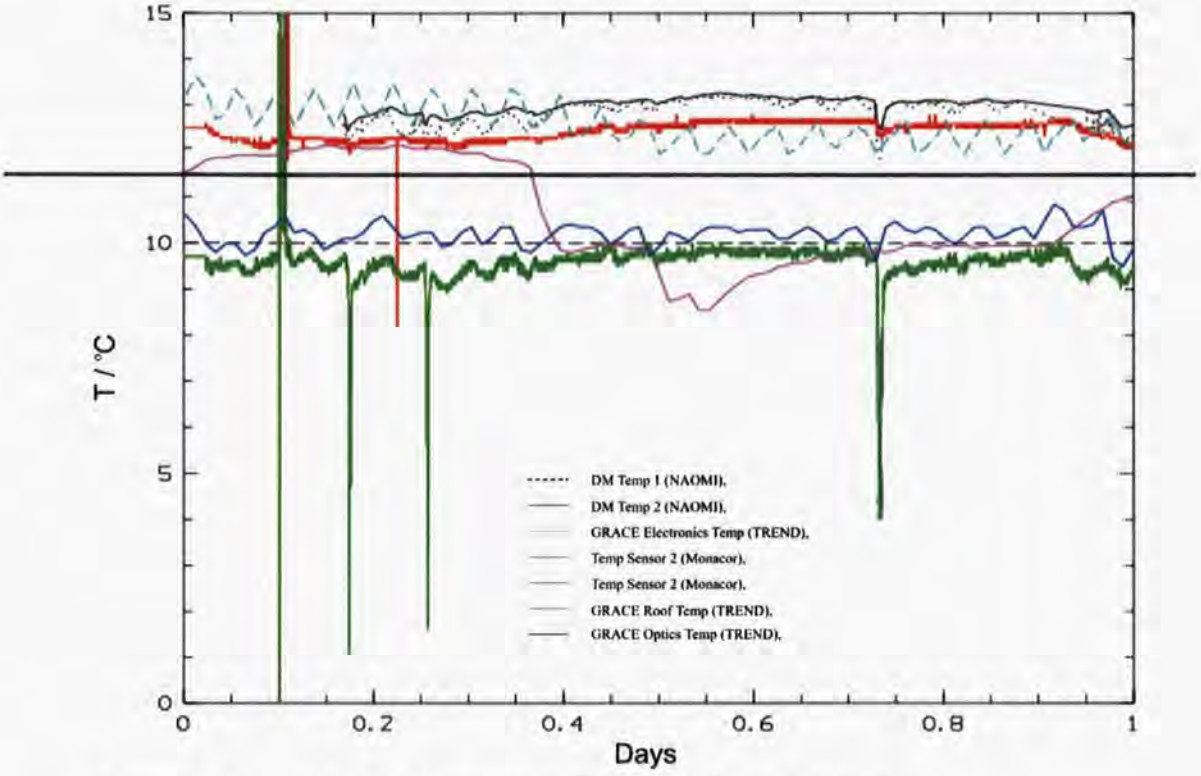

Figure 5.2 *Plot of the Temperature Data for 1st December 2003*

Actions

- The temperature of the Electronics Room was lowered from 13 to 11 °C.

Observations

- The GRACE Electronics Temp (TREND) oscillates over 1 °C every 64 minutes. The oscillation mirrors the oscillation found within the chiller unit (stored externally).
- The GRACE Electronics Temp (TREND) doesn't reach its 11 °C set point. This is because the fan speed was set to 40%, which is inadequate to cool the room to 11 °C.
- The DM temp (NAOMI) sensors and the DM Casing (Monacor) sensor follow the same trends.
- The DM Casing (Monacor) temperature is 0.5 °C cooler than the temperature read by the DM temp (NAOMI) sensors. The DM acts as a heat source. The DM temp is 2-3 °C above the air temperature.
- The DM temp (NAOMI) sensors stay within 0.2 °C of each other.
- The first big spike should be ignored, it was produced during sensor installation.
- The INGRID and OASIS cryostats in GRACE are filled three times a day and are indicated by the other big drops in the GRACE Optics Room Temperature. The temperature eventually stabilises at ~10 °C after ~15 minutes.

5.1.2.2 2nd December 2003 Actions, Results and Observations

The data gathered for 2nd December 2003 is graphically displayed in Figure 5.3.

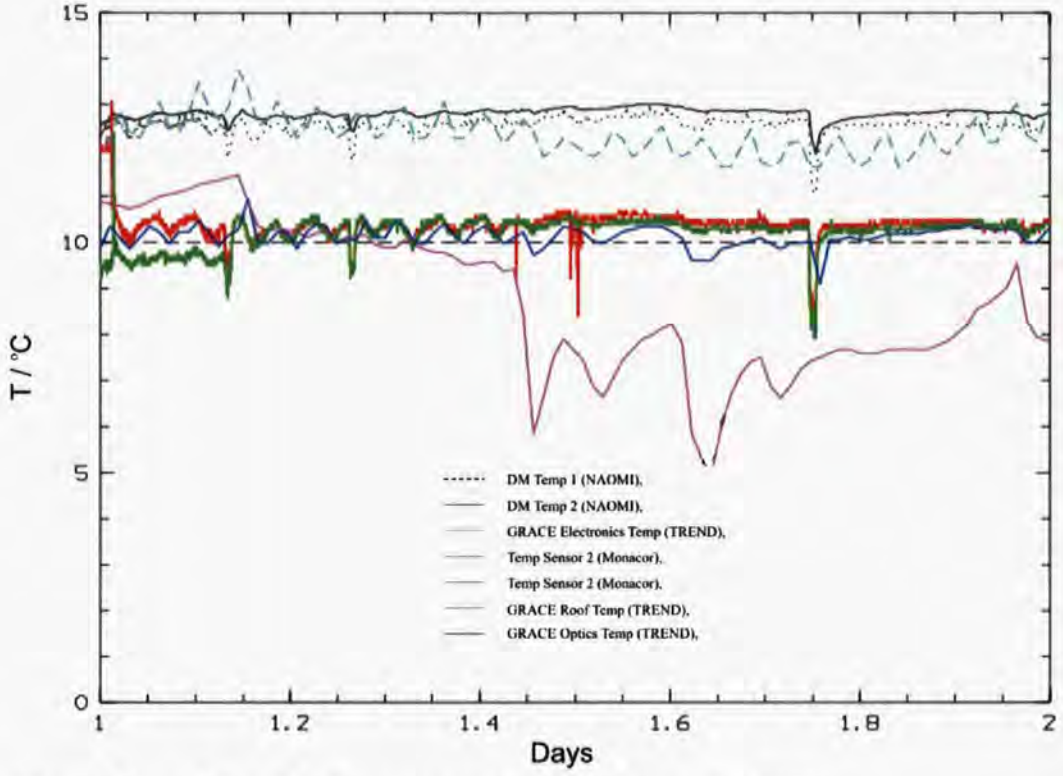

Figure 5.3 *Plot of the Temperature Data for 2nd December 2003*

Actions

- The Roof sensor was placed facedown on the roof of GRACE.

Conclusions

- The dome temperature drops significantly once the Roof Sensor was placed on the roof of GRACE.
- When moving the Monacor probe from the bench to 30 cm above the bench, the temperature reading increased by 0.5 °C. This was verified later with the Technoterm.
- The cause of the small spikes recorded by DM Temp 1 (NAOMI) is unknown.
- Filling the INGRID and OASIS cryostats caused less of an effect than the previous day.

5.1.2.3 3rd December 2003 Actions, Results and Observations

The data gathered for 3rd December 2003 is graphically displayed in Figure 5.4.

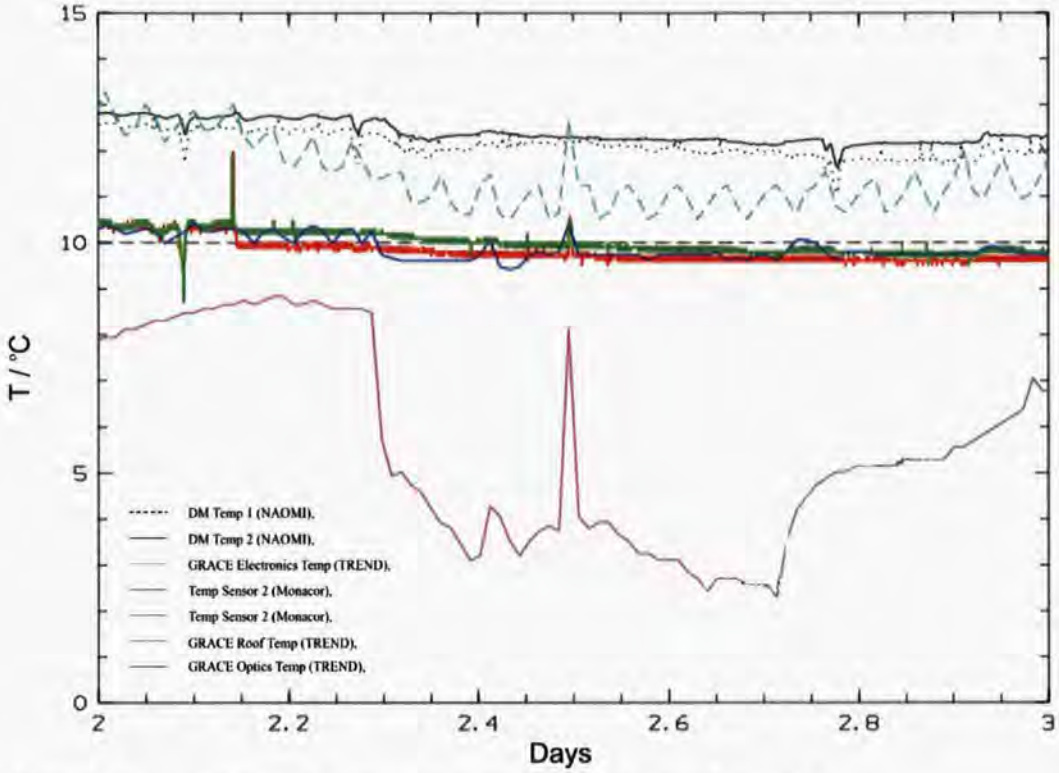

Figure 5.4 *Plot of the Temperature Data for 3rd December 2003*

Actions

- The speed of the fan in the Electronics Room was increased to 50%.
- The DM was flattened using FISBA and examined over a 24-hour period.
- The Dome sensor again was moved. It was placed further away from its housing face-down on the roof on GRACE.

Observations

- After 24 hours the DM gained on average one fringe per segment.
- The Monacor probes were placed inside the WFS and over a period of 17 hours converged from 0.3 °C to 0.15 °C.
- The Electronics Room temperature lowered to 11 °C, but still oscillated.
- There is an unexplained peak in the temperature of all 3 TREND sensors.

5.1.2.4 4th December 2003 Actions, Results and Observations

The data gathered for 4th December 2003 are graphically displayed in Figure 5.5.

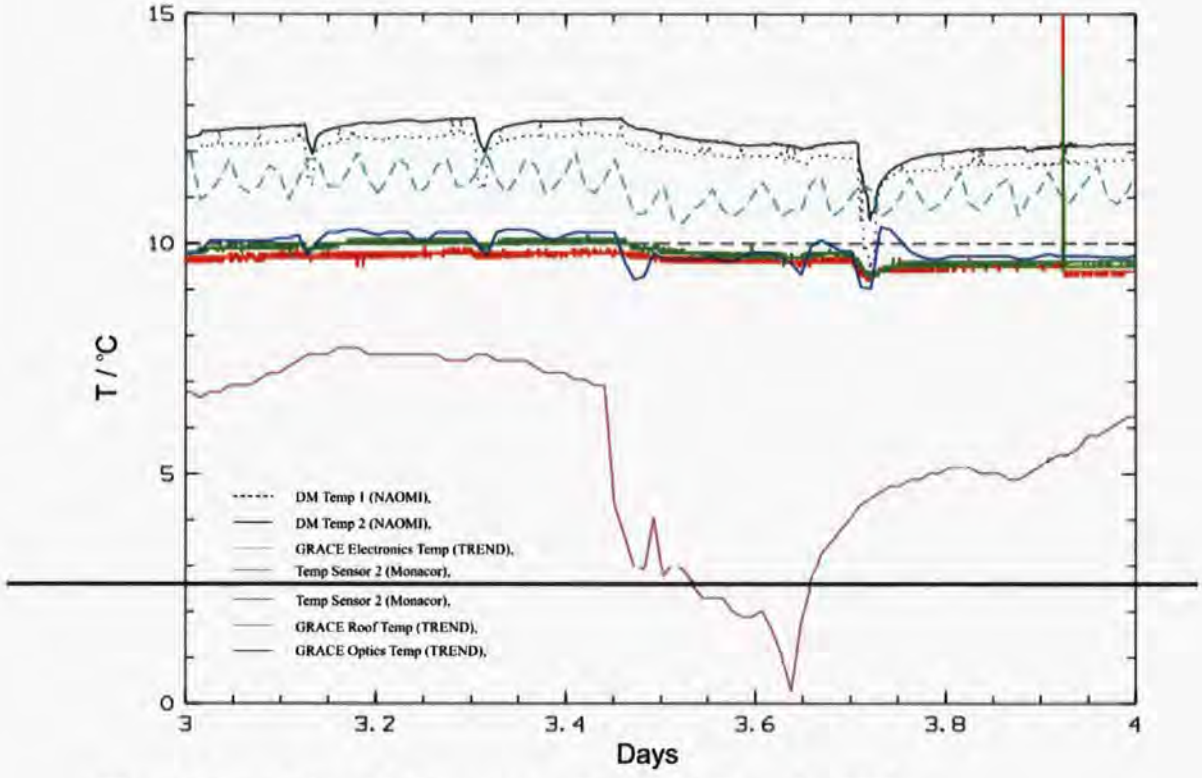

Figure 5.5 *Plot of the Temperature Data for 4th December 2003*

Actions

- The derotator aperture was covered to minimise heat loss.

The Technoterm mobile probe was used to record different temperatures (°C) as shown in Table 5.3.

Location	Temp (°C)	Probe
Dome Air Temperature (met probe)	3.3	met sensor
Dome Air Temperature (cass)	4.3	Technoterm probe
Dome Air Temperature (dome floor GRACE)	4.0	Technoterm probe
Dome Air Temperature (dome floor GHRIL)	3.9	Technoterm probe
GRACE Roof Air Temperature	4.3	Technoterm probe
GRACE Roof (mob probe)	5.3	Technoterm probe
GRACE Roof (TREND sensor)	6.3	TREND sensor
GRACE TREND sensor case	6.3	Technoterm probe
Temp Sensor ECS box	6.6	Technoterm probe
Electronics Room Air Duct (OUT)	10.0	Technoterm probe
Electronics Room Air Duct (IN)	9.0	Technoterm probe
Optics Room Air Duct (OUT)	9.0	Technoterm probe
Optics Room Air Duct (OUT)	10.0	Technoterm probe

Table 5.3 *Independent Temperature Measurements*

5.1.2.5 5th December 2003 Actions, Results and Observations

The data gathered for 5th December 2003 is graphically displayed in Figure 5.6.

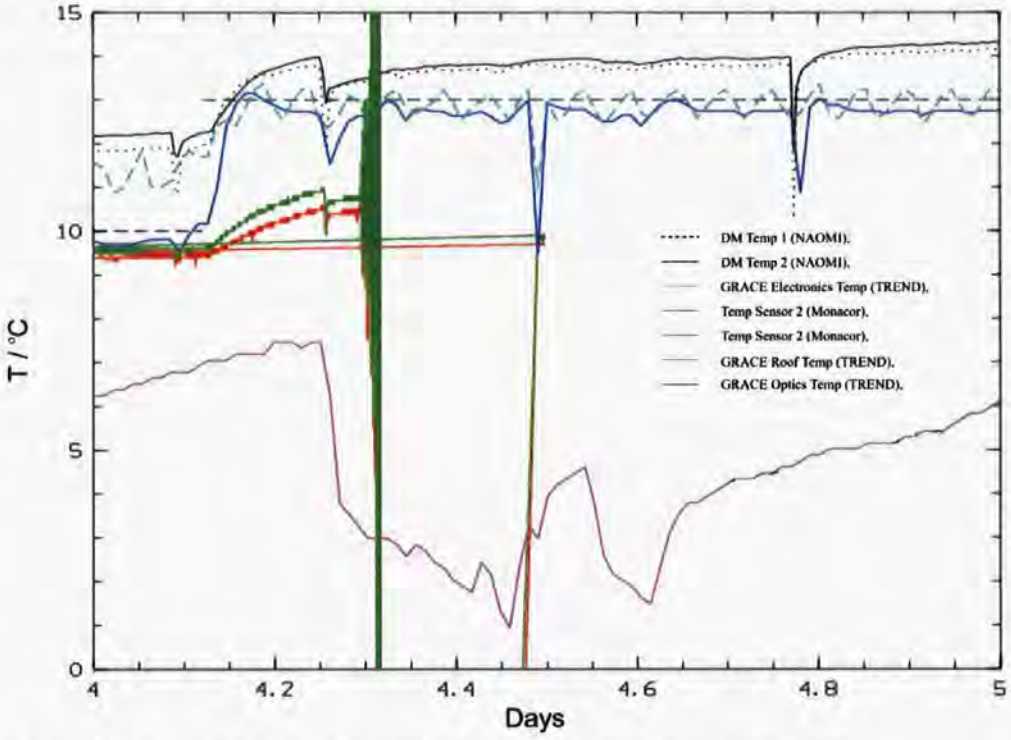

Figure 5.6 *Plot of the Temperature Data for the 5th December 2003*

Actions

- The temperature of the Electronics and Optics room was set to 13 °C.

Observations

- It took about 90 minutes for the Optics and Electronics room to stabilise at 13 °C.
- It took about 200 minutes for the DM temperature to rise and stabilise at 14 °C.
- The difference between the DM and the air temperature reduced to about 1 °C from 2.5 °C.
- The Monacor system drained its batteries.

5.1.3 GRACE Characterisation Conclusions

The main conclusions from the GRACE Characterisation are:

GRACE

- Stable to within ±0.5 °C.
- Slight dependence on temperature of dome, if Temp ≤7 °C (See Figure 5.7).
- Roof 1.0 °C higher than Optics Room Temp.
- No temperature gradient between GRACE and GHRIL side of the dome.

NAOMI

- Temperature of the bench is 0.5 °C less than air temperature above bench.
- Air temperature 30 cm above bench is 0.5 °C less than room air temperature.
- The DM is a heat source and is ~ 3 °C higher than room at 10 °C and ~ 1 °C higher than room at 13 °C.
- There is no temperature gradient within the WFS.
- The impact of filling is minimal; it takes about 15 minutes for the room to stabilise.
- It takes between 3-4 hours for the room to reach equilibrium when increasing the room temperature by 3 °C.

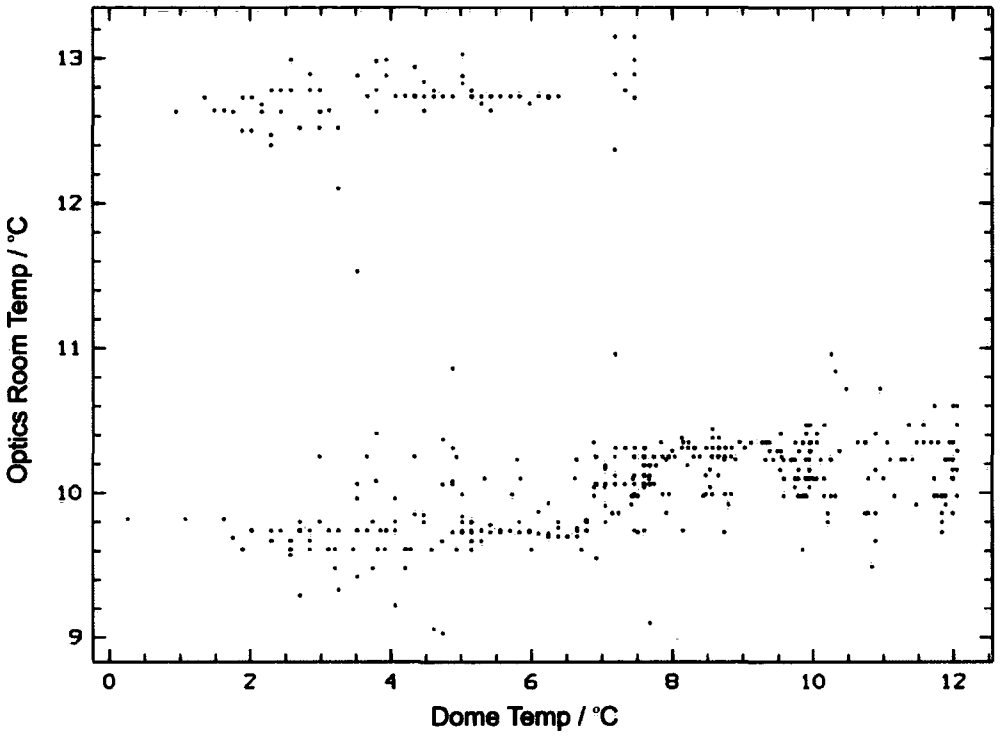

Figure 5.7 *Correlation between the Optics Room and Dome Temperature*

Follow on Actions:

- The experiments led to the design of a remote Cryostats filling system.
- The ING investigated the ideal setpoint of the optics room given the trade-off between IR and optical observation.
- The ING planned on further investigations, understanding through experiment the effects of having a temperature gradient between the bench and the light path.
- The ING considered insulating the bench from the ground by using balls of an insulating material to reduce the gradient between the bench and the ground.
- Further GRACE stability tests were postponed as the characterisation investigation revealed that NAOMI's environment was no longer varying by over 10 °C during an observing night.

5.2 FSM Characterisation

Between January and May 2004 the author investigated the performance of the FSM.

On the 15th January 2004, the ING made the decision to investigate NAOMI's performance limitation on bright stars. This was to be done with the aid of a tip/tilt simulator. The first stage of the investigation was to obtain the response curve of the FSM mirror, hence characterising its performance before examining the performance of the SDM.

5.2.1 Main Characterisation Equipment

Unfortunately, the NCU#2 didn't have a tip-tilt injector (TTI), and therefore additional equipment was required. The NCU#2 was driven to one limit and was deactivated to prevent damage through accidental use. A temporary TTI consisting of a white-light source and vibrating pinhole was placed at the f/11 focus. A photosensor was located at the other side of the FSM to measure its response. A video camera was placed at the science focus just before the INGRID position and was used for real-time viewing of the oscillating spot.

A dedicated laptop containing Matlab and the signal analyser extension Siglab was used to generate and capture signals. Input signals came from the photosensor, the FSM and the FSM Filter as required.

5.2.2 Initial Experiments (Jan 04)

The TTI was aligned and the system was calibrated. When the FSM was tipped 0.5" in x, the spot moved by 9 degrees along the WFS x axis and when the FSM was tipped 0.5" in y, the spot moved by 3 degrees along the WFS y axis. Both were measured using the WFS alignment tool.

The initial experiments revealed a serious problem with the FSM. With a flat mirror in front of the DM, the pinhole stationary and the AO loop closed, the FSM oscillates, instead of remaining stationary. The frequency and amplitude of the oscillations depended on altering a number of system parameters such as integration time, the DM gain, the TT limit and the FSM gain. A plot of integration time against frequency is shown in Figure 5.8. The power spectrum of the signal sent to the FSM X axis was also analysed. Closing the loop on a stationary pinhole revealed the characteristics of an unstable system.

These initial experiments suggested that the FSM was introducing tip/tilt errors into the system, forcing the DM to correct for them in normal operation. This helped explain why there was no apparent benefit in changing lenslets for different seeing conditions.

Shortly after the initial investigation, NAOMI went back on sky and was achieving optical correction of between 0.8 – 0.5 arcsec FWHM, implying that the FSM problems weren't new. Indeed switching the FSM off (FSM gain = 0) gave the same level of correction on sky.

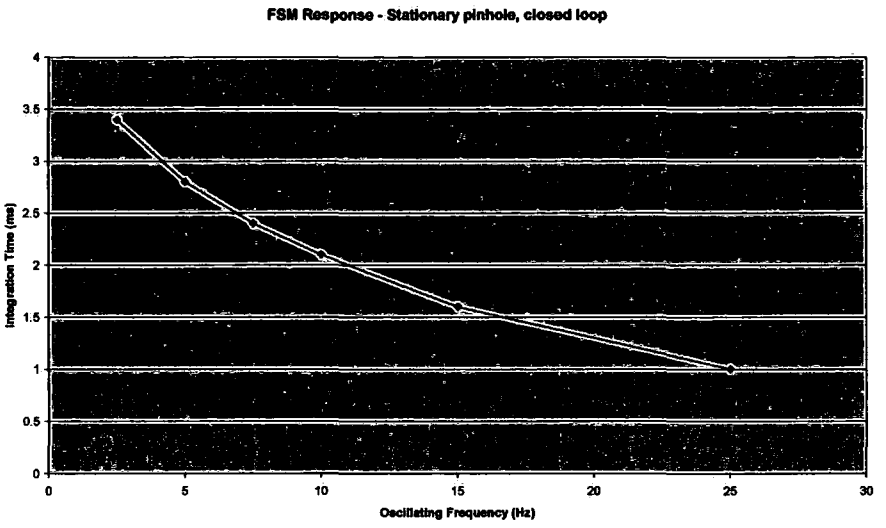

Figure 5.8 *FSM Frequency Response (Integration Time vs Frequency of Oscillation)*

The investigation changed focus. Instead of finding NAOMI's performance limitation on bright stars, the NAOMI team's task was to understand why the FSM was causing problems and to resolve them. Full characterisation was required.

With each WFS iteration taking 8ms (2ms exposure time + 6ms overhead), the AO loop should run at around ~120Hz. In each cycle, the full correction signal was sent to the DM, and the FSM was sent the mean tip/tilt applied to the DM segments on the previous iteration. Hence useful frequency response of the FSM should be ~ 10x slower, ~12 Hz at 0 db correction. The instrument had been engineered for the FSM to work at 20 Hz at 0 db correction.

The next phase of the investigation was to remove the FSM hardware from NAOMI and to test it in isolation.

5.2.3 Initial Testing of the FSM Hardware (Feb 04)

After a few days of testing in early February, the NAOMI team confirmed that the FSM and Zeiss drive electronics were behaving as expected. By optically encoding the mirror position, test results agreed with figures presented in Zeiss's acceptance test report. Phase lag was approximately 1.5 ms at 20 Hz. Tests indicated that the capacitative transducer system wasn't working and was switched off at the time. It was later discovered that the on/off switch had been mistakenly inversely labelled in delivered documentation.

The NAOMI team then turned their attention to the FSM Filter. Initial tests used Siglab to measure the transfer function of the system by exploring the frequency range in several subranges, with an adequate internal filter and sampling rate, to minimise the effects of noise. Figure 5.9 and Figure 5.10 shows the results for the X axis of the FSM filter. Both channels displayed similar frequency response (3 dB bandpass above 20 Hz). The amplitude of phase lag increases continuously. It was less than 10 degrees below 3 Hz, 30 degrees at 6 Hz and 60 degrees at 10 Hz. It was reported that the lag wasn't greater than 10 ms; this was passed by at the time but was addressed later, see section 5.2.6.

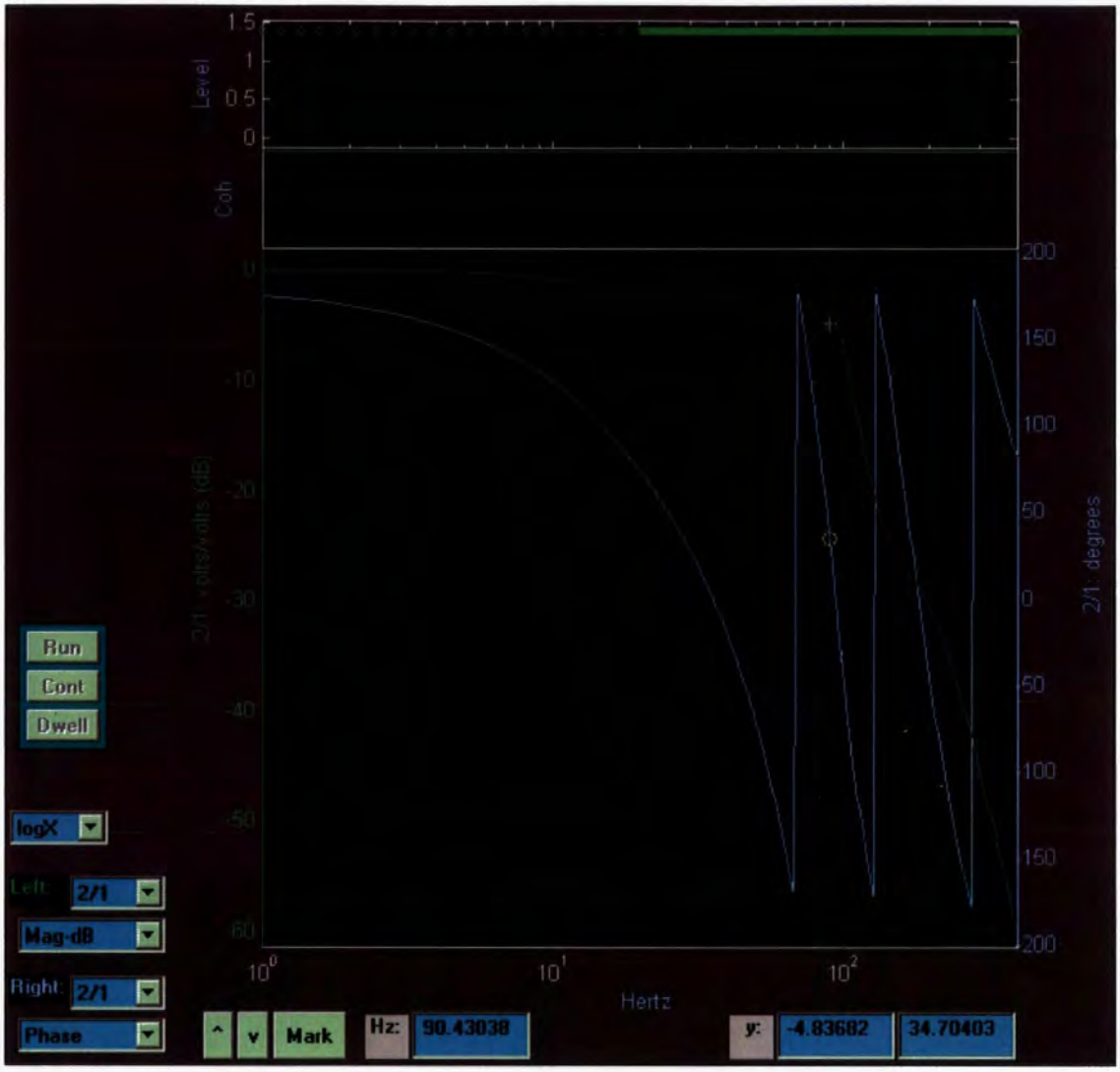

Figure 5.9 *The FSM Filter Response (1- 1kHz)*

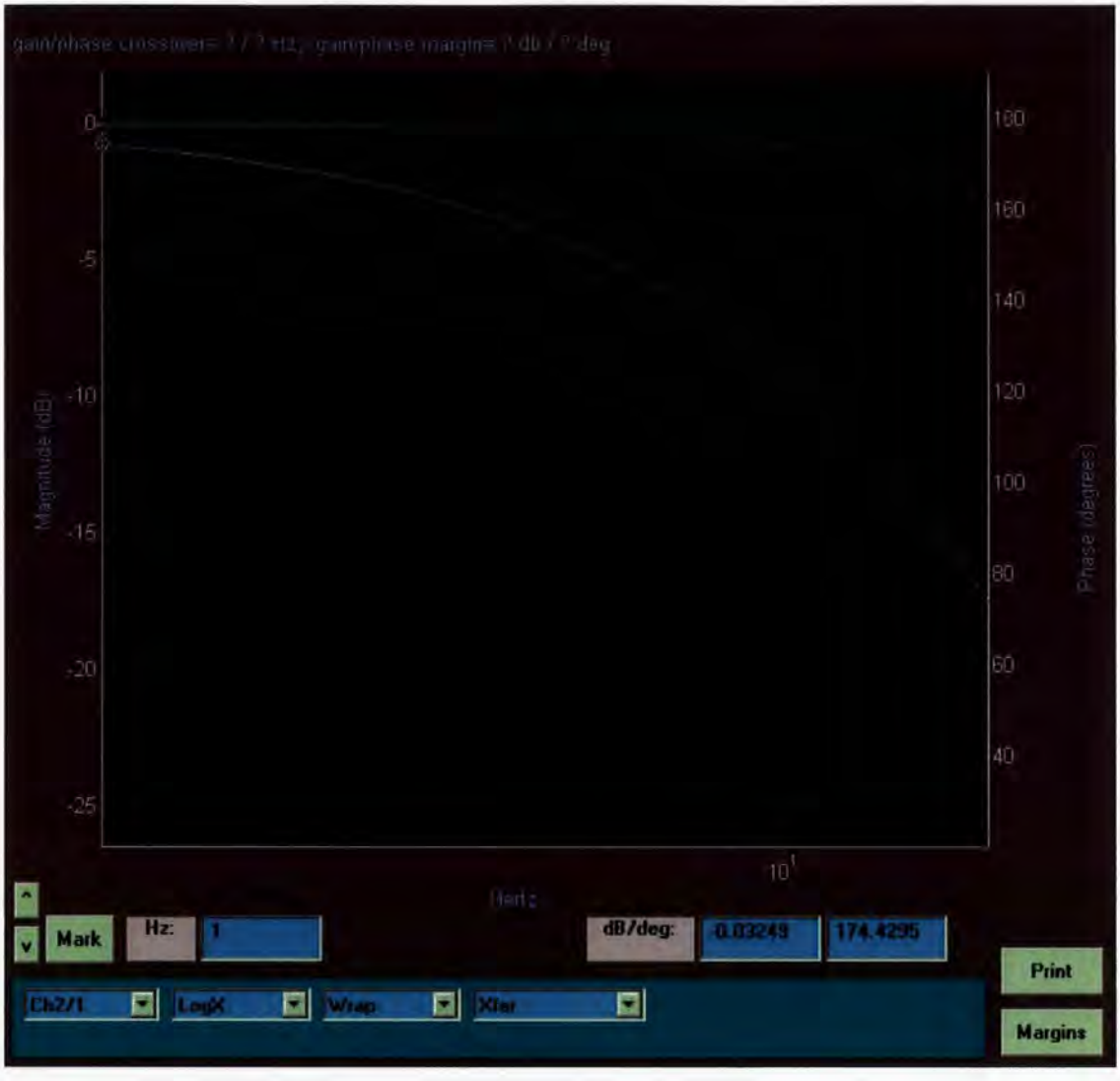

Figure 5.10 *FSM Filter Response 1 – 20Hz*

5.2.4 Further Investigations (Feb 04)

Some voltage signals were captured from the system before reaching the filter. The pinhole was translated and the loop was closed. The AO limit, AO gain and TT gain values were varied to measure the rise time and damping after overshoot. The results are shown in Table 5.4, with the plot for configuration 4 given in Figure 5.11.

	AO Limit	TT gain	DM gain	Rise time	Stablised
1	0	0	0	0.45	
2	0.1	20	0	0.5	0.65
3	0.1	10	0.1	1.15	2
4	0	50	0	0.14	0.78
5	0	20	0.5	0.54	0.54

Table 5.4 *Investigation of Rise time*

The results implied that the NAOMI RTCS never enabled the FSM to respond at a rate greater than 2Hz. This was because the output to the DM is calculated before that for the FSM, and

included the DM tilt limit. Reducing the tilt limit therefore reduced the FSM response. The full global tilt was sent to the DM as well as the FSM. The control software required modification.

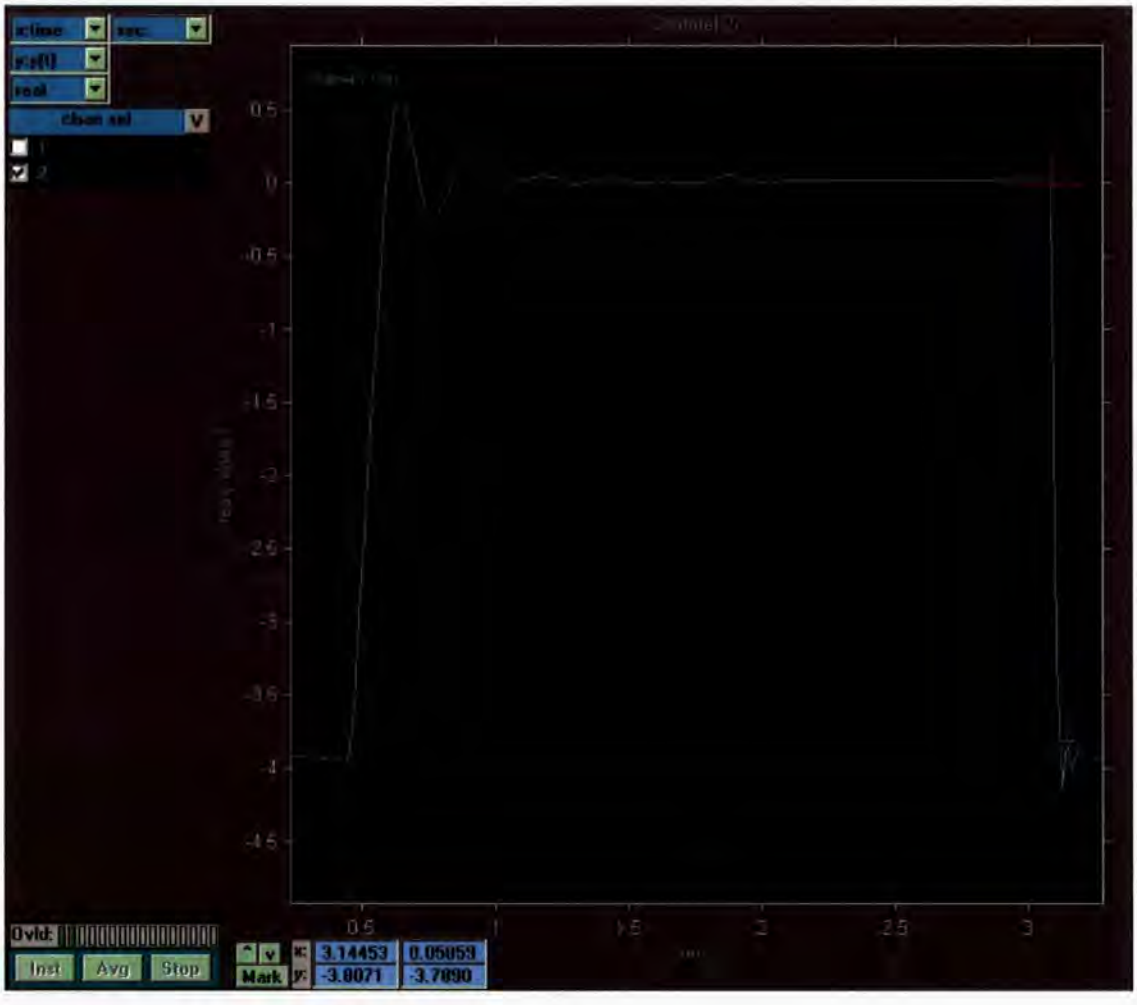

Figure 5.11 *Plot for Configuration 4*

5.2.5 Modifying the Control Software Gains (Feb 04)

For each read of the WFS, a signal arrives at the FSM and DM. The DM receives the full signal (including tip-tilt), and the FSM receives a tilt signal based on the average tilt of the DM during the last iteration.

After investigation, the conclusion was reached that the control software code has to be changed to send the tip-tilt offsets directly to the FSM at the beginning of each iteration rather than being passed through the DM. The modification used the centroid values rather than the calculated segment values to determine the Global Tilt and control the FSM.

The WFS centroids were created by AlgNaomiInterleave.c creating a marginal sum in x and y for the cell around each spot, then determining the shape of each spot. The pixels in each box are multiplied by 2 weight matrices, one of which delivers an x-centroid and one a y-centroid.

After successfully changing the code the oscillations reduced on a stationary pinhole from 0.7" to 0.06", solving one of the issues related with the FSM performance.

5.2.6 Testing the FSM Hardware: Part 2 (Mar 04)

Six weeks after the original tests, the filter was revisited. Further extensive tests revealed that the output signal lags the input signal by 15 ms for frequencies between 2 and 21 Hz. Figure 5.12 and Figure 5.13 compares the pinhole voltage (normalised) against the FSM voltage, both before and after the filter.

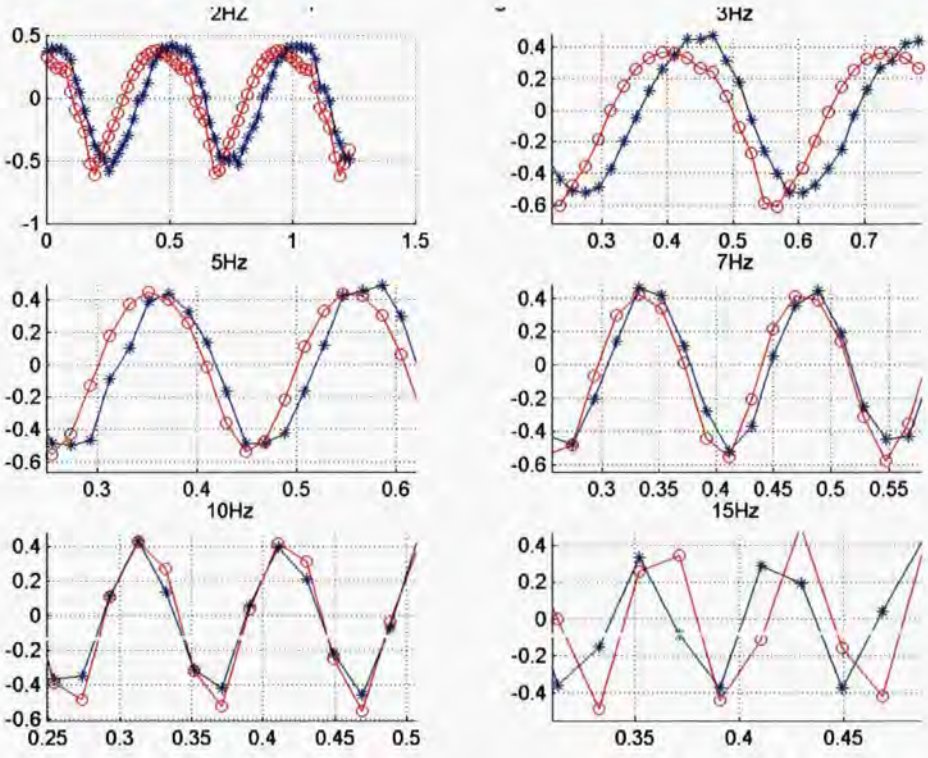

Figure 5.12 *FSM Loop closed: DAC signal taken before FSM Filter*

This delay confirmed that no matter how optimised the software was, the 15ms lag would cause problems when trying to correct at a frequency greater than 3 Hz.

The decision was made to perform some tests without the filter. Without attempting to optimise the system, the correction improved from noticeable correction at 3Hz to 8Hz.

In April the NAOMI team received confirmation from the ATC that the FSM filter was supposed to be replaced by a digital filter before commissioning and wasn't supposed to be part of the commissioned system.

After the test the NAOMI team decide to contact Zeiss for information on the mirror's internal protection. After receiving information, it was decided by ING Management to acquire a filter because of potential risk to the mirror.

The ING specified a replacement low-pass filter with a maximum permitted delay/latency of 0.5ms. The ING placed a contract with Anacircuit to produce two units of two different filters. See section 5.2.8.

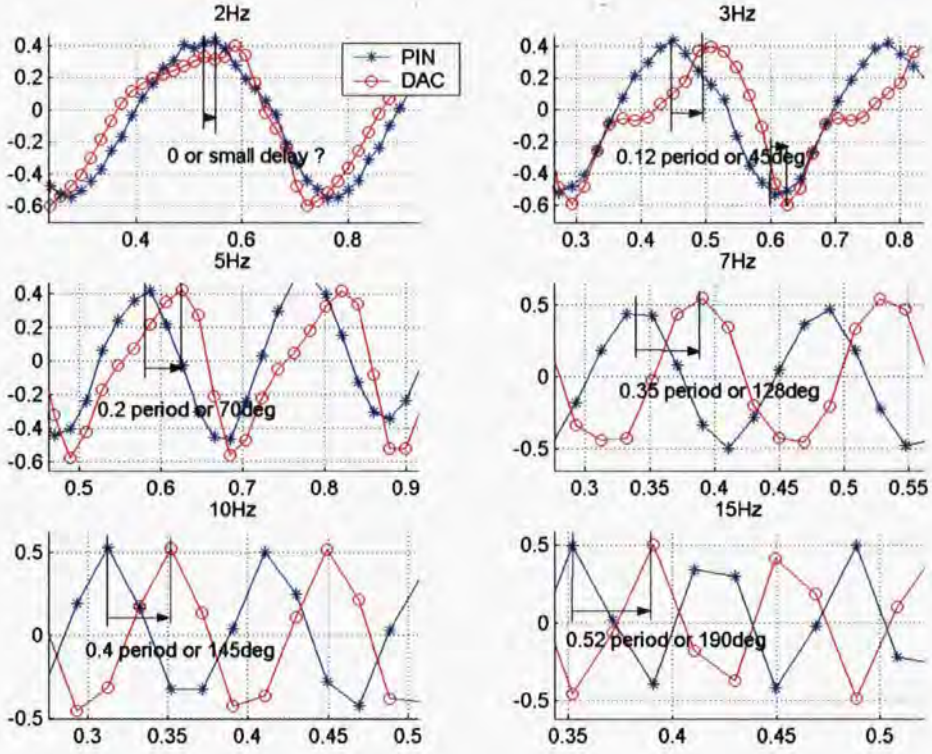

Figure 5.13 *FSM Loop closed: DAC signal taken after the FSM Filter*

5.2.7 Preparing a PID Controller (Mar/Apr 04)

Modifications were made to a test version of TopGui to include an additional PID Controller page.

A PID Controller for the FSM was coded to give three configurable parameters: Proportional Gain (PG), Integral Gain (IG) and Differential Gain (DG). The software was modified to change the gains without needing to recompile.

In April 2004 the NAOMI team developed and followed a 12-stage FSM test plan to implement and tune the PID controller. The first 9 stages on the plan were completed and are described in Table 5.5.

Stage	Task / Comments	Parameters / Correction
0	Test the system works as before. The TTI was reinstalled and performance checked.	Axis: X only Freq.: 5 Hz Gains: P&D Seg: 1 only Range: ±1400 DACS WFS Noise: Considerable
1	Realign Tip-tilt Injector	The TTI mirror was realigned to use both x and y axis to correct
2	Test Software Change A Software change sends signals to both X and Y channels of FSM	Axis: X and Y Freq.: 3 Hz Gains: P&D Seg: 1 only Range: ±1400 DACS WFS Noise: Considerable
3	Test Software Change B The software was modified to start the integral term accumulating only when closing the WFS loop and not when you start the WFS framing. This stopped the FSM going to a software limit and allowed the use of the integration term.	Axis: X and Y Freq.: 3 Hz Gains: P, I & D Seg: 1 only Range: ±1400 DACS WFS Noise: Considerable
4	Test Software Change C The aim was to use the full width of the WFS sub aperture, but due to an optical misalignment of the WFS sky baffle this couldn't be achieved at this time.	
5	Test Software Change D This change used centroid information from 12 segments rather than 1.	Axis: X and Y Freq.: 3 Hz Gains: P, I & D Seg: 12 Range: ±1400 DACS WFS Noise: Considerable
8	Changing WFS Modes and Integration Time Using WFS Mode 2 and 3 to reduce the integration time, the team managed to achieve excellent results.	5Hz ~ 100% correction 10Hz ~ 80% correction 15Hz ~ 30-50% correction
9	Alter code to ensure FSM and DM work together This was partially successful as can be seen in Figure 5.14.	A 20Hz – 50% correction was achieved

Table 5.5 *Results of Code Changes*

The tests revealed that the sky baffle was misaligned and needed to be removed (28th April) to test the full WFS range with the new FSM software.

Figure 5.14 shows the results of tuning the PID parameters using Software Version D6 with no FSM filter. The FSM and DM were partially fighting each other (red curve not a smooth sine but secondary peaks). Additional software changes were made.

At this stage the FSM Characterisation improvement was removed from the critical item list.

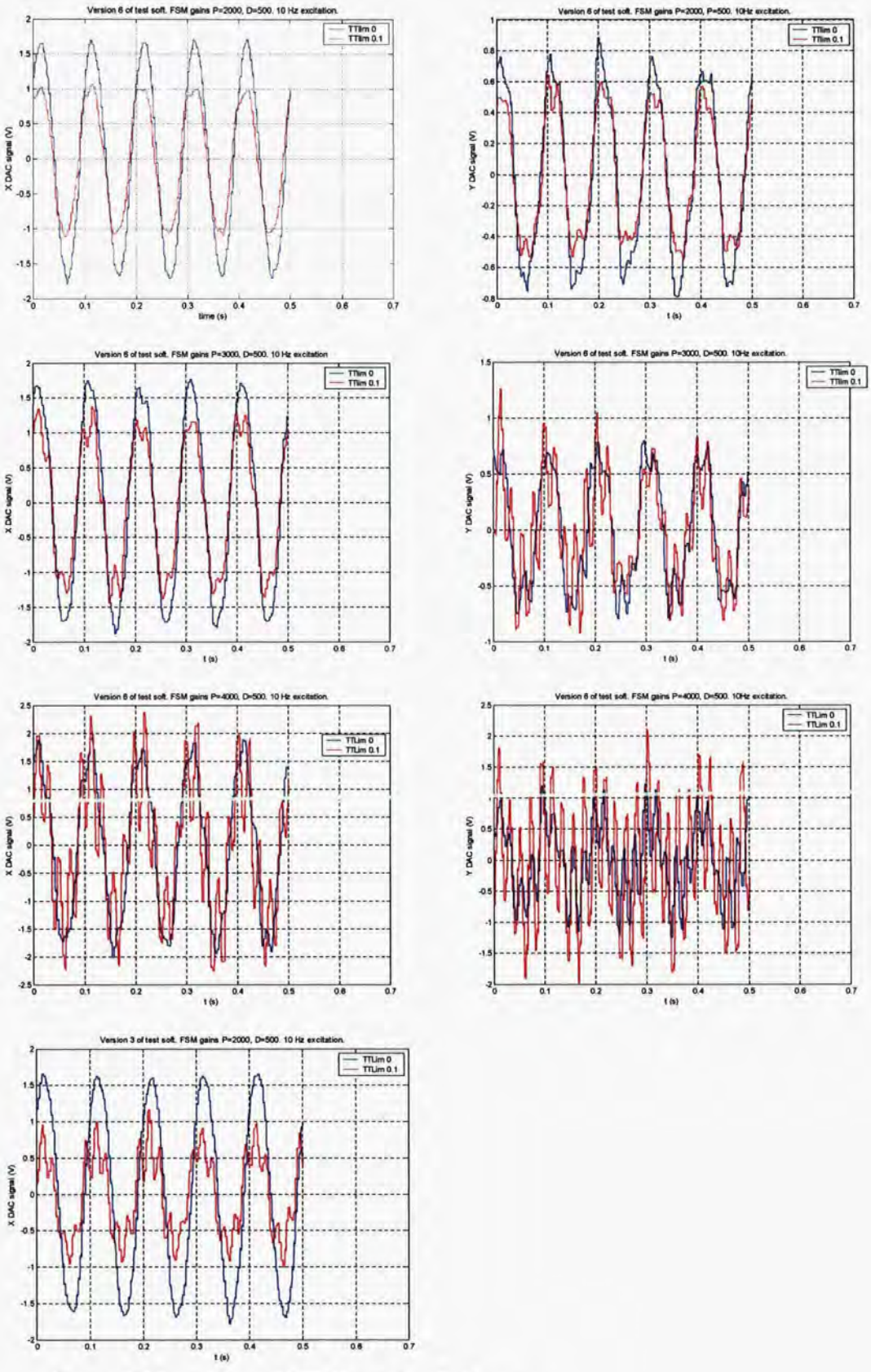

Figure 5.14 *Plots of PID Controller Software*

5.2.8 Characterisation of the new FSM Filters (May 04)

The two new filters arrived and were characterised in May. The first attenuates signals greater than 1 kHz and gives a latency of 1.27 ms. The second attenuates signals at 582 Hz and gives a latency of 2.69 ms as can be seen in Figure 5.15.

Figure 5.15 *Two new FSM Filters from Anacircuit*

Both filters were comparable at frequencies less than 50 Hz. They both gave phase delays of ~7 ° at 10Hz, 10-11 ° at 15 Hz and 14-15 ° at 20 Hz.

5.2.9 Follow on work

Through characterisation of the operational FSM system, the effective performance of the FSM has gone from being destructive (i.e. adding tip-tilt) to achieving a 50% correction at 20 Hz by the end of April 2004.

At the end of May 2004 the author stopped work on the FSM investigation to progress more critical tasks. A number of modifications to the system were required. The temporary TTI needed to be re-engineered to reduce setup time and increase reproducibility. The C40 code required to be fully integrated into the released version (not a trivial task). This task was handed to the author's successor.

The first on-sky test of the temporary PID controller software and the new filter occurred on the 8th June 2004 and gave some mixed results.

After the author and Andy Hide departed company with the ING, the ING continued the FSM characterisation and eventually developed a separate PC-based TT control system to improve the FSM performance.

5.3 SDM Characterisation

Between July 2004 and December 2004 the author investigated the performance of the SDM.

Unlike the FSM, the ING didn't rate the priority of characterising the NAOMI DM high enough to assign staff effort to the task.

There were two main reasons for characterising the DM. The first was to understand how temperature change affected the performance of individual segments. Although most of the temperature fluctuations during observations were minimised through the creation of GRACE, some evidence suggested that the temperature compensation algorithm didn't work as desired. Partial calibration had taken place during 2004, which assumed a linear response between temperature and strain gauge signals. This relationship could be confirmed by conducting a set of temperature-controlled characterisation experiments on the DM.

Secondly, a greater understanding of the DM was required to optimise the RTCS. Little information was available on its spatial and temporal characteristics. The available information was obtained either during manufacture or integration, both in different environments to GRACE. Another significant change was that the DM was part of a system and the system transfer function ideally needed to be derived in order to aid the construction of a hardware-optimised feedforward controller such as the Smith Predictor.

Finally characterising each actuator could uncover problems associated with misbehaving segments, such as segment 45. These segments had been deactivated. Recovering these segments would increase the instrument's ability to correct wavefront error.

5.3.1 Equipment

Characterisation of the DM required no additional hardware. The NAOMI SDM is described in Section 4.5.5 and its associated control hardware is described in Section 4.5.6.1.

All DM segments contain three actuators with independent strain gauge feedback. Each DM segment and actuators are located and labelled (by DAC Channel Number) as shown in Figure 5.16. As previously mentioned, the inner quadrant of segments (33, 34, 43 and 44) and the outer ring of segments (1, 2, 3, 4, 5, 10, 11, 18, 19, 28, 29, 38, 39, 48, 49, 58, 59, 66, 67, 72, 73, 74, 75 and 76) were not active in normal use. The DAC Channel Number ranges from 0 to 253, yet there are only 228 actuators and active DM channels.

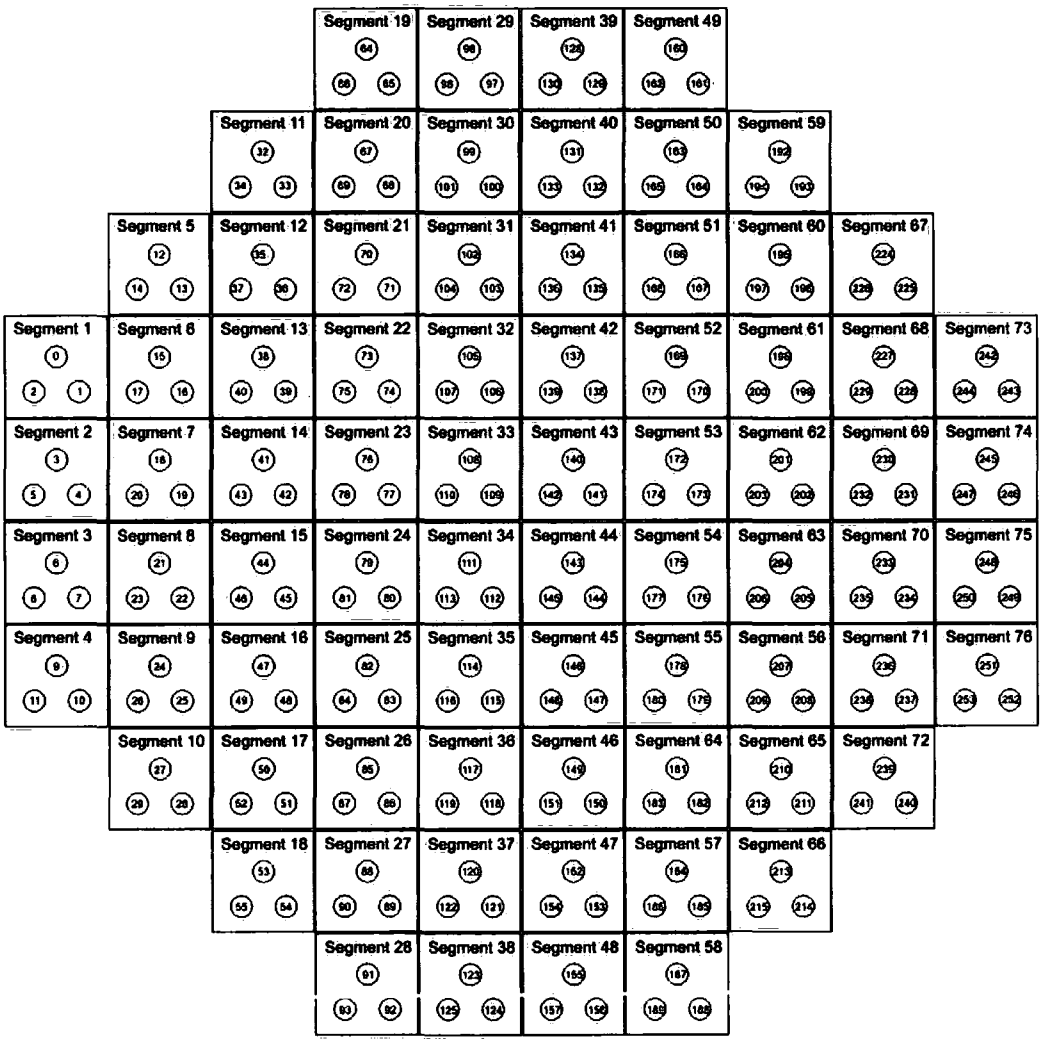

Figure 5.16 *Map locating and labelling each DM Segment and its actuators*

Each actuator contains an Actuator code, DAC Channel Number, ADC Channel Number, ADC Offset value and ADC Gain value. The values for a subset, segment 1-24 are showed in Figure 5.17.

Each value sent to a DAC channel was used to drive an actuator whereas the value read by the ADC came from the strain gauges. The DAC values ranged from 0 to 8192 and related nominally to a 6 μm stroke. I.e. 1 DAC corresponds to a 0.73 nm piston movement. The ADCs are 16-bit and hence values ranged from 0 to 65536.

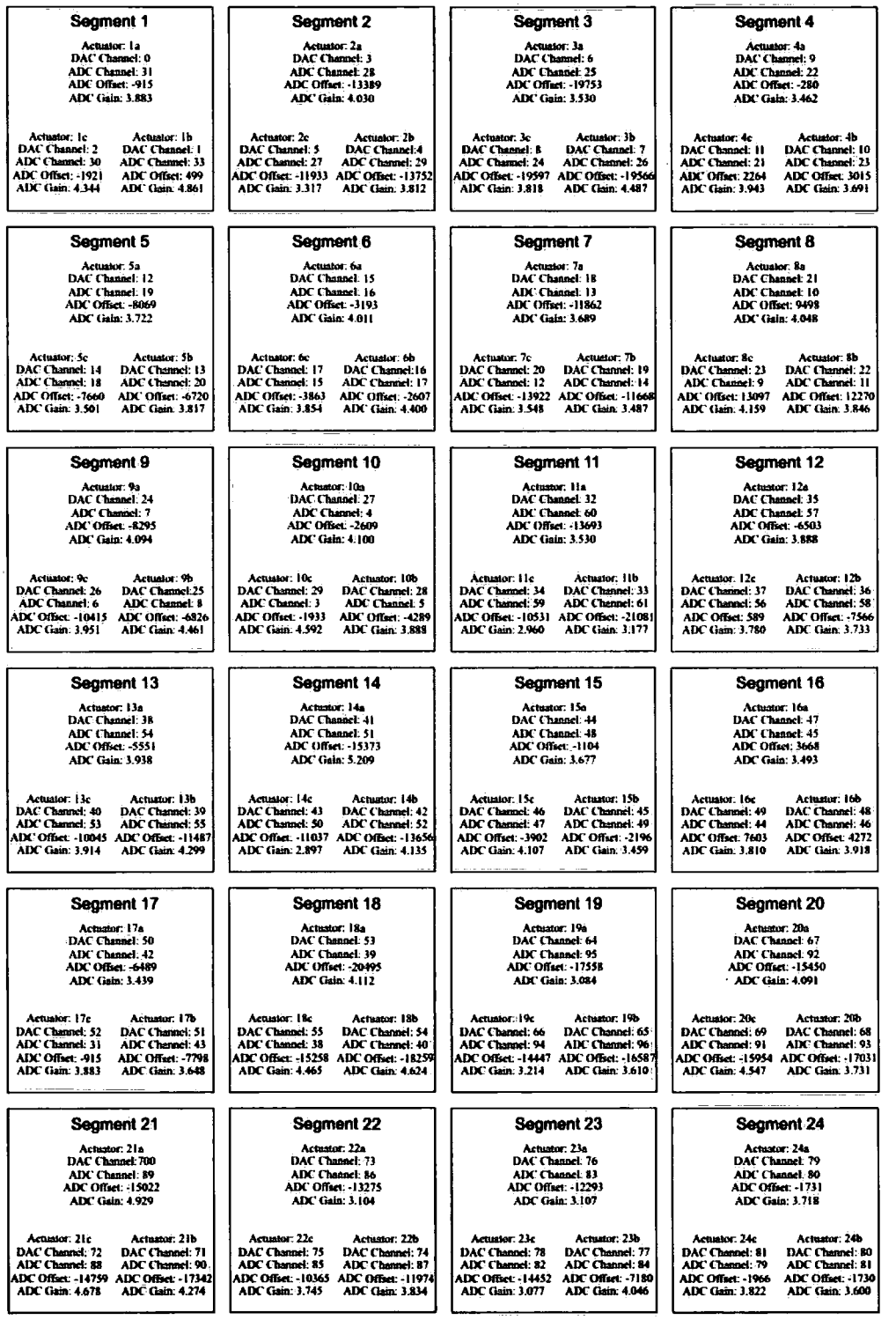

Figure 5.17 *The details of a subsection of segments*

Unlike the FSM characterisation, it was impossible to obtain permission to test the DM in isolation, and therefore signals had to be sent and received through the NAOMI RTCS. Fortunately, it was possible to drive the individual segments and obtain timestamped strain gauge values without significant C40 coding. Suitable routines had been included before commissioning. See Section 5.3.3.

5.3.2 Selecting Parameters to Measure

There were a number of key parameters detailed in Section 2.3 that needed to be measured. These included Spatial Domain parameters such as the Rise Time and Settling Time and Frequency Domain parameters such as the System Gain and Phase Shift. As with the FSM, the lag time was of great interest.

It was decided to investigate applying a number of step changes to each actuator to derive spatial domain parameters and to inject a number of sine waves to examine frequency domain parameters. The Strain Gauge ADC values would be continuously measured before and after the step changes and throughout a number of sine wave injections.

5.3.2.1 Step Response – Spatial Domain

It was decided to vary the step size, the initial and final values and the direction of the step. It was also decided to measure the noise on the strain gauge signal by leaving it in position for a number of readings. Table 5.6 contains a list of 18 steps that were to be tested.

Initial Value	Final Value	Step Size
1000	2000	1000
3598	4598	1000
7000	8000	1000
4048	4148	100
3848	4348	500
3098	5098	2000
2598	5598	3000
2098	6098	4000
4098	4098	0
2000	1000	-1000
4598	3598	-1000
8000	7000	-1000
4148	4048	-100
4348	3848	-500
5098	3098	-2000
5598	2598	-3000
6098	2098	-4000
4098	4098	0

Table 5.6 *Step Responses*

It was decided to repeat each of the 18 dataset 3 times to obtain average values, giving a total of 54 datasets per actuator. Each entry would collect 200 data points with the transition being requested on the 101st point. Hence for each actuator 57 datasets and 10,800 data points would be collected. Each of the 228 actuators were tested, giving over 2.4 million data points for the step response.

5.3.2.2 Sine wave Response – Frequency Domain

Injecting a sine wave into the DM would be a little more involved. Initially it was decided to inject 9 sine waves of varying frequency but of the same amplitude, around the DAC midpoint. Table 5.7 contains a list of the 9 frequency settings to be tested.

Frequency (Hz)	Midpoint	Amplitude	Data points
2	4096	500	14710
3	4096	500	9800
5	4096	500	5880
10	4096	500	2910
20	4096	500	1470
30	4096	500	980
50	4096	500	590
70	4096	500	420
90	4096	500	330

Table 5.7 *Sine wave demands*

Each dataset contained 10 oscillations at the chosen frequency. The 9 different datasets were repeated 3 times to obtain noise statistics, hence in total there were 27 datasets per actuator. The number of data points per dataset varied depending on the frequency, as seen in Table 5.7.

Each actuator was to produce 111k data points. For the total number of 254 actuators, there would be over 28.2 million data points. Scripts to automate testing were clearly required.

5.3.3 Test Scripts

The C40 SG library contained two tools that were useful for extracting data from the C40s. These were known as Snapshot and Capture. Both tools are built into the c40 code and are supported by *SGlib.py* and *SGtest.py*.

The aim of the Snapshot tool was to allow a full set of Strain Gauge ADC and output values to be retrieved by a workstation process.

The aim of the Capture tool was to record a whole contiguous sequence of data values from one channel per CPU to be retrieved by a workstation process.

The Capture tool was linked to the Waveform system to enable measurement with fine time resolution of the response of an actuator to a stimulus. At the beginning of the investigation the first task was to commission the Capture tool.

With the Capture Tool working, the next task was to produce batch scripts to perform the tests and collect the data described in Section 5.3.2.

The author created test Python script to include the functionality of the Capture Tool. Although the script performed both the Step Responses and Sine Wave, only one was run at a time.

5.3.4 Data Collection

The author returned to La Palma and conducted experiments between the 11th and 19th November 2004 with Richard Myers (ING).

During this period, a complete set of Step Response for each actuator was obtained and a partial set of data for the Sine Wave responses were obtained. A bug in the software caused the C40s to crash when trying to obtain Sine Wave response data for particular segments. This bug wasn't fixed before the end of the run.

In total 228 files containing Step Response data and 115 files containing Sine Wave Response data were captured. In addition a file containing the ADC gains and ADC offsets were obtained. The temperature in GRACE was 10.3±1.0 °C over the 10 hours the data was gathered.

5.3.4.1 Step Response Data

The data collection python script firstly created an appropriate file for the data and printed the following line '*Setting interval time to 5100 clock units ~340ns*'.

The script would then collect and output the 54 datasets to the file. The first dataset for Actuator 0 is given in Figure 5.18. It contains the Initial Demand Value, Final Demand Value, Step Size and Direction, Buffer length, DIAG datatype, CPU, Capture Channel and the Data Array.

```
Step Function from 1000 to 2000, step size 1000
buffer length  = 203
DIAG datatype  = 0x200
CPU            = 11
Capture channel = 0
array([-1024, -1016, -1291, -1502, -1519, -1530, -1544, -1557, -1571, -1580, -1583,
       -1598, -1593, -1591, -1593, -1596, -1601, -1602, -1600, -1613, -1611,
       -1614, -1613, -1604, -1609, -1603, -1606, -1623, -1615, -1616, -1618,
       -1619, -1621, -1621, -1627, -1631, -1629, -1613, -1615, -1621, -1622,
       -1623, -1622, -1623, -1626, -1624, -1620, -1635, -1632, -1635, -1633,
       -1627, -1630, -1631, -1634, -1630, -1636, -1643, -1633, -1627, -1629,
       -1631, -1631, -1629, -1634, -1629, -1628, -1634, -1644, -1653, -1636,
       -1631, -1631, -1635, -1635, -1640, -1637, -1633, -1647, -1640, -1646,
       -1643, -1642, -1640, -1641, -1642, -1645, -1644, -1642, -1645, -1647,
       -1644, -1643, -1643, -1641, -1638, -1646, -1648, -1649, -1653, -1645,
       -1638, -1645, -1646, -1645, -1648, -1643, -1654, -1656, -1655, -1648,
       -1647, -1647, -1648, -1650, -1651, -1652, -1656, -1648, -1653, -1654,
       -1648, -1649, -1649, -1650, -1644, -1643, -1644, -1651, -1654, -1643,
       -1651, -1650, -1649, -1648, -1648, -1648, -1644, -1645, -1650, -1656,
       -1651, -1650, -1654, -1651, -1654, -1653, -1651, -1655, -1648, -1653,
       -1606, -1525, -1453, -1412, -1405, -1421, -1446, -1457, -1469, -1458,
       -1446, -1452, -1455, -1456, -1454, -1452, -1447, -1446, -1455, -1462,
       -1459, -1458, -1454, -1454, -1461, -1462, -1458, -1459, -1445, -1448,
       -1451, -1463, -1457, -1454, -1449, -1449, -1449, -1455, -1459, -1455,
       -1454, -1453, -1460, -1460, -1461, -1456, -1455, -1466, -1455],'i')
```

Figure 5.18 *Extract of a step response data file for Actuator 0*

5.3.4.2 Sine Response Data

Again, the data collecting python script firstly created an appropriate file for the data and output the following line '*Setting interval time to 5100 clock units ~340ns*'.

The script would then collect and print the 27 datasets. The beginning of the last dataset for Actuator 0 is given in Figure 5.19. It contains the Frequency, Amplitude, Midpoint, Buffer length, DIAG datatype, CPU, Capture channel and the data array. Only one of the 10 periods for that dataset is shown.

```
The waveform starts on the 21st iteration and oscillates 10 times
Sine waveform of a frequency 90 Hz and Amplitude of 500 DAC units.  Oscillating
around 4096 DAC units
Interval = 5100, numFrames = 33
buffer length  = 36
DIAG datatype  = 0x200
CPU            = 11
Capture channel = 0
array([-943, -952, -934, -914, -890, -877, -864, -862, -858, -847, -843, -845, -855,
        -863, -869, -874, -875, -875, -904, -911, -932, -947, -952, -960,
        -966, -971, -987, -980, -984, -987, -966, -960, -949],'i')
```

Figure 5.19 *Extract of a sine wave data file for Actuator 0*

5.3.5 Post Processing Data

The collected data was taken back to Durham for post processing and analysis. Two python scripts were created to process the step data and sine wave data separately. Both scripts had two main functions: to graphically represent the data and to perform statistical analysis. The first was achieved by writing a python script that autogenerated multiple Matlab .m scripts, which in turn produced multiple graphical plots of the scaled data.

The Step Response Data Reduction script output Time Domain Statistics for each actuator channel to a text file. The Sine Wave Response Data Reduction script's statistical analysis functions were never completed.

A batch file would execute each Matlab script. Each Step Response Matlab scripts created 18 graphs each containing the complete data set. These 18 graphs were saved as .jpg files.

A 'Webpage creation' python script was created to autogenerate multiple webpages containing both the .jpg and the derived statistics.

5.3.6 Step Response Results

The results firstly show that the actuators can be divided into two main types: correctly calibrated and incorrectly calibrated. All actuators responded to demand values as expected yet seemingly a large number of actuators required retuning of the ADC Offset and ADC Gain parameters. It was found that 45 actuators were correctly calibrated whereas 183 actuators required recalibration. Two actuators are described in detail, Actuator 0 (Correctly Calibrated) and Actuator 70. (Incorrectly Calibrated)

5.3.6.1 Actuator 0 (Correctly Calibrated)

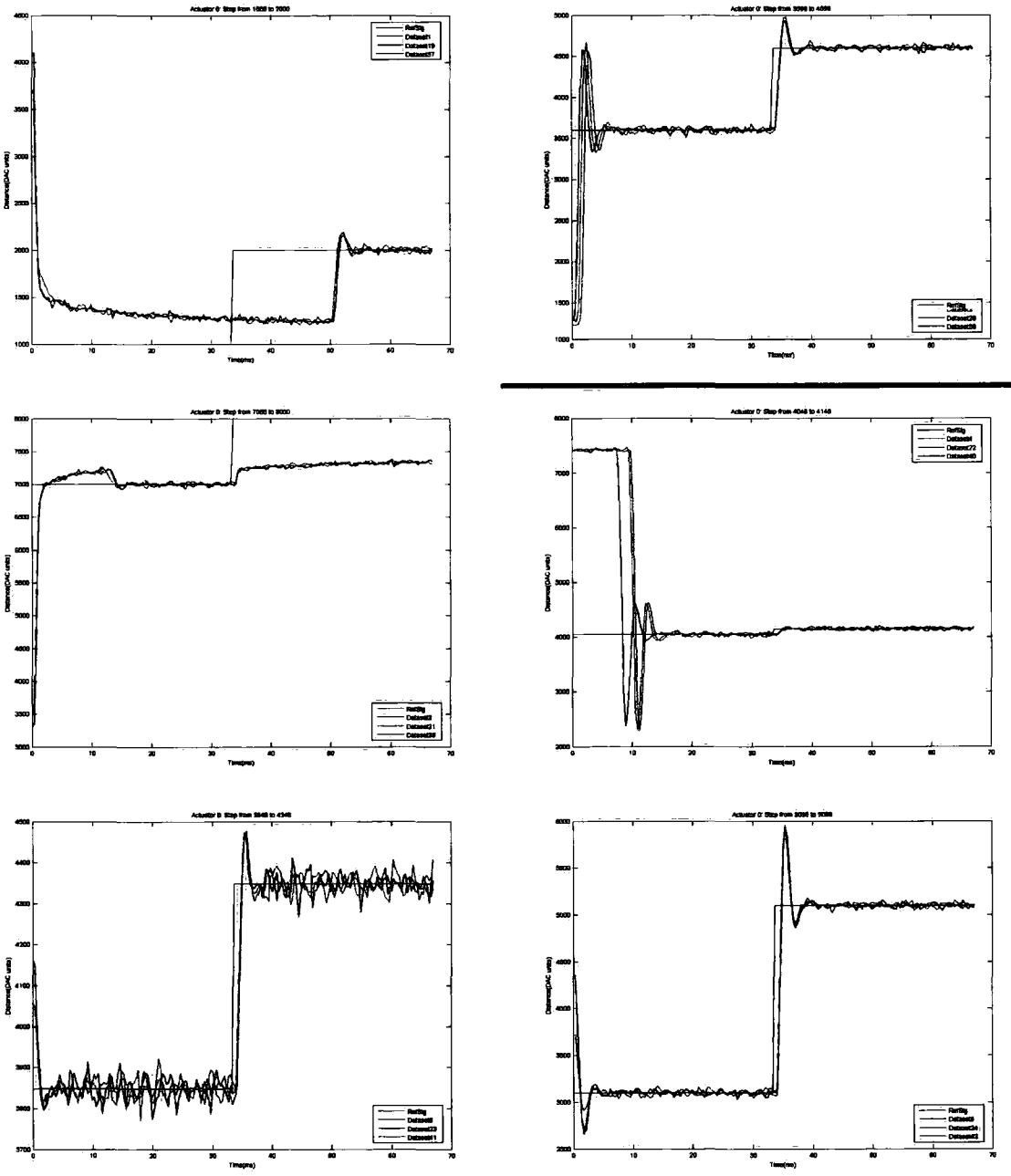

Figure 5.20 *Actuator 0 Step Response Graphs (1-6)*

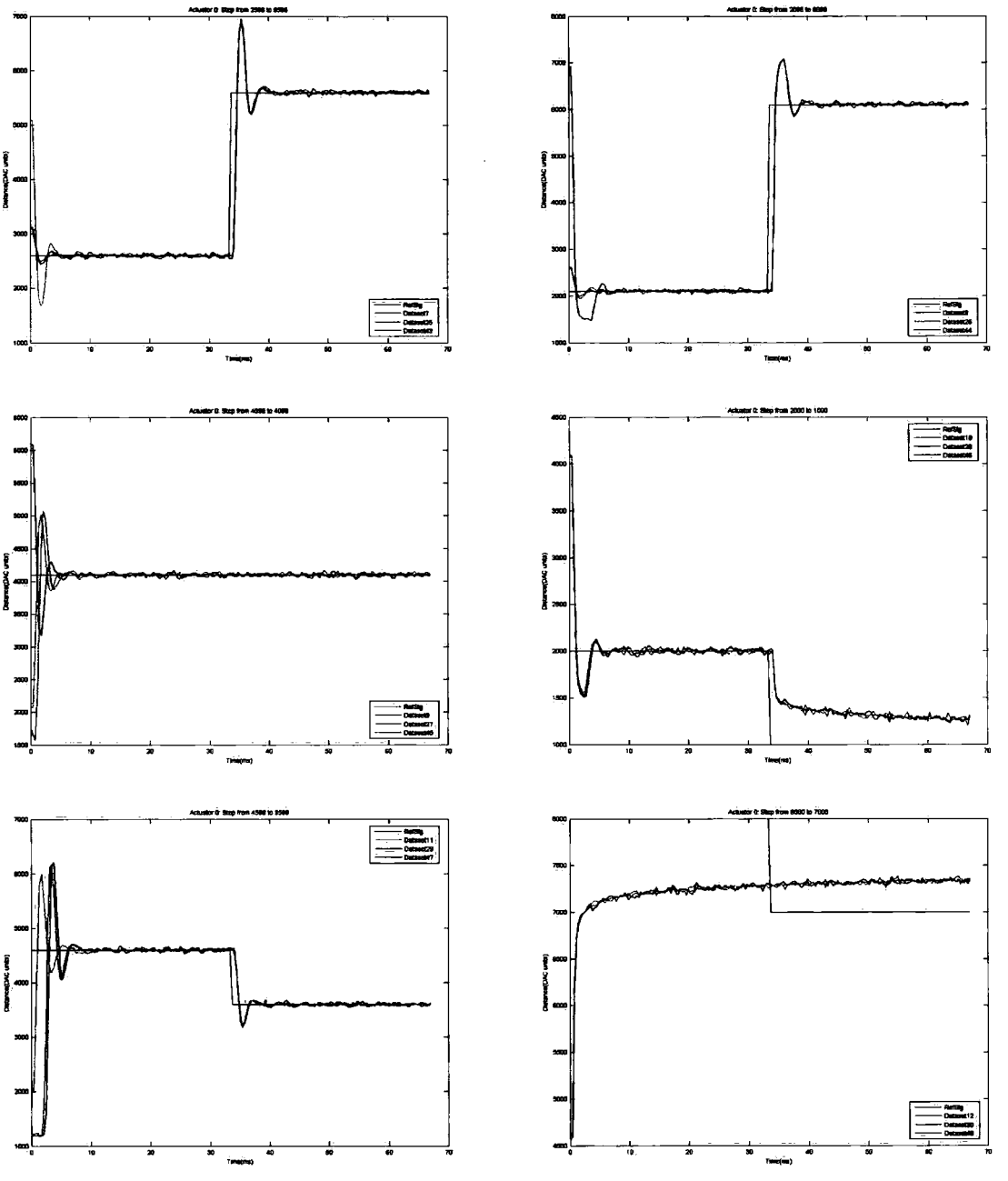

Figure 5.21 *Actuator 0 Step Response Graphs (7-12)*

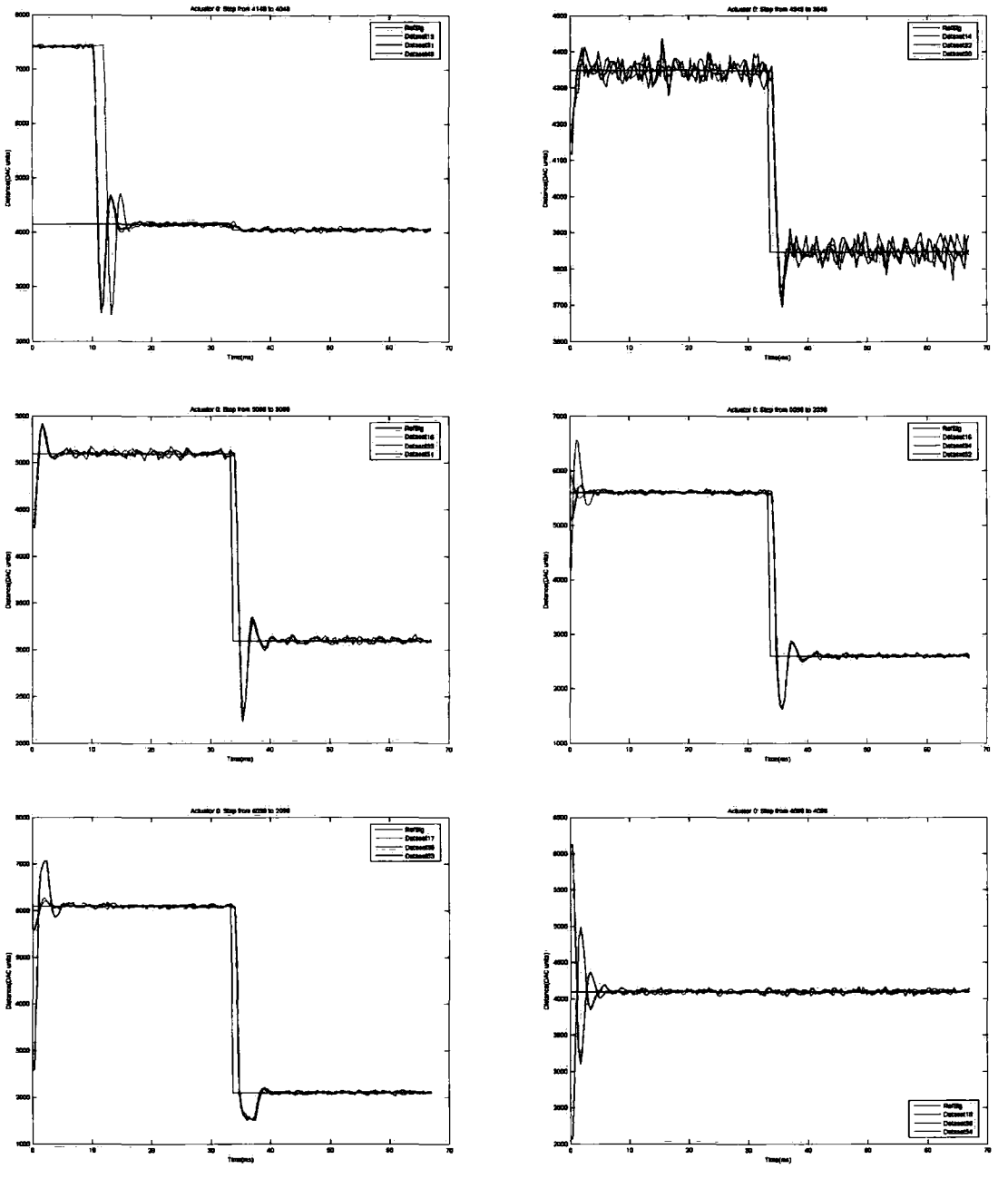

Figure 5.22 *Actuator 0 Step Response Graphs (13-18)*

DS	Step (Ref)			Step (Data)			Offset Error	Gain Error	Start Delay Time	Rise Time	Settling Time	Total Latency
	Inital	Demand	Size	Initial	Demand	Size						
1	1000	2000	1000	1315 ±46	1701 ±373	386	-315	-61.4%	17.0 ±0.17	0.34 ±0.34	16.16 ±0.34	**33.16 ±0.17**
2	3598	4598	1000	3598 ±25	4598 ±20	1000	0	0.0%	0.5 ±0.17	0.67 ±0.34	1.35 ±0.34	**2.19 ±0.17**
3	7000	8000	1000	7045 ±83	7319 ±27	274	-45	-72.6%	0.5 ±0.17	5.39 ±0.34	13.46 ±0.34	**33.16 ±0.17**
4	4048	4148	100	4409 ±1140	4148 ±20	-261	-361	-361.0%	33.16 ±0.17	0.0 ±0.34	0.34 ±0.34	**33.16 ±0.17**
5	3848	4348	500	3848 ±27	4350 ±25	502	0	0.4%	0.5 ±0.17	0.67 ±0.34	17.17 ±0.34	**26.42 ±0.17**
6	3098	5098	2000	3098 ±28	5097 ±23	1999	0	-0.05%	0.5 ±0.17	0.67 ±0.34	-1.01 ±0.34	**2.19 ±0.17**
7	2598	5598	3000	2598 ±31	5596 ±25	2998	0	-0.07%	0.5 ±0.17	0.34 ±0.34	-1.35 ±0.34	**2.19 ±0.17**
8	2098	6098	4000	2097 ±24	6098 ±32	4001	1	0.03%	0.5 ±0.17	0.34 ±0.34	2.02 ±0.34	**2.52 ±0.17**
10	2000	1000	-1000	1999 ±22	1298 ±33	-701	1	-29.9%	0.5 ±0.17	4.38 ±0.34	22.89 ±0.34	**32.82 ±0.17**
11	4598	3598	-1000	4598 ±27	3599 ±22	-999	0	-0.1%	0.5 ±0.17	0.67 ±0.34	1.35 ±0.34	**2.19 ±0.17**
12	8000	7000	-1000	7236 ±43	7328 ±22	92	764	-109.2%	33.16 ±0.17	0.34 ±0.34	-0.34 ±0.34	**32.82 ±0.17**
13	4148	4048	-100	4591 ±1197	4047 ±27	-544	-443	444.0%	-0.17 ±0.17	0.67 ±0.34	6.73 ±0.34	**24.74 ±0.17**
14	4348	3848	-500	4347 ±19	3848 ±25	-499	1	-0.2%	0.5 ±0.17	0.67 ±0.34	5.39 ±0.34	**30.46 ±0.17**
15	5098	3098	-2000	5099 ±27	3098 ±21	-2001	-1	0.05%	0.5 ±0.17	0.34 ±0.34	-1.01 ±0.34	**2.19 ±0.17**
16	5598	2598	-3000	5599 ±25	2599 ±19	-3000	-1	0.0%	0.5 ±0.17	0.34 ±0.34	2.02 ±0.34	**2.52 ±0.17**
17	6098	2098	-4000	6099 ±24	2099 ±21	-4000	-1	0.0%	0.5 ±0.17	0.34 ±0.34	3.03 ±0.34	**3.53 ±0.17**
19	1000	2000	1000	1308 ±38	1714 ±372	406	-308	-59.4%	16.66 ±0.17	0.34 ±0.34	16.49 ±0.34	**33.16 ±0.17**
20	3598	4598	1000	3598 ±26	4598 ±25	1000	0	0.0%	0.5 ±0.17	0.67 ±0.34	1.68 ±0.34	**2.52 ±0.17**
21	7000	8000	1000	7048 ±86	7306 ±26	258	-48	-74.2%	0.5 ±0.17	6.4 ±0.34	12.79 ±0.34	**32.48 ±0.17**
22	4048	4148	100	4452 ±1188	4149 ±20	-303	-404	-403.0%	33.16 ±0.17	0.34 ±0.34	0.0 ±0.34	**33.16 ±0.17**
23	3848	4348	500	3847 ±20	4347 ±17	500	1	0.0%	0.5 ±0.17	0.67 ±0.34	1.35 ±0.34	**2.19 ±0.17**
24	3098	5098	2000	3098 ±26	5097 ±20	1999	0	-0.05%	0.5 ±0.17	0.34 ±0.34	-1.01 ±0.34	**2.19 ±0.17**
25	2598	5598	3000	2598 ±24	5597 ±22	2999	0	-0.03%	0.5 ±0.17	0.34 ±0.34	-1.01 ±0.34	**2.19 ±0.17**
26	2098	6098	4000	2097 ±25	6098 ±23	4001	1	0.03%	0.5 ±0.17	0.34 ±0.34	2.02 ±0.34	**2.52 ±0.17**
28	2000	1000	-1000	2000 ±25	1310 ±37	-690	0	-31.0%	0.5 ±0.17	4.38 ±0.34	0 ±0	**12.96 ±0.17**
29	4598	3598	-1000	4602 ±29	3599 ±21	-1003	-4	0.3%	0.5 ±0.17	0.67 ±0.34	1.35 ±0.34	**2.19 ±0.17**
30	8000	7000	-1000	7234 ±41	7324 ±19	90	766	-109.0%	2.19 ±0.17	0.0 ±0.34	-1.35 ±0.34	**31.81 ±0.17**
31	4148	4048	-100	4799 ±1377	4047 ±23	-752	-651	652.0%	-0.17 ±0.17	1.01 ±0.34	0 ±0	**0.5 ±0.17**
32	4348	3848	-500	4348 ±24	3847 ±22	-501	0	0.2%	0.5 ±0.17	0.67 ±0.34	1.35 ±0.34	**19.35 ±0.17**
33	5098	3098	-2000	5098 ±25	3098 ±25	-2000	0	0.0%	0.5 ±0.17	0.34 ±0.34	-1.01 ±0.34	**2.19 ±0.17**
34	5598	2598	-3000	5597 ±23	2598 ±25	-2999	1	-0.03%	0.5 ±0.17	0.34 ±0.34	2.02 ±0.34	**2.52 ±0.17**
35	6098	2098	-4000	6099 ±26	2098 ±22	-4001	-1	0.03%	0.5 ±0.17	0.34 ±0.34	3.03 ±0.34	**3.53 ±0.17**
37	1000	2000	1000	1318 ±37	1701 ±374	383	-318	-61.7%	17.0 ±0.17	0.34 ±0.34	16.16 ±0.34	**33.16 ±0.17**
38	3598	4598	1000	3599 ±26	4598 ±22	999	-1	-0.1%	0.5 ±0.17	0.67 ±0.34	1.68 ±0.34	**2.52 ±0.17**
39	7000	8000	1000	7047 ±82	7301 ±30	254	-47	-74.6%	0.5 ±0.17	6.06 ±0.34	6.4 ±0.34	**33.16 ±0.17**
40	4048	4148	100	4172 ±774	4148 ±25	-24	-124	-124.0%	1.51 ±0.17	0.0 ±0.34	0.34 ±0.34	**33.16 ±0.17**
41	3848	4348	500	3848 ±26	4348 ±24	500	0	0.0%	0.5 ±0.17	0.67 ±0.34	12.12 ±0.34	**33.16 ±0.17**
42	3098	5098	2000	3097 ±23	5097 ±23	2000	1	0.0%	0.5 ±0.17	0.34 ±0.34	-1.01 ±0.34	**2.19 ±0.17**
43	2598	5598	3000	2596 ±26	5597 ±27	3001	2	0.03%	0.5 ±0.17	0.34 ±0.34	-1.01 ±0.34	**2.19 ±0.17**
44	2098	6098	4000	2096 ±22	6098 ±27	4002	2	0.05%	0.5 ±0.17	0.34 ±0.34	2.02 ±0.34	**2.52 ±0.17**
46	2000	1000	-1000	2000 ±22	1302 ±36	-698	0	-30.2%	0.5 ±0.17	4.71 ±0.34	19.86 ±0.34	**29.79 ±0.17**
47	4598	3598	-1000	4602 ±34	3598 ±25	-1004	-4	0.4%	0.5 ±0.17	0.67 ±0.34	1.35 ±0.34	**2.19 ±0.17**
48	8000	7000	-1000	7234 ±44	7318 ±20	84	766	-108.4%	33.16 ±0.17	0.34 ±0.34	-0.34 ±0.34	**32.82 ±0.17**
49	4148	4048	-100	4598 ±1201	4048 ±21	-550	-450	450.0%	-0.17 ±0.17	0.0 ±0.34	0 ±0	**0.5 ±0.17**
50	4348	3848	-500	4349 ±23	3847 ±24	-502	-1	0.4%	0.5 ±0.17	0.67 ±0.34	-13.8 ±0.34	**2.19 ±0.17**
51	5098	3098	-2000	5097 ±26	3099 ±23	-1998	1	-0.1%	0.5 ±0.17	0.67 ±0.34	-1.01 ±0.34	**2.19 ±0.17**
52	5598	2598	-3000	5598 ±22	2599 ±27	-2999	0	-0.03%	0.5 ±0.17	0.34 ±0.34	2.02 ±0.34	**2.52 ±0.17**
53	6098	2098	-4000	6099 ±26	2097 ±21	-4002	-1	0.05%	0.5 ±0.17	0.34 ±0.34	3.03 ±0.34	**3.53 ±0.17**

Table 5.8 *Actuator 0 Calculated Statistics*

This level of information was produced for all 228 actuators.

Figure 5.20 to Figure 5.22 displays the complete set of Matlab created images for the Step Response Data for Actuator 0. Table 5.8 contains the calculated Time Domain statistics for the Step Response Data for Actuator 0.

Latency
Key information can be extracted from the data. The latency associated with each actuator can be broken down into three components:

- Start delay time – Time taken between issuing the demand value and the actuator moving (Mostly 0.5 ms).
- Rise time – Depends on size of step.
- Settling time - Depends on size of overshoot.

The results showed that on a good transition the total delay would be between 2 and 3 ms; hence the theoretical improvement a feedforward controller could achieve is around 2 ms, as the start delay time would still exist.

Integral Wind-Up
Actuator 0 showed signs of Integral Wind-Up (Graphs 1, 3, 10 and 12). This could add an additional 30 ms and would reduce the performance of NAOMI if it was being asked to correct at the edges of its range. In some cases it couldn't reach its demand position. Considering the problems with the FSM, this would have most likely limited the performance of the system.

5.3.6.2 Actuator 70 (Incorrectly Calibrated)

A selection of Matlab-created images are displayed for the Step Response Data for Actuator 70.

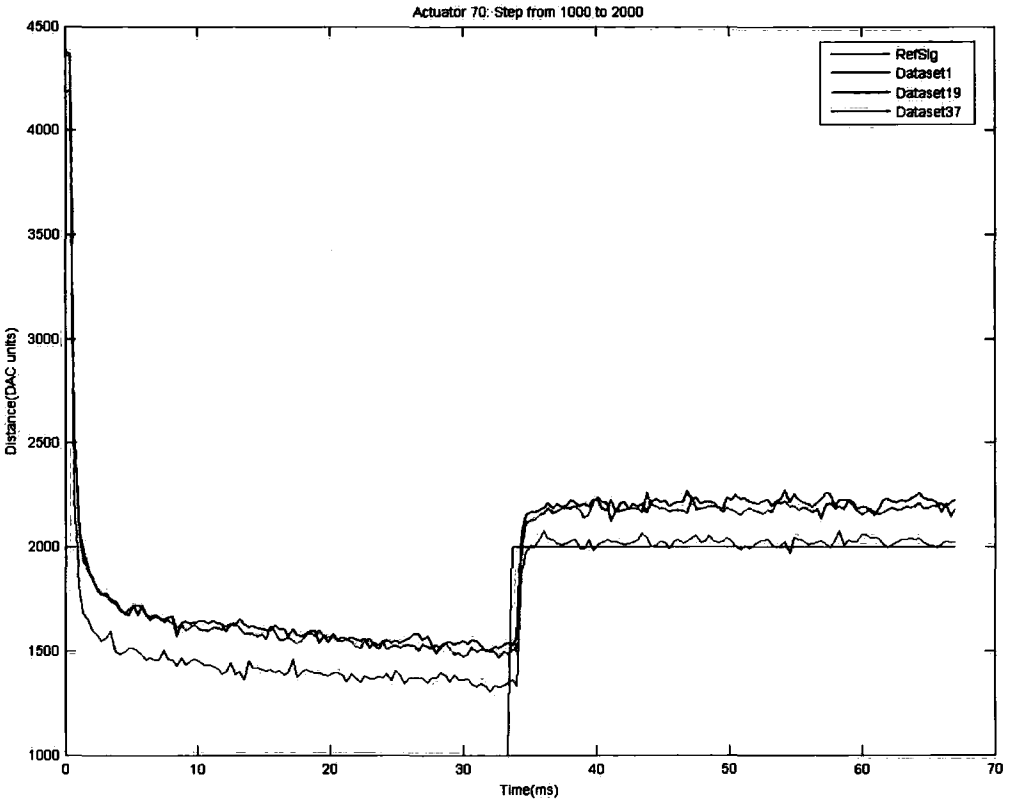

Figure 5.23 *Actuator 70: Dataset 1, 19 & 37*

Drifting

A number of 'incorrectly calibrated' actuators showed signs of drifting. Actuator 70 demonstrates this as can be seen in Figure 5.23. This could be a temperature effect due to the actuator warming up. It is difficult to say if this effect is due to the piston being driven to a different value or the strain gauge material expanding.

The effect was relatively small and could be diagnosed using an independent optical measuring system to establish if it is a due to the piston or sensor.

Hysteresis

The final demand value for Dataset 8 is 6098 and the initial demand value for Dataset 9 is 4098. The final demand value for Dataset 17 is 2098 with the initial demand value for Dataset 18 is 4098. Hence the actuator is driven to 4098 by an equal step size from opposite directions. Figure 5.24 shows that there is a 400 DAC Value difference in final value. This could be due to hysteresis.

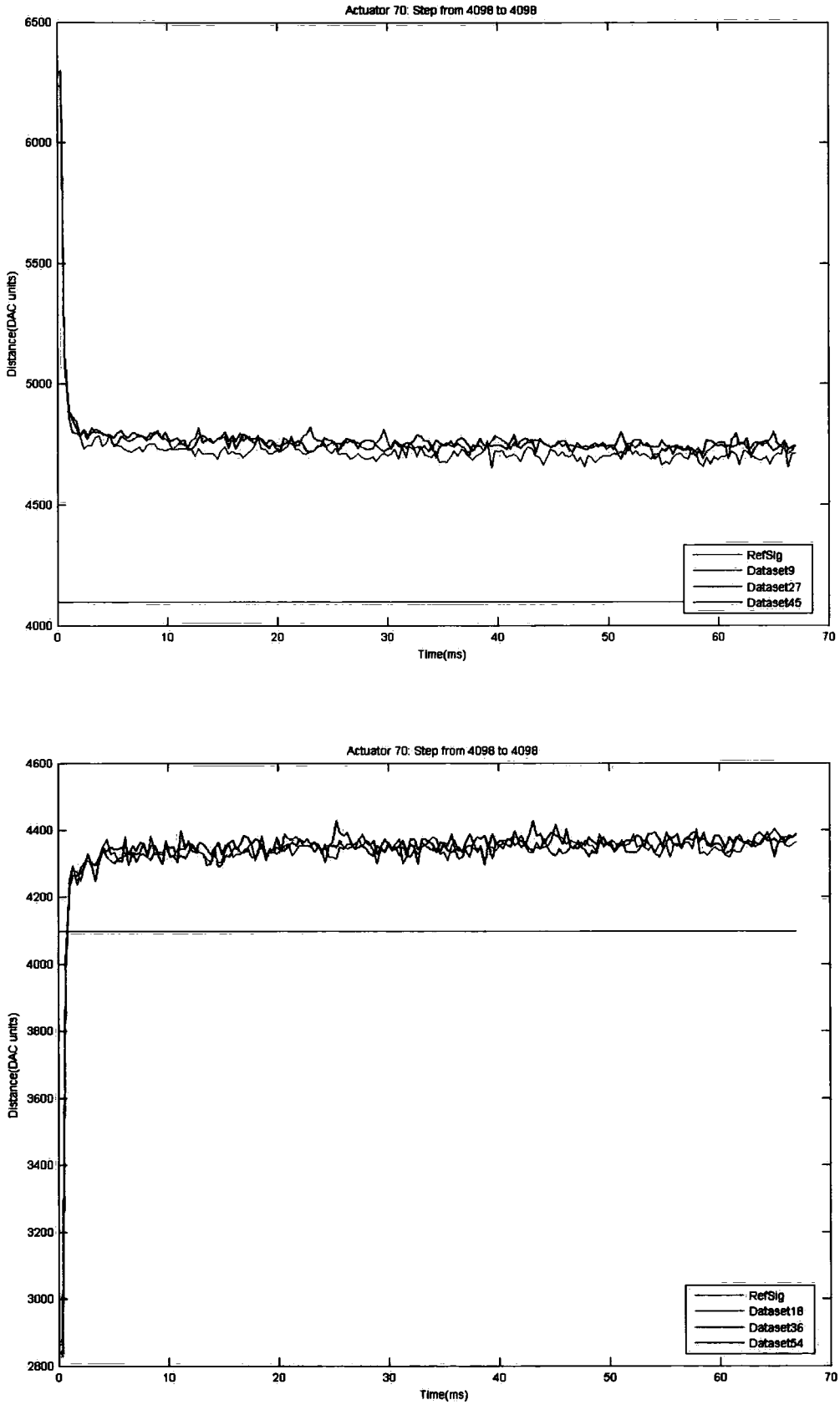

Figure 5.24 *Actuator 70: Example of Hysteresis*

5.3.7 Sine Wave Response Results

The characteristics of the Sine Wave patterns reflected those of the Step Response. The intention was to calculate statistics for the Sine Wave Response Data. However after interpreting the statistics calculated from the Step Response Data it was decided to only create the Matlab images. Figure 5.25 shows two of the dataset (2 Hz and 90 Hz) for Actuator 0. The demand signal and measured signal are indistinguishable. Figure 5.26 shows two of the datasets for Actuator 120 (2 Hz and 90 Hz). The plots demonstrate the requirement for recalibration as both the amplitude (gain) and position (offset) of the demand signal and measured signal are different.

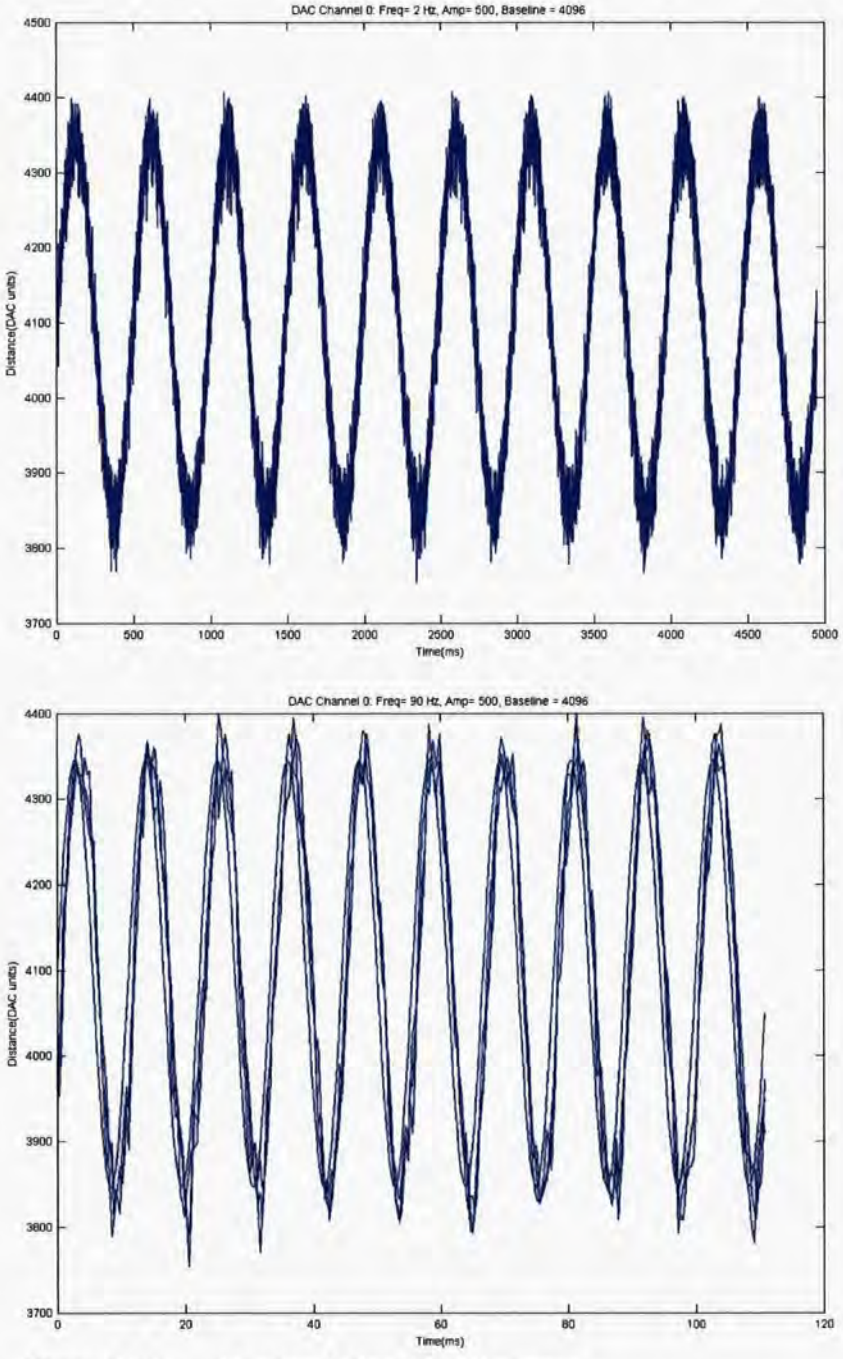

Figure 5.25 *Actuator 0 Sine Wave Response*

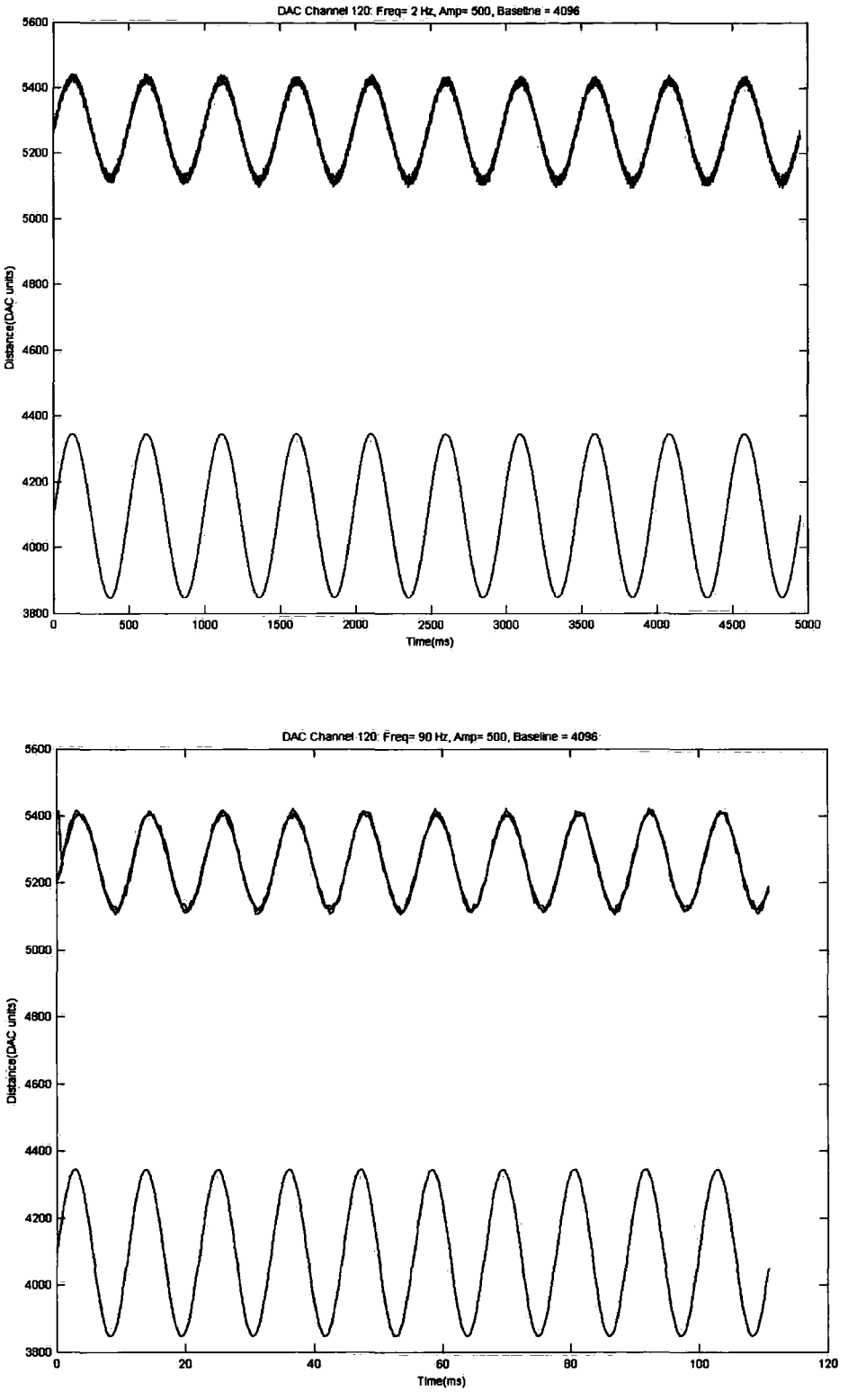

Figure 5.26 *Actuator 120 Sine Wave Response*

It was confirmed that the actuators were capable of being driven at 90 Hz without demonstrating significant phase lag, i.e., the demand signal and measured response are in phase.

5.3.8 Offset and Gain Calibration

DAC	DataSet											
	9 (-ve)		18 (+ve)		27 (-ve)		36 (+ve)		45 (-ve)		54 (+ve)	
	Mean	Stderr	Mean	Stderr	Mean	Stderr	Mean	Stderr	Mean	Stderr	Mean	Stderr
0	4098	23	4098	24	4098	23	4098	22	4098	24	4099	24
2	4098	28	4098	22	4098	25	4099	27	4098	26	4098	26
4	4098	25	4099	26	4098	25	4098	25	4099	24	4098	22
6	4097	17	4098	22	4097	20	4098	19	4098	19	4097	19
8	4098	19	4098	22	4098	22	4098	18	4098	20	4098	20
10	4098	20	4098	18	4098	19	4098	19	4098	23	4098	16
12	4098	20	4098	17	4098	17	4098	18	4098	17	4098	17
14	4098	14	4098	21	4098	19	4098	18	4098	21	4097	19
16	4098	23	4098	21	4098	21	4098	25	4098	26	4098	22
18	4098	11	4098	12	4098	11	4098	11	4098	13	4098	11
20	4098	10	4098	10	4098	8	4098	9	4098	10	4098	9
22	4098	10	4098	10	4098	10	4098	9	4098	10	4098	9
24	4098	9	4098	10	4098	9	4098	12	4098	9	4098	8
26	4098	9	4098	9	4098	9	4098	10	4098	9	4098	8
28	4098	8	4098	9	4098	9	4098	9	4098	8	4098	9
32	-2354	161	-2090	177	-2369	184	-2095	159	-2322	174	-2098	169
34	-61724	0	-61724	0	-61724	0	-61724	0	-61724	0	-61724	0
36	4098	18	4098	22	4098	17	4098	21	4098	18	4098	20
38	4098	19	4098	18	4098	20	4098	16	4098	18	4098	19
40	4099	21	4098	23	4098	20	4098	21	4098	19	4098	22
42	4033	19	4354	20	4071	20	4324	20	4091	20	4403	17
44	4098	16	4098	18	4098	16	4098	16	4098	16	4098	17
46	4098	8	4098	9	4098	8	4098	8	4098	9	4098	9
48	4098	10	4098	11	4098	10	4098	10	4098	11	4098	9
50	4098	10	4098	10	4098	11	4098	9	4098	10	4098	10
52	4098	8	4098	8	4098	8	4098	7	4098	8	4098	9
54	5732	12	5742	12	5879	9	6285	11	5869	9	6316	12
64	3848	13	3555	14	3858	14	3545	12	3847	15	3554	12
66	4174	13	3914	13	4217	16	3923	13	4238	14	3947	12
68	4204	18	3906	17	4267	17	3930	18	3983	19	3953	19
70	4706	23	4350	20	4744	22	4351	19	4749	19	4363	19
72	4491	17	4501	19	4880	19	4529	18	4892	18	4900	21
74	4543	15	4188	16	4604	16	4222	16	4619	17	4240	18
76	4021	12	3747	13	4057	13	3768	12	4069	13	3783	14
78	4893	12	4650	12	4937	13	4674	12	4685	10	4680	12
80	5205	16	4861	16	5229	16	4878	15	5245	14	4906	14
82	5133	9	4760	8	4786	7	5069	7	5152	8	4782	8
84	5193	7	4867	8	5210	9	4890	7	5228	8	4888	7
86	5718	9	5388	8	5718	9	5374	8	5437	7	5378	8
88	5478	9	5143	9	5500	10	5142	9	5504	9	5147	10
90	5444	10	5069	10	5122	8	5072	10	5461	11	5077	9
92	6090	9	5792	8	6150	9	5830	8	6171	8	5836	8
96	3568	50	3767	50	3539	52	3772	55	3528	56	3799	50
98	3378	725	3788	670	3462	743	3961	721	3571	647	3906	738
100	3652	39	4074	42	3698	41	4083	40	3742	39	4114	41

Colour Key:

DAC Channel	Mean
Light Path	4098±10
Outer Ring	4098±100
Inner Square	4098>±100

Table 5.9 *Even actuators (1-100) Offset Adjustment Information*

Offset calibration information can be taken from either the Step or Sine Wave Response data. Table 5.9 displays the actual positions of a selection of actuators when the demand value was 4098. This information can be used to calculate the new offset value for each actuator. Gain calibration information can be derived by calculating the scaling factor required to match the amplitude of actual oscillations with that of the amplitude of the demand value. For example, Figure 5.26 shows that the amplitude of the demand values is greater than that of the actual values. Hence the gain should be increased accordingly.

5.3.9 Conclusions and Follow on work

The main conclusions were that 45 of the 228 actuators behaved as expected. Suspiciously, these were the early-numbered DAC channels. Scripts were double-checked to ensure that the correct gain and offset values were being used in the data-reduction post-processing routines. It is possible to recalibrate the other 183 channels, yet beforehand further tests are required. Some channels showed characteristics explained by Integral Wind Up and Hysteresis. There was a drift in some actuators. Without isolating the DM or having an independent way of measuring the position of the mirror (such as an optical setup), there isn't an easy way of confirming whether the discrepancies are associated with positioning or the strain gauge sensor.

The results indicated that the latency of a well behaved actuator moving to its demand value was around 3 ms. The latency could be reduced to around 0.5 ms given an optimised hardware feedforward controller such as the Smith Predictor by eliminating the settling time and rise time. The average overshoot relates to around a 50 DAC (37 nm) piston error.

Optimising the DM in other areas, such as removing Integral Wind Up and recalibrating the actuators would improve performance far more than introducing an optimised controller. Considering the FSM was adding tilt for a number of years, the Integral Wind Up of the DM would have limited the effectiveness of the instrument during that period; hence it helps explain why the instrument would suddenly stop correcting during an observation.

The investigation uncovered some interesting discoveries yet it didn't achieve all of its original goals. Only one set of experiments was conducted at one fixed temperature, hence the effect of changing temperature and the performance of the temperature compensation algorithm within GRACE wasn't understood. The temperature of GRACE doesn't vary significantly overnight but the set point does change season to season.

Assuming it was possible to eliminate the effects of temperature and to fix the other problems associated with the system at the moment in time of conducting the experiments then it was possible to more accurately estimate the potential improvements that a feedforward controller could give.

The bug associated with collecting Sine Wave data from all channels needs to be resolved and the actuators need to be oscillated at a frequency greater than 90Hz to extract useful information. Again, having independent equipment to measure the response to the DM is crucial.

5.4 WFS Characterisation

Between November 2003 and February 2004 the author was part of the ING NAOMI team that characterised the performance of the WFS.

5.4.1 Background

The NAOMI WFS is briefly described in Section 4.5.3. Dr Ilona Sochting (ING) was tasked to take ownership of the modelling and simulation of NAOMI from Durham in 2003.[239, 257]

During NAOMI operation the best choice of WFS readout mode, readout speed and lenslet array depends on atmospheric conditions and the luminosity of the guide star. As the ING conducted their simulations, astronomers performed on-sky characterisation of different readout modes under varying atmospheric conditions. Astronomers were seeing no difference in good seeing and bad seeing performance (contrary to simulations). It became clear that the instrument was not performing as expected and this became the main reason for the WFS characterisation investigation.

Initially two additional WFS modes (11 and 12) were added to the original set to aid the investigation. In addition, two of the original modes (8 and 9) were configured so that they both could be uploaded to the WFS SDSUII Controller at the same time to allow fast switching between the two without rebooting. The significant reduction in switching time allowed the user to open the AO loop, switch mode and close the AO loop during observation without losing the guide star or introducing significant wavefront error to the observed targets. These tests confirmed that there were problems and hence further ING resources were assigned to the investigation.

Three additional WFS modes (13, 14 and 15) were required to help characterise the problems on-sky and to optimise performance. In addition, an independent check of the latencies associated with the WFS subsystem was required. This became the responsibility of the author. Understanding the performance of the WFS would provide useful information that could be used to tune an optimised controller.

5.4.2 WFS Readout Modes

Table 5.10 displays the complete set of modes required for on-sky characterisation of the instrument. The schematics contained within Figure 5.27 and Figure 5.28 helps explain the difference between WFS modes. Firstly Figure 5.27 shows the schematic template, which displays a quadrant of the CCD39. This includes the underscan region (first four columns on the left) consisting of 4 x 40 pixels and the active area of the quadrant consisting of 40 x 40 pixels. The serial register can be seen at the bottom of the diagram. The pixel on the far left of the serial register is the readout pixel.

All formats, with the exception of the tip-tilt mode (10) are displayed. The dark spot represents light from the lenslet array. The readout pixels are coloured grey. Binned pixels (Mega pixels) are identified by larger squares. The schematics are consistent with the information contained within Table 5.10.

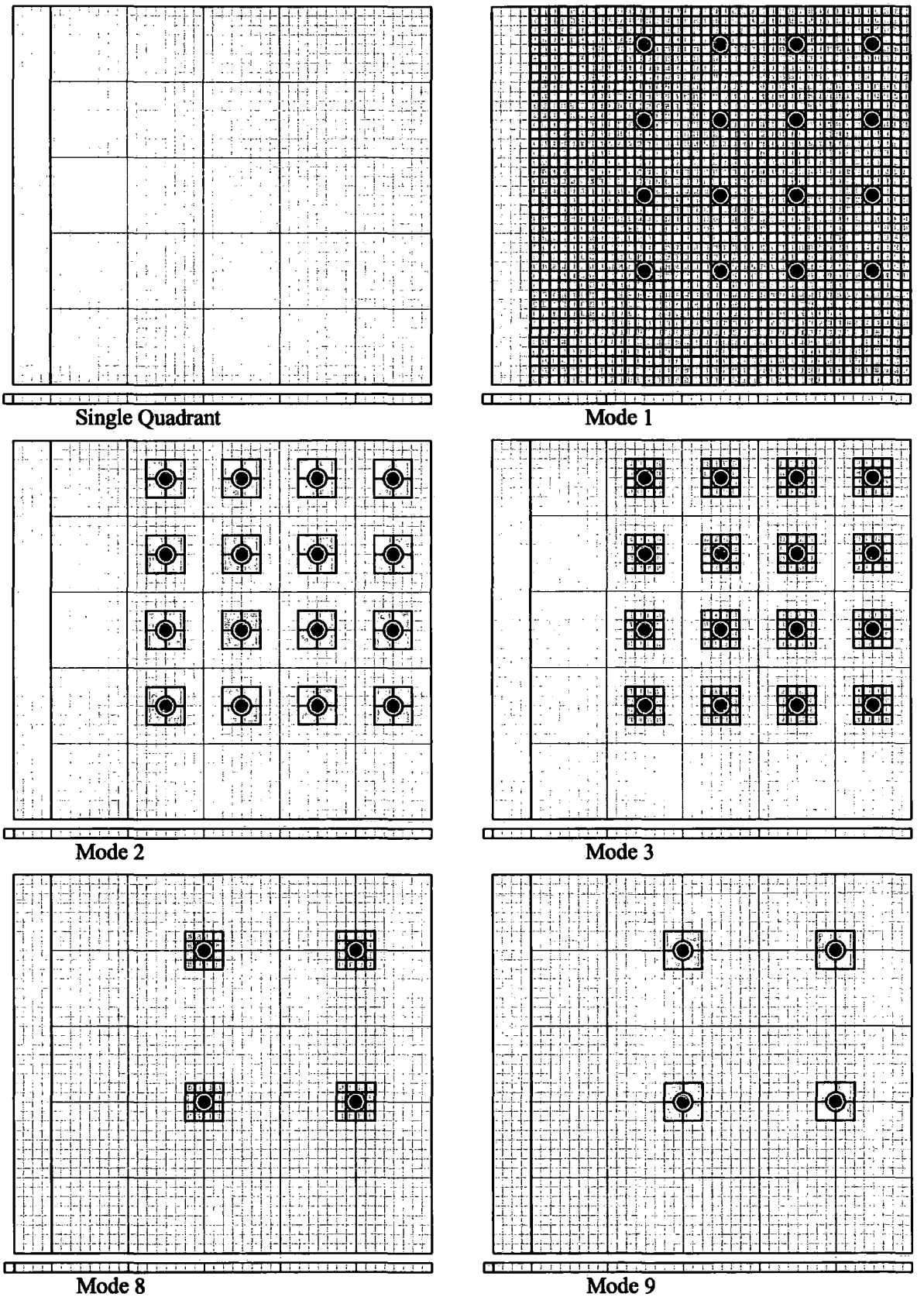

Figure 5.27 *CCD39 Layout for WFS Modes 1, 2, 3, 8 and 9*

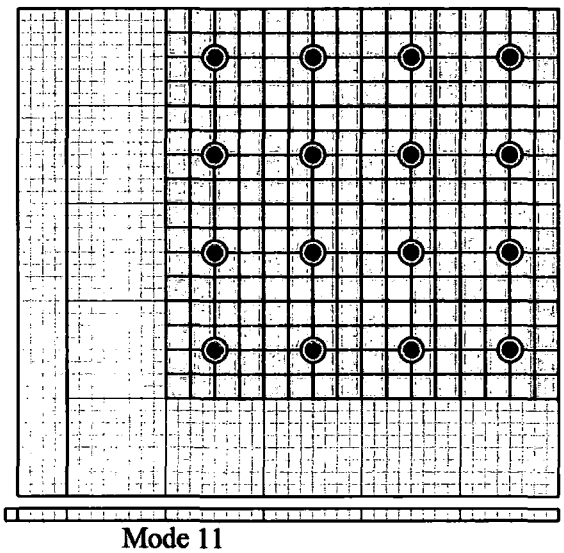

Mode 11

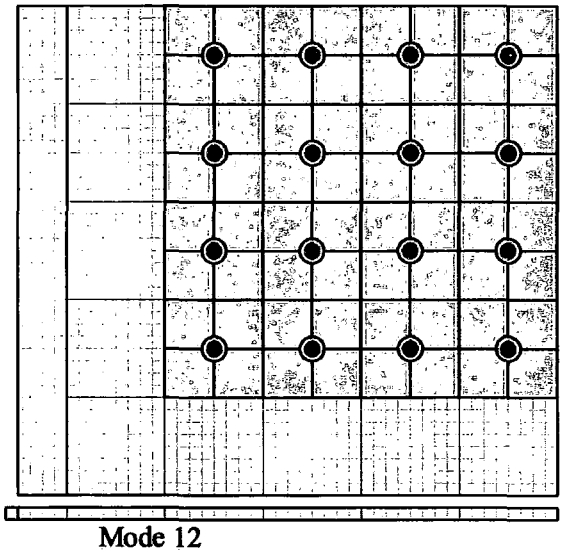

Mode 12

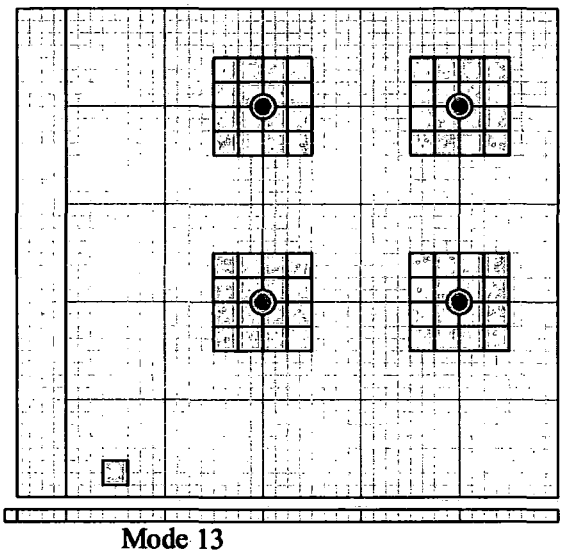

Mode 13

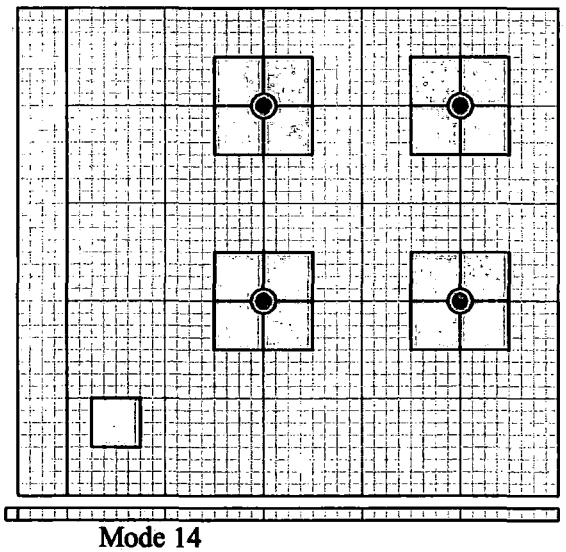

Mode 14

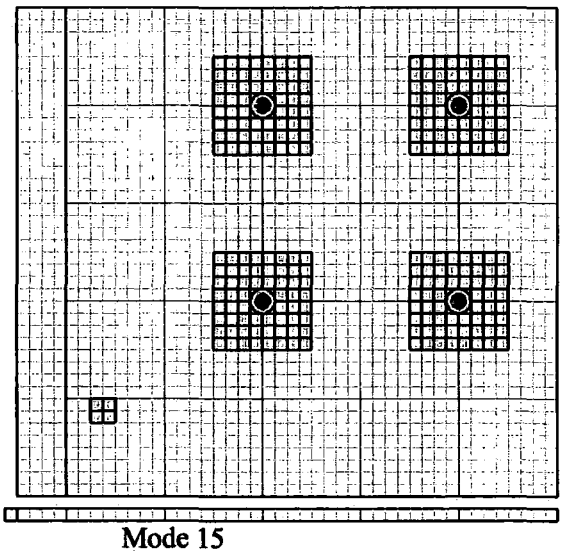

Mode 15

Figure 5.28 *CCD39 Layout of WFS Modes 11, 12, 13, 14 and 15*

Mode	Lenslet	Sub-Aps	Visible Pixels	Binning	Name
1	8 x 8	8 x 8	8 x 8	1 x 1	8x8_8x8_1x1
2	8 x 8	8 x 8	2 x 2	2 x 2	8x8_2x2_2x2
3	8 x 8	8 x 8	4 x 4	1 x 1	8x8_4x4_1x1
8	4 x 4	4 x 4	4 x 4	1 x 1	4x4_4x4_1x1
9	4 x 4	4 x 4	2 x 2	2 x 2	4x4_2x2_2x2
10	Doublet	1 x 1	2 x 2	2 x 2	1x1_2x2_2x2
11	8 x 8	8 x 8	4 x 4	2 x 2	8x8_4x4_2x2
12	8 x 8	8 x 8	2 x 2	4 x 4	8x8_2x2_4x4
13	4 x 4	4 x 4	4 x 4	2 x 2	4x4_4x4_2x2
14	4 x 4	4 x 4	2 x 2	4 x 4	4x4_2x2_4x4
15	4 x 4	4 x 4	8 x 8	1 x 1	4x4_8x8_1x1

Table 5.10 *WFS Modes*

Mode 13, 14 and 15 in Figure 5.28 identifies the background subtraction readout pixels.

5.4.3 Measuring the Existing Modes

It was decided to measure the latency associated with the existing modes before creating the new modes. Measuring the latency was relatively quick and easy.

The latency associated with the WFS can be divided into the following components:

- Integration Time.
- Image to Storage Transfer Time.
- Readout Time.
- SDSUII Controller to C40 Transfer Time.

The **Integration Time** was set by the user. It was set to be as low as possible depending on the seeing, guide star brightness, noise levels, centroid accuracy, the limitations of the CCD (~1000 frames per second) and CCD controller (~400 frames per second). It was found that an Integration Time of 1.875 ms or less caused the system to become unstable and crash.

The **Image to Storage Transfer Time** was estimated by information contained within the split frame device's manual. With the image clock running at typically 1 MHz (1 μs per clock), the time taken to transfer the data from the image area to the store area was around 40 μs. This time delay is negligible and not seen considering that the minimum stable integration time was 2.5 ms.

The **Readout Time** was both CCD mode and WFS mode dependent. Firstly there are two different pre-programmed read out speeds (fast and slow); fast mode gave a read noise of 7.2 e^- RMS and the slow mode gave a read out noise of 4.7 e^- RMS. This choice depends on SNR. For the latency characterisation, only the fast mode was considered.

It was possible to calculate the readout time for each mode by understanding the mode's associated assembly code and the workings of the SDSUII Controller. The difference in readout time relates to the number of clock cycles required in extracting the pixel data. Discarding and binning pixels reduces the readout time, hence the greatest readout time is associated with full frame readout, Mode 1.

The **SDSUII Controller to C40 Transfer Time** was the time taken to transfer the data from the controller to the C40 RTCS. The time taken to transfer information from the SDSUII Controller via Fibre Optics to the Interface card and across the card to the RTCS was difficult to test in isolation. As the data transfer didn't use the VME backplane and used relatively high-speed links, it was estimated to be negligible compared with the integration and readout times.

An additional benefit of conducting latency tests was to provide information for estimating the benefit of using faster hardware, such as the SDSUIII Controller, see Section 5.4.5.

It was decided to use the C40 Strain Gauge logging facility to establish when a new frame arrived into the system. It was also decided to test the full range of pre-programmed integration times ranging from 50 ms down to the unstable 1.875 ms.

The author produced a test plan which included the use of the C40 SG Log command. The aim was to modify the log statement on line 573 of the AlgMartini.c algorithm running on DSP#4 to help derive the latency.

A script was created to read the output of the Log command, strip away the headers and manipulate the timing information, hence calculating the time taken between issuing the command and receiving the data. 20 sets of information for each combination were obtained and the average timing values were calculated. The original results were scaled, as a C40 clock tick was 66 ns (instead of 60 ns as originally used in the code). Table 5.11 contains the results that were obtained on the 28th January 2004.

t_{int} (ms)	f (Hz)	Mode 1	Mode 2	Mode 3	Mode 8	Mode 9
50	20	55.96	51.06	52.60	51.12	50.30
25	40	31.13	26.28	27.81	26.35	25.52
10	100	16.28	11.41	12.94	11.46	10.65
5	200	11.33	6.45	7.99	6.50	5.68
2.5	400	8.84	3.97	5.50	4.03	3.20
1.875	533	8.32	3.36	4.87	3.40	3.86

t_{int} (ms)	f (Hz)	Mode 88	Mode 89	Mode 11	Mode 12	Mode 10
50	20	51.13	50.30	52.09	50.49	49.84
25	40	26.33	25.53	27.28	25.70	25.08
10	100	11.46	10.64	12.43	10.82	10.19
5	200	6.50	5.68	7.45	5.86	5.23
2.5	400	4.03	3.21	4.97	3.39	2.75
1.875	533	3.40	3.96	4.35	2.76	4.27

Table 5.11 *WFS Modes Latency Results*

The integration time was then subtracted from the measured time to leave a combination of the Readout time and Transfer time. These results are shown in Table 5.12.

t_{int} (ms)	f (Hz)	Mode 1	Mode 2	Mode 3	Mode 8	Mode 9
50	20	5.96	1.06	2.60	1.12	0.30
25	40	6.13	1.28	2.81	1.35	0.52
10	100	6.28	1.41	2.94	1.46	0.65
5	200	6.33	1.45	2.99	1.50	0.68
2.5	400	6.34	1.47	3.00	1.53	0.70
1.875	533	6.44	1.48	3.00	1.52	1.99

t_{int} (ms)	f (Hz)	Mode 88	Mode 89	Mode 11	Mode 12	Mode 10
50	20	1.13	0.30	2.09	0.49	-0.16
25	40	1.33	0.53	2.28	0.70	0.08
10	100	1.46	0.64	2.43	0.82	0.19
5	200	1.50	0.68	2.45	0.86	0.23
2.5	400	1.53	0.71	2.47	0.89	0.25
1.875	533	1.52	2.09	2.47	0.89	2.39

Table 5.12 *WFS Modes Readout Times*

The first positive observation was that Mode 1 gave the greatest readout time and Mode 9 the shortest readout time, excluding Mode 10, as expected. Mode 1 results ranged between 6.0 and 6.5 ms depending on mode.

A few months after these tests were conducted, it was discovered that the ATC had conducted some tests before commissioning using a C40 Interface card to measure the readout latency from the SDSUII Controller and they had also conducted calculations based on timing. Both of these were in agreement. For the fast readout mode the ING were told that the readout time for Mode 1 was 6.17 ms and Mode 2 was 1.5 ms. As these results matched the measured results to the required accuracy, they were never verified at the ING.

5.4.4 Creation of Modes 13, 14 and 15

In February 2004 the author travelled to the ATC to create new WFS Readout modes.

Assembly code for modes 13, 14 and 15 was written, as was the accompanying VxWorks application script. A section of the Mode13appl_code.asm file is displayed in Figure 5.29 and the complete App13.m script is contained within Figure 5.30.

When the SDSUII Controller is powered, the DSP automatically loads bootstrap code from the E^2PROM into its P, X and Y memory. Its initialisation data is stored within its P memory, allowing application data to be uploaded to its X and Y memory. It is possible to assemble DSP assembly data (.asm) files and to upload these (.s) objects to the E^2PROM using an RS232 connection. As the total application code for NAOMI is bigger than the E^2PROM memory and is modified frequently, it is uploaded into memory using the SDSUII controller link when required, hence the need for VxWorks scripts.

```
; ************* START APPLICATION CODE HERE ***************************
; ******************** Acquire a complete image **********************
; Acquire real data continously until aborted
APPLICATION
        BSET    #COM_MOD,X:<STATUS    ; Put controller in camera run mode
        MOVE    X:<OP_MODE,X0         ; tell system which application is running
        MOVE    X0,P:$7
READ_CCD

; Integrate signal for specified time first the minimum exposure time will be the time it takes to run
; all the code above from START to the time the frame transfer takes place
        MOVE    #L_MRA1,R7
        JMP     <EXPOSE         ; Delay for specified exposure time
L_MRA1
        BSET    #WW,X:PBD               ; Set WW to 1 for image data
        NOP
        JSR     <TX_HEADER              ; tx header info at start of frame
; shift image from image area to storage area first
        DO      #40,END_VCLK1           ; frame transfer CCD - only 40 real active rows
        MOVE    #<V_ISCLK,R0            ; per quadrant
        JSR     <CLOCK
        NOP
END_VCLK1

; Get BIAS (2x2) MegaPixel
; shift vertically to prepare bias area line (2 rows)
        DO      #2,PREBIAS_VSFT
        MOVE    #<V_SCLK,R0
        JSR     <CLOCK
        NOP
PREBIAS_VSFT
; clear the serial register (under scan)
        DO      #44,CLRREG1
        MOVE    #<H_CLK,R0
        JSR     <CLOCK
        NOP
CLRREG1
; shift vertically to bias area line (2 rows)
        DO      #2,BIASINREG
        MOVE    #<V_SCLK,R0
        JSR     <CLOCK
        NOP
BIASINREG
; dump the first 6 pixels (4 underscan)
        DO      #6,DUMP1
        MOVE    #<H_CLK,R0
        JSR     <CLOCK
        NOP
DUMP1
; now collect 2x2 for bias reading
        MOVE    #<PIX_BIN2R,R0
        JSR     <CLOCK
        NOP
; dump last 36 pixels
        DO      #36,DUMP2
        MOVE    #<H_CLK,R0
        JSR     <CLOCK
        NOP
DUMP2
```

Figure 5.29 *Part of Mode13appl_code.asm file*

```
# This script is to set the camera to application 13 (mode 4)
# Lenslet 4x4, Readout 8x8 binned into 4x4 array (4 pixels in each bin)
# This assumes Mode 1 was used first (or a startup script to "PON" the CCD)
# See Readout Script for Mode 1
# S.Goodsell  03/02/2003

# stop readout before download application 13
sdsuCommand("cam1",1,"ABT");
sdsuMemory ("cam1", 2, "FDL", "../timing/ap_13/master_download.lod");
taskDelay(1);

sdsuReadoutRDS("cam1", 50)
sdsuCommand("cam1",2,"LDP",0)
sdsuCommand("cam1",2,"SYC",0,0)

sdsuCommand("cam1",2,"SET",200,0)
sdsuCommand("cam1",2,"SYC",0,0)

sdsuCommand("cam1",2,"HIH",0,0)
sdsuCommand("cam1",2,"SYC",0,0)
```

Figure 5.30 *App13.m file*

The assembly code for the new modes was successfully compiled, placed in the required directory and in turn successfully uploaded to the SDSUII Controller. Checksum tests reported no problems with the compiled code. The functionality contained within the source code was independently checked by the ATC.

For the modes to be used in operation, other modifications were required to the NAOMI software. Modifications were made to the C40 DSPs to correctly interpret and process the data for the new modes. Additional modifications were required to TopGui and other middleware components before the new WFS Modes could be used.

The author was sent to Durham to take ownership of TopGUI and the associated middleware with the aim of modifying the code to change to the new modes and to view the associated WFS pixel data.

Before these required modifications were made, the FSM investigation (which had started in parallel) had made a key discovery which partially explained why switching between WFS modes caused little or no difference. (See Section 5.2)

Hence, resources were reallocated and the required modifications to TopGui were never made. Modes 13, 14 and 15 were never fully commissioned.

5.4.5 The SDSUIII Controller

The final aspect of the investigation was to determine the potential gains in upgrading the SDSUII to a SDSUIII controller. Associated with this was the replacement of the CCD39 with a CCD60.

The SDSUIII contained a Motorola 250 Hz DSP56301, which was twice as fast as the SDSUII DSP. This, combined with greater on-chip memory, would approximately halve the readout time for each mode. Another benefit of the SDSUIII controller was that it should operate twice as fast (~800 Hz) without crashing, hence approaching the 1 kHz limits of the CCD39.

The limiting latency factor was the integration time of the controller. One major limitation at the time was the number of photons required to perform WFSing. The integration time (time taken to obtain the photons from a guide target) is inversely related to the brightness of the object. Increasing the speed and reducing the readout time would be of most benefit when guiding on bright objects. GLAS would benefit the most from this upgrade.

5.4.6 Conclusion

The main conclusion of the investigation before it came to an early end was that the latencies associated with the WFS were as expected and didn't explain the lack of relative performance between modes. The readout time for Modes 9 and 12 are 6 to 8 times smaller than Mode 1, yet no performance benefits were witnessed.

5.5 RTCS Characterisation

In July 2002 the author was given the task of taking ownership of the NAOMI RTCS from Durham University. Between July 2002 and November 2003 the author began to characterise and develop the RTCS.

RTCS characterisation was required partially to assess the potential improvements any optimisation tasks would deliver. The investigation was to begin with the initial task of measuring the Strain Gauge (SG) loop speed.

The aim was to follow this by attempting two minor optimisation upgrades before fully optimising the RTCS by introducing a feedforward controller. The two optimisation tasks were:

- Balancing the Load.
- Oversampling the Strain Gauges.

5.5.1 Measuring the speed of the strain gauge loop

One of the first characterisation tasks was to measure the speed of the SG loop. This was done using the python script command:

SG Log <cpuNumber>

This command invokes the Log function of the Electra/RealTime/pythonModules/SGtest.py library and prints out the data from LOG statements (macros) within each C40 C source file.

These cause a number of argument to be recorded in a circular log buffer along with the frame number, line number, and timer value in 66 ns clock units (Twice the 33 ns cycle time). The script retrieves and prints this log from the selected CPU. Hence, it is then possible to time any part of the algorithm by looking at the delta-times between any pair of LOG statements.

This command was invoked twice for CPU 11 and the output is shown in Figure 5.31. The useful data has been extracted and is displayed in Figure 5.32. As the TI TMS320C44 DSP's 33 ns cycle time gives a 66 ns clock unit; a complete clock cycle is around 342±2 μs.

```
naomi@navis> SG Log 11
cpu 11:
         t  delta_t     frame      line         value        (hex)
1010115680      171 287334400       608             0 (0x00000000)
1010115746       66 287334400       657          3402 (0x00000d4a)
1010110529    -5217 287334399       608             0 (0x00000000)
1010110594       65 287334399       657          3413 (0x00000d55)
1010112332     1738 287334400       201             0 (0x00000000)
1010112368       36 287334400        31             7 (0x00000007)
1010112487      119 287334400       315             0 (0x00000000)
1010112516       29 287334400       169           555 (0x0000022b)
1010112950      434 287334400       319             0 (0x00000000)
1010113355      405 287334400       391             0 (0x00000000)
1010113499      144 287334400       436    1242808640 (0x4a13c140)
1010113516       17 287334400       440             0 (0x00000000)
1010113674      158 287334400       477             0 (0x00000000)
1010114899     1225 287334400       572             0 (0x00000000)
1010115278      379 287334400       580             0 (0x00000000)
1010115509      231 287334400       600             0 (0x00000000)

naomi@navis> SG Log 11
cpu 11:
         t  delta_t     frame      line         value        (hex)
1052999042      119 287342651       315             0 (0x00000000)
1052999071       29 287342651       169           555 (0x0000022b)
1052999510      439 287342651       319             0 (0x00000000)
1052999914      404 287342651       391             0 (0x00000000)
1053000058      144 287342651       436    1242808640 (0x4a13c140)
1053000076       18 287342651       440             0 (0x00000000)
1053000234      158 287342651       477             0 (0x00000000)
1053001459     1225 287342651       572             0 (0x00000000)
1053001837      378 287342651       580             0 (0x00000000)
1053002068      231 287342651       600             0 (0x00000000)
1053002240      172 287342651       608             0 (0x00000000)
1053002305       65 287342651       657          3407 (0x00000d4f)
1052997043    -5262 287342650       608             0 (0x00000000)
1052997109       66 287342650       657          3410 (0x00000d52)
1052998887     1778 287342651       201             0 (0x00000000)
1052998923       36 287342651        31             7 (0x00000007)
```

Figure 5.31 *Output of SG Log 11 Command*

line	Frame	t (ticks)	Frame	t (ticks)	Δt (ticks)	t (μs)	f (kHz)
608	287334399	1010110529	287334400	1010115680	5151	340	2.9
657	287334399	1010110594	287334400	1010115746	5152	340	2.9
608	287342650	*1052997043*	287342651	*1053002240*	5197	343	2.9
657	287342650	*1052997109*	287342651	*1053002305*	5196	343	2.9

Figure 5.32 *Extracted SG Loop Timing information for CPU 11*

5.5.2 'Balancing the Load' Optimisation Task Description

As described in Section 4.5.6, the eight SG DSPs read the state of the SDM SGs using the three Pentland ADC cards. The ADCs delivered the data via six c40 communications ports to the c40 CPUs. Four CPUs receive 32 channels of data per sample (CPU 12, 13, 15 & 16), two received 64 channels (CPU 11 & 17), and two, having no ADC communications port connections, received none (CPU 14 & 18). Processing was therefore unevenly balanced because two of the CPUs had twice as many channels to process as the nominal load, whilst two had none to process.

The two CPUs receiving 64 channels were each immediately upstream (in the real-time communications ring sense) from a CPU receiving none. Hence to 'Balance the Load' the new software must therefore take 32 of the 64 channels in the large blocks and transmit them to their downstream neighbour CPUs, which must process them.

Functions for transmitting and receiving the data blocks should be available in the lower-level data-transmission procedures called by BarrierSynch. The implementation was therefore straightforward in principle: the two idling CPUs must run aspects of the AlgSGadc data-processing algorithm, which must be modified to allow optional transmission and receipt of the 32 channels to be transferred.

The complication lay in the fact that the CPUs 14 and 18 ran specialised algorithms for performing particular functions.

CPU18 was the timer CPU and ran AlgSGtimer; it was responsible for setting up the internal timer which triggers ISR invocations on this ring. It then sent the trigger pulse to the ADC cards. CPU18 was also the ringleader.

CPU14 was the mirror CPU and ran AlgSGmirror; it was responsible for transmitting final demand data to the mirror DACs. If these two CPUs were to run a new version of AlgSGadc then that algorithm must be modified to optionally perform these additional functions and must be configured to actually do so in the case of these two CPUs.

As the Strain Gauge Loop speed (for CPU 11) was measured to be ~340 μs, the maximum reduction in time would be ~ 170 μs. This assumes halving the load would double the bandwidth frequency to 5.8 kHz. This doesn't allow for overheads or the time taken to execute the mirror or timer function, although they should be minimal.

5.5.3 'Oversampling' Optimisation Task Description

The aim was to measure the strain gauge noise in DAU (equivalent DAC units) for each actuator. The basis for this may be seen in the following utility:

SG ChanPrint <dacChannel> <numSamples>

Each DAU is equivalent to an Optical Path Difference (OPD) of about 1.5 nm. As there are 3 actuators per segment, one must calculate how the noise in individual actuator positions translates to a waveform error.

An approximate value is obtained by adding the sum of the squares of the noise on the three actuators on each segment. Summing the squares of all these segment errors gives the OPD variance estimate across the whole mirror.

The fractional degradation of Strehl Ratio can be approximated by:

$$SR = \exp\left[\left(\frac{-\sigma}{\lambda}\right)^2\right] \tag{3.1}$$

Hence the fractional degradation of Strehl Ratio is wavelength dependant.

An alternative approach would be to use the Monte Carlo wavefront error and Fourier Transform method, which would allow the prediction of an actual point-spread function due to these errors. This is achieved by averaging the effects of several randomly configured wavefronts whose statistical properties are forced to mimic those measured for the actual mirror (i.e. the noise levels).

5.5.4 Limitations of DSPs

An attempt was made to balance the load. A generic AlgSGcombine algorithm was developed with the aim to place the algorithm on all 8 SG DSPs. Details of the modifications are given in Appendix D.

The code was modified and successfully compiled. However, problems occurred when executing the C40 code in real-time. The DSPs were incapable of balancing the load without sacrificing the ability to debug the system's amount of on-chip memory. (8 kB) As it was nearly impossible to debug, it was decided to focus efforts instead on overcoming the limitations of the NAOMI RTCS rather than trying to struggle with modifying the existing RTCS.

A seemingly natural upgrade path would be to replace the C44 DSPs with C67 DSPs, yet after an initial feasibility study based on interaction with Hunt Electronics, it was realised that upgrading the RTCS would be a time-consuming and a complex task. Table 5.13 compares the specification of a C44 with a C67.

	C44	**C6713-200**
Performance	30 MIPS	1600 MIPS
	60 MFLOPS	1200 MFLOPS
Memory (Bytes)	8	264
Cycle Time (ns)	33	5
DMA	6	16 EDMA
CMOS Technology	0.72 micron	0.13 micron

Table 5.13 *Comparison of C67s and C40s*

5.6 Characterisation Conclusions

Table 5.14 summarises the component latencies both before and after the documented characterisation investigation.

Component	Source	Latency (Before)	Latency (After)
FSM	FSM	1.5 ms	1.5 ms
	FSM Filter	15 ms	2.7 ms (new Filter) 0 ms (Removed)
SDM	Actuators Lag	0.5 ms	0.5 ms
	Actuator stabilisation	2.5 ms	2.5 ms
WFS	Integration Time	2.5 ms	2.5 ms
	Readout Time	6.2 ms (Mode 1)	0.7 (Mode 9)
RTCS	SG Loop	0.3 ms	0.3 ms

Table 5.14 *Characterisation Investigation Latency Measurements*

The characterisation investigation contained some successful (and unsuccessful) attempts at improving the performance and stability of the system.

GRACE characterisation revealed that the internal temperature was stable to 1 °C overnight; hence recalibration between observations was no longer required as they were when NAOMI was in GHRIL. A further investigation is required to measure the effects the 1 °C temperature change has on NAOMI's performance; especially the DM. Another outcome of the investigation was the identified requirement for remote cryostat filling. A GRACE upgrade plan was conceived and pursued.

FSM characterisation revealed an unexpected source of unacceptable latency, introduced by the commissioned FSM Filter. The FSM was introducing tip/tilt errors into the system instead of reducing them. The filter was replaced, although NAOMI could operate safely without it, and the latency reduced from 15 ms to 2.7 ms. The latency of the FSM itself was measured to be 1.5 ms. A PID Controller was introduced and tuned to eliminate integral wind-up and improve performance. Further characterisation saw an increase in performance from being destructive to correcting tip/tilt well 20 Hz.

SDM characterisation revealed well behaved and badly behaved actuators. The badly behaved actuators required retuning. Sufficient information was gathered to calculate new offset and gain values for each actuator. A further investigation is required to see how temperature changes affect the strain gauge readings around a nominal value. Well behaved actuators demonstrated measurable characteristics. The average latency associated with rise time, overshoot and settling time was measured to be 2.5 ms. This 'Actuator Stabilisation' latency could be removed by the introduction of an optimised controller. An additional lag of 0.5 ms was associated with the DM electronics; DAC cards and HVA.

WFS characterisation divided latency into two major sources, the Integration Time and Readout Time. The Integration Time was limited by the brightness of the guide object and to a lesser extent the characteristics of the CCD. The readout time was limited by the SDSUII Controller. Before the FSM Filter was diagnosed further WFS modes were planned to improve performance. These were abandoned when the FSM Filter latency was discovered. Once the original FSM Filter was replaced, the performance of Mode 9 became noticeably better, which effectively reduced the readout time.

RTCS characterisation was relatively short. The C40 loop speeds were measured. The WFS loop latency couldn't be deduced through timing experiments and is mode dependent. It was estimated to be 0.5 ms. The SG loop time was measured to be 0.34 ms which is small compared to the other sources of latency. The total latency of the RTCS was no more than 1 ms. Some initial optimisation changes were identified and maximum potential benefits quantified.

Table 5.15 lists a set of NAOMI Hardware configurations and Table 5.16 gives related timing information. It lists whether the FSM and DM will reach their desired positions before the RTCS receives the next WFS frame.

Config.	WFS Controller	WFS Mode	FSM Filter	DM Controller	RTCS
1.	SDSU II	1	old	Proportional	C40
2a	SDSU II	1	new (2.7 ms)	Proportional	C40
2b	SDSU II	9	none	Proportional	C40
3	SDSU II	9	none	Feedforward	C40
4	SDSU III	9	none	Feedforward	C40
5	SDSU III	9	none	Feedforward	New

Table 5.15 *NAOMI Component Configurations*

Configurations 1 and 2 contains the NAOMI components before and after the characterisation investigation respectively. To benefit from Mode 9, it shows that the DM response-time needs to be reduced. This can be achieved by introducing a feed-forward controller as shown in Configuration 3.

Config.	Int. Time	Read. Time	Time to act	RTCS	FSM	DM	In time
1	2.5	6.2	**6.2**	1	**16.5**	3	**NO**
2a	2.5	6.2	**6.2**	1	4.2	3	**YES**
2b	2.5	0.7	**2.5**	1	1.5	**3**	**NO**
3	2.5	0.7	**2.5**	1	1.5	0.5	**YES**
4	1.0	0.4	**1**	**1**	**1.5**	0.5	**NO**
5	1.0	0.4	**1**	0.5	0.5	0.5	**YES**

Table 5.16 *Timing different Scenarios (times in ms)*

As suspected, attempts at implementing the simplest of RTCS pre-optimisation changes were futile. Only the simplest changes could be made, such as coding a FSM PID Controller and coding basic WFS modes changes (required for GLAS). The following shortfalls were identified:

- **Limited on-chip memory**
  The on-chip memory of each C40 was relatively tiny. When combining Strain Gauge algorithms in an attempt to 'Balance the Load', the C40s run out of on-chip memory. During development some blocks of memory were removed which caused problems as the system became impossible to debug. As the DSPs used a self-optimising compiler, it was very difficult to see how many ticks each operation would take and which memory the processors would use. It was quicker to implement the changes than to calculate/estimate whether the changes were possible.
- **Limited Support / Development Tools**

The C40s were obsolete; Texas Instrument had stop supporting them. TI gave training courses on the newer DSPs (such as the C67) and taught users how to use their comprehensive Development Suite of Tools. Unfortunately these tools weren't available for the C40s. A primitive simulator existed but was never used at the ING.

- **Lack of Development System**
  The ING didn't have a development system. All development had to be conducted on the live system, which resulted in limited access and general difficulties. The lack of ability to perform control testing further restricted development.
- **Limited Upgradeability**
  It was impossible to upgrade the process without upgrading the whole system, and as the system was live (I.e. the ING didn't have a spare) upgrading the processors on the boards was risky and would have been extremely costly.

Implementing an optimised feedforward controller such as the Smith Predictor on the existing control hardware would be a struggle if not impossible. In addition to make the most of the planned SDSUIII Controller, an upgrade in RTCS would be required to halve its latency.

Hence this led to the investigation into Real-time Control Hardware and to the NAOMI Next Generation Real-time Controller (NNGRTC).

6 NAOMI Next Generation Real-time Controller (NNGRTC)

The ING assigned a low priority to replacing or upgrading the RTCS and couldn't justify funding the activity when other costly upgrades, such as GLAS and the potential SDSUIII Controller, would be more beneficial.

Conversely ESO (and Durham) were interested in designing a new RTCS, to meet the challenging processing and bandwidth requirements of the VLT's 2nd Generation Suite of AO instruments. As the general requirements of the two were mostly the same, the author became involved in the European Union funded research that evolved into the 'Standard Platform for Adaptive optics Real-time Applications' (SPARTA) project. Although primarily targeted for ESO systems, the platform could be adapted for NAOMI to produce the NAOMI Next Generation Real-time Controller (NNGRTC).

The author's active involvement in SPARTA at Durham lasted between Aug 2004 and June 2007 when the project successful passed ESO PDR. Table 6.1 contains a list of SPARTA acknowledgements.

Acknowledgements	Project Role
Enrico Fedrigo (ESO)	ESO Project Manager
Rob Donaldson (ESO)	Software Engineer
Christian Soenke (ESO)	Software Engineer
Deli Geng (Durham)	FPGA Engineer
Chris Saunter (Durham)	FPGA Consultant

Table 6.1 *SPARTA Acknowledgements*

The NNGRTC concept and design are based on SPARTA work, and some of the material in this section originated from material contained in the SPIE papers listed in Table 6.2.

Paper	Year	Author
FPGA based AO projects at Durham University [258]	2005	Goodsell et al
DARTS: a low-cost high-performance FPGA implemented real-time control platform for adaptive optics [259]	2005	Goodsell et al
FPGA Cluster for High Performance AO Real-time Control System [260]	2006	Geng et al
FPGA developments for the SPARTA project [261]	2005	Goodsell et al
FPGA developments for the SPARTA project: Part 2 [262]	2006	Goodsell et al
FPGA developments for the SPARTA project: Part 3 [263]	2007	Goodsell et al
SPARTA, the ESO Standard Platform for Adaptive optics Real-time Applications [264]	2006	Fedrigo et al

Table 6.2 *NNGRTC material sources*

The NNGRTC chapter begins by examining the general requirements, section 6.1, of an AO RTCS and the top-level specific requirements, section 6.2, based on the NAOMI instrument. These requirements can be extracted from the previous NAOMI and Characterisation chapters.

Whilst considering the NNGRTC requirements the control hardware components are selected; see section 6.3. A number of options were considered for each component which included processing devices, the backplane and interconnect and the I/O communication protocol. For example, the following devices were considered for the main processing architecture: CPU, DSP or FPGA. The NNGRTC and development-control hardware is selected and described.

Section 6.4 considers the NNGRTC Software Development Environment. It examines the tools associated with the chosen real-time operating system.

The NNGRTC FPGA Development Environment is discussed in Section 6.5. The design flow process resulted in the selection of a number of tools covering design entry, design synthesis, design implementation, design verification and simulation.

Section 6.6 describes the general design of the NNGRTC real-time pipeline architecture. The modular design is divided into two units; the Wavefront Sensor Processor Unit (WPU) and the Mirror Positioning Processing Unit (MPPU). The modularity of the design, including the Wishbone Architecture control bus is described before examining both the specific requirements and associated design of the WPU and MPPU.

The NNTRCS Performance Measurements follows in section 6.7. The section starts by reviewing the latency and bandwidth test results of a Durham-coded sFPDP core. The WPU pipeline latency measurements follow. The Reconstruction latency CPU measurements and FPGA simulations are discussed.

Section 6.8 discusses other system considerations such as having a simulation environment, communication debugging hardware, pipeline configuration, software and hardware compatibility and the feasibility of integrating GLAS.

.

6.1 General Requirements for NNGRTC

The general requirements for the NNGRTC were initially derived from the author's personal experience of developing and maintaining RTCSs, especially NAOMI. These general requirements are contained within Table 6.3 and are subsequently described in this section.

Code	Requirement
GR1	Scalable
GR2	Maintainable
GR3	Upgradeable
GR4	Development Environment (Tools and System)
GR5	Useable

Table 6.3 *List of NNGRTC Generic Requirements*

The ESO AO RTCS group came to similar conclusions following their involvement in 1st generation AO systems. They found that around 80% of the AO RTCS code for NAOS and MACAO was common; having the same functions implemented in slightly different ways. The NNGRTC general requirements in Table 6.3 are also the general requirements for the SPARTA platform.

When designing a RTCS it is good practice to use a standard hardware platform, which must be **scalable** to accommodate differing needs which may occur from future expansions or changing requirements. The NAOMI RTCS isn't scalable. For example the GLAS NGS Tip-tilt System has its own controller.

Scalability can be achieved through modularity, for example a future upgrade such as a LGS may require additional computational boards. A modular system that tracks technology as much as possible should be used. A scalable platform could allow for additional components such as multiple WFS or DMs to be added if required.

A RTCS must be **maintainable.** This can be fulfilled through the use of Commercial Off The Shelf (COTS) components that are easier to procure and repair than custom-developed hardware. COTS components help also in terms of reliability since these are components used in other projects and other companies and so are better tested than a custom component specifically developed for a single project. The NAOMI RTCS mainly used COTS components such as the C40s, although it did contain some custom made electronic boards produced by Durham University. The software also must be maintainable. Commercial packages and tools must be used. NAOMI RTCS contains customs protocols such as the GP messaging system and highly specialised software that aren't easily maintainable. The RTCS was commissioned without documentation and its source tree contained redundant software.

The RTCS must be **upgradeable** to follow the technological evolution. This is also fulfilled by the use of COTS products: in many cases it could be true that a custom development can achieve better performance or better integration than a collection of COTS elements. However, COTS elements are faster in following the technological evolution and quickly surpass the custom development. In turn, the custom development requires a heavy investment to benefit from the same technological evolution.

The next general requirement is to have a **powerful development environment** to make development efficient and the final product reliable. This must be easy to use and strictly follow standard operational scenarios. The C40s predate the excellent development tools that are available for later TI DSPs such as the C67s. A rich development environment can be met by using standard industry environments (including operating systems) that are widely used and thus feature a large portfolio of tools. A development environment separate from the live system should be maintained and used for testing before attempting to commission changes.

Finally, **usability** can be achieved by capitalising on the previous experience and by a strict collaboration between developers and observatory personnel from the early stages of design. Having experience of working in both a development environment and observatory is helpful.

All these requirements are even better fulfilled when the platform definition uses the smallest possible set of components, including protocols.

6.2 Specific Requirements for NNGRTC

Table 6.4 contains a list of the most demanding parameters relating to NAOMI Hardware Configuration 5; see Section 5.6.

		NAOMI (Configuration 5)
WFS (Input)	Number of detectors	1
	Detector size	80 x 80
	Number of pixels (full frame readout)	6400
	No of subaperatures (Most demanding)	64
	Pixels per subaperature (Most demanding)	64
	Maximum frame rate (Hz)	1000
	Int. time (μs)	1000
	Pixel Data Size	16 bit
	Maximum WFS input bandwidth ($Mbits^{-1}$) (full frame)	**102.4** (i.e. 16 x 6400 x 1000 bits)
DM (Input & Output)	DM type	Segmented
	Number of actuators & strain gauges	228
	Strain gauge ADC Digitisation	16 bit
	Maximum strain gauge frequency (kHz)	10
	Max strain gauge input bandwidth ($Mbits^{-1}$)	**36.8** (i.e. 16 x 228 x 10000 bits)
	Mirror DACs	13 bit
	Maximum required DM drive frequency (kHz)	10
	Maximum DM Output bandwidth ($Mbits^{-1}$)	**29.7** (i.e. 13 x 228 x 10000 bits)
Control	Controller type	Feedforward
	Number of elements in matrix	228
	Estimated number of look up tables	12
	Element Size	16 bit
	Memory bandwidth for Feedforward Controller (kB)	**7** (i.e. 16 x 12 x 228 bits)

Table 6.4 *RTCS Requirements for NAOMI*

Table 6.4. derives four specific requirements for the NNGRTC. They have been extracted and placed in Table 6.6.

The required WFS input, SG input and DM output bandwidths are calculated based on the hardware specifications. The maximum DM output bandwidth assumes the DM is driven at 10 kHz. The mirror's resonant frequency is between 2.4 and 2.7 kHz. The mirror can be driven faster than this, although driving the mirror near full voltage isn't recommended. As the mirror has never been operated above 2.9 kHz; the resonant effects at higher frequencies would have to be characterised and compensated for.

The memory bandwidth for the feedforward controller is based on required Look Up Tables (LUT); see Table 6.5. LUT 1 to 6 already exist in the C40 code. LUT 7-10 would be to perform feedforward calculations. LUT 11 and 12 should be included to counteract the effects of hysteresis. The desired position is calculated by the reconstructor and the demand position takes into account the feedforward controller calculations.

LOT no.	Title	Description	Memory Requirement
1	pt_0 DAC	Initial Position at time t_0 (in ADC units)	4.6 kb (288 * 16 bit)
2	g	SG ADC Gain Values	4.6 kb (288 * 16 bit)
3	o	SG ADC Offset Values	4.6 kb (288 * 16 bit)
4	pt_0 ADC	Initial Position at time t_0 (in DAC units)	4.6 kb (288 * 16 bit)
5	dt_0 ADC	Desired Position at time t_0 (in DAC units)	4.6 kb (288 * 16 bit)
6	ft_0 ADC	Demand Position at time t_0 (in DAC units)	4.6 kb (288 * 16 bit)
7	pt_{-1} DAC	Desired Position at time t_{-1} (in DAC units)	4.6 kb (288 * 16 bit)
8	ft_{-1} ADC	Demand Position at time t_{-1} (in DAC units)	4.6 kb (288 * 16 bit)
9	pt_{-2} DAC	Desired Position at time t_{-2} (in DAC units)	4.6 kb (288 * 16 bit)
10	ft_{-2} ADC	Demand Position at time t_{-2} (in DAC units)	4.6 kb (288 * 16 bit)
11	h+	Hysteresis positive direction scale	4.6 kb (288 * 16 bit)
12	h-	Hysteresis negative direction scale	4.6 kb (288 * 16 bit)
TOTAL MEMORY REQUIREMENT			7 kB (12 * 288 * 16 bit)

Table 6.5 *RTCS Requirements for NAOMI*

If a Snapshot/Capture equivalent debug development tool was to require similar memory buffers then the memory requirement would double to 14 kB.

Each TMS320C44 had a 512 B Instruction Cache and an 8 kB of Single-Cycle Dual-Access Program or Data RAM. The amount of memory the TMS320C44 had is tiny compared to any modern processing device. The total memory requirement makes the fourth specific requirement in Table 6.6.

The fifth and final requirement listed in Table 6.6 originates from Section 5.6: Table 5.16, the latency requirement for the RTCS.

Table 6.6 compares the NNGRTC requirements with the SPHERE (See Section 3.1.7) requirements for SPARTA. It assumes that the SPHERE 1370 actuator DM is running at 15 kHz. (10x the maximum frame rate)

Code	Requirement	NAOMI	SPHERE (PDR)
SR1	WFS Input Bandwidth	102.4 $Mbits^{-1}$	1.3 $Gbits^{-1}$
SR2	SG Input Bandwidth	36.8 $Mbits^{-1}$	N/A
SR3	DM Output Bandwidth	29.7 $Mbits^{-1}$	321.6 $Mbits^{-1}$
SR4	Controller Memory Bandwidth	7 kB	11.5 MB (Control Matrix)
SR5	RTCS Latency	< 0.5 ms	0.08 ms

Table 6.6 *Comparison of the NNGRTC and SPHERE Specific Requirements*

The comparison shows that the SPHERE SPARTA requirements are an order of magnitude more challenging than the NNGRTC requirements. As the general requirements are similar; the NNGRTC will reuse as much as the Control Hardware and Controller Design from SPARTA as possible.

6.3 NNGRTC Control Hardware

The NNGRTC control hardware was researched and selected to meet the general requirements (GR1-5) and top-level specific requirements (SP1-5).

The control hardware has to receive pixel and strain gauge data in addition to sending actuator data. The amount of data and data transfer rate are both important considerations when selecting the I/O protocol and hardware.

Once the data has entered the RTCS control hardware it must be processed, hence the requirement for processing device(s). The size of the data, required latency and parallelisation of processing aids selection.

The data must be stored in memory at various stages of processing to allow access for diagnostics, statistical machinery and calibration. The amount of data and data access speeds define the type and volume of memory required. The interconnectivity between processing devices, including backplane, are also important selections.

The selected NNGRTC control hardware consists of a chassis and a computation board. Various development boards, which also act as alternative choices, are briefly discussed.

6.3.1 Processing Devices

Three processing devices were investigated considering the general and top-level specific requirements. These were the Central Processing Unit (CPU), the Digital Signal Processor (DSP) and the Field Programmable Gate Array (FPGA).

Any of these 2005 processing devices would outperform the NAOMI RTCS and could easily meet the applicable specific requirements. The relative strengths and weaknesses of each device are displayed in Table 6.7

Device	Latency	Flexibility	Development Time
CPU	High	High	Low
DSP	Medium	Medium	Medium
FPGA	Low	Low	High

Table 6.7 *NNGRTC Component Choices*

6.3.1.1 Central Processing Unit (CPU)

CPUs are the most widely used device. In embedded systems they are used for operations which require significant algorithmic complexity and whose definition is not well fixed. This environment has the fastest development cycle allowing rapid prototyping and modifications of algorithms.

The CPU architecture is fundamentally a von Neumann machine (i.e. a serial machine) where instructions are fetched from memory and executed sequentially, data must be stored in central memory and retrieved by the CPU one by one and the results stored again in central memory. The bottleneck of this architecture is the bus because it is shared. In practice, once the processing system includes more CPUs, or, worse, more boards, the price to pay to make the various CPUs to communicate is too high with respect to the latency.

6.3.1.2 Digital Signal Processor (DSP)

A DSP is fundamentally a CPU, so it shares the same problems if used as a CPU. However, a DSP is also equipped with fast communication ports and significant on-chip memory that should be accessible at core speed. The core speed of a DSP can be higher than the one of an FPGA, but much slower than a CPU. Still, using fast I/O and the internal memory a DSP can deliver a quite high throughput while significantly simplifying the development cycle. A DSP can be programmed in C and the development tools are similar to the ones used to program a CPU.

DSPs are used for floating point operations and operations which require significant memory. Since DSPs are programmed in "C" they offer a faster development cycle than FPGA but development is still significantly more complicated than for CPUs.

6.3.1.3 Field Programmable Gate Array (FPGA)

An FPGA is a chip that provides millions of gates that can be connected by means of a program to create any logical function that will then execute at the speed of the FPGA core clock. Moreover, many logical functions can be programmed, until all gates are used. All of these functions run in parallel. This is the great advantage of FPGAs.

FPGAs programming language is VHDL. VHDL is the same language used to design ASICs and microprocessors. FPGA's programming philosophy is quite different from C/C++ and a VHDL programmer has to think rather differently from a C/C++ programmer. Consequently the development cycle of an FPGA application is much slower and the debugging much more difficult. In addition FPGAs cannot handle floating point arithmetic natively and special resource-consuming modules must be used.

In any case FPGAs still suffer from a problem similar to the CPUs: their internal memory is limited so external memory banks must be used. Even if they can run in parallel, given that their speed is much lower than a CPU and that only a limited number of memory banks are available (i.e. A limited number of parallel operations can be performed), the final performance of an FPGA in floating point is not too far from a CPU. However, an FPGA is able to deliver constantly the peak rate, while a CPU is unlikely to deliver at the peak rate. However, being limited by the memory transfer rate and size, the FPGA becomes under-utilised, i.e.: the number of floating point multipliers is not limited by the available gates but by the number of memory banks.

The FPGA can be used in the communication infrastructure: a communication protocol does not require memory access and can run in parallel, one instance per communication line. Being implemented in hardware, there is no additional latency. The perfect application for the FPGA is to manage all the critical communication so that data and results are routed within the system at the fastest possible speed and the lowest possible latency. The FPGA can also be used for some processing, including floating point where memory is not an issue and where convenient.

FPGAs are used for input/output processing and operations that are largely integer based and highly parallel. Only operations that are considered well defined are hosted in FPGA space as the development cycle is significantly longer than for other types of processing elements.

6.3.1.4 Processor Selection

The SPARTA platform builds on the idea of modularity. SPARTA uses FPGAs, DSP and CPUs at different processing stages of the system. For the NNTRC it was decided to initially use FPGAs and CPUs with an aim of only using FPGAs in the final system.

To begin with, communication and wavefront processing would occur in FPGA space and the reconstruction and controller would occur in CPU space. Only once the optimised algorithms were frozen would they be recoded in FPGA space. This is because it is fast to reprogram a CPU compared to the FPGA. The FPGA was selected for the wavefront processing because it is possible to parallelise the processing. As the system is designed to be modular, it will be possible to replace hardware cards of one processor type with another of alternative type.

6.3.2 Backplane and Interconnect Options

The VITA 41 (VXS) standard was selected. VXS is a switched fabric for VME. The VITA 41.0 defines the connectors, dimensions, pin designations and mechanical structures for the backplanes and cards. This definition is independent of specific fabrics or protocols.

VXS defines two types of cards: the payload card and the switch card, both utilise the same mechanical outline as the standard 6U VMEbus card. Each payload card can connect to any two other payload cards according to the routing paths provided by the switch card.

The VXS provides a fast serial interconnect inside the system. The backplane is compliant with the VITA 2eSST[265] specification, which allows for a data rate of up to 320 MBs^{-1} on the VME bus. All slots are fully backward compatible with VME32 and VME64.

Given VME's heritage, industrial standard and success, it was decided that VXS meets all the general requirements.

6.3.3 I/O Communication Protocol

The VITA 17.18/10 serial Front Panel Data Port (sFPDP)[266] was adopted as the standard external interface, including sensor interface, actuator interface and strain gauge feedback interface. The sFPDP is a high-speed low-latency serial link originally aiming to transfer parallel FPDP signals in a serial format. It is a low-overhead point-to-point protocol which currently offers a maximum speed of 2.5 Gbs^{-1}, with the future roadmap expecting it to raise to 4 Gbs^{-1} and then 10 Gbs^{-1}. IP cores are commercially available to implement the protocol on the Xilinx FPGA. As the protocol is a standard, it is possible to develop the protocol for any FPGA. In addition, a large number of commercial products are available for sFPDP: interface cards (PMC, PCI, CMC), data recorders and protocol analysers.

The protocol meets GR1, GR2, GR3 and GR5. GR4 (and to a lesser extend GR3) is hardware dependent rather than associated with the actual protocol. The selection achieves the specific top-level requirements (SR1, SR2 and SR3) with ease.

6.3.4 NNGRTC Control Hardware Choice and Capabilities

With the NNGRTC processor devices, backplane and interconnect and I/O protocol selected, suitable control hardware had to be identified. A number of feasibility studies conducted at Durham for SPARTA, DARTS and CANARY RTCS projects reviewed a number of potential items. It was decided to select items from the SPARTA platform as baseline components as they have already been demonstrated to fulfil the general requirements of SPARTA and hence the requirements of the NNGRTC. A SPARTA VXS Chassis and a VPF1 board were thus selected.

A number of alternative hardware choices were used in developing parts of the SPARTA system. These hardware choices are somewhat interchangeable and are briefly introduced. With the design being modular it is possible to replace two hardware components with minimum rework.

6.3.4.1 SPARTA VXS Chassis

The standard SPARTA chassis was selected for the NNGRTC, it provides the following specifications:

- Dimensions: W:19 ", H:6 U (without fans), D: ~300 mm.
- Efficient air-cooling (~930 m^3/h ventilation per chassis).
- "Closed" chassis for EMC compatibility.
- Injector/extractor rails for VME64/VXS boards.
- 80 mm rear IO compatibility.
- ±12 V, ±5 V and ±3 V Kniel Power supply.

This is specified to house the boards required for SPARTA hence it contains a much greater capacity required for the NNGRTC as it currently stands.

The chassis contains monolithic backplane containing:

- 2 VME64x slots.
- 7 VXS payload slots.
- 1 VXS slot.

Each VXS payload slot offers 8 full-duplex serial links that are routed to the switch slot. Through a switch card, any link of any payload can be routed to any other serial link of any other payload slot in the system. The serial links offer a data rate of up to 6.25 Gbs^{-1}.

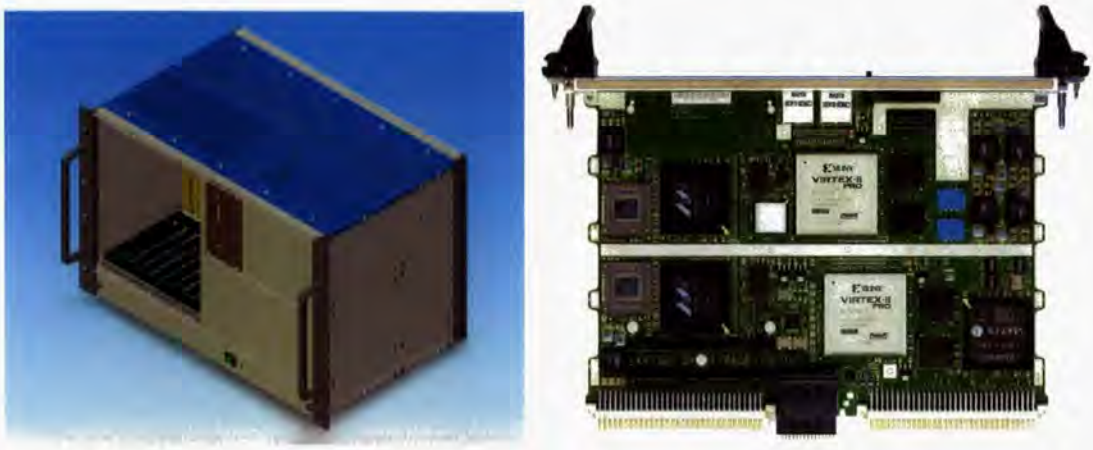

Figure 6.1 *SPARTA VXS Chassis and a VPF1 Card*

6.3.4.2 VPF1 Card

The VPF1 board contains two 7447 PowerPCs and two Virtex-II Pro XC2VP70-6 FPGAs. The board is shown in Figure 6.1 and the board specifications are summarised in Table 6.8.

VPF1 Board Specifications	
2x PowerPC Nodes, each node has: • PowerPC 7447 running at 1GHz • 256 Mbytes DDR SDRAM • 64 Mbytes FLASH (plus boot FLASH/BIOS) • 64-bit/ 125 MHz link to Virtex-II Pro • Front panel Ethernet (via PHY/SERDES device)	2x FPGA Nodes, each node has: • Virtex-II Pro XC2VP70-6 FPGA • 4 High speed 2.5 Gbps serial communications between FPGAs • four banks of QDR SRAM (4 MB per bank) • 128 Mbytes DDR SDRAM (two banks of 64 Mbytes)
Other Specifications: • Multi Gbps off-board serial links (up to 3.125Gbps per link) via VXS connector (alternative speeds available) • Multiple JTAG chains • VME64x/VXS interface, 64-bit PMC site • Built-In Test • Commercial / convection-cooled (Level 1)	

Table 6.8 *VPF1 Specification*

6.3.5 Development and Alternative Hardware

To meet the requirements of SPHERE SPARTA other control hardware modules had to be chosen. The following was selected to take full advantage of the VXS capability and the modularity:

- **VPF1 Board**: Contains FPGA for Wavefront Processing, CPU for controller.
- **Bitware DSP Card**: Contains DSP for reconstructor.
- **VXS Switch board**: For sFPDP board communication.

PMC03F Card

XUP VUP Card

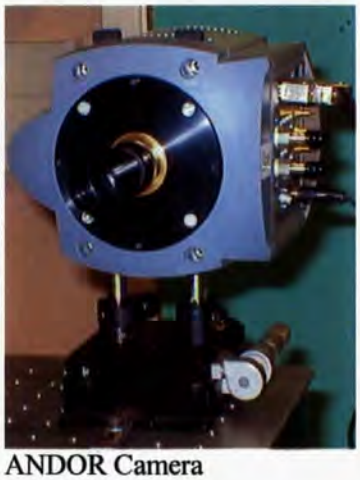

ANDOR Camera

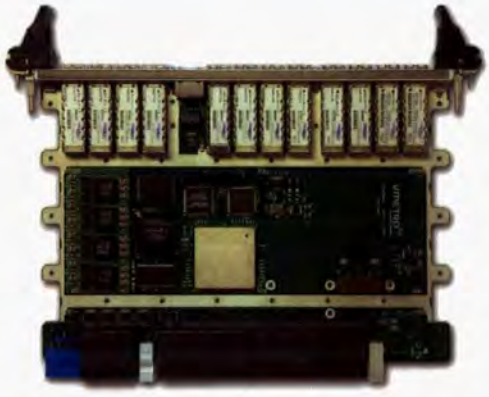

Zero Latench VXS Switch Card

TVG5 Card

Figure 6.2 *NNGRTC Development Hardware*

Due to the modular characteristics of the platform other components (to reduce cost) could be used for development. The following hardware components, see Figure 6.2, were used:

- **TVG5 Card**: This VME64 card contains a single PowerPC MPC7457 card running at 1 GHz and 512 MB ECC DDR DRAM. It contains two PMC slots. The board was used to originally host the PMC03F Card.
- **PMC03F Card**: This PMC daughter board contains a single Virtex IIPro XCV2VP50-6 FPGA device connected to four optical transceivers. The board was used to develop RTCS FPGA code and to test the FPGA sFPDP protocol.

- **XUP VUP Development Board**: This board hosting a Virtex IIPro FPGA was used to develop the sFPDP core at Durham and used to test communications.
- **Systran FibreXtreme Card**: Commercial board containing a preparatory sFPDP IP core used to test communications.
- **ZeroLatency VXS Switch Card**: Use to test VXS sFPDP communications between VPF1 boards.
- **ANDOR iXon Camera**: Used to capture and send SHWFS data to the PMC03F card.

6.4 NNGRTC Software Development Environment

Wind River System's **VxWorks** has been selected as the real-time operating system (RTOS) to run on the VPF1 board. C/C++ has been selected as the software programming language of choice with Python being the preferred scripting language.

VxWorks is being used in the SPARTA project. It was selected because of its superior development environment, board support packages and customer support. VxWorks is the most widely adopted real-time operating system in the embedded industry. ESO use VxWorks for SPARTA.

VxWorks has a strong history and has supported various processors including the PowerPC, ColdFire, 68K, M-CORE, x86/Pentium, StrongARM, Xscale, MIPS, ARM and SuperH architecture.

VxWorks comprises the core capabilities of its microkernel with advanced networking support, powerful file system and I/O management, and C++ and other standard run-time support.

VxWorks is supplied with an impressive development environment. The latest stable version of VxWorks would be used for development. VxWorks 5.4 is examined here to review its development environment.

VxWorks v5.4 was supplied with Tornado II, which comprises a comprehensive suite of core and optional cross-development tools and utilities.

Standard Tornado II tools:

- ***WindSh:*** The WindSh shell interface allows users to interact with all target facilities. Unlike other "shells", the Tornado shell can interpret and execute almost all C-language expressions, including calls to functions and references to variables whose names are found in the system symbol table. Interpreted C statements give an easy-to-use interface to the target environment.
- ***Browser***: The Tornado browser is a graphical companion to the Tornado shell, presenting information symbolically whenever possible. The browser gives the overall state of the system and allows developers to launch dedicated displays that monitor the state of target operating-system objects, such as tasks, semaphores, message queues, memory partitions and watchdog timers.
- ***WindNavigator***: The WindNavigator Multilanguage browsing tool enables developers to dramatically reduce the time to evaluate existing C and C++ source code, even if the code is incomplete or erroneous. With WindNavigator, developers can see the relationship between objects and functions and can easily build programs using existing, proven modules.

Other standard Tornado II tools include CrossWind, MemScope, Project, Rshell and LmServer. All of these tools are described in detail in the Tornado User's Guide. Wind River's optional WindPower tools include: WindView, VxSim, ScopePak, PerformancePak, CodeTEST, Visual SlickEdit, Wind Foundation Classes and Look. A similar complete range of comprehensively documented development tools is available for the latest version of VxWorks.

6.5 NNGRTC FPGA Development Environment

The FPGA design flow process is displayed in Figure 6.3. A number of tools are required for the design entry, design synthesis, design implementation, design verification and finally simulation. These are summarised below.

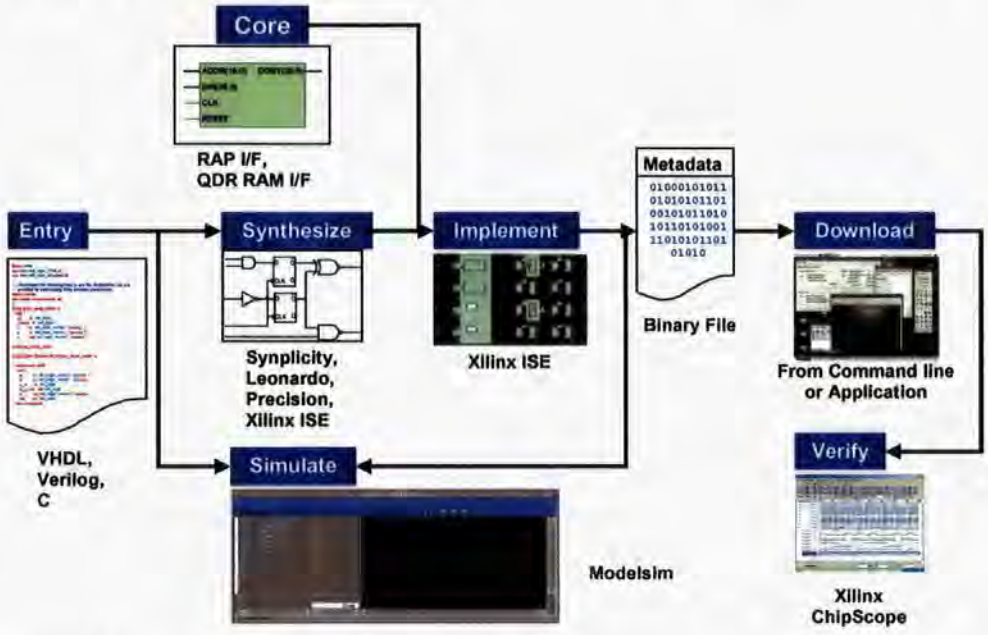

Figure 6.3 *Typical FPGA Toolchain*

6.5.1 Design Entry

The FPGA engineer first creates the Design Entry. The development of the FPGA logic will use the Hardware Description Language (HDL) for constructing the hardware logic model. HDL can either be written using a general purpose or dedicated editor.

Xilinx ISE, the Integrated Development Environment (IDE) was selected to create the Design Entry. The FPGA design will be coded in **VHDL**.

6.5.2 Design Synthesis

The Design Synthesis translates the HDL hardware logic model to a low level flattened netlist. This tool is similar to a compiler, which converts high level programming language to low-level assembler or machine code. Logic optimisation can be conducted at the stage. The translated netlist can also be simulated to ensure there is nothing wrong with the translation.

Xilinx ISE was selected for FPGA logic synthesising.

6.5.3 Design Implementation

The Design Implementation can further optimise the netlist by considering the dedicated structure of the real silicon chip. At this stage the netlist will be fitted into the real silicon chip, which includes mapping, placing and routing. Finally, the binary code is generated for the FPGA configuration, i.e. programming the FPGA chip. The detailed timing model of the

design is also generated. Such models can be simulated, and this is very useful to check the physical timing constraints.

Xilinx XST was selected for FPGA design implementation.

6.5.4 Design Verification

The Design Verification plays an essential role during the whole design procedure to guarantee correctness and quality. There are mainly three parts: static reporting, simulation and field testing. The static report gives an overview of the implementation and its performance. The simulation is a way of examining the dynamic performance of the logic design. It's normally conducted at every stage before proceeding to the next. The purpose is to discover and remove any bugs or errors as early as possible to avoid later, more expensive, costs. The field test verifies the design.

ModelSim (Mentor Graphics) shall be used for design verification if required. Modular functions can be written in Matlab, C, Tcl, Python among others.

6.5.5 Simulation

Simulation of the FPGA design makes the logic model run without the real target hardware platform. Therefore, the FPGA logic model can be developed before the hardware is ready; the behaviour of the logic model can be checked against the specifications; the internal values can be examined for debugging and optimisation.

ModelSim is the selected VHDL simulation tool. ModelSim is a high-performance system with an easy to use interface. ModelSim is capable of simulating the NNGRTC FPGA code. ModelSim has good support for the latest technologies, like SystemVerilog, and it can link to Matlab.

6.5.6 Host Platform

The host platform that was selected for the FPGA development for the RTCS was an **AMD 64bit processor** running **Linux**.

6.6 NNGRTC Real-time Pipeline Design

The NNGRTC hardware components have been selected based on the top-level requirements. The next stage of the design is to investigate a modular pipeline architecture, the basis of which can be placed into multiple hardware boards.

The design divides the RTCS functionality into two units, the Wavefront Processing Unit (WPU) and the Mirror Positioning Processing Unit. (MPPU) Each unit contains a number of modules as shown in Figure 6.4. Each module should contain a standard input and output format. A module should be responsible for processing a certain algorithm. A standard modular system has a number of advantages. Firstly it can be followed regardless of the processing device and hardware. Secondly modules can be added, removed, replaced or bypassed. Modules can be coded and tested without having knowledge of the complete system. Fixed resources can be allocated to a module. The system should have the ability to store and extract information at any stage in the pipeline for analysis and statistical machinery.

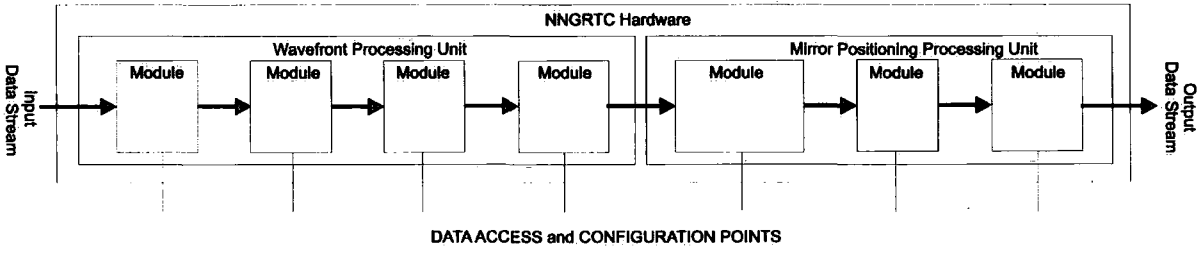

Figure 6.4 *NNGRTC Modular Pipeline Design*

In CPU and DSP space the modules could be functions or instances linked in a particular sequence. In FPGA space the modules are linked together by a control bus. The FPGA control bus selected follows the Wishbone Architecture and is subsequently described.

6.6.1 Wishbone Architecture (Control Bus)

Parameters of each module can be accessed (downloaded, uploaded or synchronously updated) from the control bus. The Wishbone bus along with predefined registers provides a standard way to access the WPU AO modules. The FPGA logic is designed to run at the system clock. The processing units provide a transparent facility for using the FPGA to accelerate the processing of the data. The two units contain several AO modules.

The modular architecture within the FPGA design gives a standard interface. The FPGA modules are designed to be flexible:

- Each module is parameterised and hence can be configured for different requirements.
- The modules have uniform data flow interfaces, so they are replaceable. Different implementations can be developed, connected, interchanged and compared easily.
- The modules composing a system have standard accessing/control interfaces. Again, they can be easily connected to the internal control bus. It also means a standard system control interface and software can be adopted.
- Modules are designed to have all key parameters modified at runtime (e.g. for the WPU - background subtraction map, flat field map etc.)

There are two kinds of flow: the data processing flow and the control flow. The thick single arrowed line represents the data processing flow. The central line represents the control bus for accessing each module, i.e., for configuration and control. The result from the gradient processing module is fed into the System Control module, which acts as a bridge between the data flow and the control bus.

Hence an FPGA implementation of the pipeline can be seen in Figure 6.5.

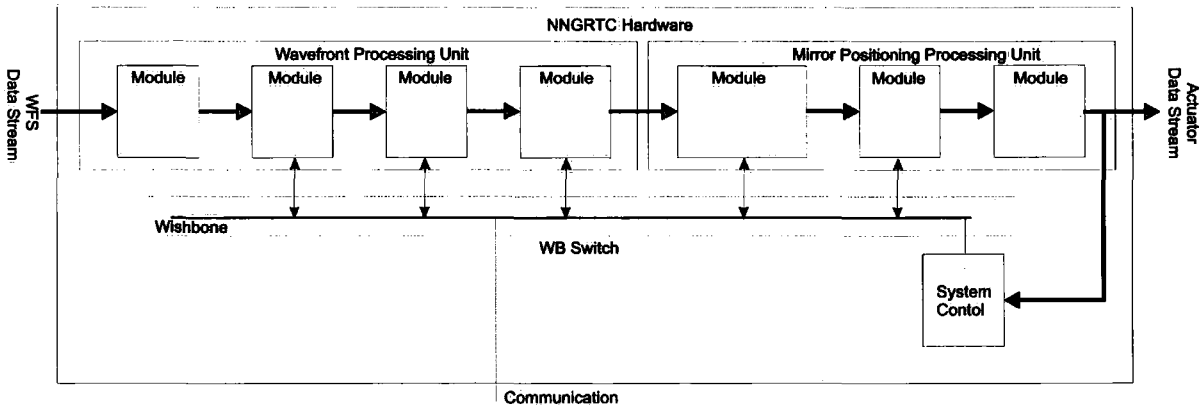

Figure 6.5 *FPGA Wishbone Bus pipeline Architecture*

6.6.2 Wavefront Processing

The specific requirements for the NAOMI WFS processing are described and compared with the SPARTA SPHERE WFS requirement. As modules can be added, removed, modified or bypassed, it was sensible to describe the SPARTA requirements and WPU design.

6.6.2.1 WFS Requirements

The specific NAOMI WFS processing pipeline was extracted from the NAOMI RTCS Programmers Guide.[250] (Myers & Goodsell)

NAOMI specific WFS requirements include:

- During configuration of the WPU, the selected NAOMI WFS Mode would be sent to each module so it could configure itself appropriately.
- In the case of the CCD39 the SDSUIII Controller would interleave before streaming the data into the NNGRTC using the sFPFP protocol.
- In the case of the CCD60 the SDSUIII Controller needn't interleave the pixel data as it contains one readout port.
- The NAOMI WFS pipeline should perform background and sky subtraction.

SPARTA applications contain additional WFS requirements to those originally required by NAOMI. Modules can be removed or bypassed so it was decided to progress with the complete functional set. The impact on performance by providing NAOMI with the additional functionality has not been assessed. Figure 6.6 includes the NNGRTC WPU requirements.

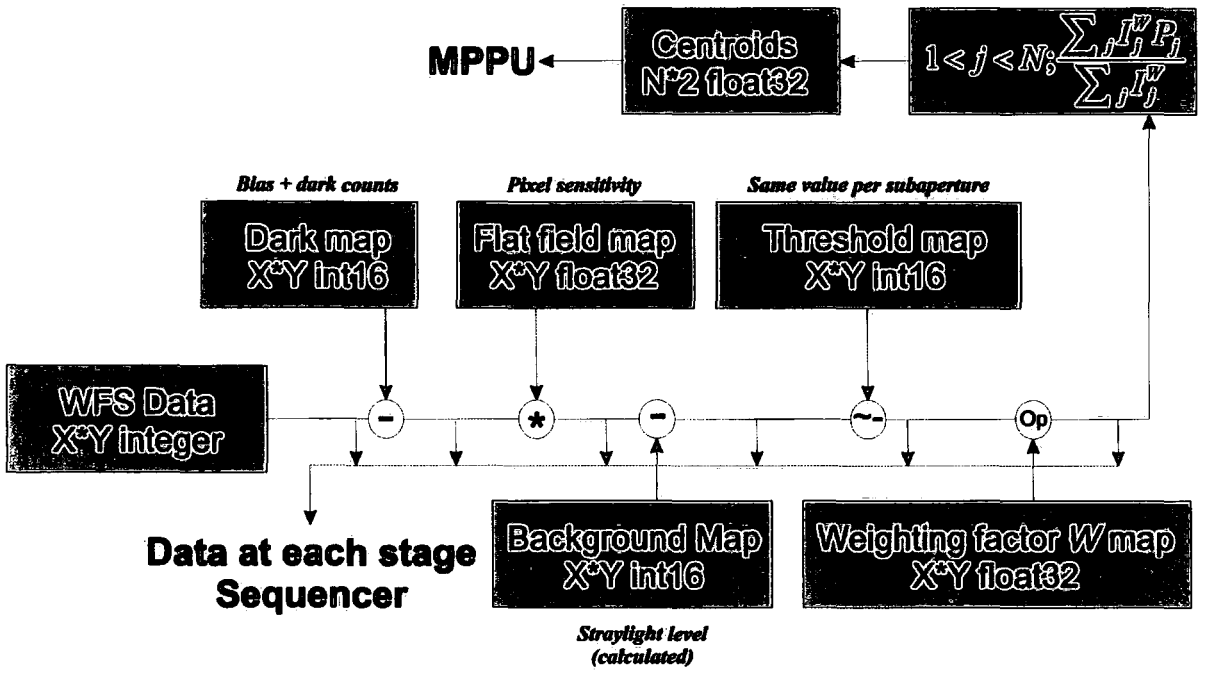

Figure 6.6 *NNGRTC WFS Requirements*

6.6.2.2 WFS Processing Unit

The WPU design is given in Figure 6.7. Each module can be broken down into further detail as shown for the Pixel Calibration Module in Figure 6.8.

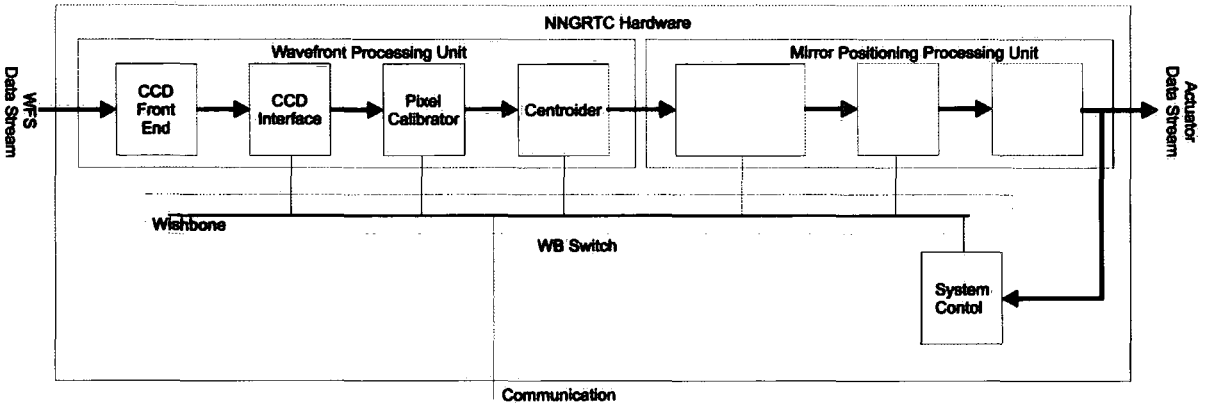

Figure 6.7 *WPU modules connected to the Wishbone Bus*

The WFS data first enters the **CCD Front End** module from the hardware, which provides an abstract layer between the individual WFS and the following processing modules. As a result, by changing this module, which is a small amount of code, the whole FPGA processing system can be adapted for any WFS.

The CCD geometry resulting from the selected WFS mode is handled within the front-end module only. The parameter of each front-end module is configurable, for example, the WFS Mode, the size of the CCD, etc.

The **CCD Interface** module is optional. It can bypass the CCD front-end signals to the next stage during normal operation. In addition, it can divert the WFS data to the control bus, hence making the raw WFS data accessible. Furthermore, this module can upload the data from the control bus to the WFS data flow, i.e., emulating signals for testing purpose. It can act as a frame grabber or test frame provider.

There are three functions inside the CCD interface module:

- CCD signal bypass function forwards the CCD pixel signals from the input port to the output ports. In a real system, small amounts of glue logic will interface the actual CCD camera data signal to this CCD interface format.
- CCD image generator produces the CCD signals according to its buffer content, which is uploaded.
- Pixel image frame grabber function stores a pixel frame into the internal buffer and can be downloaded.

The design can accommodate up to four pixel ports in one FPGA device allowing for a total of 10 Gbs^{-1}. NAOMI would require one for the WFS, hence a quarter of the total FPGA resource would be used. The internal buffer for the CCD image generator or the image grabber is divided into two banks.

The **Pixel Calibration** module subtracts the background from the pixel data and flattens them to a normalized value, it corrects both the offset and gain error on a per-pixel basis. The pixel calibration module also performs thresholding. Its parameters can be synchronously updated at runtime.

Since not all the pixels are useful to produce the sub-aperture data, a pixel filter is designed at the front stage to cut off unused pixels, although binning and rejection could occur in the controller. The pixel calibration module takes the same interface to CCD image sensor / front-end as the CCD interface module. It means a CCD front-end can be directly connected to the pixel calibrator if the functions provided by the CCD interface module are not required.

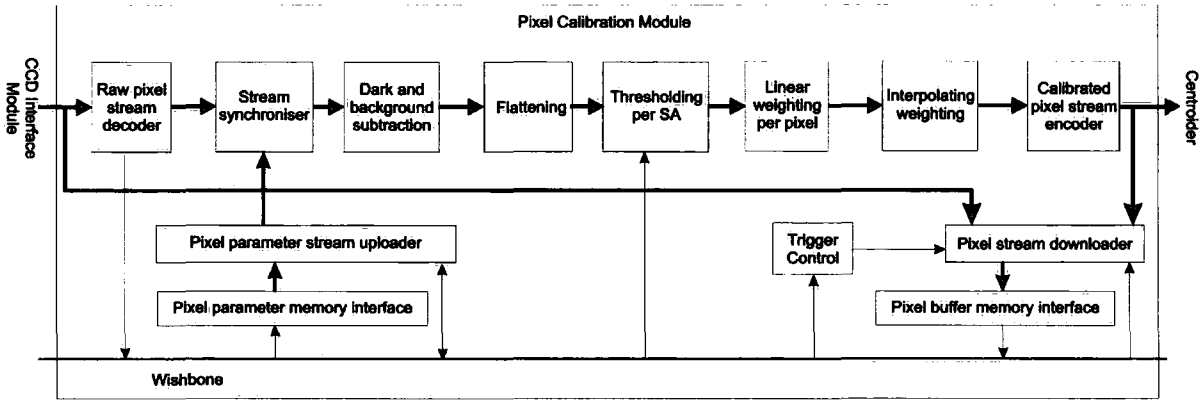

Figure 6.8 *Details of the modular Pixel Calibration Module*

The pixel calibrator needs three kinds of parameters: pixel filter mask, pixel background data, and pixel flattening factor. The pixel filter mask is stored in a separate table, while the pixel background data and pixel flattening factor are stored in the same table. Setting up these parameters is through the Wishbone data transfer channel. Calibrated pixel data along with its

sub-aperture position information is passed to the Centroider module. The pixel calibration module is further broken down into modular segments as shown in Figure 6.8.

The **Centroider** module converts the calibrated raw WFS data into wavefront aberration data (typically wavefront derivatives). It has been designed with configurability. The number of the pixels per sub-aperture and the weight of each pixel inside a sub-aperture are software configurable.

The order of the pixel arrival is not important for the centroiding processing, because the pixels arriving will be re-ordered for best performance at the accumulating stage. Dual-port (DP) RAM is used to store the temporary data for the accumulation. No successive pixels from the same sub-aperture will be sent to the accumulating stage.

6.6.3 Mirror Positioning Processing

The specific requirements for the NAOMI Mirror Positioning processing are described. The mirror positioning processing includes the reconstructor and the controller. For NAOMI the existing MVM reconstructor would be used although the modular design easily allows alternative reconstructor to be included. NAOMI's existing controller could be coded although the new feedforward controller is considered here.

6.6.3.1 Mirror Positioning Processing Unit Requirements

The specific NAOMI Mirror Positioning processing pipeline was extracted from the NAOMI RTCS Programmers Guide [250] (Myers & Goodsell) and from the shortcoming arising from the Characterisation Chapter.

NAOMI specific Mirror Positioning Requirements include:

- Derive the x, y slopes from the centroid data.
- The implementation of the existing MVM reconstructor to create the x, y, piston data.
- Conversion of the x, y piston data to a, b, c actuator data.
- The implementation of the existing DAC to ADC unit conversion using uploadable offset and gain tables.
- Due to the architecture there is no requirement to 'balance the load'.
- The strain gauges can be 'oversampled' at 10 kHz and an averaged value used as the current position. Alternatively a 10 kHz data stream can be read without averaging.
- Adjustments are made to the demand value based on the last two sets of initial and demand values.
- The values are further modified by the hysteresis gain based on the direction and current value of the actuator.
- Finally the temperature of the DM gives a final adjustment before sending the values to the mirror's drive electronics.

SPARTA requirements for this stage of the processing are different to NAOMIs and aren't considered. Figure 6.9 includes the NNGRTC MPPU requirements.

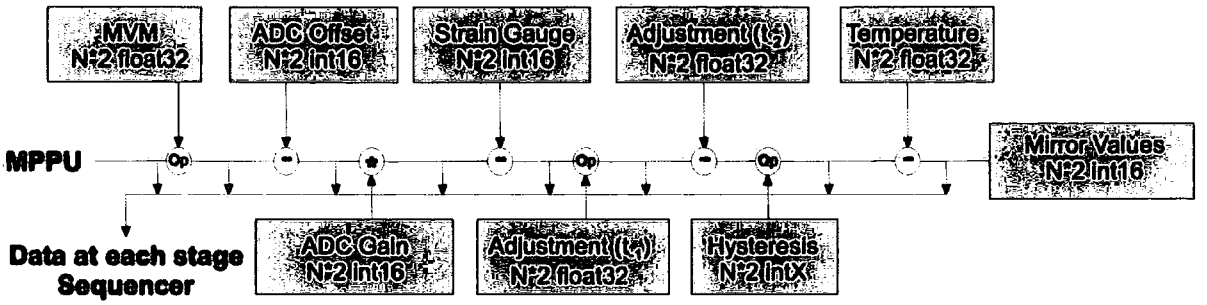

Figure 6.9 *NNGRTC Mirror Positioning Requirements*

6.6.3.2 Feedforward Controller

In the existing NAOMI Controller, a fraction of the current error signal is applied to the actuator as it creeps to its demand value over a number of iterations. The response of every individual NAOMI DM actuator was measured, see Section 5.3.

The feedforward controller would apply the total error signal minus a signal equal to the predicted effects of the feedback system. This would be related to the overshoot information obtained in Section 5.3.6. Instead of causing violent oscillations, the mirror would go directly to the demand value. The next iteration would stop the signal falling beneath its original overshoot by applying an additional correction. If this iteration had another demand position then it would have to factor in that demand position. Hence to implement a feedforward controller a number of signals would have to be stored and a number of calculations would have to take place every iteration; three should be sufficient. It is important that the time taken to process these calculations is less than the potential saving in time. The closed loop bandwidth is therefore potentially much higher if the calculation overhead is less.

In the existing NAOMI controller, the mirror-write DMA begins almost straightaway with a view to it happening shortly after the ADC sample for evaluating the results of the previous write. This allows the maximum time for the effects of the mirror update to have taken effect before sampling the residual error. A true feedforward system (as opposed to the initial approximation) would write to the mirror immediately the demand was computed and would predictively compensate subsequent feedback accordingly.

For a feedforward controller to be tuned:

1. Each actuator would have to be fully characterised at a number of frequencies. The effect on temperature would have to be well understood.
2. Ideally an independent optical measuring system (DM Figure Sensor) would have to be deployed to sense the mirror's shape.

For the feedforward controller to work effectively a number of previous demand values would have to be stored in memory for the corrective demand values to be accurately calculated. Three sets of lookup tables updated every iteration should be sufficient.

6.6.3.3 Mirror Positioning Processing Unit Design

The Mirror Positioning Processing Unit Design is given in Figure 6.10. Each module can be broken down into further detail as shown in the Controller Module; see Figure 6.11.

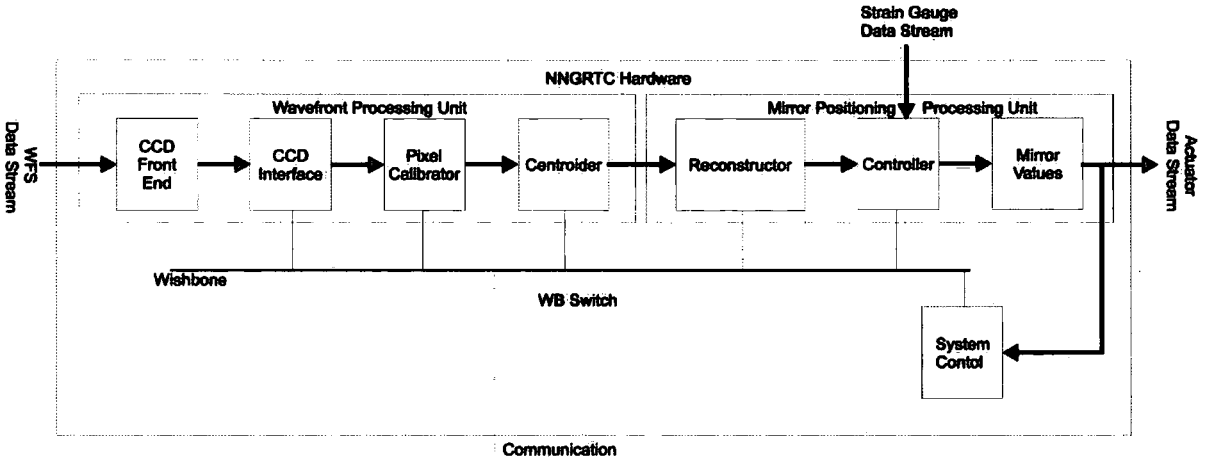

Figure 6.10 *Complete NNGRTC Pipeline*

The MPPU module algorithms would be developed and tested in CPU space. Once functionally tested they would be coded into FPGA space and form an extension of the existing WPU pipeline. This description assumes a FPGA implementation; hence the MPPU data enters from the WPU and there is no need for a MPPU front-end module. Strictly both the WPU should have Front End and Back End modules to allow easy implementation on different FPGA devices.

The centroid values from the WPU enter the **Reconstructor** module. The reconstructor module converts the centroids to x, y slopes and then performs a matrix multiply on the vector of the x, y slope demands. At this stage the global tip/tilt would be calculated and passed to the Mirror Values module to send to the FSM mirror. The result of the matrix multiply is a vector of piston values: one per subaperature. The reconstructor then converts the x, y piston command for each mirror segment into the A, B, C equilaterally sectored actuator commands that are required to drive the mirror by applying an offset and gain. This command vector is the reconstructed mirror demand values. The WFS Mode and MVM Matrix are uploaded on initialisation to configure the reconstructor module. The MVM Matrix can be uploaded at any time during operation.

The reconstructed mirror demand values then enters the **Controller** module. The module has been broken down into components, see Figure 6.11.

Strain gauge data would arrive into the system in the sFPDP format via a fibre transceiver. The data would be reformatted before being fed into the oversampling module. This component would be preconfigured to oversample between 1 and 100 readings before sending the averaged strain gauge data into the main pipeline.

The strain gauge data would be used to adjust the 'mirror input demand' values. Further adjustments would be made considering the previous two sets of demand values, strain gauge data, strain gauge hysteresis and temperature. The final 'feed-forward' adjusted mirror demand values are sent to the Mirror Values Module. The tuning of the algorithm would depend on further characterisation of the DM.

The **Mirror Values** module sends the demand values to the mirror electronics via sFPDP.

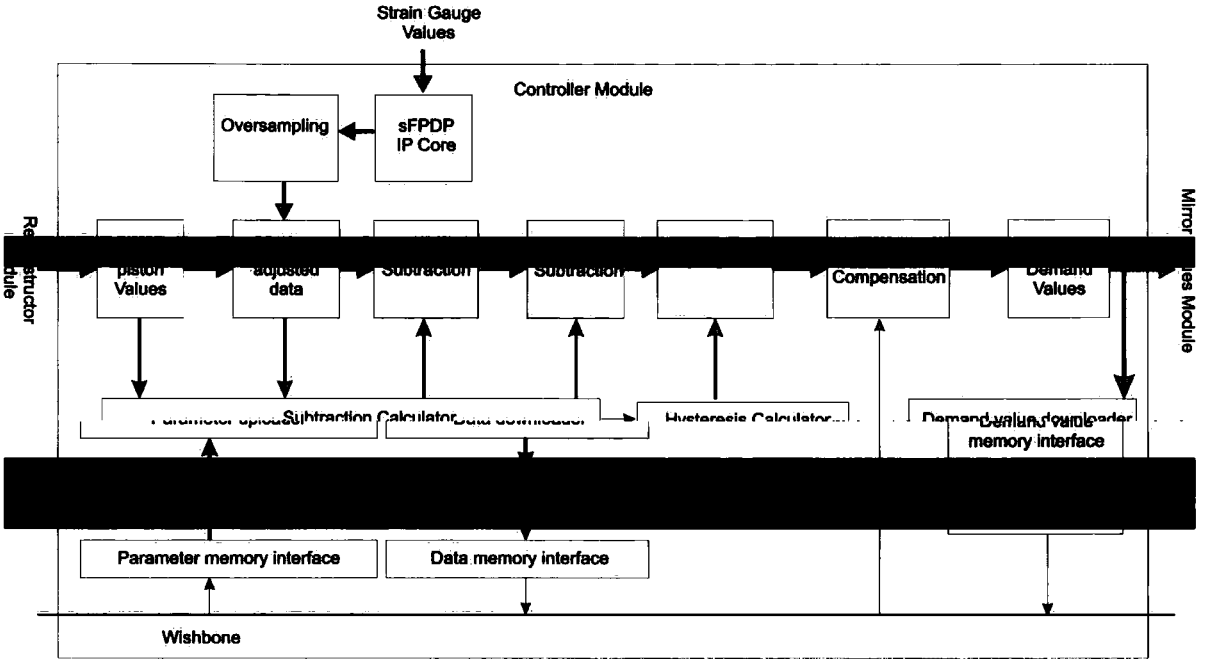

Figure 6.11 *NNGRTC Controller Module*

6.7 NNGRTC Performance Measurements

Although a NNGRTC hasn't been constructed, parts of the system have been tested or simulated for other projects.

6.7.1 sFPDP Measurements

Durham coded a sFPDP core in FPGA and has demonstrated the core operating on 3 different VirtexIIPro FPGA cards: XUP V2P, PMC03F and VPF1. The core has been tested against commercial products such as a Systran FibreXtreme card. It has also been used to communicate with an ANDOR camera as part of the ESO HOT project.[267]

6.7.1.1 sFPDP Latency Test Results

Idle Link Test - When there is no data being transferred along the sFPDP link, an idle frame (zero frame data size) should be sent to update the PIO status. This indicates the existence of a link. Although VITA17.1 suggested sending such idle frames to ensure the link, it does not specify the interval of the frames. The core has a parameter for such idle period.

The length of an idle frame is **64 ns**, which is considered to be the worst-case latency estimation; this is shown in Figure 6.12.

Data Link Test - The latency is defined by the time taken for the data to be sent from the transceiver's sFPDP parallel port and for the correct data to appear at the parallel port of the receiver's sFPDP module. The latency is tested by sending a small data frame when the channel is idle, i.e. no data in the TM FIFO and no data in the RM FIFO.

Valid data received is indicated by a data valid signal and this signal is connected to a pin on the FPGA. Small data frames were sent at random intervals. Such intervals were long enough to let the transmitter and the receiver clear their buffers. An oscilloscope measured the time difference between the sending flag and the receiving flag, which gives the serial FPDP latency. Figure 6.12 shows a latency of **491 ns**.

The latency measured was between **487ns** and **491ns**. In theory it can vary up to 16 ns, which is the length of an IDLE symbol due to the automatic adjustment of the elastic buffer at the RM side of the RocketIO.

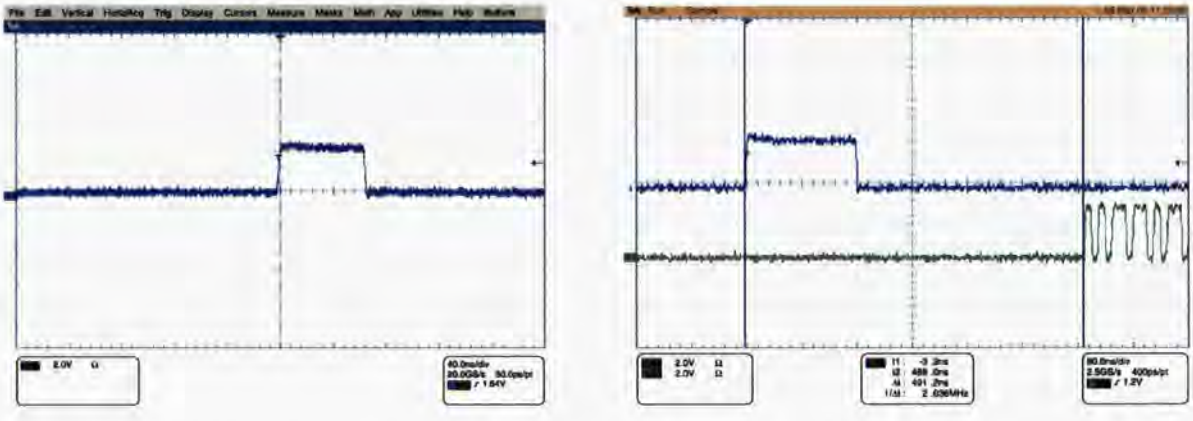

Figure 6.12 *Left: Idle frame period* *Right: TM to RM latency*

6.7.1.2 sFPDP Bandwidth Test Results

Due to the FIFO between the user logic and the sFPDP core, small frames and interval frames will be merged into large block transfers. Moreover, for a point-to-point connection like the sFPDP, the overhead is usually predictable and fixed. Therefore, the bandwidth test was conducted with flooding data regardless of the user data packet size. The test monitored the 9th bit of a sending word counter. The captured waveform is displayed in Figure 6.13.

The bandwidth was measured to be **247.4 MBs^{-1}**.

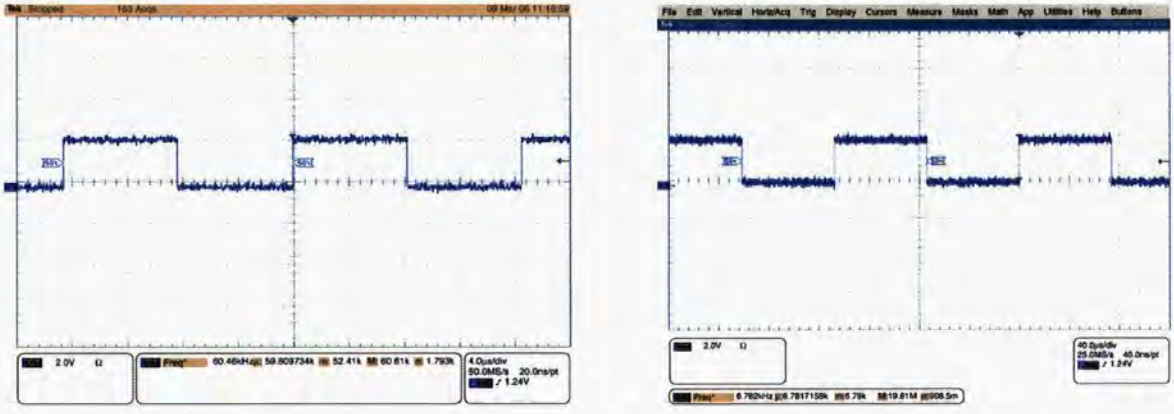

Figure 6.13 Left: *Bandwidth waveform* Right: *The bandwidth waveform (SYNC) only*

To conclude, the Durham sFPDP core was created, tested and verified. Successful protocol link were reliably established at the 2.5Gbs^{-1} without error. Data frames of various lengths can be sent and received. Durham is now in a strong position to have the 4 Gbps^{-1} and 10 Gbps^{-1} protocols operational when the optical transceivers become available. The core is also being developed by NOAO to operate on a Virtex V FPGA device.

6.7.2 WPU Pipeline Measurements

A fully ESO 2nd Generation SPARTA version of the WPU has been demonstrated both on the PMC03F card and the VPF1 card. The PMC03F was used on the HOT system and the test results are described here.

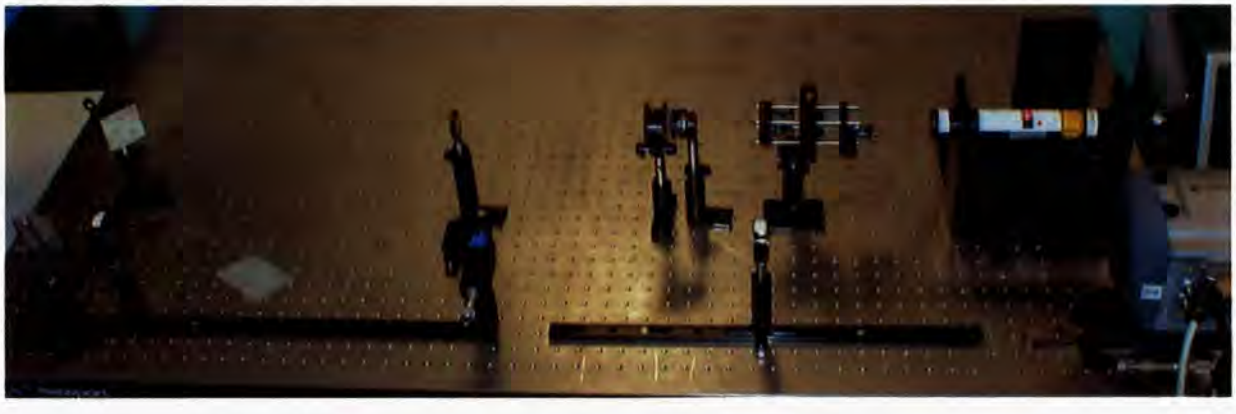

Figure 6.14 *HOT Test Setup*

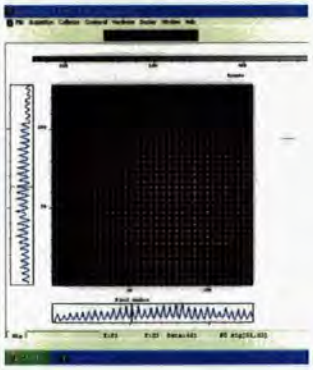

Figure 6.15 *TVG5 + PMC03F card in VME64 crate & SHSWFS from Andor Camera*

A WPU latency-timing diagram for the WPU on the PMC03F card is shown in Figure 6.16. The delay within the WPU FPGA processing logic is about 53 cycles in total. This delay is from the arrival of the last pixel of a sub-aperture to the arrival of the gradient data at the PCI interface chip on the PMC03F FPGA board. Given the working clock of 125MHz, the delay is about **0.42 µs**. In addition to this are the interface delay from the serial FPDP and the delay of DMA between the PCI bus and the host memory.

For the VPF1 board, SPARTA required the data to transfer from the VXS VPF1 board via sFPDP. Here there is the latency of **0.26 µs** (33 cycles - to the Bridge interface in Figure 6.16). Giving a total latency of **0.68 µs.**

If the CPU's in the VPF1 are to calculate the reconstructor and controller then we would expect a delay similar to that of a PMC03F card. This hasn't been measured but isn't expected to be more than **1.0 µs.**

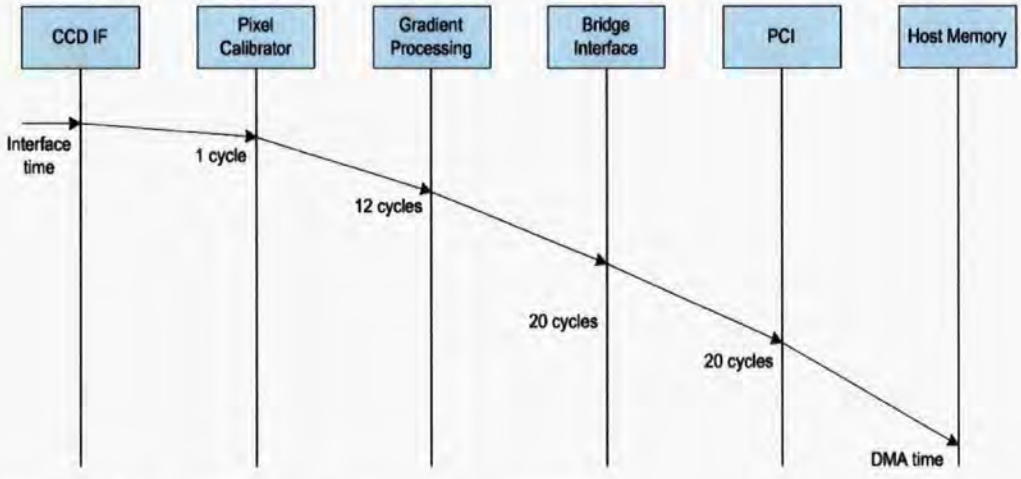

Figure 6.16 *WPU Latency Diagram on PMC03F*

6.8 NNGRTC Other Considerations

There are a number of other considerations regarding the design, construction, testing and integration of the suggested NNGRTC. They include simulating systems to predict performance, the use of communication debugging hardware, the use of APIs, software compatibility, hardware compatibility and the integration of GLAS.

6.8.1 Simulation Environment

Section 5.6 described the requirement of having a dedicated development system. A standalone development NNGRTC would be able to allow a developer to test the functionality of a new module. However it wouldn't allow the user to assess the effect on performance. Measuring the theoretical effect on performance is something that is important. To be able to do this a simulator connected to the development RTCS is required.

An ideal solution would be to combine Durham's simulation platform (to simulate a target, guide star, atmospheric turbulence, telescope and the NAOMI RTCS components such as the DM) and connect to the RTCS to simulate inputs and outputs of the RTCS. I.e. Figure 6.17.

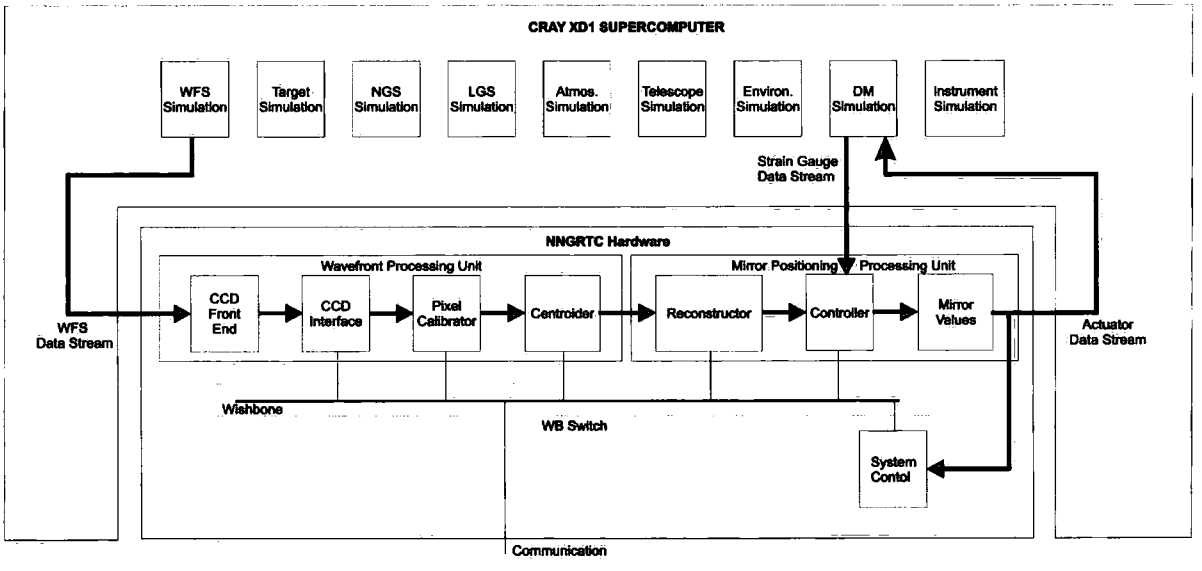

Figure 6.17 *CRAY interacting with the NNGRTC*

The Durham simulation platform is on the Cray XD1 Supercomputer, which is subsequently described.

The Durham AO simulation platform is a single-chassis XD1 containing six processing nodes connected by a high-performance interconnect (Cray RapidArray). This interconnect provides a sustainable bandwidth of 1.6 GBs^{-1}. Each processing node contains two 64-bit processors (Opteron) at 2.2 GHz, a Xilinx Virtex II-pro FPGA, which is used for application acceleration, and 8 GB memory.

Figure 6.18 *CRAY XD1 Supercomputer and Interconnect*

6.8.2 Communication Debugging

It is foreseen that most of the system debugging could take place on either the development system or with the use of the simulation platform to read outputs.

Potentially other operational problems could occur with the data. The NNGRTC will have the facilities to output raw data coming into the system. Two further pieces of hardware will help develop and debug the system, these being the sFPDP Data Recorder and the sFPDP protocol analyzer.

6.8.2.1 Serial FPDP data recorder

For testing and debugging, it may be required to record data-streams to or from the NNGRTC or to record internal data streams. Because of the high volume of data produced by the applications, storage in memory is very limited in time and storage on a disk is not always possible because the throughput is too high. To overcome this problem, dedicated commercial recording solutions can be used. Typically these recording systems use disk arrays with dedicated controllers and a front-end, which interfaces with the data stream to be recorded. The existing systems can record up to tens of minutes at the full Serial FPDP data rate (247MB/s).

In addition to data storage, these systems can also replay the recorded data or replay data loaded through a different interface (e.g. Ethernet).

An identified commercial Serial FPDP data recorder is the VMETRO Quad Serial FPDP Data Recorder & Playback System.

6.8.2.2 Serial FPDP protocol analyzer

Commercial Serial FPDP protocol analyzers are available such as the Absolute Analysis Investigator Serial FPDP Analyzer.

```
int SetCCDNumber(int noc); // set the number of the CCDs
int SetCCDSize(int det_id, int x, int y); // set the size of the CCD
int SetSANumber(int det_id, int nx, int ny); // set the No of SAs
int SetSASize(int det_id, int sx, int sy); // set the size of the SAs
int OpenMaps(int time_out = 0); // returns a transaction id, or on fail
returns WPU_NA or WPU_TIMEOUT
int SetSAMap(int tid, int det_id, int * sa_num_map, int * sa_pos_map, int
* sa_init_map, bool copy = true); // define pixel order
int SetDarkMap(int tid, int det_id, int * map, bool copy = true); // load
dark map(detector id, map)
int SetFlatMap(int tid, int det_id, double * map, bool copy = true); //
load flat map (detector id, map)
int SetBackgroundMap(int tid, int det_id, int * map, bool copy = true);
// load background map (detector id, map)
int SetThresholdMap(int tid, int det_id, int * map, bool copy = true); //
load threshold map (detector id, map)
int SetWeightingMap(int tid, int det_id, double * map, bool copy = true);
// load weighting map (detector id, map)
int SetSAWeightingMap(int tid, int det_id, uint32 * map); // load
weighting map for the slope calculation (detector id, map)
int CloseMaps(int tid);
int SetScalar(int det_id, int * map); // load non-linear value scaler map

// capture the pixel stream frames
int SetPixelTap(int pixel_tap); // select which pixel stream to capture
int GetCCDFrameLength(void); // returns the buffer length (32bit DWORD)
int GetSingleCCDFrame(int * buffer); // get next single ccd frame
int StartCCDSubsampling(int subsample); // start ccd subsampling
int StopCCDSubsampling();
int GetSubsampledFrame(int * buffer); // get subsampled frame ()

// capture the SA result
int StartSACapture(void); // start SA result acquisition
int StopSACapture(void); // stop SA result acquisition
int GetSlopeFrameLength(void); // returns the frame length (32bit DWORD)
int GetFluxFrameLength(void); // returns the frame length (32bit DWORD)
int GetSlopes(int * buffer, int n); // get slope buffer (n)
int GetSAFlux(int * buffer, int n); // get flux buffer (n)
int GetSAResultFrameLength(void); // SA Result frame is a combined frame
of SA number, SA slopes and flux
int GetSAResult(int * buffer, int n); // it is only available when
SACapture is at stop mode

// other diagnostic interfaces
int GetAccumulatedFrame(int * buffer, int nof); // get averaged frame()
int GetTotalFlux(int * buffer, int len); // get last total flux per frame

// simulation interface
int SetSimulatedCCDFrames(int nof, int * buffer); // load simulated ccd
frames (simulated data)
int StartSimulatedCCDReplay(int nTimes, int nFrames); // start simulated
ccd replay (nTimes, nFrames)
int StopSimulatedCCDReplay(); // stop the ccd replay
int SetSimulatedSlopes(int nof, int * buffer); // start simulated slopes
int StartSimulatedSlopesReplay(int nTimes, int nFrames); // start
simulated slopes(start value, range, step)
int StopSimulatedSlopesReplay(); // stop the slopes replay
```

Figure 6.19 *WPU API*

6.8.3 Pipeline Configuration (API)

Software and Wishbone driver configuration will be done with the aid of an Application Programming Interface (API).

The implementation of the Wishbone driver would rely on the specific hardware and operating system. However the API is standardised by using the generic Initialisation, Open, Close, Read, Write and Control functions.

The Software WPU library API, which exists for SPARTA is given in Figure 6.19.

6.8.4 NNGRTC Software Compatibility

Replacing the existing NAOMI RTCS can't be considered in isolation. All inputs and outputs have to be considered. The supervisory communication stream taking commands from NAVIS to the RTCS and sending data from the RTCS to NAVIS requires consideration. There are reasons for and against replacing TopGUI and the NAOMI middleware, yet an understanding of all the issues is required

The three options are:

- Replacing the higher level software.
- Modifying the sequencer/EPM.
- Introducing an interface layer above the NNGRTC.

Each would have to be assessed in terms of cost, complexity and effort.

For NAOMI to operate, the higher-level functional scripts relating to setup and calibration would still have to successfully execute.

SPARTA has a co-processing cluster which conducts auxiliary processes such as statistical machinery and parameter optimisation. This could be implemented for the NNGRTC. There would be many benefits in increasing the communication capabilities and bandwidth to take advantage of some of the SPARTA higher level software and GUIs.

6.8.5 NNGRTC Hardware Compatibility

There are a number of modifications that would be required to the existing control electronics to send and receive the data to the NNGRTC in a sFPDP format. The idea of introducing sFPDP signal converters was first explored in the DARTS project. The proposed architecture is seen in Figure 6.20.

The Signal Converters help keep the design modular, flexible and easily upgradeable. The 'Signal Converter' should introduce a minimum latency. They could be small, cheap FPGA devices with no intelligence, other than to convert signals into the correct format. Standardising the interface and keeping the control hardware modular, keeping to DARTS requirements. The additional latency to performing the signal conversion is well within the 0.5 ms system latency requirement. Similar modifications are required for future ESO AO components for SPARTA. The ANDOR camera has a sFPDP signal converter.

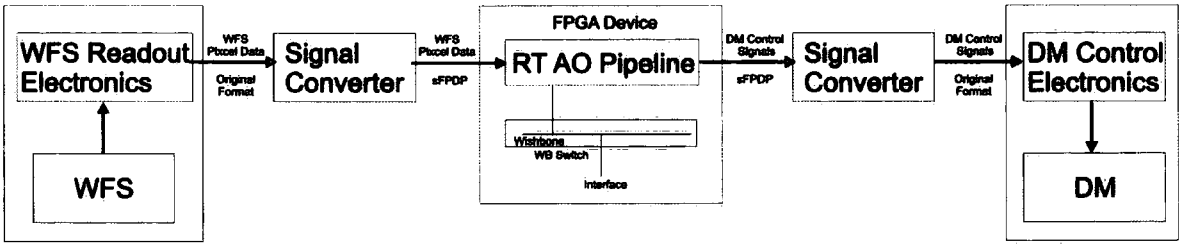

Figure 6.20 *Signal Converters are required to keep the design modular*

In addition the CRAY XD1 would require a modification to input and output data in this format.

6.8.6 Integration of the GLAS WFS Control System into NNGRTC

The GLAS tip-tilt controller can easily be reintegrated into the NNGRTC as the design allows for expansion and the use of multiple WFS detectors. The topology required for SPARTA includes those displayed in Figure 6.21:

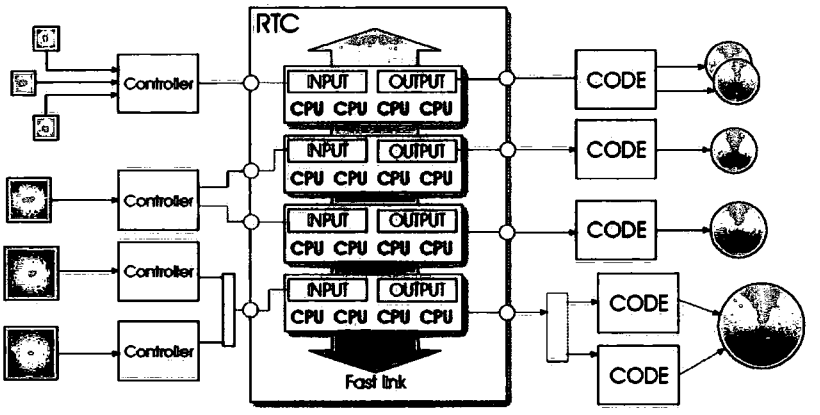

Figure 6.21 *SPARTA Topology*

6.8.7 NAOMI performance gain with SPARTA

It is impossible to predict if the on-sky performance of NAOMI would improve given the introduction of a SDSUIII Controller and a SPARTA system with a feedforward controller. There are other factors that aren't considered such as the spatial registration of the lenslet arrays.

Simulations are required to calculate the maximum potential correction given the seeing statistics of La Palma and a perfectly corrected system at a 1 kHz rate.

7 Conclusion

This investigation has had a successful outcome. The most significant achievements are that the study improved the performance of NAOMI and that it produced a NNGRTC design, which has contributed to the design of a generic SPARTA platform that will serve Second-Generation VLT AO Systems and first light E-ELT AO systems. The modular control system includes the concept of a hardware optimised feedforward controller opposed to a standard PID variant controller.

At this moment in time technology cannot provide a perfect astronomical AO system. An ideal system would wavefront sense all layers of turbulence over the complete FOV of the telescope to the resolution greater than the science instrument and send signals to the wavefront corrector(s) fast enough to allow the wavefront to correct before the light moves onto an adjacent pixel on the science image detector. Understanding Atmospheric Turbulence Theory, Image Correction Theory, Control Theory and AO Component Theory will help physicists and engineers understand fundamental physical principals. Some are external processes over which they have no control over such as the propagation of light and atmospheric turbulence. Some, such as component theory, aid engineers and physicist in designing AO systems.

NAOMI was a first common-user AO facility designed for a telescope that was commissioned before astronomical adaptive optics was feasible on a 4.2 m telescope. Achieving AO correction was a great achievement. For example, it contained a RTCS working at its very limits. However, as a common user instrument, NAOMI had a lot to be desired.

Characterisation revealed a number of key discoveries. It gave an understanding of the actual system as opposed to a theoretical model. Characterisation showed that a number of improvements would benefit the performance of the facility before optimising the RTCS would. The FSM investigation uncovered that the FSM Filter was providing the main source of system error at the time. Once corrected, the various WFS modes became effective. Only the introduction of GLAS and the SDSUIII Controller would leave the RTCS as being the 'bottleneck', due to the effectiveness of its controller. As the RTCS hardware required upgrading before such a controller could be introduced, it was decided to look at an upgrade, especially since both the GLAS project and SDSUIII project was running in parallel.

Attention was turned to examining the worldwide state of astronomical adaptive optics systems and instrumentations. Doing so demonstrated that there was a vast number of different AO RTCS in the community. ESO also realised that highly valued time and effort was being wasted in repeating work. Fortunately, forming a collaboration with ESO AO RTCS group, the author was able to investigate creating a suitable platform by looking at the lessons learned particular by NAOMI and other ESO AO instruments.

In particular, because NAOMI has no development system, was extremely difficult to program and was at the limit of its capabilities, the author wanted to create a future system that was maintainable, scalable, upgrable and developable. The architecture had to be modular to achieve this.

As the ESO Second-Generation AO RTCS requirements were of a magnitude in order more demanding that the NAOMI requirements, the investigation focused on producing a RTCS to

satisfy those. The NNGTC shared the same principles but novel components such as the strain gauges required variations. Table 7.1 summarises the selections made for the NNGRTC.

Item	Choice
NNGRTC Backplane:	VXS
NNGRTC SBC:	VPF1
NNGRTC Processor:	PowerPC 7455 (x2)
NNGRTC Processor Speed:	1 GHz
NNGRTC FPGA:	Xilinx Virtex-II Pro XC2VP70-6
NNGRTC Communication Protocol:	sFPDP
NNGRTC Communication Bandwidth:	2.5 Gbs^{-1}
NNGRTC RTOS:	VxWorks
NNGRTC Cross Development Platform:	Linux
NNGRTC RTOS:	VxWorks
NNGRTC FPGA ISE:	Xilinx ISE
NNGRTC FPGA Simulation Tool:	Mentor Graphic ModelSim
NNGRTC FPGA Synthesis Tool:	Xilinx XST
NNGRTC FPGA Development Host:	AMD 64bit
NNGRTC FPGA Development OS:	Linux

Table 7.1 *NNGRTC Component Choices*

A modular FPGA-based design for NNGRTC was presented. This included a feedforward controller. This controller would have to be tuned based on further characterisation of the DM. The RTCS would allow the strain gauges to sample at 10 kHz and to drive the DM to its limits. The tuning of the feedforward controller would depend on access to the instrument and it isn't clear that the NNGRTC would ever receive funding.

However, the Second-Generation VLT instruments are funded as is the CANARY project, an E-ELT risk mitigating LGS MOAO demonstrator. CANARY's RTCS is currently in its design phase. Lessons learned from this research should be fed into the CANARY project. The general requirements for an AO system should apply to demonstrators, not just common-user instruments as instrument scientists will always try and push systems to their limits.

In addition to having a feedforward controller, implementing an active or an adaptive self optimising controller would be the next evolutionary stage. This could be achieved by statistical machinery algorithms calculating atmospheric parameters such as the seeing and DM data and updating controller parameters at a reasonable rate. Another upgrade would be the introduction of independent optical DM figure sensor information into the RTCS. This information potentially would be more reliable than the strain gauge feeback information.

Adaptive Optics will be a fundamental part of the next generation of Extremely Large Telescopes (30 – 50 m), which are currently in their design phase. The E-ELT AO systems are being designed and controllers, continual component characterisation and self-optimisation algorithms are required for astronomers to take full advantage of the telescope. Such systems and ideas need to be conceived at the design phase of a system and not be an afterthought.

Appendix A Alternative Wavefront Sensors

A.1 Curvature WFS

The **Curvature WFS** (CWFS) measures both the radial tilts and the Laplacian, the second spatial derivative, of the WF. The resulting data can be used to reconstruct the WF by solving the Poisson equation with the Neumann boundary conditions.

The principle of the CWFS is shown in Figure A.1. The curvature sensor consists of two detector arrays placed at two defocused pupil planes, P_1 and P_2, at equidistance, l, either side of the telescopes focal plane. The two detector arrays record the irradiance distribution, $I(r)$, produced from the light source.

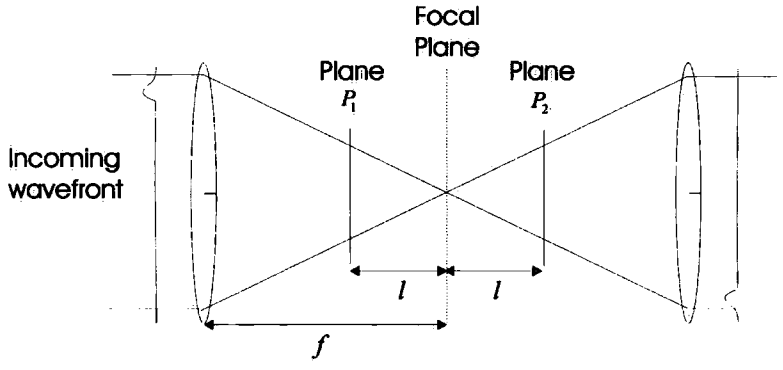

Figure A.1 *Principles of a curvature WFS*

Geometrical optics approximation is used to give the result that local WF curvature inside the beam and of the WF radial first derivative at the edge of the beam can be measured by the irradiance transport equation, the difference between the two-plane irradiance.[268] The measured signal is the normalised difference between the illuminations $I_1(\boldsymbol{r})$ and $I_2(-\boldsymbol{r})$ in planes P_1 and P_2 respectively. This is related to the WF phase ϕ in the pupil plane by:

$$\frac{I_1(\boldsymbol{r})-I_2(-\boldsymbol{r})}{I_1(\boldsymbol{r})+I_2(-\boldsymbol{r})}=\frac{\lambda f(f-1)}{2\pi l}\left[\frac{\partial\phi}{\partial n}\left(\frac{f\boldsymbol{r}}{l}\right)\delta_c-\nabla^2\phi\left(\frac{f\boldsymbol{r}}{l}\right)\right] \qquad \text{(A.1)}$$

Where $\dfrac{\partial\phi}{\partial n}$ is the radial first derivative of the WF at the edge,

δ_c is a linear pulse distribution around the pupil edge, ∇^2 is the Laplacian operator.

For the approximation to remain valid, the distance l takes on the condition:

$$l \geq f\left[1+d/(f\theta_b)\right]^{-1} \qquad \text{(A.2)}$$

Where θ_b is the blur angle and d is the subaperture size.

The normalisation, $I_1(\boldsymbol{r})+I_2(-\boldsymbol{r})$, of the irradiance transport equation (A.1) leads yields to a sensor relatively insensitive to scintillation, making it achromatic.

The blur angle, θ_b, is generally small. Examining equation (A.2) reveals that for a very large blur angle, l tends to f and the measurement is made in the pupil plane. To avoid any smearing of the intensity variations, the blur produced in the defocused pupil planes must be small compared to the size of the WF fluctuations.

Examining some point source cases reveals that if the SA size is greater than the fried coherence length, r_0, then only low-order aberrations will be measured. If the SA size is smaller than r_0, then higher aberrations of spatial scale d must be measured.

This analysis concludes that, firstly for high-order aberration measurements, the distance l to focus must be larger than for small aberrations. For extended sources, l must also be larger than for point sources. An increase of l means a decrease of the sensitivity (but an increase of the dynamics) of the CWFS as expressed by equation (A.1). The distance l is very similar to the distance l in the SHWFS. When the distance l is decreased to the minimum, the CWFS is only able to measure tilts and can be reduced to a quad cell. In this limiting case the CWFS provides four edge measurements and no curvature.

Increasing the distance l results in an increase in spatial resolution but decreases the sensitivity. Thus a smaller distance yields a higher sensitivity to low-order aberrations and reduces the aliasing of the high-order aberrations on the low-order ones because of the diffraction effect. The sensitivity and dynamics are easily adjusted by the distance l.

Finally, the WF can be reconstructed directly when using a bimorph or membrane mirror as a WFC. The system's mechanical behaviour removes the need for any matrix multiplication in the feedback loop.

A.2 Pyramid Wavefront Sensor

The **Pyramid Wavefront Sensor** (PWFS) is a pupil plane sensor that is an extension of the Foucault knife-edge test used to measure WF gradients. Figure A.2 shows a transparent pyramid dissecting a light beam into four parts. The pyramid is used as an image splitter, having its tip placed in the pupil plane. Relay lens are placed behind the pyramid and the light is split forming four images of the telescope pupil onto a detector.

Like other WFS, it is possible to detect light either using a CCD or a quad-cell. Variations in the WF will lead to detected intensity fluctuations. Two signals proportional to the WF slopes are obtained by computing the normalised intensity differences in two directions.

If diffraction effects occur on a point source, the intensity distributions in the four pupil images become non-linear functions of the WF shape, leading to a failure to measure WF slopes.

If the amplitude of the aberration is much less than the wavelength, although complex, it is still possible to reconstruct the WF shape. If the star is rapidly moved over the edge of the pyramid in a circular pattern, it is possible to retrieve the linearity. This effect smears the point source, because the signal is integrated over one or more wobble cycles.

The SAs are defined by the detector pixels, the PWFS has no lenslet array. It means that for faint stars the number of SAs can be reduced simply by binning the CCD.

Secondly, the amplitude of the star wobble can be adjusted as a trade-off between the sensitivity (smaller wobble) and linearity (larger wobble). At small amplitudes the sensitivity of a PWFS can be higher than that of a SHWFS.[269]

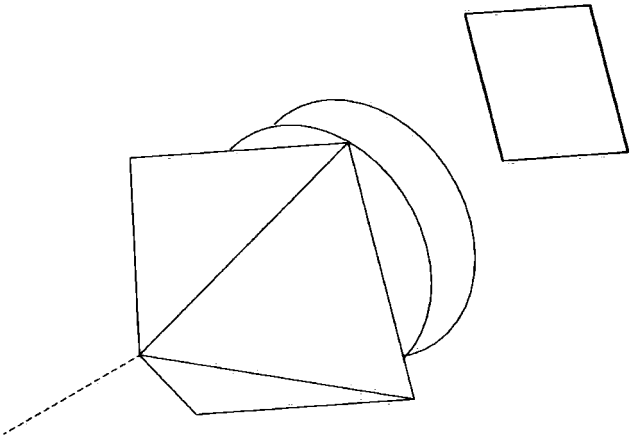

Figure A.2 *Pyramid Wavefront Sensor*

Another of the PWFS strengths is that it is theoretically possible to combine the light from several faint guide stars on a single detector by placing several pyramids in the focal plane, making the PWFS suitable for MCAO.

A.3 Lateral Shearing Interferometer

The Interferometer isn't currently used in astronomical AOS but has been included for completeness. In AO the interferometer is required to be self-referencing due to the lack of a plane wave reference beam. Many types of interferometer have been developed, including shearing the WF rotationally, radially or laterally. The most commonly used interferometer in AO is the **Lateral Shearing Interferometer** (LSI).[273,270,271]

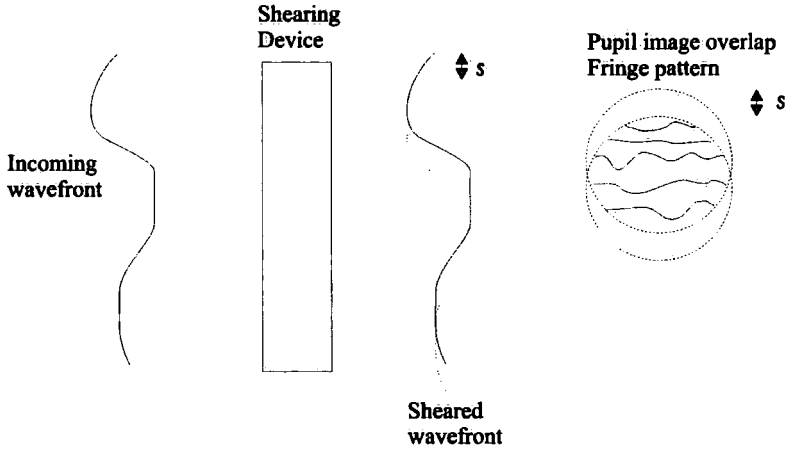

Figure A.3 *Principles of the Lateral Shearing Interferometer*

Figure A.3 displays the LSI shows a shearing device splitting the incoming WF into two components and superimposing them by a shear distance *s*, forming an interference pattern.

The interference fringes are a measurement of the phase difference over the shear distance in the shear direction. In a pupil image plane, the resulting intensity, *I(r)*, is given by:

$$I(\boldsymbol{r}) = \frac{1}{2}\left|\exp\left[i\phi(\boldsymbol{r})\right] + \exp\left[i\phi(\boldsymbol{r}+\boldsymbol{s})\right]\right|^2 = 1 + \cos\left[\phi(\boldsymbol{r}) - \phi(\boldsymbol{r}+\boldsymbol{s})\right] \qquad \text{(A.3)}$$

In principle, the LSI measures the phase difference for a shear s in the pupil. Equation (A.3) states that the phase is inversely proportional to the wavelength, giving a chromatic expression. The phase is given by:

$$\phi(\boldsymbol{r}) = \frac{2\pi}{\lambda}\delta(\boldsymbol{r}) \qquad \text{(A.4)}$$

Where $\delta(\boldsymbol{r})$ is the optical path difference OPD induced by the atmospheric turbulence.

To determine the complete WF the beam must be sheared in both the x and y direction. To allow for orthogonal shearing the beam should be equally divided into two similar channels, each containing a detector to map each WF gradient. Each detector corresponds to SAs of the telescope's pupil, determining the spatial sampling of the WF and provides spatial filtering of the phase gradients. Thus, the measurement represents the average slope of the OPD in the shear direction, over each SA. The classical technique is of heterodyne modulation can be used to eliminate detector calibration.[272]

There are two main reasons why LSI isn't used for astronomical WFSing; firstly, the efficiency is limited to about 70% owning to the light losses in higher diffracted orders. Since two channels are required for x-slope and y-slope measurements, the LSI has at least two channels per SA. Maximum light efficiency requires four detectors as indicated by Hardy.[273] Secondly, the LSI also leads to relatively complex hardware and implementation difficulties.

Appendix B Alternative Wavefront Correctors

B.1 Continuous Facesheet Deformable Mirror

The required characteristics of a **Continuous Facesheet Deformable Mirror** (CFDM) are dictated by the statistical spatial and temporal properties of the phase fluctuations resulting predominantly from the atmosphere and the required degree of correction required for the AO application. I.e. XAO will require a higher spatial correction than GLAO. For astronomical applications, the number of actuators, N_A, is proportional to:

$$N_A = \left(\frac{D}{r_0}\right)^2 \tag{B.1}$$

Where D is the telescope diameter and r_0 is Fried's diameter.

The number of actuators range from at least two (tip/tilt) to several hundreds, depending on many factors associated with the application such as the observed wavelength, the brightness of the guide star and the mode of AO. The required stroke is proportional to the ratio:

$$z_s = \lambda\left(\frac{D}{r_0}\right)^{5/6} \tag{B.2}$$

In practise this is independent over the range of several microns. The required actuator response time is proportional to the ratio:

$$t = \frac{r_0}{\bar{v}} \tag{B.3}$$

The response time is in the order of at least a few milliseconds and increases as the degree of correction decreases. The required optical quality (RMS surface error) varies in proportion to the observed wavelength and is in the order of a few tens of nanometers.

B.1.1 Actuators Types

The widely used actuators in AO DMs operate using of the **piezoelectric effect**, which is the creation of a strain-inducing stress under an applied electric field. Astronomical AO requires reliable components which are economically viable, lead ziconate titanate Pb(Zr,Ti)O3 (**PZT**) and lead magnesium niobate, Pb(Mg1/3, Nb2/3)O3 (**PMN**) have emerged the popular material for actuators over the last decade for conventional DMs of diameters greater than 2cm.

A CFDM contains this reflective faceplate using a regular grid of push pull actuators.

There are three ways that CFDM can be deformed: by push-pull actuators, by flexing the surface by differential lateral forces and by using electrostatic forces on small (integrated circuit scale) sub-components.

Monolithic Piezoelectric Mirrors (MPM) was an early type of CFDM constructed by Itek from single crystals of piezoelectric material into which a number of actuation electrodes had been

introduced. The mirror surface was deposited onto a polished face of a crystal. Although operating voltages very high (10,000 V), the characteristics of these mirrors in terms of temporal response (1 kHz corrections) and reliability (no failures) were superb. A fundamental drawback was that the stroke was restricted to less than a micron.

A CFSM, when suitably arranged with a SHWFS (for example, in the Fried or Hudgin Geometries), allows the detection of actuation errors by the measurement of the resultant slopes at the surrounding SA centres. A CFSM only allows the detection of piston error as an apparent slope; it does not enable direct measurement of atmospheric piston value.

B.2 Bimorph Deformable Mirrors

An example of a **Bimorph Deformable Mirror** (BDM) is displayed in Figure B.1. It shows a layer of glass containing a reflective coating, glued to a PZT ceramic. Either a thin conductive film or a number of separate electrodes is wedged between the mirror and the ceramic. The glue used for bonding will not shrink after application. After gluing, the reflective surface is usually coating and polished. The inner electrodes are connected to various back electrodes, placed on the other side of the PZT ceramic to form different patterns.[274,275,276]

The dimensions of the PZT changes when a voltage is applied between a pair, front and back, of electrodes. The amount of deformation depends on the electric field and the coefficient of the piezoelectric tensor d_{13}. , Neglecting the stiffness of the layers, the local radius of curvature of the mirror, R, is proportion to the voltage supplied V:

$$R = \frac{Vd_{13}}{t^2} \tag{B.4}$$

Where t is the thickness of the ceramic and the facesheet.

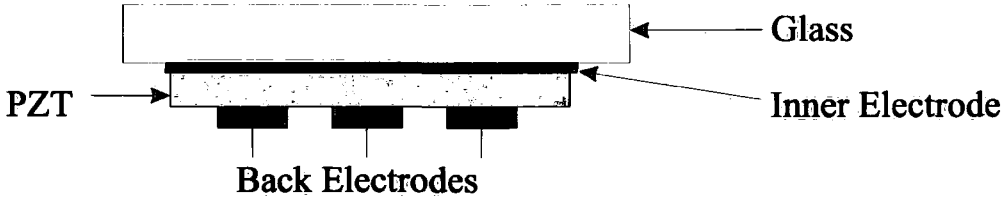

Figure B.1 *Bimorph Deformable Mirror*

For a back electrode of diameter D, the voltage necessary for a center-to-edge deformation for a particular wavelength, λ is given by:

$$V_\lambda = \frac{2t^2\lambda}{D^2 d_{13}} \tag{B.5}$$

Another example of a BDM consists of an array of electrodes placed between two oppositely polarized piezoelectric ceramic wafers bonded together. When a voltage is passed through the electrodes the ceramics contract laterally.[2]

The BDM performance matches very well with a CWFS. It is possible to obtain a nearly diagonal control matrix with a minimum number of seeing elements and bimorph electrodes

required to correct a given number of low-order Zernike modes, thus complex reconstruction circuitry isn't required.

They are relatively easy to manufacture and inexpensive, particular attention must be paid to durability.

BDMs have successfully been used in astronomical AO systems and are planned to be used in the future. A technical limit has been predicted at around Zernike radial degree 7, occurring from current bimorph construction technology. Currently there exists an operational system with Zernike radial degree 5. Many scientists continue to work on improving the ability, design and configuration of the BDM, including segmented zonal bimorphs.[276,277,278]

B.3 Micro-electric Mechanical Deformable Mirror

Micro-Electric deformable Mirrors (MEM) technology is rapidly evolving. Although prototypes have been formed, one hasn't been deployed in an operational astronomical AOS to date.

MEMs technology uses IC fabrication technologies to produce very small DM arrays and will be critical to the future of AO, especially in the area of MOAO where small mirrors will be required. AOS miniaturisation implies cost reduction. The overcome the ~7 mm minimum actuator spacing for conventional mirrors which drives pupil and hence beam sizes and establishes the physical scale of AOSs, which in general will benefit non astronomical AO.

A MEM device is schematically displayed in Figure B.2.

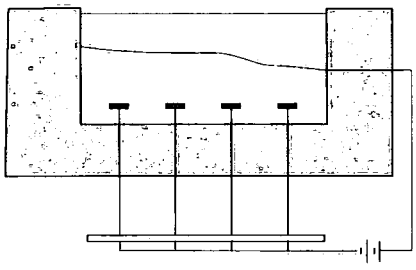

Figure B.2 *A Membrane Mirror*

B.4 Liquid Crystal Devices

Liquid Crystal Devices (LC) are included for completeness, it is an emerging technology that is evolving and although the devices currently aren't suitable for astronomical AOS.[279,280,281]

LCDs are attractive because of their compact size, small power consumption, low cost, large number of correcting elements and they contain no macroscopic moving parts.

A LCD is displayed in Figure B.3. The optical property of interest is their birefringence. For a refractive index of 1.5, the birefringence is of around 0.2, higher than electro-optical crystals.

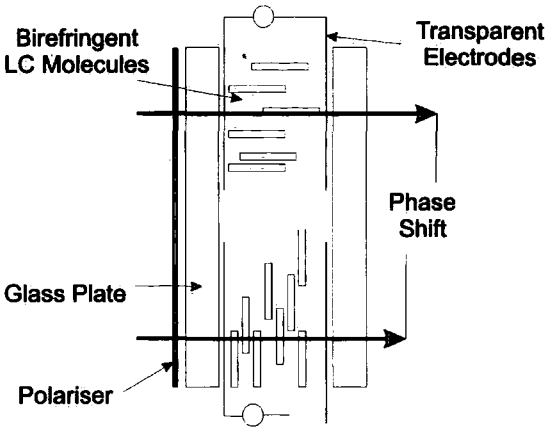

Figure B.3 *Neumatic Liquid Crystal Wavefront Corrector*

Liquid crystals exist in the intermediate state of matter between liquid and solid. They are categories into two types, nematic and smectic crystals, depending on the center of gravity of their molecules. This difference leads to different electrical properties.[282]

Nematic crystals provide continuous index control, which is of interest to AO. Their rise time is related to the forced alignment of molecules by the applied electric field, and it is of the order of 10 ms. The general problem with these crystals is the time taken to return from a modulated value, the relaxation time, this is in the order of 100 ms. The decay time may be forced to reach the rise time by using two excitation frequencies.[283] Phase correction has been demonstrated but with the LC devices producing a response frequency of about 10 Hz with a 1μm stroke, the device won't fully compensate the turbulence effects of the atmosphere. Another drawback of the device is their potential limited spectral range.[284,285,286]

The **smectic crystals** of interest are the ones that contain ferroelectric properties. Ferroelectric liquid crystals only display binary modulation, but have a faster response time than the nematic crystals. It is possible to have a multiple pass configuration with multiple polarisation states but then you compromise greatly on throughput.

Appendix C Other Reconstructors

A better method than the least squares reconstructor is the **optimal reconstructor** as it minimises the actual WFS error directly, maximising the Strehl ratio in the image.[287] This method takes WFS noise. This analysis leads to the "optimal" control matrix:[288]

$$\boldsymbol{C} = -\left[\boldsymbol{M}^T\boldsymbol{M}\right]^{-1}\boldsymbol{M}^T\left\langle\phi_0\phi_0^T\right\rangle\boldsymbol{S}^T\left[\boldsymbol{S}\left\langle\phi_0\phi_0^T\right\rangle\boldsymbol{S}^T + nn^T\right]^{-1} \qquad \text{(C.1)}$$

Where $\boldsymbol{C}$ is the Control Matrix, $\boldsymbol{M}$ is the Mirror Matrix, $\boldsymbol{S}$ is the Interaction Matrix,
ϕ_0 is the WF aberration and n is the noise on the WFS signals.

This reconstructor makes no assumption about the nature of the statistics. Assuming Gaussian statistics would produce a **maximum likelihood reconstructor**.

When calculating the control matrix, $\boldsymbol{C}$, both the WF aberration statistics and the noise statistics are taken into account, which would be known to before practical implementation. The implementation of the optical reconstructor requires explicit forms of the interaction and influence matrices.

There are many minor variations of the least squares and the optimal reconstructor methods used in AO, all containing the same fundamental principles. The main differences are the choice of basis functions used for any intermediary reconstruction stage. In the least-squares reconstructor, system modes are used as an intermediary stage. By varying the basis functions it is possible to produce a completely modal reconstructor or a completely zonal reconstructor.[288]

The reconstructors discussed have shown the strength of modal analysis. Another advantage is the ability to control several WFC simultaneously. A DM and a TTM is a common example, the FSM is used to reduce the mechanical stroke on the DM. As the two mirrors aren't completely independent, it is important to use a control mode basis where some modes fully define the coupling between them. If the bandwidth of the TTM is sufficiently high, there is no need for the DM to correct for the tip and tilt, otherwise it is useful to compensate for high stroke slowly evolving tip and tilt with the DM. In both cases, a set of control modes must be determined.

There are times when linear reconstructors are insufficient. If strong scintillation occurs the WF may contain optical dislocations or vortices. For well-developed speckle, there are roughly as many dislocations as speckles. In such cases dislocations are present; therefore it can no longer be assumed that the phase can be represented as a linear superposition of basis functions. Roggemann and Koivunen showed that the nonlinear reconstructor Goldstein algorithm can give better reconstruction in such situations.[289] Other techniques being researched are the use of neural networks and analogue reconstructors.

Appendix D Balancing the Load

D.1 AlgSGcombine (C40 Code Modifications)

A generic AlgSGcombine algorithm was developed with the aim to place the same algorithm on all 8 SG DSPs.

AlgSGcombine (1393 lines of code) file combined the functionality of:

- AlgSGtimer (version: 1.10 12th August 2001: 338 lines of code).
- AlgSGmirror (version: 1.16 23rd December 2000: 548 lines of code).
- AlgSGadc (version: 1.21 24th May 2000: 1068 lines of code).

The development largely consisted of including the functionality of AlgSGtimer and AlgSGmirror into AlgSGadc and then adding the options for transmission and receipt of the 32 channels of ADC data. The majority of the 'merge' occurred in the Interrupt Service Routines (ISRs), the SetParameters and GetParameters functions.

Header Files					
RT.h	ISRutility.h	BarrierSync.h	packet40.h	C40Commands.h	SG.h
Stdio40.h	C40timer	packBuffer	C40Diag.h	Signals.h	

Table D.1 *Included Header Files*

Additional merges were required. The AlgCGcombine included Header Files can be seen in Table D.1. These were already common to each algorithm. The combined global #defines are viewed in Table D.2.

#define	Value	Taken From
DEBUG		
MINIMUM_ISR_GAP	250	AlgSGtimer
DAC_MIN	300	AlgSGadc.c
DAC_MAX	(8192 – DAC_MIN)	AlgSGadc.c
MAX_SYNCH_TRIGGER	300	AlgSGmirror.c
MIN_SYNCH_TRIGGER	2	AlgSGmirror.c
MAX_SYNCH_CLOCKS	20000	AlgSGmirror.c
TT_DAC_MIN	0	AlgSGmirror.c
TT_DAC_MAX	8191	AlgSGmirror.c
TT_SLEW_LIMIT	50	AlgSGmirror.c
TT_SLEW_LIMIT_2F	2500.0	AlgSGmirror.c
#define TT_INDEX	15	AlgSGmirror.c

Table D.2 *Global #defines*

The contents of the global parameter structure and snapshot structure for AlgCGcombine are displayed in Table D.3 and Table D.4 respectively. The forward declarations are contained within Table D.5.

The main function of the AlgSGtimer.c sends a trigger pulse to the ADC. The combined algorithm would have to send the tigger pulse as soon as possible after the AlgSGtimer goes into its ISR (i.e. after its self-induced timer interrupt). In doing so the other processors can

then be all interrupted and waiting when data starts to arrive from the ADCs into their DMA buffers. The algorithm sat in Electra/Realtime/StrainGauge.

type	Parameter	type	Parameter	type	Parameter
int	ADCport	int	ADCblockSize	int	waveformLength
int	demandPort	int	waveformChannel	int	waveformRepeat
int32	snapshotDecimate	int	waveformID	int	tableOffset
int32	ADCcaptureDecimate	int	captureChannel	int	snapshotFlag
uint32	synchClocks	int	synchronise	int	feedforward
uint32	demandFrameGap				
uint32	*demandBuffer	int	*outputBuffer	int	*ringBuffer
Int	*ADCbuffer;	int	*ADC	int	*unpackedDemand
int	*feedforwardDemand	float	*accumulator	int	*lastOutput
struct	snapshotStruc *snapshot;	struct	snapshotStruc *dummySnapshot	uint32	*finalDemand

type	Parameter
uint32	initialDemand[SG_PACKED_DEMAND_BUF_SIZE];
float	ADCcalGain[SG_UNPACKED_DEMAND_BUF_SIZE];
float	ADCcalOffset[SG_UNPACKED_DEMAND_BUF_SIZE];
float	ADCservoGain[SG_UNPACKED_DEMAND_BUF_SIZE];
int	passThrough[SG_UNPACKED_DEMAND_BUF_SIZE];
int	ADCreorderTable[SG_ADC_MAX_BLOCK_SIZE];
int	waveform[SG_MAX_WAVEFORM_SIZE];
int32	triggerPort
int32	interruptInterval
int32	lastISRperiod
int	DACreorderTable[SG_MIRROR_REORDER_MAX_SIZE]
int32	mirrorDataPort
int32	mirrorSyncPort

Table D.3 *Global 'parameter' structure contents*

type	Parameter	from
float	accu[SG_ADC_MAX_BLOCK_SIZE]	AlgSGadc.c
int	ADC[SG_ADC_MAX_BLOCK_SIZE]	AlgSGadc.c
int	output[SG_ADC_MAX_BLOCK_SIZE]	AlgSGadc.c
int	inputDemand[SG_PACKED_DEMAND_BUF_SIZE]	AlgSGmirror.c
int	finalDemand[SG_PACKED_DEMAND_BUF_SIZE]	AlgSGmirror.c

Table D.4 *Global 'snapshot' structure contents*

type	function	Description
void	ISR	The interrupt service routine
Algorithm	*Create	Create/copy an algorithm instance
void	Destroy	Release resources used by an instance
void	GetParamters	Return a instance parameter set in a binary format
void	SetParameters	Set/alter the parameters of an instance
void	PrintParameters	Print parameter set values to stderr

Table D.5 *Forward Declarations of static functions*

The new AlgSGcombine would then be able to respond to all the parameters that AlgSGtimer and AlgSGmirror currently do.

The main changes to the AlgSGcombine algorithm are summarised:

- The rollback code included in AlgSGtimer was included.(AlgSGtimer – line 90-92)
- Removal of ISRglobal.heap[-2] = 14; (AlgSGtimer – line 97)
- Trigger code was placed into code after if (CowCatherRemove()) Panic ();

In addition to the modification required to the C40 code, modifications to other software layers to allow AlgCombine.c to be correctly compiled and correctly uploaded to the designated CPUs in the required manner were required.

D.2 Workstation Code Modification

Further modifications were required to compile, upload and execute the new AlgSGcombine code on the desired CPUs. These included:

- Creating a new version of SGBSP2.c (SGBSP3.c)
- Creating a new versions of the Makefile (Makefilenew)
- Creating a new version of RTconfig.py
- Creating a new version of SGlib.py (SGlibnew.py)
- Creating a new version of C40Run (C40RunSGDev)
- Creating a new version of SGtest.py (SGtestDevSG.py)
- Editing the existing version of c40RealTimeAlgorithms

D.2.1 SGBSP3.c

SGBSP3.c (see Figure D.1) was created by copying and editing SGBSP2.c to include:

- ALG_SG_STARTER
- ALG_SG_COMBINE

```
/* Main program for doing SG c40 real-time code */
#include <packet40.h>
#include <RT.h>
#include <WFS.h>

#ifndef LINT
static char rcsid[] = "$Id: SGBSP3.c,v 1.2 2003/04/12 12:04:23 sjg Exp $";
#endif

/* Table to hold the set of available algorithms. Used in RTcallback()
 * to define the real-time algorithms available in this executable.
 */
extern struct AlgorithmMethods SGstarterMethods;
extern struct AlgorithmMethods SGcombineMethods;

const struct AlgorithmMethods *algorithmMethods[] = {
  &SGstarterMethods,
  &SGcombineMethods,
  NULL /* Required to mark the end of the table */
};
/* define the global which nominates the ringleader */
/* this definition must be common to all CPUs in a ring */
int ringLeaderCPU = 18;

void main()
{
  ExcStatus *status, _status;

  status = &_status;
  ExcInitStatus(status);

  GPsetup(status);
  GPaddCallback(RT_CLASS, &RTcallback, status);
  GPmainLoop(status);
}
```

Figure D.1 *SGBSP3.c*

D.2.2 Makefilenew

The Electra/RealTime/Makefile and Electra/RealTime/StrainGauge/Makefile were copied and edited as shown in Figure D.2 and Figure D.3 respectively. The latter refers to the build in the former. Hence the 'gmake' created the AlgSGcombine.o40 object and the SGBSP3.x40 executable, both targeted for the c40s. It was possible to copy the functionality and parameters incrementally and test each stage. This created the SGBSP3.x40 file. (Which could be uploaded into the C40s.)

Then I could make the whole thing from Electra/RealTime using:

gmake StrainGauge/SGBSP.x40

```
# Make the fast realtime system
# Make 'all' the default target

# Things to make in StrainGauge

here := $(top)/StrainGauge
C40_EXES +=  $(here)/SGBSP3.x40
SG_OBJS1:=$(here)/AlgSGtimer.o40 $(here)/AlgSGconveyor.o40 \
      $(here)/AlgSGdemand.o40 $(here)/AlgSGstarter.o40
SG_OBJS2:=$(here)/AlgSGtimer.o40 $(here)/AlgSGstarter.o40 \
      $(here)/AlgSGadc.o40 $(here)/AlgSGmirror.o40
SG_OBJS3:=$(here)/AlgSGcombine.o40 $(here)/AlgSGstarter.o40
OBJS:=$(SG_OBJS1) $(SG_OBJS2) $(SG_OBJS3)


$(here)/SGBSP.x40 : $(here)/SGBSP.o40 $(SG_OBJS1) $(LIB_OBJS)
$(top)/WFS/WFScallback.o40 $(libs)
      $(C40_CC) -o $@ $(C40_CFLAGS) $(C40_CPPFLAGS) $(C40_LDFLAGS)
$^  $(C40_LDLIBS)
$(here)/SGBSP2.x40 : $(here)/SGBSP2.o40  $(SG_OBJS2) $(LIB_OBJS)
$(top)/WFS/WFScallback.o40 $(libs)
      $(C40_CC) -o $@ $(C40_CFLAGS) $(C40_CPPFLAGS) $(C40_LDFLAGS)
$^  $(C40_LDLIBS)
$(here)/SGBSP3.x40 : $(here)/SGBSP3.o40  $(SG_OBJS3) $(LIB_OBJS)
$(top)/WFS/WFScallback.o40 $(libs)
      $(C40_CC) -o $@ $(C40_CFLAGS) $(C40_CPPFLAGS) $(C40_LDFLAGS)
$^  $(C40_LDLIBS)
```

Figure D.2 *Highlighted changes in Electra/Realtime/Makefilenew (excerpt)*

```
# $Id: Makefile,v 1.2 1999/04/22 17:41:03 dfb Exp $
all :
      cd ..; $(MAKE) StrainGauge/SGBSP3.x40

clean veryclean :
      cd ..; $(MAKE) $@

install :
      cd ..; $(MAKE) install.sg
```

Figure D.3 *Highlighted changes in Electra/Realtime/StrainGauge/Makefilenew*

D.2.3 RTconfig.py

New software configuration in Electra/RealTime/pythonModules/RTconfig.py was required. SGBSP3.x40 instead of SGBSP2.x40). The new version of RTconfig.py was installed on both aocontrol1 and navis, as boot scripts run on aocontrol1.

D.2.4 SGlibnew.py

SGlib.py was cloned and modified. A new version of Open, Close and booting function Run was created for testing purposes. See Figure D.4, Figure D.5 and Figure D.6 respectively in SGlibnew.py. Hence the old versions of the functions were preserved. The Run booting function was modified to refer to 'ALG_SG_COMBINE' instead of 'ALG_SG_TIMER',

'ALG_SG_MIRROR' and 'ALG_SG_ADC'. In addition the code was configured to include the copying of the 32 channels.

```
# Changed algorithm all to ALG_SG_COMBINE - sjg 17-07-03

algorithm = {
   timerCPU: 'ALG_SG_COMBINE',
   diagLinkCPU: 'ALG_SG_COMBINE',
   12: 'ALG_SG_COMBINE',
   13: 'ALG_SG_COMBINE',
   mirrorCPU: 'ALG_SG_COMBINE',
   15: 'ALG_SG_COMBINE',
   demandCPU: 'ALG_SG_COMBINE',
   17: 'ALG_SG_COMBINE'
}

def Open():
   """Open the SG control loops"""

   from GP import rpc

   allpassthroughs=[]
   for i in range(256):
      allpassthroughs.append(1)

   # break transaction if required

   try:
      Transact((
            (11, SGalg("combine"), 'PB_SG_ACCUM_ZERO_HOLD', [1]),
      ))
   except:
      rpc(18, 'RT_BREAK_TRANSACTION', timeout=10000)

   Transact((
      (11, SGalg("combine"), 'PB_SG_ACCUM_ZERO_HOLD', [1]),
      (12, SGalg("combine"), 'PB_SG_ACCUM_ZERO_HOLD', [1]),
      (13, SGalg("combine"), 'PB_SG_ACCUM_ZERO_HOLD', [1]),
      (15, SGalg("combine"), 'PB_SG_ACCUM_ZERO_HOLD', [1]),
      (16, SGalg("combine"), 'PB_SG_ACCUM_ZERO_HOLD', [1]),
      (17, SGalg("combine"), 'PB_SG_ACCUM_ZERO_HOLD', [1]),
      (11, SGalg("combine"), 'PB_SG_PASS_THROUGH', allpassthroughs),
      (12, SGalg("combine"), 'PB_SG_PASS_THROUGH', allpassthroughs),
      (13, SGalg("combine"), 'PB_SG_PASS_THROUGH', allpassthroughs),
      (15, SGalg("combine"), 'PB_SG_PASS_THROUGH', allpassthroughs),
      (16, SGalg("combine"), 'PB_SG_PASS_THROUGH', allpassthroughs),
      (17, SGalg("combine"), 'PB_SG_PASS_THROUGH', allpassthroughs)
   ))
```

Figure D.4 *SGlibnew.py modified (algorithm list and Open function)*

```
def Close(conveyPassTable=None):
    """Close SG control loops"""

    if conveyPassTable == None:
            conveyPassTable = DeadADpassThroughConvey()

# Changed this from ALG_SG_ADC to ALG_SG_COMBINE - sjg 17-07-03

    Transact((
            (11, 'ALG_SG_COMBINE', 'PB_SG_ACCUM_ZERO_HOLD', [0]),
            (12, 'ALG_SG_COMBINE', 'PB_SG_ACCUM_ZERO_HOLD', [0]),
            (13, 'ALG_SG_COMBINE', 'PB_SG_ACCUM_ZERO_HOLD', [0]),
            (15, 'ALG_SG_COMBINE', 'PB_SG_ACCUM_ZERO_HOLD', [0]),
            (16, 'ALG_SG_COMBINE', 'PB_SG_ACCUM_ZERO_HOLD', [0]),
            (17, 'ALG_SG_COMBINE', 'PB_SG_ACCUM_ZERO_HOLD', [0]),
            (11, 'ALG_SG_COMBINE', 'PB_SG_PASS_THROUGH', conveyPassTable),
            (12, 'ALG_SG_COMBINE', 'PB_SG_PASS_THROUGH', conveyPassTable),
            (13, 'ALG_SG_COMBINE', 'PB_SG_PASS_THROUGH', conveyPassTable),
            (15, 'ALG_SG_COMBINE', 'PB_SG_PASS_THROUGH', conveyPassTable),
            (16, 'ALG_SG_COMBINE', 'PB_SG_PASS_THROUGH', conveyPassTable),
            (17, 'ALG_SG_COMBINE', 'PB_SG_PASS_THROUGH', conveyPassTable)
            ))
```

Figure D.5 *SGlibnew.py (modified Close function)*

```
def Run(SWconfig, verbose = 0):
    # boot and startup the Strain gauge ring

    SGring.Boot(SWconfig)

    # Now setup the Pentland ADC board (again)
    SetupPentland()

    # initialise the real-time system
    SGring.Init()

    # the default SG real-time algorithm is now loaded  on each CPU.
    # It does not do real-time processing. Its purpose is to execute a one-shot transaction to swap in
    #  the real-time algorithms which must all switch in at the same time.

    # configure the real-time algorithms for the swap-in. The initial setup is for ADC
    # triggering but no reads

# changed algorithms to ALG_SG_COMBINE (14 is the mirror) - sjg 17-07-03

    Transact((
      (timerCPU, 'ALG_SG_COMBINE', 'PB_SG_TIMER_INTERVAL', [5100]),
      (timerCPU, 'ALG_SG_COMBINE', 'PB_SG_TIMER_TRIGGER_PORT', [5]),
      (timerCPU, 'ALG_SG_COMBINE', 'PB_SG_ADC_BLOCK_SIZE', [32]),
      (timerCPU, 'ALG_SG_COMBINE', 'PB_SG_ADC_PORT', [-1]),
      (11, 'ALG_SG_COMBINE', 'PB_SG_ADC_BLOCK_SIZE', [32]),
      (11, 'ALG_SG_COMBINE', 'PB_SG_ADC_PORT', [-5]),
      (12, 'ALG_SG_COMBINE', 'PB_SG_ADC_BLOCK_SIZE', [32]),
      (12, 'ALG_SG_COMBINE', 'PB_SG_ADC_PORT', [-4]),
      (13, 'ALG_SG_COMBINE', 'PB_SG_ADC_BLOCK_SIZE', [32]),
      (13, 'ALG_SG_COMBINE', 'PB_SG_ADC_PORT', [-1]),
      (14, 'ALG_SG_COMBINE', 'PB_SG_MIRROR_DATA_PORT', [-2]),
      (14, 'ALG_SG_COMBINE', 'PB_SG_MIRROR_SYNC_PORT', [-4]),
      (14, 'ALG_SG_COMBINE', 'PB_SG_DAC_REORDER_TABLE', mirrorReorder),
      (14, 'ALG_SG_COMBINE', 'PB_SG_ADC_BLOCK_SIZE', [32]),
      (14, 'ALG_SG_COMBINE', 'PB_SG_ADC_PORT', [-1]),
      (15, 'ALG_SG_COMBINE', 'PB_SG_ADC_BLOCK_SIZE', [32]),
      (15, 'ALG_SG_COMBINE', 'PB_SG_ADC_PORT', [-2]),
      (16, 'ALG_SG_COMBINE', 'PB_SG_DEMAND_PORT', [demandPort]),
      (16, 'ALG_SG_COMBINE', 'PB_SG_ADC_BLOCK_SIZE', [32]),
      (16, 'ALG_SG_COMBINE', 'PB_SG_ADC_PORT', [-2]),
      (17, 'ALG_SG_COMBINE', 'PB_SG_ADC_BLOCK_SIZE', [64]),
      (17, 'ALG_SG_COMBINE', 'PB_SG_ADC_PORT', [-5]),
      ))
    # run the default algorithm (once-only) to complete the first swap-in transaction

    SGring.StartFraming()

    # at this point the real-time algorithms are swapped in but the ring is not started
    # - that will require another Start()
    # We need to perform one ring to provide a single ADC trigger
    # but no reads. At the same time we swap in the ADC read code to begin on the start after that.

    # now generate the parameter tables for real-time operation
```

Figure D.6 *SGlibnew.py (extract of Run function)*

D.2.5 C40RunSGDev.py

Run with a new name that was invoked by a different version of c40Run and c40Run.py, the boot interfaces. Changes are highlighted in Figure D.7.

```
#!/usr/bin/env python
#
# C40 unified boot functions

if GP.host == "aocontrol1":
    import SGlibDevSG

def Run(SWconfig, verbose = 0):
    if verbose:
       print "Host: ", GP.host
       print "Requested software configuration: ", SWconfig
       print "\nChecking compatibility with hardware configuration"
    if (RTconfig.HWRTcompatible(SWconfig)):
       if verbose:
           print "Requested software configuration and hardware are
COMPATIBLE"
    else:
       # requested software config is incomptabible with hardware
       # signal an error and provide an explaination
       incompatibilityList = RTconfig.GetIncompatibleHW(SWconfig)
       HWconfig = RTconfig.GetHWconfiguration()
       if verbose:
           print "\nRequested software configuration:",SWconfig
           print "is NOT COMPATIBILE WITH HARDWARE:"
           for hw in incompatibilityList:
              print hw, ":", HWconfig[hw]
           sys.exit(1)

       else:
           raise RTconfig.configError, "software/hardware incompatible: "+
incompatibilityList

    if verbose:
       print "Resetting c40 System"
    RTlib.ResetSystem(verbose)
    RTlib.ResetSystem(verbose) # sometimes needed after power up

    if verbose:
       print "Booting Wavefront Sensor C40 Ring and diagnostic CPU"
    WFSlib.Run(SWconfig, verbose)

    if GP.host == 'aocontrol1' :
       if verbose:
           print "Booting Strain Gauge C40 Ring"
       SGlibDevSG.RunDevSG(SWconfig, verbose)

    if verbose:
       print "Recording Configuration"
    RTconfig.RecordRTconfiguration(SWconfig)
```

Figure D.7 *C40RunSGDev.p*

D.2.6 C40RealTimeAlgorithms

The file was edited to include ALG_SG_COMBINE into the relevant algorithm table.

References

[1] J. W. Hardy, '*Adaptive Optics for Astronomical Telescopes*' Oxford University Press, (1998).
[2] F. Roddier, '*Adaptive Optics for Astronomy*' Cambridge University Press, (1999).
[3] R. K. Tyson, '*Principle of Adaptive Optics*' 2nd Edition, Academic Press, (1998).
[4] J. W. Hardy, 'Active Optics: A new technology for the control of light' *Proc. IEEE* **66**, p1287, (1978).
[5] I. Newton, '*Opticks*' Based on 4th Edition, Dover, New York (1979).
[6] H. W. Babcock, '*The possibility of compensating atmospheric seeing*' PASP **65**, p229-236, (1953).
[7] A. Labeyrie, '*Attainment of diffraction-limited resolution in large telescopes by Fourier Analysis speckle patterns in star images*' Astron Astrophys **6**, p85-87, (1970).
[8] J. W. Hardy, J. E. Lefebvre, C. L. Koliopoulos, '*Real-time atmospheric compensation*' J. Opt. Soc. Am. **67**, p360-69, (1977).
[9] F. Zernike, 'Beugungstheorie des schneidenver-fahrens und seiner verbesserten form, der phasenkontrastmethode' Physica **1**, p689-704, (1934).
[10] M. Born, E. Wolf, '*Principles of Optics*' 5th Edition, Pergamon Press, Oxford, (1975).
[11] R. J. Noll, '*Zernike polynomials and atmospheric turbulence*' J Opt Soc Am **66**, Suppl 14-1, p307-310, (1975).
[12] L. A. Chernov, '*Wave Properties in a Random Medium*', McGraw-Hill, New York, (1960).
[13] A. Ishimaru, '*Wave Propagation and Scattering in Random Media*' Academic Press, New York, (1977).
[14] J. W. Strohbehn, '*Laser Beam Propagation in the Atmosphere*' Springer-Verlag, New York, (1978).
[15] A. N. Kolmogorov, '*The local structure of turbulence in incompressible fluids for very large Reynolds number*' Proc. Roy. Soc. Lond. A **434**, p9-13, (1991).
[16] D. L. Fried, '*Atmospheric turbulence optical effects: Understanding the adaptive-optics implications*' Adaptive Optics in Astronomy, p25-57, Kluwer Academic Publishers, (1994).
[17] S. Corrsin, '*On the Spectrum of Isotropic Temperature Fluctuations in an Isotropic Turbulence*' J. Appl. Phys. **22**, p469, (1951).
[18] V. I. Tatarskii, '*Wave Propagation in a Turbulent Medium*' McGraw-Hill, New York, (1961).
[19] J. W. Strohbehn, '*Laser Beam Propagation in the Atmosphere*' Springer-Verlag, New York, (1978).
[20] R. F. Lutomirski, H. T. Yura, '*Propagation of a Finite Optical Beam in an Inhomogeneous Medium*' Appl. Opt. **10**, p1652-1658, (1971).
[21] D. L. Fried, '*The Effect of Wave-front Distortion on the Performance of an Ideal Optical Heterodyne Receiver and an Ideal Camera*' Conf. on Atmospheric Limitations to Optical Propagation, U. S. Nat. Bur. Stds. CRPL, (1965).
[22] S. N. Bezdid'ko, '*Optimization of optical systems using orthogonal polynomials*' Opt. Spektrosk. **48**, p670-671, (1980).
[23] J-M. Conan, G. Rousset, P-Y. Madec, '*Wave-front temporal spectra in high resolution imaging through turbulence*' J. Opt. Soc. Am. A **12**, p1559-1570, (1995).
[24] D. L. Fried, '*Statistics of a geometric representation of wavefront distortion*' J. Opt. Soc. Am. **55**, p1427-35, (1965).
[25] D. M. Auslander, Y. Takahashi, M. J. Rabins, '*Introducing Systems and Control*' McGraw-Hill, New York, (1974).
[26] R. H. Cannon, '*Dynamics of Physical Systems*' McGraw-Hill, New York (1967).

[27] C. F. Chen, I. J. Haas, '*Elements of Control Systems Analysis*' Prentice-Hall, Englewood Cliffs, NJ, (1968).
[28] I. McCausland, '*Introduction to Optimal Control*' Wiley, New York, (1979).
[29] K. Ogata, '*Modern Control Engineering*' Prentice-Hall, Englewood Cliffs, NJ, (1970).
[30] J. Van de Vegte, '*Feedback Control Systems*' 2nd Edition, Prentice-Hall, Englewood Cliffs, NJ, (1990).
[31] G. F. Franklin, J. D. Powell, M. L. Workman, '*Digital Control of Dynamic Systems*' 2nd Edition, Addison Wesley Publ. Reading, MA, (1990).
[32] J. Wilkie, M. Johnson, R. Katebi, '*Control Enginnering: An introductory Course*' 1st Edition, Palrave, (2002).
[33] M. S. Tsai, J. S. Chen, '*Robust tracking control of a piezoactuator using a new approximate hysteresis model' J. Dynamic Systems Measurement & Control-Transactions of the ASME*' **125**, p96-102, (2003)
[34] J. Hartmann, '*Bemerkungen uber den Bau und die Justirung von Spektrographen*' Zt. Instrumentenkd. **20**, p47-58, (1900).
[35] J. Hartmann, '*Objektivuntersuchungen*' Zt. Instrumentenkd. **24**, p1-21, (1904).
[36] M. Elbaum, M. Greenebaum, 'Annular apertures for angular tracking' Appl. Opt. **16**, p2438-2440, (1977).
[37] K. A. Winick, '*Cramer-Rao lower bounds on the performance of charge-coupled-device optical position estimators*' J. Opt. Soc. Am. A, **3**, p1809-15, (1986).
[38] G. Genson, A. K. Rue, '*Tracking system: The InfraRed Handbook*' Environmental Research Institute of Michigan, Ann Arbor, C22, (1989).
[39] J. W. Hardy, 'Instrumental limitation in adaptive optics for astronomy' Proc. SPIE **1114**, p2-13, (1989).
[40] J. K. Bowker, '*Pulsed Laser Wavefront Sensor*' Adaptive Optics Assoc. Tech. Report 78-1, Cambridge, MA, (1978).
[41] C. A. Lors, '*I-cubed sensor wavefront correction system*' Pratt and Whitney Aircraft internal memorandum, Aug 28, (1978).
[42] U. S. Patent 4,141,652.
[43] I. S. McLean, '*Electronic Imaging in Astronomy*' Wiley, (1997).
[44] C. R. Kitchin, '*Astrophysical Techniques*' IOP Publishing, (1998).
[45] F. Zappa, A. L. Lacaita, S. D. Cova, P. Lovati, '*Solid-state single-photon detectors*' Opt. Eng. **35**, p938-945, (1996).
[46] S. A. Kokorowski, M. E. Pedinoff, J. E. Pearson, '*Analytical, experimental, and computer-simulation results on the interactive effects of speckle with multidither adaptive optics systems*' JOSA **67**, p333-345, (1977).
[47] E. S. Claflin, N. Bareket, '*Configuring an electrostatic membrane mirror by least-squares fitting with analytically derived influence functions*' JOSA A **3**, p1833-1839, (1986).
[48] V. G. Taranenko, G. P. Koshelev, N. S. Romanyuk, '*Local deformation of solid mirrors and their frequency dependence*' Sov. J. Opt, Technol. **48**, p650-652, (1981).
[49] R. H. Hudgin, '*Wave-front compensation error due to finite corrector-element size*' J. Opt. Soc. Am **67**, p393-395, (1977).
[50] L. Germann, J. Braccio, '*Fine-Steering Mirror Technology supports 10 nano-radian systems*' Opt. Engr. **29**, p1351-9, (1990).
[51] G. C. Loney, '*Design of a small-aperture steering mirror for high bandwidth acquisition tracking*' Opt. Eng. **29** p1360-5, (1990).
[52] H. Marth, M. Donat, C. Pohlhammer, '*Latest experience in design of piezoelectric driven fine steering mirrors*' Proc. SPIE **1543**, p248-61, (1991).

[53] J. P. Gafford, P. Jagourel, P. Gigan, '*Adaptive optics: description of available components at Laserdot*' Proc. SPIE **2201,** p688-702, (1994).
[54] D. Bruns, T. Barrett, G. Brusa, R. Biasi, D. Gallieni, '*Adaptive Secondary Development*' Tech Digest Series **13**, p302-4, (1996).
[55] J. W. Hardy, '*Instrumental Limitations in adaptive optics for astronomy*' Proc. SPIE **1114,** p2-13, (1989).
[56] B. Hulburd, D. Sandler, '*Segmented mirrors for atmospheric compensation*' Opt. Eng. **29** p1186-90, (1990).
[57] B. Hulburd, T. Barrett, L. Cuellar, D. Sandler, '*High bandwidth, long stroke, segmented mirror for atmospheric compensation*' Proc. SPIE **1543**, p64-75, (1991).
[58] M. N. Malakhov, V. F. Matyukhin, B. V. Pilepskii, '*Estimating the parameters of a multielement mirror of an adaptive optical system*' Sov. J. Opt. Technol. **51**, p141-4 (1984).
[59] C. Boyer, J. P. Gaffard, G. Rousset, '*Adaptive Optics: Interaction matrix measurement and real-time control algorithm for the Come-On Project*' Proc. SPIE **1271**, p63-81, (1990).
[60] C. Paterson, I. Munro, J. C. Dainty, '*A low cost adaptive optics system using a membrane mirror*' Optics Express, **6**, p175-185, (2000).
[61] T. R. O'Meara, '*Stability of an N-loop ensemble-reference phase control system*' J. Opt. Soc. Am. **67**(3), p315-318, (1977).
[62] J. Winocur, '*Modal compensation of atmospheric turbulence induced wave front aberrations*' App. Opt. **21**(3), p433-8, (1982).
[63] J. P. Gafford, G. Ledanois, '*Adaptive Optical Transfer Function Modeling*' Proc. SPIE **1542** p34-45, (1991).
[64] J. P. Gafford, C. Boyer, '*Adaptive Optics: Effect of sampling rate and time lags on the closed-loop bandwidth*' Proc. SPIE **1271**, p33-50, (1991).
[65] C. Boyer, J. P. Gaffard, '*Adaptive Optics, transfer loops modelling*' Proc. SPIE **1542**, p46-61, (1991).
[66] M. Demerlé, P. Y. Madec, G. Rousset, '*Servo-loop analysis for adaptive optics*' Adaptive Optics for Astronomy, NATO ASIS on AO for Astronomy, p73-88 (1993).
[67] http://www.eso.org (2008).
[68] N. Hubin '*Adaptive Optics Status and Roadmap at ESO*' Proc. SPIE **5490,** p195-206, (2004).
[69] N. Hubin, B. Théodore, P. Petitjean, B. Delabre, '*The Adaptive Optics system for the VLT*' Proc. SPIE **2201,** p34-45, (1994).
[70] M. Kasper, J. Charton, B. Delabre, R. Donaldson, E. Fedrigo, G. Hess, N. Hubin, J. L. Lizon, M. Nylund, C. Soenke, G. Zins, '*LGS implementation for NAOS*' Proc. SPIE **5490,** p1071-1078, (2004).
[71] D. Bonaccini, E. Allaert, J. L. Alvarez, C. Araujo Hauck, G. Avila, E. Bendek, B. Buzzoni, M. Comin, M. Cullum, R. Davies, M. Dimmler, I. Guidolin, W. Hackenberg, S. Hippler, S. Kellner, A. van Kesteren, F. Kock, U. Neumann, T. Ott, D. Popovic, F. Pedichini, M. Quattri, J. Quentin, S. Rabien, A. Silber and M. Tapia, '*First Light of the ESO Laser Guide Star Facility*' Proc. SPIE **6272,** 7, (2006).
[72] F. Merkle, G. Gehring, F. Rigaut, P. Léna, G. Rousset, J.C. Fontanella, J. P. Gaffard, '*Adaptive optics system tests at the ESO 3.6m telescope*' Proc. SPIE **1542,** p308-318, (1991).
[73] E. Gendron, J. G. Cuby, F. Rigaut, P. Lena, J. C. Fontanella, G. Rousset, J.P. Gaffard, C. Boyer, J. C. Richard, M. Vittot, F. Merkle, N. Hubin, '*The COME-ON-PLUS Project: An Upgrade of the COME-ON Adaptive Optics Prototype System*' Proc. SPIE **1542,** p297-307, (1991).

[74] G. Rousset, J. L. Beuzit, N. Hubin, E. Gendron, P. Y. Madec, C. Boyer, J. P. Gaffard, J. C. Richard, M. Vittot, P. Gigan, P. Léna, '*Performance and results of the COME-ON+ adaptive optics system at the ESO 3.6-meter telescope*' Proc. SPIE **2201,** p1088-1098, (1994).
[75] J. L. Beuzit, N. Hubin, E. Gendron, L. Demailly, P. Gigan, F. Lacombe, F. Chazallet, D. Rabaud, G. Rousset, '*ADONIS: a user-friendly adaptive optics system for the ESO 3.6m telescope*' Proc. SPIE **2201,** p955-961, (1994).
[76] D. Bonaccini, E. Prieto, P. Corporon, J. Christou, D. Le. Mignan, P. Prado, R. Gredel, N. Hubin, '*Performance of the ESO AO system, Adonis, at La Silla 3.6m telescope*' Proc. SPIE **3126,** p589-594, (1997).
[77] G. Rousset, F. Lacombe, P. Puget, N. Hubin, E. Gendron, J. M. Conan, P. Kern, P. Y. Madec, D. Rabaud, D. Mouillet, A. M. Lagrange and F. Rigaut, '*Design of the Nasmyth Adaptive Optics System (NAOS) of the VLT*' Proc. SPIE **3353,** p508-516, (1998).
[78] P. Feautrier, G. Rousset, R. Dorn, C. Cavadore, J. Charton, C. Cumani, T. Fusco, N. Hubin, P. Kern, J. L. Lizon, Y. Magnard, P. Puget, D. Rabaud, P. Rabou, E. Stadler, '*Performances and results on the sky of the NAOS visible wavefront sensor*' Proc. SPIE **4839,** p250-258, (2003).
[79] G. Rousset, F. Lacombe, P. Puget, N. Hubin, E. Gendron, T. Fusco, R. Arsenault, J. Charton, P. Feautrier, P. Gigan, P. Kern, A. M. Lagrange, P. Y. Madec, D. Mouillet, D. Rabaud, P. Rabou, E. Stadler, G. Zins, '*NAOS, the first AO system of the VLT: on-sky performance*' Proc. SPIE **4839,** p140-149, (2002).
[80] P. Feautrier, P. Kern, R. Dorn, G. Rousset, P. Rabou, S. Laurent, J. L. Lizon, E. Stadler, Y. Magnard, O. Rondeaux, M. Cochard, D. Rabaud, A. Delboulbe, P. Puget, N. Hubin, '*The NAOS visible wave front sensor*' Proc. SPIE **4007,** p396-407, (2000).
[81] E. Gendron, F. Lacombe, D. Rouan, J. Charton, C. Collin, B. Lefort, C. Marlot, G. Michete, G. Nicol, S. Pau, V. D. Phan, B. Talureau, J. L. Lizon, N. Hubin, '*NAOS Infrared wave-front sensor design and performance*' Proc. SPIE **4839,** p195-205, (2003).
[82] D. Rabaud, F. Chazallet, G. Rousset, C. Amra, B. Argast, J. Montri, G. Dumont, B. Sorrente, P. Y. Madec, E. Gendron, R. Arsenault, D. Mouillet, N. Hubin, J. Charton, '*NAOS Real-Time Computer for optimized closed loop and on-line performance estimation*' Proc. SPIE **4007,** p659-670, (2000).
[83] T. Fusco, N. Ageorges, G. Rousset, D. Rabaud, E. Gendron, D. Mouillet, F. Lacombe, G. Zins, J. Charton, C. Lidman and N. Hubin, '*NAOS performance characterization and turbulence parameters estimation using closed-loop data*' Proc. SPIE **5490,** p118-129, (2004).
[84] N. Hubin, R. Arsenault, H. Bonnet, R. Conan, B. Delabre, R. Donaldson, C. Dupuy, E. Fedrigo, L. Ivanescu, M. Kasper, M. Kissler-Patig, J. L. Lizon, M. Le Louarn, E. Marchetti, J. Paufique, S. Stroebele, S. Tordo, '*Adaptive Optics Projects at ESO*' Proc. SPIE **4839,** p1-8, (2003).
[85] R. Arsenault, J. Alonso, H. Bonnet, J. Brynnel, B. Delabre, R. Donaldson, C. Dupuy, E. Fedrigo, J. Farinato, N. Hubin, L. Ivanescu, M. Kasper, J. Paufique, S. Rossi, S. Tordo, S. Stroebele, J. L. Lizon, P. Gigan, F. Delplancke, A. Silber, M. Quattri, R. Reiss, '*MACAO-VLTI: An Adaptive Optics System for the ESO Interferometer*' Proc. SPIE **4839,** p174-185, (2003).
[86] J. Paufique, P. Biereichel, R. Donaldson, B. Delabre, E. Fedrigo, F. Franza, P. Gigan, D. Gojak, N. Hubin, M. Kasper, U. Käufl, J. L. Lizon, S. Oberti, J. F. Pirard, E. Pozna, J. Santos, S. Stroebele, '*MACAO-CRIRES, a step towards high-resolution spectroscopy*' Proc. SPIE **5490,** p216-227, (2004).
[87] D. Bonaccini, F. Rigaut, A. Glindemann, G. Dudziak, J. M. Mariotti and F. Paresce, '*Adaptive Optics for ESO VLT-Interferometer*' Proc. SPIE **3353,** p224-232, (1998).

[88] R. Arsenault, P. Kervella, R. Donaldson, M. Kasper, E. Fedrigo, A. Wallander, M. Schöller, N. Housen, F. Delplancke, F. Salgado, C. Dupuy, N. Hubin, L. Ivanescu, S. Oberti, J. Paufique, S. Rossi, M. Wittkowski, '*Interferometric fringes with MACAO-VLTI corrected star light and VINCI*' Proc. SPIE **5490,** p97-106, (2004).

[89] R. Arsenault, R. Donaldson, C. Dupuy, E. Fedrigo, N. Hubin, L. Ivanescu, M. Kasper, S. Oberti, J. Paufique, S. Rossi, A. Silber, B. Delabre, J. L. Lizon, P. Gigan, '*MACAO-VLTI Adaptive Optics System Performance*' Proc. SPIE **5490,** p47-58, (2004).

[90] H. Bonnet, S. Ströbele, F. Biancat-Marchet, J. Brynnel, R. Conzelmann, B. Delabre, R. Donaldson, J. Farinato, E. Fedrigo, N. Hubin, M. Kasper, M. Kissler-Patig, '*Implementation of MACAO for SINFONI at the Cassegrain focus of VLT, in NGS and LGS modes*' Proc. SPIE **4839,** p329-343, (2003).

[91] H. Bonnet, R. Conzelmann, B. Delabre, R. Donaldson, E. Fedrigo, N. Hubin, M. Kissler-Patig, J. L. Lizon, J. Paufique, S. Rossi, S. Stöbelee, S. Tordo, '*First Light of SINFONI AO-Module at VLT*' Proc. SPIE **5490,** p130-138, (2004).

[92] A. Moorwood, P. Biereichel, J. Brynnel, B. Delabre, R. Dorn, G. Finger, F. Franza, G. Huster, Y. Jung, H. U. Käufl, F. Koch, M. Kasper, R. Lescouzeres, J. L. Lizon, H. Mehrgan, M. Meyer, J. F. Pirad, R. Siebenmorgen, B. Sokar, J. Stegmeier, G. Wiedemann, '*CRIRES: a high-resolution infrared spectroscopy for the VLT*' Proc. SPIE **4841,** p1592-1599, (2003).

[93] H. U. Käufl, P. Ballester, P. Biereichel, B. Delabre, R. Donaldson, R. Dorn, E. Fedrigo, G. Finger, G. Fischer, F. Franza, D. Gojak, G. Huster, Y. Jung, J. L. Lizon, L. Mehrgan, M. Meyer, A. Moorwood, J. F. Pirard, J. Paufique, E. Pozna, R. Siebenmorgen, A. Silber, J. Stegmeier, S. Wegerer, '*CRIRES: A High Resolution Infrared Spectrograph for ESO's VLT*' Proc. SPIE **5492,** p1218-1227, (2004).

[94] J. Paufique, P. Biereichel, B. Delabre, R. Donaldson, R. Esteves, E. Fedrigo, P. Gigan, D. Gojak, N. Hubin, M. Kasper, U. Kaufl, J. L. Lizon, E. Marchetti, S. Oberti, J. F. Pirard, E. Pozna, J. Santos, S. Stroebele, S. Tordo, '*On-sky results of the adaptive optics MACAO for the new IR-spectrograph CRIRES at VLT*' Proc. SPIE **6272,** 16, (2006).

[95] E. Marchetti, N. Hubin, E. Fedrigo, J. Brynnel, B. Delabre, R. Donaldson, F. Franza, R. Conan, M. Le Louarn, C. Cavadore, A. Balestra, D. Baade, J. L. Lizon, R. Gilmozzi, G. Monnet, R. Ragazzoni, C. Arcidiacono, A. Baruffolo, E. Diolaiti, J. Farinato, E. Viard, D. Butler, S. Hippler, A. Amorim, '*MAD the ESO multi-conjugate adaptive optics demonstrator*' Proc. SPIE **4839,** p317-328, (2003).

[96] E. Marchetti, R. Brast, B. Delabre, R. Donaldson, E. Fedrigo, C. Frank, N. Hubin, J. Kolb, M. Le Louarn, J. L. Lizon, S. Oberti, R. Reiss, J. Santos, S. Tordo, R. Ragazzoni, C. Arcidiacono, A. Baruffolo, E. Diolaiti, J. Farinato, E. Vernet, '*MAD status report*' Proc. SPIE **5490,** p236-247, (2004).

[97] E. Fedrigo, R. Donaldson, '*Architecture of the MAD Real Time Computer*' Proc. SPIE **4839,** p600-611, (2003).

[98] E. Marchetti, R. Brast, B. Delabre, R. Donaldson, E. Fedrigo, C. Frank, N. Hubin, J. Kolb, M. L. Louarn, J. L. Lizon, S. Oberti, F. Quiros-Pacheco, R. Reiss, J. Santos, S. Tordo, A. Baruffolo, P. Bagnara, A. Amorim, J. Lima, '*MAD Star Oriented: laboratory results for Ground Layer and Multi- Conjugate Adaptive Optics*' Proc. SPIE **6272,** O, (2006).

[99] A. Moorwood, '*Instrumentation at the ESO VLT*' Proc. SPIE **5492,** p13-22, (2004).

[100] S. Strobele, R. Arsenault, R. Bacon, R. Biasi, D. Bonaccini, M. Downing, R. D. Conzelmann, B. Delabre, R. Donaldson, M. Duchateau, S. Esposito, D. Gallieni, W. K. P. Hackenberg, N. Hubin, M. Kasper, M. Kissler-Patig, M. Le Louarn, R. McDermid, S. Oberti, J. Paufique, A. Riccardi, R. Stuik, E. Vernet, '*The ESO Adaptive Optics Facility*' Proc. SPIE **6272,** B, (2006).

[101] R. Arsenault, R. Biasi, D. Gallieni, A. Riccardi, P. Lazzarini, N. Hubin, E. Fedrigo, R. Donaldson, S. Oberti, S. Stroebele, R. Conzelmann, M. Duchateau, '*A Deformable Secondary Mirror for the VLT*' Proc. SPIE **6272,** V, (2006).
[102] J. F. Pirard, M. Kissler-Patig, A. Moorwood, P. Biereichel, B. Delabre, R. Dorn, G. Finger, D. Gojak, G. Huster, Y. Jung, F. Koch, M. Le Louarn, J. L. Lizon, L. Mehrgan, E. Pozna, A. Silber, B. Sokar, J. Stegmeier, '*HAWK-I: A new 'Wide Field' 1-2.5μm Imager for the VLT*' Proc. SPIE **5492,** p1763-1772, (2004).
[103] M. Casali, J. F. Pirad, M. Missler-Patig, A. Moorwood, L. Bedin, P. Biereichel, B. Delabre, R. Dorn, G. Finger, D. Gojak, G. Huster, Y. Jung, F. Koch, J. L. Lizon, L. Mehrgan, E. Pozna, A. Silber, B. Sokar, J. Stegmeier, '*HAWK-I: the new wide-field IR imager for the VLT*' Proc. SPIE **6269,** W, (2006).
[104] F. Hénault, R. Bacon, C. Bonneville, D. Boudon, R. Davis, P. Ferruit, G. Gilmore, O. Le Fevre, J. P. Lemonnier, S. Lilly, S. Morris, E. Prieto, M. Steinmetz, T. de Zeeuw, '*MUSE, a second generaton integral spectrometer for the VLT*' Proc. SPIE **4841,** p1096-1107, (2003).
[105] F. Hénault, R. Bacon, H. Dekker, B. Delabre, S. Djidel, J. P. Dubois, N. Hubin, B. Lantz, W. Lau, M. Le Louarn, I. Lewis, J. L. Lizon, J. Lynn, L. Pasuini, R. Reiss, M. Roth, '*MUSE opto-mechanical design and performance*' Proc. SPIE **5492,** p909-920, (2004).
[106] R. Bacon, S. Bauer, P. Boehm, D. Boudon, S. Brau-Nogue, P. Cailler, L. Capoani, C. M. Carollo, N. Champavert, T. Contini, E. Daguise, D. Dalle, B. Delabre, J. Devriendt, S. Drizler, J. Dubois, M. Dupiex, J. P. Dupin, E. Emsellem, P. Ferruit, M. Frax, G. Gallou, J. Gerssen, B. Guiderdoni, T. Hahn, D. Hofmann, A. Jarno, A. Kelz, C. Koehler, W. Kollatschny, J. Kosmalski, F. Laurent, S. J. Lilly, J. Lizon, M. Loupias, S. Lynn, A. Manescau, R. M. McDermid, C. Monstein, H. Nicklas, L. Pares, L. Pasquini, A. Pecontal-Rousset, E. Pecontal, R Pello, C. Petit, J. P. Picat, E. Popow, A. Quirrenbach, R. Reiss, E. Renault, M. Roth, J. Schaye, G. Soucail, M. Steinmetz, S. Stroebele, R. Stuik, P. Weilbacher, H. Wozniak, P. T. de Zeeuw, '*Probing unexplored territories with MUSE: a second generation instrument for the VLT*' Proc. SPIE **6269,** J, (2006).
[107] K. Dohlen, J. L. Beuzit, M. Feldt, D. Mouillet, P. Puget, J. Antichi, A. Baruffolo, P. Baudoz, A. Berton, A. Boccaletti, M. Carbillet, J. Charton, R. Claudi, M. Downing, C. Fabron, P. Feautrier, E. Fedrigo, T. Fusco, J. L. Gach, R. Gratton, N. Hubin, M. Kasper, M. Langlois, A. Longmore, C. Moutou, C. Petit, J. Pragt, P. Rabou, G. Rousset, M. Saisse, H. M. Schmid, E. Stadler, D. Stamm, M. Turatto, R. Waters, F. Wildi, '*SPHERE, a Planet Finder instrument for the VLT*' Proc. SPIE **6269,** Q, (2006).
[108] T. Fusco, C. Petit, G. Rousset, J.-F. Sauvage, K. Dohlen, D. Mouillet, J. Charton, P. Baudoz, M. Kasper, E. Fedrigo, P. Rabou, P. Feautrier, M. Downing, P. Gigan, J. M. Conan, J. L. Beuzit, N. Hubin, P. Puget, '*Design of the extreme AO system for SPHERE, the planet-finder instrument of the VLT*' Proc. SPIE **6269,** K, (2006).
[109] http://www.gemini.edu, (2008).
[110] Gemini Project, Gemini Newsletter **2,** (1992).
[111] Gemini Project, Gemini Newsletter **4,** (1993).
[112] Gemini Project, Gemini Newsletter **9,** (1994).
[113] Gemini Project, Gemini Newsletter **12,** (1996).
[114] G. Herriot, S. Morris, S. Roberts, M. Flecter, L. Saddlemyer, G. Singh, J. P. Véran, E. Richardson, '*Innovations in Gemini Adaptive Optics System Design*' Proc. SPIE **3353,** p488-499, (1998).
[115] G. Herriot, S. Morris, A. Anthony, D. Derdall, D. Ducan, J. Dunn, A. Ebbers, J. M. Fletcher, T. Hardy, B. Leckie, A. Mirza, C. Morbey, M. Pfleger, S. Roberts, P. Shott, M. Smith, L. Saddlemyer, J. Sebesta, K. Szeto, B. Wooff, W. Windels, J. P. Véran, '*Progress on Altair: The Gemini North Adaptive Optics System*' Proc. SPIE **4007,** p115-125, (2000).

[116] Mauna Kea Infrared, '*Near Infrared Coronographic Imager Operational Concepts Definition Document – CDR Version*', Mauna Kea Infrared, (2002).
[117] B. L. Ellerbroek, F. Rigaut, B. Bauman, C. Boyer, S. Browne, R. Buchroeder, J. Catone, P. Clark, C. d'Orgeville, D. Gavel, G. Herriot, M. R. Hunten, E. James, E. Kibblewhite, I. McKinnie, J. Murray, D. Rabaut,L. Saddlemyer, J. Sebag, J. Stillburn, J. Telle and J. P. Véran, '*MCAO for Gemini-South*' Proc. SPIE **4839,** p55-66, (2003).
[118] Gemini Project, Gemini Newsletter **23**, (2001).
[119] Gemini Project, Gemini Newsletter **35**, (2007).
[120] Gemini Project, Gemini Newsletter **34**, (2007).
[121] D. A. Simons, J. B. Jensen, C. d'Orgeville, P. M. Gray, M. Lazo, R. Rogers, M. P. Sheehan, J. K. White, '*Past, Present and Future Instrumentation at Gemini Observatory*' Proc. SPIE **6269,** 6, (2006).
[122] D. A. Simons, J. B. Jensen, P. Gray, M. Lazo, R. Rogers, J. White, '*Current and Future Facility Instruments at the Gemini Observatory*' Proc. SPIE **5492,** p35-48, (2004).
[123] Gemini Project, Gemini Newsletter **21** (2000).
[124] J. E. Graves, M. Northcott, F. Roddier, C. Roddier, D. Potter, D. O'Connor, F. Rigaut M. Chun, '*First Light for Hokupa'a 36 on Gemini North*' Proc. SPIE **4007,** p26-30, (2000).
[125] F. Roddier, J. E. Graves, D. McKenna, M. Northcott, '*The University of Hawaii adaptive optics system I. General approach*' Proc. SPIE **1542,** p248-253, (1991).
[126] F. Roddier, J. Anuskiewicz, J. E. Graves, M. J. Northcott, C. Roddier, '*Adaptive optics at the University of Hawaii I: Current performance at the telescope*' Proc. SPIE **2201,** p2-9, (1994).
[127] J. E. Graves, M. Northcott, F. Roddier, C. Roddier and L. Close, '*First Light for Hokupa'a 36 Element Curvature AO System at UH*' Proc. SPIE **3353,** p34-43, (1998).
[128] J. A. Stoesz, J. P. Véran, F. Rigaut, G. Herriot, L. Jolissaint, D. Frenette, J. Dunn, M. Smith, '*Evaluation of the on-sky performance of Altair*' Proc. SPIE **5490,** p67-78, (2004).
[129] L. K. Saddlemyer, G. Herriot, J. P. Véran, '*Design and current status of the reconstructor for Altair: the Gemini North adaptive optics system*' Proc. SPIE **4007,** p649-658, (2000).
[130] M. J. Smith, J. P. Véran, '*Implementation of the Altair Optimization Process*' Proc. SPIE **4839,** p964-971, (2003).
[131] K. W. Hodapp, J. Hora, J. E. Graves, E. M. Irwin, H. Yamada, J. W. Douglass, T. T. Young, L. Robertson, '*Gemini Near Infrared Imager (NIRI)*' Proc. SPIE **4008,** p1334-1341, (2000).
[132] K. W. Hodapp, E. M. Irwin, H. Yamada, R. Chung, K. Fletcher, J. Jensen, W. Mays, R. Nolan, D. A. Simons, C. Aspin, '*Gemini near-infrared imager (NIRI): a discussion of its design features and performance*' Proc. SPIE **4841,** p869-880, (2003).
[133] P. J. McGregor, J. Hart, P. G. Conrot, M. L. Pfitzner, G. J. Bloxham, D. J. Jones, M. D. Downing, M. Dawson, P. Young, M. Jarnyk, J. V. Harmelen, '*Gemini near-infrared integral field spectrograph (NIFS)*' Proc. SPIE **4841,** p1581-1591, (2003).
[134] D. Crampton, R. Murowinski, '*Scientific and technical performance of GMOS: the Gemini Multi-Object Spectrograph*' Proc. SPIE **5492,** p181-189, (2004).
[135] I. Hook, J. R. Allington-Smith, S. M. Beard, D. Crampton, R. L. Davies, C. G. Dickson, A. W. Ebbers, J. M. Fletcher, I. Jorgensen, I. Jean, S. Juneau, R. G. Murowinski, R. Nolan, K. Laidlaw, B. Leckie, G. E. Marshall, T. Purkins, I. M. Richarson, S. C. Roberts, D. A. Simons, M. J. Smith, J. R. Stilburn, K. Szeto, C. Tierney, R. J. Wolff, R. Wooff, '*Gemini-north muliobject spectrograph integration, test and commissioning*' Proc. SPIE **4841,** p1645-1656, (2003).
[136] D. W. Toomey, C. Ftaclas, '*Near Infrared Coronagraphic Imager for Gemini South*' Proc. SPIE **4841,** p889-900, (2003).

[137] E. James, C. Boyer, R. A. Buchroeder, B. L. Ellerbroek, M. Hunten, '*Design considerations of the AO module for the Gemini South multi-conjugate adaptive optics system*' Proc. SPIE **4839,** p67-80, (2003).
[138] C. Boyer, J. Sebag, M. Hunten, L. Saddlemyer, '*Gemini MCAO Control System*' Proc. SPIE **4494,** p167-180, (2001).
[139] R. Elston, S. N. Raines, K. T. Hanna, D. B. Hon, J. Julian, M. Horrobin, C. F. Harmer, H. W. Epps, '*Performance of the FLAMINGOS near-IR multi-object spectrometer and imager and plns for the FLAMINGOS-2: a fully cryogenic near-IR MOS for Gemini South*' Proc. SPIE **4841,** p1611-1624, (2003).
[140] H. W. Epps, R. Elston, '*Preliminary optical design for the Flamingos-2 near-infrared multi-slit spectrograph and imager for Gemini-South*' Proc. SPIE **4841,** p1280-1294, (2003).
[141] P. McGregor, J. Hart, D. Stevanovic, G. Bloxham, D. Jones, J. Van Harmelen, J. Griesbach, M. Dawson, P. Young, M. A. Jarnyk, '*Gemini South Adaptive Optics Imager (GSAOI)*' Proc. SPIE **5492,** p1033-1044, (2004).
[142] B. Macintosh, J. Graham, D. Palmer, R. Doyon, D. Gavel, J. Larkin, B. Oppenheimer, L. Saddlemyer, J. K. Wallace, B. Bauman, J. Evans, D. Erikson, K. Morzinski, D. Phillion, L. Poyneer, A. Sivaramakrishnan, R. Soummer, S. Thibault, J. P. Veran, '*The Gemini Planet Imager*' Proc. SPIE **6272,** L, (2006).
[143] K. Szeto, D. Andersen, D. Crampton, S. Morris, M. Lloyd-Hart, R. Myers, J. B. Jensen, M. Fletcher, W. Rusty Gardhouse, N. M. Milton, J. Pazder, J. Stoesz, D. Simons, J. P. Veran, '*A Proposed Implementation of a Ground Layer Adaptive Optics System on the Gemini Telescope*' Proc. SPIE **6269,** 58, (2006).
[144] D. R. Andersen, D. Crampton, K. Szeto, S. Morris, M. Lloyd-Hart, R. Myers, J. Stoesz, A. Tokovinin, T. Butterley, N. M. Milton, J. P. Veran, R. Wilson, '*Modeling a GLAO system for the Gemini Observatory*' Proc. SPIE **6272,** 5B, (2006).
[145] http://www2.keck.hawaii.edu/ (2008).
[146] P. L. Wizinowich, J. E. Nelson,T.S. Mast and A.D. Gleckler, '*W. M. Keck Observatory Adaptive Optics Program*' Proc. SPIE **2201,** p22-33, (1994).
[147] A. D. Gleckler, P. L. Wizinowich, '*W. M. Keck Observatory Adaptive Optics Program*' Proc. SPIE **2534,** p386-400, (1995).
[148] P. L. Wizinowich, D. S. Acton, T. Gregory, P. Stomski, '*Status of the W. M. Keck Observatory Adaptive Optics Facility*' Proc. SPIE **3353,** p568-578, (1998).
[149] P. L. Wizinowich, D. S. Acton, O. Lai, J. Gathright, W. Lupton, P. Stomski, '*Performance of the W. M. Keck Observatory Natural Guide Star Adaptive Optics Facility: the first year at the telescope*' Proc. SPIE **4007,** p2-13, (2000).
[150] P. L. Wizinowich, J. Chin, E. Johansson, S. Kellner, R. Lafon, D. Le Mignant, C. Neyman, P. Stomski, D. Summers, R. Sumner, M. van Dam, '*Adaptive Optics Developments at Keck Observatory*' Proc. SPIE **6272,** 9, (2006).
[151] P. L. Wizinowich, D. Le Mignant, P. Stomski, D. S. Acton, A. R. Contos, C. R. Neyman, '*Adaptive Optics Development at Keck Observatory*' Proc. SPIE **4839,** p9-20, (2003)
[152] I. S. McLean, S. M. Adkins, '*Instrumentation Developments at the W. M. Keck Observatory*' Proc. SPIE **6269,** 3, (2006).
[153] M. van Dam, E. Johansson, P. Stomski, R. Sumner, J. Chin, P. Wizinowich, '*Performance of the Keck II AO system*' Keck Adaptive Optics Note **489,** (2007).
[154] P. L. Wizinowich, D. Le Mignant, A. Bouchez, J. Chin, A. Contos, S. Hartman, E. Johansson, R. Lafon, C. R. Neyman, P. Stomski, D. Summers, M. V. Dam, '*Adaptive Optics Developments at Keck Observatory*' Proc. SPIE **5490,** p1-11, (2004).
[155] B. R. Oppenheimer, D. Palmer, R. Dekany, A. Sivaramakrishnan, M. Ealey, T. Price, '*Investigating a Xinetics Inc. Deformable Mirror*' Proc. SPIE **3126,** p569-579, (1998).

[156] K. Avicola, J. A. Watson, B. Beeman, J. Taylor, '*Design and Performance of the Tip-Tilt Subsystem for the Keck II Telescope Adaptive Optics System*' Proc. SPIE **3353,** p628-637, (1998).
[157] A. R. Contos, P. L. Wizinowich, S. K. Hartman, D. Le Mignant, C. R. Neyman, P. J. Stomski Jr, D. Summers, '*Laser guide star adaptive optics at the Keck Observatory*' Proc. SPIE **4839,** p370-380, (2003).
[158] J. M. Brase, J. An, K. Avicola, B. V. Beeman, D. T. Gavel, R. Hurd, B. Johnston, H. Jones, T. Kuklo, C. E. Max, S. S. Olivier, K. Waltjen and J. A. Watson, '*The wavefront control system for the Keck Telescope*' Proc. SPIE **3353,** p517-521, (1998).
[159] M. A. van Dam, D. L. Mignant, B. A. Macintosh, '*Performance of the Keck Observatory adaptive optics system*' Applied Optics **43,** p5458-5467 (2004).
[160] E. Johansson, D. S. Acton, J. R. An, K. Avicola, B. V. Beeman, J. M. Brase, C. J. Carraon, J. Gathright, D. T. Gavel, R. L. Hurd, O. Lai, W. Lupton, B. A. Macintosh, C. E. Max, S. S. Olivier, J. C. Shelton, P. J. Stomski, K. Tsubota, K. E. Waltjen, J. A. Watson, P. L. Wizinowich, '*Initial performance of the Keck AO wavefront controller system*' Proc. SPIE **4007,** p600-607, (2000).
[161] I. S. McLean, S. Adkins, '*Instrumentation at the Keck Observatory*' Proc. SPIE **5492,** p1-12, (2004).
[162] M. A. Van Dam, B. A. Macintosh, '*Characterization of adaptive optics at Keck Observatory*' Proc. SPIE **5169,** p1-10, (2003).
[163] M. A. Van Dam, D. Le Mignant, B. A. Macintosh, '*Characterization of adaptive optics at Keck Observatory: part II*' Proc. SPIE **5490,** p174-183, (2004).
[164] http://www.naoj.org (2008).
[165] M. Iye, '*Subaru Instrumentation: Today and Tomorrow*' Proc. SPIE **5492,** p23-34, (2004).
[166] H. Takami, M. Iye, '*Membrane deformable mirror for SUBARU adaptive optics*' Proc. SPIE **2201,** p762-767, (1994).
[167] H. Takami, N. Takato, M. Otsubo, T. Kanzawa, Y. Kamata, K. Nakashima, M. Iye, '*Adaptive optics system for Cassegrain focus of Subaru 8.2m telescope*' Proc. SPIE **3353,** p500-507, (1998).
[168] Y. Hayano, H. Takami, N. Takato, T. Kanzawa, Y. Kamata, K. Nakashima, M. Iye, S. Oya, '*Preliminary experiments of prototype laser guide star system for Subaru Telescope*' Proc. SPIE **4007,** p149-154, (2000).
[169] M. Iye, '*Current and Future Subaru Instruments*' Proc. SPIE **6269,** 5, (2006).
[170] H. Takami, M. Watanabe, N. Takato, S. Colley, M. Eldred, T. Kane, O. Guyon, M. Hattori, M. Goto, M. Iye, Y. Hayano, Y. Kamata, N. Arimoto, N. Kobayashi, Y. Minowa, '*Laser guide star AO project at the Subaru Telescope*' Proc. SPIE **5490,** p837-845, (2004).
[171] Y. Hayano, H. Takami, W. Gaessler, N. Takato, M. Goto, Y. Kamata, Y. Minowa, N. Kobayashi, M. Iye, '*Upgrade plans for Subaru AO system*' Proc. SPIE **4839,** p32-43, (2003).
[172] W. Gaessler, H. Takani, N. Takato, Y. Hayano, Y. Kamata, D. Saint-Jacques, Y. Minowa, M. Iye, '*First results from the Subaru AO system*' Proc. SPIE **4494,** p30-39, (2002).
[173] H. Takami, N. Takato, Y. Hayano, M. Iye, Y. Kamata, Y. Minowa, T. Kanzawa, W. Gaessler, '*Performance of Subaru adaptive optics system and the scientific results*' Proc. SPIE **4839,** p21-31, (2003).
[174] S. Oya, N. Takato, H. Takami, Y. Hayano, M. Iye, H. Terada, K. Murakawa, Y. Minowa, M. Hattori, M. Watanabe, Y. Kamata, T. Kanzawa, T. Kane, W. Gaessler, '*Subaru adaptive optics system after two years of open use*' Proc. SPIE **5490,** p409-420, (2004).
[175] W. Gaessler, H. Takami, N. Takato, Y. Hayano, Y. Kamata, D. Saint-Jacques, Y. Minowa, M.Iye, '*Software and Algorithms of Subaru AO*' Proc. SPIE **4839,** p954-963, (2003).

[176] N. Kobayashi, A. T. Tokunaga, H. Terada, M. Goto, M. Weber, R. Potter, P. M. Onaka, G. K. Ching, T. T. Young, K. Fletcher, D. Neil, L. Robertson, D. Cook, M. Imanishi and D. W. Warren, '*IRCS: infrared camera and spectrograph for the Subaru Telescope*' Proc. SPIE **4008,** p1056-1066, (2000).
[177] M. Tamura, H. Suto, Y. Itoh, N. Ebizuka, Y. Doi, K. Murakawa, S. S. Hayashi, Y. Oasa, H. Takami, N. Kaifu, '*Coronagraph imager with adaptive optics (CIAO): description and first results*' Proc. SPIE **4008,** p1153-1161, (2000).
[178] M. Watanabe, H. Takami, N. Takato, S. Colley, M. Eldred, T. Kane, O. Guyon, M. Hattori, M. Goto, M. Iye, Y. Hayano, Y. Kamata, N. Arimoto, N. Kobayashi, Y. Minowa, '*Design of the Subaru laser guide star adaptive optics module*' Proc. SPIE **5490,** p1096-1104, (2004).
[179] H. Takami, S. Colley, M. Dinkins, M. Eldred, O. Guyon, T. Golota, M. Hattori, Y. Hayano, M. Ito, M. Iye, S. Oya, Y. Saito, M. Watanabe, '*Status of Subaru Laser Guide Star AO System*' Proc. SPIE **6272,** C, (2006).
[180] S. Oya, O. Guyon, M. Watanabe, Y. Hayano, H. Takami, M. Iye, N. Arimoto, S. Colley, M. Eldred, T. Kane, M. Hattori, Y. Saito, Y. Kamata, N. Kobayashi, Y. Minowa, M. Goto, N. Takato, '*Deformable mirror design of Subaru LGSAO system*' Proc. SPIE **5490,** p1546-1555, (2004).
[181] Y. Hayano, Y. Saito, N. Saito, K. Akagawa, Y. Kamata, T. Kanzawa, T. Kurakami, N. Takato, S. Colley, M. Eldred, T. Kane, O. Guyon, S. Oya, M. Watanabe, M. Hattori, T. Golota, M. Dinkins, N. Kobayashi, Y. Minowa, M. Goto, N. Arimoto, S. Wada, H. Takami, M. Iye, '*Design of laser system for Subaru LGS AO*' Proc. SPIE **5490,** p1088-1095, (2004).
[182] http://www.mmto.org/ (2008).
[183] D. L. Miller, G. Brusa, M. Kenworthy, P. Hinz, D. Fisher, '*Status of the NGS Adaptive Optic System at the MMT Telescope*' Proc. SPIE **5490,** p207-215, (2004).
[184] http://webserv.caha.es/CAHA/ (2008).
[185] J. B. Costa, M. Feldt, K. Wagner, P. Bizenberger, S. Hippler, H. Baumeister, M. Stumpf, R. Ragazzoni, S. Esposito, T. Henning, '*Status Report of PYRAMIR – A Near-Infrared Pyramid Wavefront Sensor for ALFA*' Proc. SPIE **5490,** p1189-1199, (2004).
[186] http://www.tng.iac.es (2008).
[187] A. Ghedina, W. Gaessler, M. Cecconi, R. Ragazzoni, A. Puglisi, F. De Bonis, '*Latest developments on the loop control system of AdOpt@TNG*' Proc. SPIE **5490,** p1347-1355, (2004).
[188] http://www.ucolick.org/ (2008).
[189] B. J. Bauman, D. T. Gavel, K. E. Waltjen, G. J. Freeze, R. L. Hurd, E. L. Gates, C. E. Max, S. S. Olivier, D. M. Pennington, '*Update on optical design of adaptive optics system at Lick Observatory*' Proc. SPIE **4494,** p19-29, (2002).
[190] http://www.cfht.hawaii.edu (2008).
[191] O. Lai, F. Ménard, J. C. Cuillandre, '*PUEO NUI: a feasible AND fast upgrade of the CFHT adaptive optics system for high dynamic range imaging*' Proc. SPIE **4839,** p659-672, (2003).
[192] http://www.gtc.iac.es/home.html (2008).
[193] N. Devaney, D. Bello, B. Fermenia, J. Castro, A. V. Lopez, M. Reyes, J. J. Fuensalida, '*Preliminary design and plans for the GTC adaptive optics system*' Proc. SPIE **5490,** p913-923, (2004).
[194] R. M. Wagner, '*An Overview of Instrumentation for the Large Binocular Telescope*' Proc. SPIE **6269,** 9, (2006).
[195] http://www.lbto.org/ (2008).
[196] R. Biasi, M. Andrighettoni, A. Riccardi, V. Biliotti, L. Fini, P. Mantegazza, D. Gallieni, '*Dedicated flexible electronics for adaptive secondary control*' Proc. SPIE **5490,** p1502-1513, (2004).

[197] J. Farinato, R. Ragazzoni, C. Arcidiacono, G. Giorgia, E. Diolaiti, I. Foppiani, M. Lombini, L. Schreiber, D. Lorenzetti, F. D'Alessio, G. Li Causi, F. Pedichini, F. Vitali, T. Herbst, M. Kurster, P. Bizenberger, F. Briegel, F. De Bonis, S. Egner, W. Gassler, L. Mohr, A. Pavlov, R. R. Rohloff, R. Soci, '*The MCAO wavefront sensing system of LINC-NIRVANA: status report*' Proc. SPIE **6272,** 29, (2006).
[198] T. R. Rimmele, '*Recent advances in solar adaptive optics*' Proc. SPIE **5490,** p34-46, (2004).
[199] http://www.astro.lsa.umich.edu/magellan/ (2008).
[200] M. Johns, R. Angel, S. Shectman, R. Bernstein, D. Fabricant, P. McCarthy, M. Phillips, '*Status of the Giant Magellan Telescope (GMT) Project*' Proc. SPIE **5489,** p441-453, (2004).
[201] A. Athey, S. Shectman, P. Schechter, B. Lane, '*The GMT Ground Layer AO Experiment at the Magellan Telescopes*' Proc. SPIE **5490,** p960-965, (2004).
[202] Giant Magellan Telescope Organization, '*GMT Conceptual Design Document*' http://www.gmto.org/CoDRpublic, (2007).
[203] http://www.tmt/org (2008).
[204] TMT Observatory Corporation, '*TMT Construction Proposal*', TMT.PMO.MGT.07.009, (2007).
[205] http://www.eso.org/public/astronomy/projects/e-elt.html (2008).
[206] ELT-AO Working Group Document
[207] http://www.ing.iac.es (2008).
[208] D. Carter, R. E. S. Clegg, '*Observers' Guide*' ING La Palma, (1994).
[209] A. P. Doel, C. N. Dunlop, J. V. Major, R. M. Myers & R. M. Sharples, '*MARTINI: System Operation and Astronomical Performance*' Proc. SPIE **1542,** p319-325, (1991).
[210] R. M. Myers, A. P. Doel, C. N. Dunlop, J. V. Major, R. M. Sharples, A. J. A. Vick, '*An astronomical AO system for use on a 4m-class telescope at optical wavelengths*' Proc. SPIE **2201,** p437-445, (1994).
[211] A.P. Doel, C. N. Dunlop, J.V. Major, R. M. Myers, R. M. Sharples, '*MARTINI: sensing and control system design*' Proc. SPIE **1543,** p472-478, (1991).
[212] A. P. Doel, C. N. Dunlop, D. F. Buscher, R. M. Myers, R. M. Sharples, J. V. Major, '*The MARTINI adaptive optics instrument*' New Astronomy, **5,** p223-233, (2000).
[213] A. P. Doel, '*An Adaptive Optics System for Astronomical Image Sharpening*' PhD Thesis, (1990).
[214] R. M. Myers, A. J. Longmore, R. Humphreys, G. Gilmore, B. Gentles, M. Wells, R. W. Wilson, '*The UK Adaptive Optics Programme*', Proc. SPIE **2534,** p48-52, (1995).
[215] B. Gentles, M. Wells, A. Longmore, R. M. Myers, R. Humphreys, '*Natural guide star AO System for the WHT*', Proc. SPIE **2534,** p62-71, (1995).
[216] A. Longmore, M. Wells, M. Strachan, D. Dixon, T. Peacocke, R. M. Myers, R. Humphreys, B. Gentles, S. Worswick, A. Weise, '*Progress on the WHT Natural Guide Star AO System – NAOMI*' Proc. SPIE **3126,** p18-26, (1997).
[217] D. F. Buscher, A. P. Doel, C. A. Haniff, R. W. Wilson, '*Visible wavelength diffraction-limited imaging using low-order adaptive optics*' Proc. SPIE **2534,** p53-61, (1995).
[218] M. P. J. L. Chang, A. Zadrozny, D. F. Buscher, C. N. Dunlop and D. J. Robertson, '*Hysterisis correction of a piezoelectrically actuated segmented mirror*' Proc. SPIE **3353,** p864-870, (1998).
[219] R. M. Brockie, M. Wells, P. Gallant, G. J. M. Aitken '*Predictors in the servo-loop of an AO system*', Proc. SPIE **3353,** p1186-1192, (1998).
[220] NAOMI Project Team, '*Durham University ELECTRA-NAOMI-Agreement*' wht-naomi-65, (1996).

[221] R. G. Talbot, D. Abrams, C. R. Benn, A. K. Chopping, K. M. Dee, S. Els, M. Fisher, S. J. Goodsell, D. Gray, P. D. Jolley, '*GRACE: a controlled environment for adaptive optics at the William Herschel Telescope*' Proc. SPIE **5490,** p462-472, (2004).
[222] C. Packham, K. L. Thompson, A. Zurita, J. H. Knapen, I. Smail, R. Breimel, D. F. M. Folha, C. Benn, A. Humphrey, R. Rutten, D. Ciardi, M. Bec, R. Bingham, S. Craig, K. M. Dee, D. Ives, P. D. Jolley, P. Moore, M. Puig, S. G. Rees, R. G. Talbot, S. Worswick, '*INGRID: A near-infrared camera for the William Herschel Telescope*', MNRAS, **345**, p395-405, (2003).
[223] S. G. Rees, P. D. Jolley, M. van der Hoeven, A. W. Ridings, M. Blanken, '*INGRID: retrofitting an improved mechanism control system to an operational cryogenic instrument*' Proc. SPIE **5492,** p1665-1677, (2004).
[224] S. Thompson, P. Doel, R. Bingham, A. Charalambous, N. Bissonauth, P. Clark, R. M. Myers, R. G. Talbot, '*OSCA, an Optimised Stellar Coronagraph for Adaptive optics: Description and first light*', Proc. SPIE **4839,** p1085-1092, (2003).
[225] S. J. Thompson, A. P. Doel, R. G. Bingham, A. Charalambous, R. M. Myers, N. Bissonauth, P. Clark, R. G. Talbot, '*Results from the adaptive optics coronagraph at the William Herschel Telescope*', MNRAS **364**, p1203-1210, (2005).
[226] R. McDermid, R. Bacon, G. Adam, C. Benn, M. Cappellari, '*Adaptive Optics- Assisted Integral Field Spectroscopy with OASIS and NAOMI*', Proc. SPIE **5492**, p822-829, (2004).
[227] P. Jolley, S. J. Goodsell, C. R. Benn, T. Gregory, S. G. Rees, M. van der Hoeven, M. F. Blanken, R. Pitt, '*Recent Enhancements to the NAOMI AO System*' Proc. SPIE **5490,** p280-288, (2004).
[228] P. Clark, N. Bissonauth, J. O'Byrne, C. N. Dunlop, T. Gregory, T. J. Morris, R. M. Myers, C. D. Saunter, R. W. Wilson, '*Rayleigh guide star AO demonstrator for the 4.2m William Herschel Telescope*' Proc. SPIE **4839,** p516-523, (2003).
[229] R. G. M. Rutten, P. Clark, R. M. Myers, R. W. Wilson, R. G. Bingham, E. Emsellem, T. Gregory, R. A. Humphreys, J. H. Knapen, G. Moretto, S. L. Morris, R. G. Talbot, '*Facility class Rayleigh beacon AO system for the 4.2m William Herschel Telescope*' Proc. SPIE **4839** p360-369 (2002).
[230] R. Rutten, M. Blanken, R. McDermid, T. Gregory, P. Jolley, T. Morris, R. M. Myers, J. Pragt, T. Schoenmaker, R. Stuik, R. G. Talbot, '*Prospects for the GLAS Rayleigh laser beacon on the 4.2m WHT*' New Astronomy Reviews **49**, p632-638, (2006).
[231] R. G. Talbot, D. C. Abrams, R. Bassom, M. F. Blanken, D. C. Infantes, A. K. Chopping, K. M. Dee, N. A. Dipper, E. Elswijk, T. Gregory, R. ter Horst, R. Humphreys, P. D. Jolley, S. Kuindersma, R. McDermid, T. J. Morris, R. M. Myers, S. Pico, J. Pragt, S. G. Rees, J. Ruerg, M. Reyes, R. G. M. Rutten, T. Schoenmaker, J. Skvarc, N. Tromp, S. Tulloch, A. Veninga, '*GLAS: engineering a common-user Rayleigh laser guide star for adaptive optics on the William Herschel Telescope*', Proc. SPIE **6272,** 2H, (2006).
[232] C. Packham, N. O'Mahony, R. W. Wilson, '*Recent developments in the Half Arcsecond Programme*' New Astronomy Reviews, **42**, p431-433, (1998).
[233] R. W. Wilson, N. O'Mahony, C. Packham and M. Azzaro, '*The seeing at the William Herschel Telescope*', MNRAS, **309**, p379-387, (1999).
[234] C. Packham, R. W. Wilson, M. Azzaro, N. O'Mahony, S. Fine, D. Gray, V. Reyes, C. Martin, '*The Half Arcsecond Programme (I)*', The ING Newsletter, **2**, p21-23, (2000).
[235] R. W. Wilson, '*Results of the JOSE site evaluation project for adaptive optics at the William Herschel Telescope*', NAR, **42**, p465-469, (1998).
[236] NAOMI Project Team, '*Baseline Optical Chassis Work Package Description*', wht-naomi-56, (1998).

[237] NAOMI Project Team, '*Baseline Wavefront Sensor Work Package Description*', wht-naomi-57, (1997).
[238] R. W. Wilson, '*SLODAR: measuring optical turbulence altitude with a Shack-Hartmann wavefront sensor*', MNRAS, **337**, p103-108, (2002).
[239] I. K. Sochting, R. W. Wilson, A. Longmore, C. R. Benn, R. Ostensen, S. Els, S. J. Goodsell, T. Gregory, R. G. Talbot, '*Influence of restricted FOV and CCD binning in SH-WFS on the performance of NAOMI*' Proc. SPIE **5490**, p574-579, (2004).
[240] T. J. Morris, R. W. Wilson, R. M. Myers, T. Butterley, R. G. M. Rutten, R. G. Talbot, '*Performance predictions for the GLAS Rayleigh LGS AO system*' Proc. SPIE **6272**, 37, (2006).
[241] T. J. Morris, '*An Experimental Rayleigh Laser Guide Star Ground Layer Adaptive Optics System for the William Herschel Telescope*' PhD Thesis, (2005).
[242] NAOMI Project Team, '*NAOMI CCD CAMERAS – Test Results*' wht-naomi-31, (2000).
[243] D. Ives, '*NAOMI WFS CCD Camera Control*' wht-naomi-1, (1999).
[244] X. Gao, '*ICD 1.0 version for NAOMI WFS Camera – Part 2*' wht-naomi-2, (2000).
[245] X. Gao, '*ICD 1.0 version for NAOMI WFS Camera – Part 3*' wht-naomi-3, (2000).
[246] X. Gao, '*Setup and Test Procedure for NAOMI SDSU software*' wht-naomi-28, (2003).
[247] X. Gao, '*NAOMI WFS CCD Results*', wht-naomi-29, (2003).
[248] NAOMI Project Team, '*Fast Steering Mirror Test Procedure*' wht-naomi-37, (1998).
[249] D. Buscher, '*The GP messing library*' wht-naomi-9, (1999).
[250] R. M. Myers, S. J. Goodsell, '*The Real Time Control System Programmers Guide*' wht-naomi-24, (2002).
[251] R. M. Myers, S. J. Goodsell, '*The Real Time Control System Users Guide*' wht-naomi-25, (2002).
[252] B. Graham, '*NAOMI Electronic system Overview*' wht-naomi-13, (2000).
[253] P. Clark, '*NAOMI Hardware Reference Manual*' wht-naomi-10, (2000).
[254] S. J. Goodsell, R. M. Myers, P. Clark, D. Buscher, '*The Real-time Control System of NAOMI*' Proc. SPIE **5496**, p618-628, (2004).
[255] http://en.wikipedia.org/wiki/Bulk_synchronous_parallel (2008).
[256] J. C. Carson, '*The Cornell High-order Adaptive Optics Survey for Brown Dwarf Companions and Related Instrumentation Studies for Brown Dwarf Research*' PhD Thesis, Cornell University (2005).
[257] I. K. Sochting, '*Modeling the Performance of NAOMI*', wht-naomi-106, (2003).
[258] S. J. Goodsell, A. G. Basden, E. Fedrigo, D. Geng, R. M. Myers, '*FPGA based AO projects at Durham University*', OSA Adaptive Optics: Analysis and Methods (AO) paper (2005).
[259] S. J. Goodsell, N. A. Dipper, D. Geng, R. M. Myers, C. D. Saunter, '*DARTS: a low-cost high-performance FPGA implemented real-time control platform for adaptive optics*', Proc. SPIE **5903**, E, (2005).
[260] D. Geng, C. D. Saunter, N. A. Dipper, R. M. Myers, S. J. Goodsell, E. Fedrigo, R. Donaldson, C. Soenke, '*FPGA Cluster for High Performance AO Real-time Control System*' Proc. SPIE **6272**, 40, (2006).
[261] S. J. Goodsell, E. Fedrigo, N. A. Dipper, R. Donaldson, D. Geng, R. M. Myers, C. D. Saunter, C. Soenke, '*FPGA developments for the SPARTA project*' Proc. SPIE **5903**, G, (2005).
[262] S. J. Goodsell, E. Fedrigo, N. A. Dipper, R. Donaldson, D. Geng, R. M. Myers, C. D. Saunter, C. Soenke, '*FPGA developments for the SPARTA project: Part 2*' Proc. SPIE **6272**, 41, (2006).

[263] S. J. Goodsell, E. Fedrigo, N. A. Dipper, R. Donaldson, D. Geng, R. M. Myers, E. Younger, C. Soenke, '*FPGA developments for the SPARTA project: Part 3*' Proc. SPIE **6691**, 3, (2007).
[264] E. Fedrigo, R. Donaldson, C. Soenke, R. M. Myers, S. J. Goodsell, D. Geng, C. D. Saunter, N. A. Dipper, '*SPARTA, the ESO Standard Platform for Adaptive optics Real Time Applications*', Proc. SPIE **6272**, 10, (2006).
[265] VITA, '*2eSST Source Synchronous Transfer, ANSI/VITA 1.5-2003*' http://www.vita.com/pubslist.html, (2003).
[266] VITA, '*Serial Front Panel Data Port (FPDP), ANSI/VITA 17.1-2003*' http://www.vita.com/pubslist.html, (2003).
[267] E. Vernet, M. Kasper, C. Verinaud, E. Fedrigo, S. Tordo, N. Hubin, S. Esposito, E. Pinna, A. Puglisi, A. Tozzi, A.G. Basden, S. J. Goodsell, G. D. Love, R. M. Myers, '*Extreme adaptive optics system optimization with the High Order Test bench*', Proc. SPIE **6272**, 2W, (2006)
[268] F. Roddier, '*Curvature Sensing: a Diffraction Theory*' NOAO R&D Note No 87-3, (1987).
[269] S. Esposito, A. Riccardi, '*Pyramid wavefront sensor behaviour in partial correction adaptive optics system*' Astron. Astrophys. **369**, L9-L12, (2001).
[270] D. P Greenwood, C. A. Primmerman, '*Adaptive optics research at Lincoln Laboratory*' Lincoln Lab. J. **5**, p3-23 (1992).
[271] D. G. Sandler, L. Cuellar, M. Lefebvre, R. Barrett, R. Arnold, P. Johnson, '*Shearing interferometry for laser-guide-star atmospheric correction at large D/r_0*' J. Opt. Soc. Am. A, **11**, p858-873 (1994).
[272] C. L. Koliopoulos, '*Radial grating lateral shear heterodyne interferometer*' Appl. Opt. **19**, p1523-8, (1980).
[273] J. W. Hardy, J. E. Lefebvre, C. L. Koliopoulos, '*Real-time atmospheric compensation*' J. Opt. Soc. Am **67**, p360-369 (1977).
[274] E. Steinhaus, S. G. Lipson, '*Bimorph piezoelectric flexible mirror*' J. Opt. Soc. Am. **69**, p478-481, (1979).
[275] N. T. Adelman, '*Spherical mirror with piezoelectrically controlled curvature*' Appl Opt **16**, p3075-3077, (1977).
[276] P. Halevi, '*Bimorph piezoelectric flexible mirror: graphical solution and comparison with experiment*' J. Opt. Soc. Am **73**, p110-113, (1983).
[277] S. A. Kokorowski, '*Analysis of adaptive optical elements made from piezoelectric bimorphs*' J. Opt. Soc. Am. **69**, p181-187, (1979).
[278] M. A. Vorontsov, A. V. Kudryashov, S. I. Nazarkin, V. I. Shmal'gauzen, '*Flexible mirror for adaptive light-beam formation systems*' Sov. J. Quantum Electron. **14**, p839-841, (1984).
[279] J. Riehl, E. Taufflieb, M. Sechaud, '*Modulateurs spatiaux de phase: applications a l'optique adaptative*' ONERA Technical Report 65/7177 SY, Nov 1988, (1988).
[280] M. A. Vorontsov, V. A. Katulin, A. F. Naumov, '*Wavefront control by an optical-feedback interferometer*' Opt. Commun. **71**, p35-8, (1989).
[281] D. Bonaccini, G. Brusa, S. Esposito, P. Salinari, P. Stefanini, V. Biliotto, '*Adaptive optics wavefront corrector using addressable liquid crystal retarders II*' Proc. SPIE **1543**, p422-9, (1991).
[282] P. G. De Gennes, '*The Physics of Liquid Crystals*' Clarendon Press, Oxford, (1975).
[283] S. T. Wu, '*Toward high speed modulation by nematic liquid crystals*' Proc. SPIE **567**, p74, (1985).
[284] G. D. Love, J. V. Major, A. Purvis, '*Liquid-crystal prisms for tip-tilt adaptive optics*' Opt. Lett. **19** p1170-2, (1994).

[285] G. D. Love, S. R. Restino, '*High quality liquid crystal spatial light modulators for adaptive optics*' OSA Technical Digest Series **23**, p223-5, (1995).
[286] G. D. Love, J. Gourlay, '*Intensity-only modulation for atmospheric scintillation correction by liquid-crystal spatial light modulators*' Opt. Lett. **21**, p1496-8, (1996).
[287] E. P. Wallner, '*Optimal wave-front correction using slope measurements*' J. Opt. Soc. Am. **73**, p1771, (1983).
[288] C. Dainty, G. D. Love, C. Paterson, '*A Short Course in Adaptive Optics*' Imperial College London, (2003).
[289] M. C. Roggemann, A. C. Koivunen, '*Branch-point reconstruction in laser beam projection through turbulence with finite-degree-of-freedom phase-only wave-front correction*' J. Optical Soc. America A – Optics Image Science Vision, **17**, p53-62, (2000).